OCTOBER-DECEMBER 2021 VOL. 13 № 4 (51)

ISSN 2075-8251

ActaNaturae

Molecular Tools for Targeted Control of Nerve Cell Electrical Activity

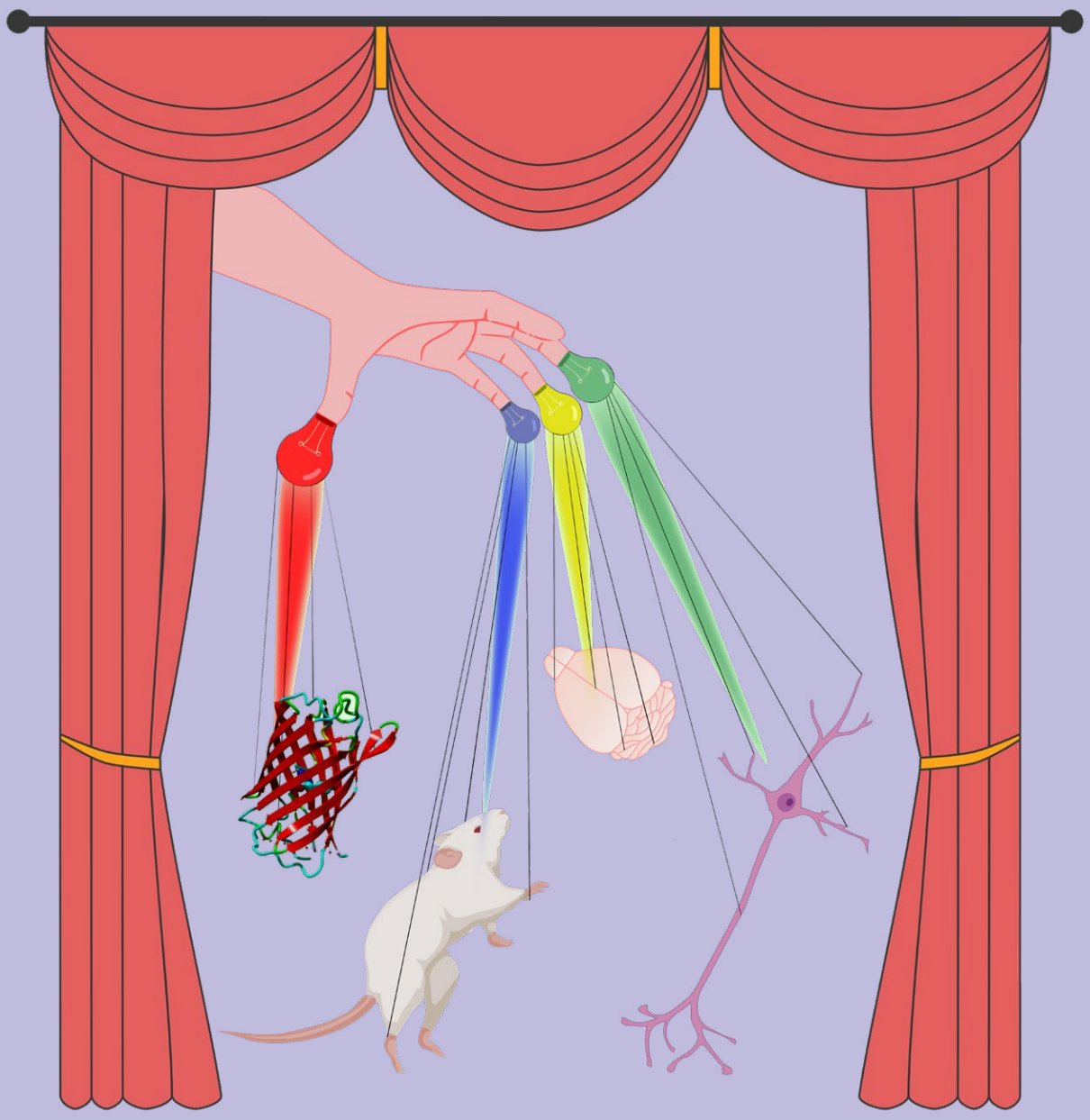

Mechanism of Action of Monoclonal Antibodies That Block the Activity of the Lethal Toxin of *Bacillus Anthracis*

Ya. O. Romanenko, A. K. Riabko, M. A. Marin, A. S. Kartseva, M. V. Silkina, I. G. Shemyakin, V. V. Firstova

A neutralizing monoclonal antibody 1E10 against lethal toxin *Bacillus anthracis* was obtain. The stepwise mechanism for the inhibition of lethal toxin by the 1E10 monoclonal antibody was studied. The interaction between the 1E10 monoclonal antibody and the protective antigen ensures inhibition of enzyme activity of the lethal factor at the stage of true pore formation.

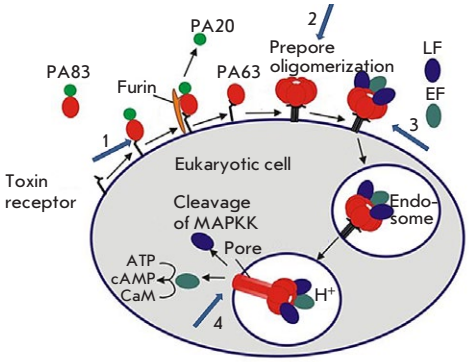

Schematic model of the assembly and activity *of B. anthracis* toxins

Extracellular Vesicles from Mycoplasmas Can Penetrate Eukaryotic Cells *In Vitro* and Modulate the Cellular Proteome

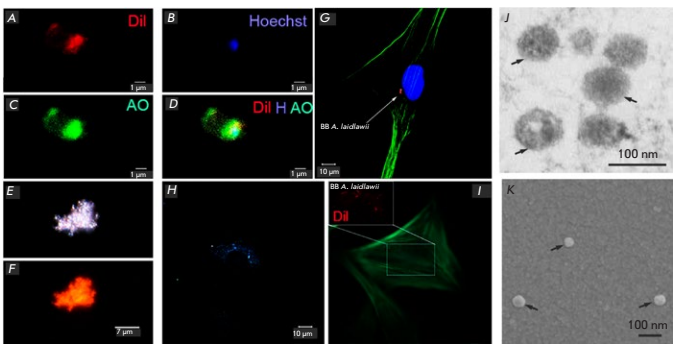

Interaction of human skin fibroblasts with EVs of *A. laidlawii*

A. A. Mouzykantov, E. V. Rozhina, R. F. Fakhrullin, M. O. Gomzikova, M. A. Zolotykh, O. A. Chernova, V. M. Chernov

Extracellular vesicles secreted by bacteria mediate the intracellular interactions and can be important participants in the mechanisms for persistence of infectious agents. This study has shown for the first time that extracellular vesicles from *Acholeplasma laidlawii* (class Mollicutes), a ubiquitous mycoplasma species that infects higher eukaryotes and is the main cell culture and vaccine contaminant, can penetrate into eukaryotic cells and modulate the cellular proteome.

The Hydrodynamics of a Swirling Blood Flow in the Left Heart and Aorta

A. V. Agafonov, E. A. Talygin, L. A. Bockeria, A. Yu. Gorodkov

This paper proposes a new approach to the quantitative analysis of the hydrodynamic structure of a blood flow in the flow channel running from the left atrium to the end of the aorta. This approach is based on the concept of the structural organization of tornado-like swirling jets in channels with a given geometric configuration.

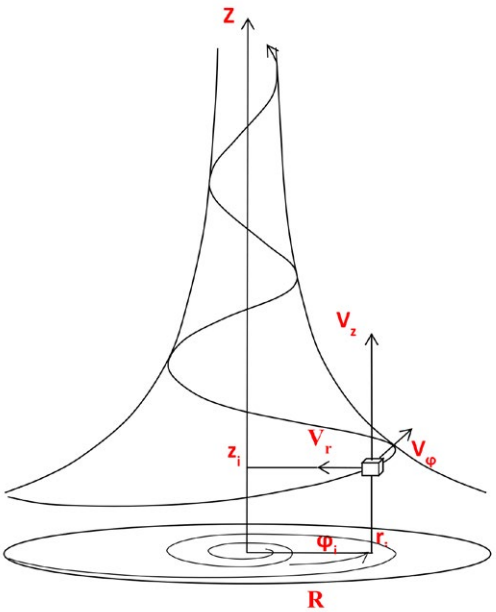

A schematic diagram of a swirling jet; the directions of coordinate axes and vectors of velocity components are indicated

ActaNaturae
OCTOBER-DECEMBER 2021 VOL. 13 № 4 (51)
since april 2009, 4 times a year

Founders
Acta Naturae, Ltd,
National Research University
Higher School of Economics

Adress: 101000, Moscow, Myasnitskaya Ulitsa, 13, str. 4
Phone/Fax: +7 (495) 727 38 60
E-mail: actanaturae@gmail.com

Номер подписан в печать 30 декабря 2021 г.
Тираж 25 экз. Цена свободная.
Отпечатано в типографии: НИУ ВШЭ,
г. Москва, Измайловское шоссе, 44, стр. 2

Indexed in Pubmed, Web of Science, Scopus, and RISC

Impact Factor: 1.845

CONTENTS

REVIEWS

RESEARCH ARTICLES

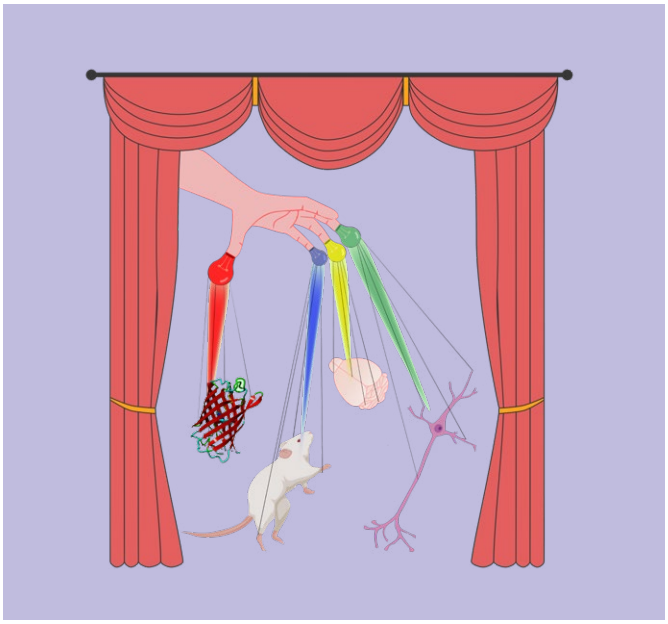

IMAGE ON THE COVER PAGE
(see the article by D. V. Kolesov et al.)

The Hydrodynamics of a Swirling Blood Flow in the Left Heart and Aorta

A. V. Agafonov, E. A. Talygin, L. A. Bockeria, A. Yu. Gorodkov*
Bakulev National Medical Research Center of Cardiovascular Surgery, Ministry of Health of the Russian Federation, Moscow, 121552 Russia
*E-mail: agorodkov@bk.ru
Received April 26, 2021; in final form, July 12, 2021
DOI: 10.32607/actanaturae.11439

ABSTRACT **This paper proposes a new approach to the quantitative analysis of the hydrodynamic structure of a blood flow in the flow channel running from the left atrium to the end of the aorta. This approach is based on the concept of the structural organization of tornado-like swirling jets in channels with a given geometric configuration. Considering the large amount of experimental data in our possession, it was shown that along the entire length of the flow channel, conditions exist for the generation and maintenance of a swirling structure of the jet throughout the entire cardiac cycle. This study has given rise to a new direction in research in fundamental physiology and medicine, which is of great practical importance for diagnosing and treating circulatory disorders accompanied by changes in the geometric configuration and biomechanical characteristics of the heart and great vessels.**
KEYWORDS **left atrium, left ventricle, aorta, swirling blood flow.**
ABBREVIATIONS **AV – aortic valve; HOCM – hypertrophic obstructive cardiomyopathy; PVs – pulmonary veins; LV – left ventricle; LA – left atrium; MV – mitral valve; MSCT – multislice computed tomography; PMs – papillary muscles; LAA – left atrial appendage; P_{lv} – left ventricular pressure; P_{LA} – left atrial pressure.**

INTRODUCTION

In a living organism, there exists a certain hierarchy between organs and organ systems which determines the degree to which life is maintained. The circulatory system ensuring uninterrupted and sustained functioning of the entire organism holds first place in this hierarchy. Therefore, there is a broad range of circulatory states that exist without a disruption of the stability of the circulatory system and ensure an excessively high level of its adaptivity. We remain insufficiently informed about what underlies the hydrodynamic stability of the blood flow, which, at first glance, cannot be an organized structure because of its non-stationarity, complex geometric shape of mobile streamlined boundary surfaces, and the biological instability of the components of both the liquid medium and the flow channel walls. Nevertheless, the circulatory system can function at high pump pressure-flow characteristics and low energy consumption, it can change in size during an individual's growth and aging without losing its stability, and it can change its performance severalfold within the regulatory reserves of the organism and maintain its function by compensating for irreversible significant geometric and functional changes under pathological conditions.

Therefore, a special mechanism ensuring this stability (like a flywheel in mechanical systems) is needed. However, this mechanism has been defined or studied in neither fundamental physiology nor clinical cardiology.

Indeed, the entire history of research focusing on blood circulation has been based on the empirical approach. There is no theoretical conception that would substantiate the general mechanisms of the blood flow. Therefore, our methods for studying the blood flow have not been systematized and do not focus on a common objective (understanding the mechanism through which blood is supplied to the target organs). As a result, the established and currently acknowledged views on blood flows are rather controversial and rely on many assumptions, making it impossible to reach a consensus based on a uniform theoretical background.

The vast body of data accumulated when studying the blood flow in the heart and aorta does not allow for an appreciably accurate explanation of (I) how the relatively weak muscle pump drives 4–5 L

of blood per minute during one's life and overcomes the evidently high resistance to a flow in vascular beds so that determined blood distribution at vascular branching points is achieved, (II) how the sufficient venous return is ensured, (III) what are the mechanisms for the regulation of and compensation for cardiac output, etc.

Among all the things known about the physiology of circulation, only one single fact has been documented phenomenologically and has not been given a functional explanation: it is the fact that a blood flow is swirling at all the stages of its evolution in the heart and great arteries. This fact was first documented in the early 1930s [1] and has recently been repeatedly proved using modern diagnostic tools [2–5]. A number of research groups have addressed this phenomenon; however, the results of their studies have not made it possible to identify the mechanisms of generation of a blood flow swirl or propose reliable quantitative criteria for assessing the quality of a swirling blood jet [6, 7]. The benefits of a flow swirl stated in these studies have been formulated rather vaguely and are confined to a size reduction of the detachment and congestion zones and prevention of boundary layer thickening as the blood flow evolves [8]. Some papers have mentioned that the blood flow swirl in the aorta is related to the distribution of the field of shear rates along the aortic wall and can affect atherogenesis in the aorta and large arteries [9]. However, no one has ever attempted to explain what the undesirable sequelae of the disturbance of a blood flow swirl are (e.g., as it happens when mechanical prosthetic heart valves are inserted). Nonetheless, it is known that the clinical effectiveness of reconstructive cardiosurgical interventions is higher if a normal anatomical configuration of the left ventricular cavity is restored during the reconstruction [10].

Many researchers have studied the blood flow structure from the standpoint of the known flows (the laminar and turbulent ones); however, they failed to take into account the swirling of the blood flow; so, the physiological sense of this phenomenon could not be explained (e.g., in [11]). These attempts have been made only in a few studies, but they actually incorporated only the general reasoning that as a flow swirl is a physiological norm, it is favorable for blood circulation [12]. Thus, a flow swirl was viewed as a result of pathological changes in the aortic wall caused by stenosis or atherogenesis [13]. In a long series of studies, the vortical structures emerging in the left ventricular cavity were viewed as a result of the separation of a jet filling the cavity at the edge of the mitral valve leaflet [14, 15]. Only a series of studies conducted with the involvement of N.B. Kuz'mina has claimed that the blood flow swirl is an intrinsic property of normal circulation (e.g., [16]).

Swirling flows commonly occur in nature [17, 18] and in technological processes [19–23]. Despite the significant number of experimental and theoretical studies in existence, many phenomena related to swirling flows still remain poorly understood. In particular, no commonly accepted models of a tornado [17, 18], vortex decay [20], or an energy separation process in Ranque–Hilsch vortex tubes [20–23] exist today. This fact impedes the interpretation of the experiments, an indication of the complex organization of interacting vortical structures, which are often accompanied by instability and turbulence.

Simple approximated models of swirling flows can be pursued in the search for exact solutions to hydrodynamic equations [24, 25]. In particular, the solutions reported in ref. [24] are group-invariant solutions to the Navier–Stokes and continuity equations [26]. A problem often confronted consists in interpreting invariant solutions as exact or asymptotic solutions of a correct initial boundary value problem that has real physical meaning. For example, these solutions can be used to perform a quasi-steady-state analysis of complex dynamic systems. Another problem related to the analytical description of swirling flows is that there are a large number of paradoxes [27], probabilities of collapse, symmetry breaking, and hysteresis [28].

Meanwhile, swirling flows are now widely used in engineering as jet-based technologies, vortex generators, heat exchangers, burner devices, etc.

Our review attempts to systematize the results of research performed at the A.N. Bakulev National Medical Research Center of Cardiovascular Surgery over the past 20 years with a view to propose a non-controversial conception of the blood flow in the heart and great vessels based on existing views on a centripetal swirling flow of a viscous fluid.

EXACT SOLUTIONS TO NON-STEADY-STATE HYDRODYNAMIC EQUATIONS FOR THE CLASS OF CENTRIPETAL SWIRLING FLOWS OF A VISCOUS FLUID

The Navier–Stokes equations describe the motion of a viscous Newtonian fluid in classical hydrodynamics and are a system of differential equations in partial derivatives. These equations have no analytical solution. Nonetheless, they are widely used in mathematical modeling of many natural phenomena and engineering problems.

A quantum leap in the study of the role played by a blood flow swirl in the pump-transport segment of the circulatory system (the heart and great arteries) was achieved after a novel class of swirling jets

generated at the bottom of dimples having a certain shape, streamlined by a flow of the medium, and called "tornado-like jets" was discovered, identified, and formally described [29, 30]. It had been shown experimentally that tornado-like jets alter the flow pattern by substantially reducing the hydrodynamic drag and intensifying the heat and mass transfer on these surfaces. These hydrodynamic features have allowed researchers to put forward a hypothesis about the longitudinal and radial potentiality of the revealed jets and obtain exact solutions to the Navier–Stokes and continuity equations describing the structure of flows belonging to this class (i.e., the field of velocities and pressures over the entire jet volume) at specified initial and boundary conditions [24, 25].

We used the obtained solutions to the Navier–Stokes and continuity equations to perform a quasi-steady-state analysis of the features of the blood flow in the central circulatory system. In accordance with these solutions, any radially converging swirling flow can be exhaustively characterized in the cylindrical coordinate system using the magnitudes of velocity vectors in the longitudinal (u_z), radial (u_r), and tangential (u_φ) directions (*Figure*). Then, the total flow velocity u_Σ is written as:

$$u_\Sigma = \sqrt{u_r^2 + u_z^2 + u_\varphi^2}$$

The expressions for each velocity component in the general form are written as:

$$\begin{cases} u_r = C_0(t)r + \dfrac{2B\nu}{r} \\ u_z = -2C_0(t)z + C_2(t) \\ u_\varphi = \dfrac{\Gamma_0(t)}{2\pi r} + \sum\limits_i \dfrac{\Gamma_i(t)}{2\pi r}\Gamma\left[C_1 + 1, \beta_i(t)r^2\right] \end{cases}$$

where ν is the kinematic viscosity; $C_0(t)$, $C_2(t)$, $\Gamma_0(t)$, $\Gamma_i(t)$, $b_i(t)$ are arbitrary functions of time; and C_1, B are arbitrary constants. Γ[...] is the Euler Gamma function. Function $b_i(t)$ is defined by the equation

$$\beta_i(t) = \frac{\beta_0(t) \times e^{-2\int_0^t C_0(\tau_1)d\tau_1}}{1 + 4\nu\beta_i(0)\int_0^t e^{-2\int_0^{\tau_2} C_0(\tau_2)d\tau_2} d\tau_1},$$

where $b_i(0)$ is an arbitrary constant.

In this class of flows, one vortical jet differs from another in terms of the structural azimuthal component of velocity u_φ, but a common feature of all vortical structures belonging to this class consists in the potentiality of the radial (u_r) and longitudinal (u_z) components of velocity. The structure of the velocity

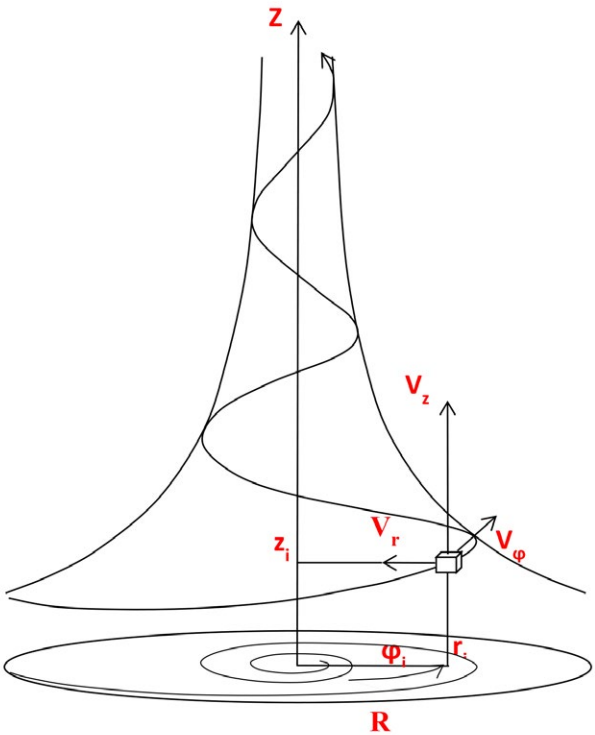

Figure. A schematic diagram of a swirling jet; the directions of coordinate axes and vectors of velocity components are indicated

of the simplest swirling jet in this class of flows is represented as

$$\begin{cases} u_z = 2C_0 z \\ u_r = -C_0 r \\ u_\varphi = \dfrac{\Gamma_0}{2\pi r}\left(1 - e^{\frac{-C_0 r^2}{2\nu}}\right) \end{cases}$$

In the relationships given above, u_z is the longitudinal component of velocity, u_r is the radial component of velocity, u_φ is the azimuthal component of velocity, $C_0(t)$ is the radial gradient of velocity (s^{-1}), $\Gamma_0(t)$ is the circulation of the jet (m^2/s), $C_0(t)$ and $\Gamma_0(t)$ are independent functions of time that vary because of the flow non-stationarity, and v is the kinematic viscosity of the medium (m^2/s).

These vortical jets spend energy for the measure of the inertance and viscosity of the swirling medium due to its rotation with an azimuthal velocity u_φ. The main dissipation depends on the vortex size and intensity and takes place in its near-axial zone with the radius

$$R = \sqrt{\frac{2k\nu}{C_0}},$$

which is a flow core, where k is a coefficient showing the degree to which the azimuthal velocity decreases as a result of energy loss in a swirling jet and C_0 is the velocity gradient in the vortex along its radius. This size determines the minimal size of the channel at which a swirling flow of the discussed type can exist at a given flow velocity and viscosity of the medium.

These expressions follow the structure of the Burgers vortex [31], with the only difference that they allow one to perform a quasi-steady-state analysis of a jet as the C_0, Γ_0 values and the geometric values in the flow channel change with time. However, the given equations meet the adhesion conditions in neither the longitudinal nor the azimuthal directions; so, it can be assumed that a special type of interactions exists at the flow boundary and in the flow core.

It should be emphasized that these jets differ qualitatively from the variety of swirling jets that are widely used in various engineering devices and are turbulent flows generated by forced swirling of the medium.

The experimental and theoretical studies of tornado-like jets have revealed evident analogies with the known properties of the blood flow and made it possible to substantiate a number of views on the mechanisms of generation, evolution, and stability of flows formed in the heart that hitherto seemed controversial [32–38].

RATIONALE FOR THE APPLICABILITY OF "EXACT SOLUTIONS" IN THE ANALYSIS OF THE SWIRLING BLOOD FLOW

Before we proceed to the analysis of these analogies, the critical aspects for the occurrence of a blood flow in the segment of the circulatory system under study should be formulated.

So, what do we expect from a blood flow in the heart and aorta?

1. Blood needs to flow constantly at an appreciably high rate.

2. Blood corpuscles need to move at the same rate, without delays, at any stage of the flow evolution, and complete the gas exchange cycle with the highest efficiency.

3. The interaction of blood corpuscles with each other and with biologically active blood cells in the flow core (to prevent their activation), as well as the interaction of blood corpuscles and biologically active blood proteins with the biologically active walls of the heart and vessels (especially at the stages when the blood flow velocity is high) at the flow boundary, needs to be minimized. In other words, there should be no flow congestion or detachment zones, while the shear stress level needs to be minimized.

4. The transition between one type of flow to another needs to occur without intermittent transitional processes (veins–heart–aorta–great arteries).

5. Changes in the size (as the organism grows) or functional characteristics of flow channels (as the organism ages) should not cause intermittent transitional processes.

6. The performance of the system in the segment under study needs to be able to change significantly (severalfold) as the geometric dimensions are minimally varied to ensure regulatory reserve of the cardiovascular system.

7. The system needs to be able to function and be stabilized if irreversible but not catastrophic changes in the geometric configuration or functional characteristics (mobility or elasticity of flow boundaries) occur, thus ensuring the system's compensatory reserve.

The "exact solutions" describing the structure of a jet emerging upon flowing past a dimple with a certain shape [24, 25] allow one to formulate the main experimentally confirmed properties of flows belonging to the class under study.

The key ones are outlined below:

1. Reduction of energy loss due to friction (viscosity). This means that the strain developing in the flow core and at the flow boundary is significantly reduced. This phenomenon was confirmed experimentally by measuring the drag in a flow past surfaces with dimples. It was shown that the swirling jets generated in the dimples and then integrated into the main flow significantly and reliably reduce hydrodynamic drag [13].

2. Structural organization; i.e., the moving elements of the medium travel along streamlines whose shape is predefined (an axially symmetric converging helix). The stream tube is a second-order hyperboloid of revolution. Within the stream tube, all elements of the medium move at the same angular velocity. The jet gets structurally organized at external swirl drivers: pre-swirling of the medium, asymmetry of the generating surface with respect to the jet axis, and guidance blades swirling the flow.

3. Transverse pressure gradients. As a jet rotates, a low-pressure region emerges in its axial zone. The larger the azimuthal velocity component, the higher the dynamic pressure gradients oriented transversely to the jet is. Therefore, the medium is sucked into the jet in the jet origination zone, where the azimuthal velocity component is maximal. Hence, the medium is supplied into the jet only at its end rather than at its

lateral boundary. This fact was proved experimentally by visualization of swirling jets in dimples [13].

4. The structure of the boundary layer. This type of swirling flow takes place only if there are special conditions in the beginning of the jet and at the jet boundary. These conditions imply that this boundary layer has a structure different from that for the Prandtl shear boundary layer. The experiments involving flowing past dimples made it possible to visualize the 3D vortex boundary layer in the jet base [13]. However, the challenges related to studying the boundary layer do not allow one to draw any definitive conclusions about its structure. The exact solutions used by us for the analysis do not take into account the condition of boundary-layer adhesion. This condition is probably met in some other way (e.g., by replacement of shear strain with rolling strain or slipping of the near-wall layers caused by the rheological properties of the medium.) The boundary layer in the circulatory bed is very thin and does not get thicker along the blood flow [11]. It is possible that these conditions are created here due to the pulsatile flow mode and the dynamically changing topography and mobility of the walls of the flow channel. They can also be met through the mechanism of the three-dimensional vortex boundary layer [39].

5. Convergence. Because of centripetal acceleration, all streamlines of a swirling flow are oriented from the jet periphery towards its axis. This means that the jet has external boundaries regardless of whether it moves inside the channel or inside the medium (with respect to the immobile medium). As its radius monotonically decreases, the jet is accelerated in the entire range of its existence. There is almost no transverse exchange with the ambient environment as demonstrated experimentally by a visualization of the swirling jets generated in the dimples [13].

6. Finiteness – a jet has a beginning and an end. The beginning of the jet corresponds to a zero point where all the velocity components are equal to zero (e.g., upon formation of a radial-azimuthal swirling flow over a concave curved surface (the generating surface)). If the rate of medium inflow inside this surface and the surface shape give rise to forces expelling the medium retaining its swirling motion, a swirling tornado-like jet is formed. The spot where the conditions maintaining the jet structure are no longer met (e.g., its radius decreases so significantly that the viscous drag forces in the axial zone of the jet become higher than its rotational inertia) can be considered the end of the jet. In this case, the jet degenerates into a turbulent or laminar flow depending on the residual velocity. The jet can be restructurized if the conditions required for its generation emerge again.

7. Stationarity/nonstationarity. The jet can be stationary. This is possible if jet generation conditions remain unchanged over time (the inflow rate, the curvature of the generating surface, and convergence of the flow channel correspond to the same stream tube). Then, the functional coefficients included in the "exact solutions" (the origin of the coordinate system, the product zr^2, and functions C_0 and Γ_0) are constants. The jet can also be nonstationary (decaying or pulsatile (i.e., periodically recurring)). In this case, the functional coefficients C_0 and Γ_0 change with time in accordance with the law of jet nonstationarity determined by external action.

8. Inertance of jet rotation – rotation of the medium in the jet has inertia; therefore, the time of jet generation is extremely short, while the time of jet decay is relatively long.

The aforelisted properties of centripetal swirling flows allow one to put forward a number of theses substantiating the possibility of using "exact solutions" to analyze the mechanism of the blood flow through the sections of the circulatory bed characterized by high velocities and appreciably large dimensions (e.g., in the arterial segment of the systemic circuit, from the left atrium to the aorta).

1. Rotation of the medium within a flow ensures blood suction from the jet origination zone along its entire evolutionary pathway from the left atrium to the aorta.

2. Longitudinal travel and acceleration of the jet take place due to its convergence. No transverse vortices develop if there are no obstacles on the way of the jet evolution.

3. Hydrodynamic drag of a jet in the channel under study can be reduced due to a specialized organization of the boundary layer, which can be created by the active muscular and passive elastic mobility of the walls, the guiding anatomical structures, and potentially the special rheological properties of blood.

4. A swirling flow can occur in an unseparated mode in a curly channel taking into account the fact that the longitudinal and radial motion is inertia-free, while jet rotation is maintained through inertia. Flow swirl resumes in each cardiac cycle. Therefore, the medium does not stop at any point of the channel.

5. The "exact solutions" imply that centripetal flows of the discussed type form around the vortex core. Therefore, it can be suggested that the volume of a pulsatile jet changes depending on the inflow of the

medium through the jet end. Taking into account the fact that the swirling jet in the analyzed bed section is submerged and has an external boundary (through which there is no exchange with the medium), the external (with respect to the jet) secondary flows ensure a proportional blood distribution over the aortic branches. Flows with identical structures form in the branches.

An advantage of the solutions being used is that the functional elements in the expressions for the velocity can be written using the values of the cylindrical coordinates of the system in which the jet is described. Since the motion of a blood jet in the heart and aorta depends on the geometric configuration of the flow channel, its structure should correspond to the geometric configuration of the channel whose instantaneous condition can be quantitatively characterized in the same coordinates. Therefore, the expressions for the field of flow velocities can be obtained from a description of the boundary dynamics, provided that these boundaries meet the conditions of tornado-like jet generation.

EXPERIMENTAL RESULTS SHOWING THAT THE BLOOD FLOW STRUCTURE CORRESPONDS TO SWIRLING IRROTATIONAL FLOWS

An experimental study conducted by our research team more than 20 years ago aimed to reveal these analogies in the geometric configuration of the flow channel of the heart and great vessels, which would allow one to identify the blood flow as a potential flow of a viscous medium described by exact solutions.

The methodology used for the search was based on its objectives: we were searching for qualitative concordance between the regularities revealed by exact solutions and the fluid flow directions set by the corresponding anatomical structures. It is important to bear in mind that the capabilities of measuring the anatomical and physiological parameters of the flow are substantially limited, because it is impossible to insert a measuring instrument into a blood flow without causing significant distortions, as well as because of the evident anatomical variability of streamlined structures and the imperfection of measuring techniques. However, if the desired effect was revealed at least once, there would be no need to accumulate statistical data, since there would be no reasons to suspect any inter-individual variability of the blood flow mechanisms.

Upon an assumption that the configuration of the flow channel is close in nature to the geometric configuration of a jet that forms in said channel, the existence of exact solutions allows one to determine specific quantitative parameters using the size characteristics of the channel; the following parameters can be employed to identify and characterize the state of a swirling jet:

1. The instantaneous position of the cylindrical coordinate system, where the jet can be described using exact solutions. This position changes according to the law determined by the kinetics of the cardiac cycle;

2. The trajectories of the streamlines and their projections on the longitudinal-radial and azimuthal-radial cross-sections of the jet. The instantaneous position of the jet axis can be calculated by reconstructing the streamlines;

3. The volume parameter of the jet, which is a product of the longitudinal coordinate by the squared radial coordinate (zr^2) of the jet in the moving cylindrical coordinate system and its dynamics during the cardiac cycle;

4. The nature of function $C_0(t)$ that shows the dynamics of the radial velocity gradient and directly depends on cardiac contraction dynamics;

5. The nature of function $\Gamma_0(t)$, which is jet circulation, and the time dependence of this value during the cardiac cycle.

6. The ratio between these values (C_0/Γ_0), which shows the degree of jet swirl and is proportional to the ratio between one of the potential velocity components to the azimuthal (viscous) velocity component;

7. The curvature of the generating surface (flowing past it results in jet initiation). This surface is the surface of revolution of the involute of the streamline; and

8. The time of jet intensity ramp-up and time of jet extinction.

Calculation methods were elaborated for each of the parameters listed above [38, 40–42].

If in the presence of swirling mechanisms the values listed above are rational numbers according to the geometric configuration of the flow channel, the structure of the flow in this channel is supposed to correspond to that of a tornado-like jet described by exact solutions.

Experimental studies by morphometry of casts of the cavities of the left heart sections and aorta, computed tomography, magnetic resonance imaging and velocimetry, angiography on human and animal specimens, as well as studies involving volunteers and cardiac patients, for the first time revealed the effects that contribute to the maintenance of the mechanism of blood flow swirling (in the semantic rather than chronological order).

I. At the level of the left atrium (LA) [42]:

1. The curvature of the streamlined surface (the ratio between the radius of curvature and depth) of

the dome of the left atrium during the ejection phase qualitatively corresponds to the curvature of the generated surface forming the streamlines of a jet whose size (the initial radius and the radius in the critical section of the open mitral valve (MV)) coincide with that of a jet filling the left ventricle (LV).

2. Additional blood evacuation from the LA at the end of the LV filling phase (the slow filling phase) is driven by a high-intensity swirling flow in the LV cavity that has to do with the dynamic gradients formed in a swirling flow.

3. During the LA filling phase, the dome curvature forms a concave surface above which a swirling flow supplied by four pulmonary veins (PVs) is generated. A blood portion from the contracting LAA is injected simultaneously.

4. The directions of the jets supplied from the PVs and LAA were visualized by selective coloration of the flows in MRI 4D-Flow images. Steady-state clockwise swirling along the flow is shown.

From the properties listed above, it can be inferred that the left atrial systole is hemodynamically insignificant and only ensures a permanent concavity of the streamlined surface, thus maintaining the conditions for the formation of a swirling flow and preventing the events of wall prolapse as the left atrium empties quickly during the phase of rapid blood ejection into the LV. When most of the blood moves from the LA into the LV, the weight of the residual blood volume in the LV is too small to maintain inertial rotation and ensure a sufficient dynamic pressure gradient sucking blood from the PVs. Meanwhile, the LAA ejects an additional portion of blood at the rotation direction, thus increasing the azimuthal velocity and the dynamic pressure gradient, which raises the rate of blood inflow through the PVs.

II. In the LV:

1. Examination of the casts of LV also revealed geometric heterogeneity in blood-flown intracardiac structures. A group of trabeculae was singled out which predominantly reside on the free and anterior walls of the LV cavity and together form a system of converging, helically oriented guide curves twisted clockwise around the axis connecting the center of the mitral valve and a point located in the apical region of the cavity but that is not the apex. An alternative system of guide curves consists of trabeculae of the anterior septal angle and papillary muscles which are oriented as a helix (also twisted clockwise) converging to the axis connecting a point lying in the lower third of the LV free wall and the center of the aortic valve. The data were obtained by stereometric cast measurements: a cast was fixed in a stereometer with a fixed coordinate system, and the coordinates of several points along one trabecula were determined. These points were connected with a line; several lines with the same direction were oriented so that one could see a helix; the axis of this helix and its orientation in the LV cavity were identified. An assumption was made that contraction of trabeculae in both systems (and, therefore, their expression in the blood flow) takes place in an alternative mode; the free wall trabeculae form the structure of a jet filling the LV cavity, while the trabeculae of the anterior septal angle and the papillary muscles form the structure of a jet forced out from the LV cavity into the aorta. These data were subsequently fully confirmed by an analysis of the dynamic contrast-enhanced MSCT ventriculography images of the LV cavity. These images clearly demonstrate the alternative nature of the functioning of both trabecular systems [32, 33].

2. These observations allowed one to calculate the orientation of both systems of trabecular guide curves with respect to the axis and the ratio between the time-dependent functions C_0/Γ_0. The resulting value was shown to obey the hyperbolic law, depending on the cumulative longitudinal coordinate along the trajectory of jet evolution (i.e., as a result of summation of axial lengths along the inflow and ejecting trabecular systems.) This gave grounds for assuming that evolution of the only swirling jet maintaining its structure upon phase transition during the cardiac cycle (ventricular diastole to systole) takes place in the LV cavity [36, 37].

3. In order to further expand these results, casts of animal LVs significantly differing in size were examined by comparative anatomy analysis. Thus, the trabecular topographies of the left ventricular casts of rats, rabbits, dogs, and humans were compared. The dependencies revealed earlier for the human LV casts were reliably reproduced for smaller animals. Therefore, a conclusion was drawn that the structure of a flow generated in the LV is independent of cavity size and does not obey the Reynolds analogy, taking into account the fact that the absolute velocity of the blood flow is almost identical for all those animals [41].

4. Furthermore, the research results obtained previously were expanded by conducting a study focusing on the architectonics of the trabecular topology in patients with hypertrophic obstructive cardiomyopathy (HOCM) before and after surgical correction compared to the normal trabecular pattern. The study was based on the dynamic MSCT ventriculography data. The diagrams showing the evolution of the C_0/Γ_0 ratio depending on time differed signifi-

cantly for otherwise healthy individuals and patients with HOCM during the entire cardiac cycle. In the case of hypertrophy, the degree of swirling of the jet filling the LV cavity declined significantly, thus substantially reducing the cardiac output. Surgical correction of hypertrophy by myectomy using the right ventricular approach partially restored the normal mechanism of evolution of a swirling jet in the cavity [38].

5. MRI 4D-Flow visualization of the jet in the LV cavity proves that the swirling jet enters through the mitral valve (while existing in the twisted state), runs towards the posterior cavity wall, and twists clockwise with respect to the axis running through the mitral valve (thus providing additional blood evacuation from the LA cavity). After mitral valve closure, this vortex turns with respect to the large curvature of the LV free wall. In terms of the ratio between the radius and depth, this curvature qualitatively corresponds to the curvature of the generating surface forming the swirling jet forced out of the LV cavity into the aorta. At the instant when the aortic valve opens, this jet, without losing its structure due to rotation inertance, rushes into the aortic valve lumen and is injected into the aorta [43, 44].

What is needed for this mechanism to occur? First, a clear separation of the dominant and secondary jets at the instant of injection, which is ensured by the absence of transversal transfer of the medium in a swirling jet, is needed. Second, it is suction of the medium from the jet origination zone (in the left atrium upon filling of the LV and in the LV upon injection into the aorta) due to the dynamic pressure gradient in the swirling jet. Third, it is the substantiation of potential absorption of smaller secondary flows by the dominant swirling jet, with allowance for the potential generation of circular vortices characterized by known stability (in particular, as reported by G. Pedrizzetti [45]). Fourth, it is the match between the outer contour of the cavity and the expressions for the corresponding projections of the streamlines of a tornado-like jet and the presence of a curvilinear generating surface that acts as a base for this jet. And fifth, it is the universal presence of conditions for the generation of a mobile vortex boundary layer that rules out the development of shear strain at the jet boundary [39]. In a normal LV and in patients with a compensated LV pathology, there are no signs that would make these conditions non-fulfillable.

The properties listed above demonstrate that the coordinated contraction of the streamlined structures of the LV cavity during the entire cardiac cycle corresponds to the instantaneous state of evolution of the intracardiac blood flow. The mechanisms ensuring the circulation of the jet supplied from the LA and the jet ejected into the aorta are maintained. The valvular heart apparatus plays a passive role by ensuring the extension of the mobile jet boundary. The dominant and the secondary jets are essential for the mechanics of valve closure.

III. In the aorta.

1. It was shown using aortic casts from various animals (a human, a pig, a dog, and a rabbit) that the flow channel radius changes along the aorta length in accordance with the regularities revealed by the exact solutions. According to this regularity, the condition that the product of the squared radius by the longitudinal coordinate remain constant needs to be met starting at the origin of the coordinates along the channel. This condition is met for the aorta if the origin of the coordinates stands at a certain distance from the aortic valve, deeper into the heart. In theory, this value is supposed to correspond to the distance to the place of initiation of a swirling jet. A study using casts showed that this distance is comparable to the sum of the doubled longitudinal dimension of the LV cavity and the longitudinal dimension of the LA. Intravital MSCT and MRI measurements showed that this value is somewhat smaller and varies during the cardiac cycle, in accordance with the logic of jet evolution (this thesis needs additional refining) [46].

2. Elastometric and angiographic measurements showed that this regularity is obeyed at normal pressure in the aortic lumen. Pressure rise to values > 150 mm Hg causes a distortion of this regularity [40].

3. Elastometric measurements have demonstrated that the elasticity of the aorta normally increases in the distal direction. The aortic flow channel retains its overall convergence; however, the calculated position of the origin of coordinates is shifted towards positive values for the closed aortic valve and towards negative values for the open aortic valve when the jets in the LV cavity and in the aorta are a unified whole. This elasticity distribution along the aorta is also distorted when the intraluminal pressure exceeds 150 mm Hg [46].

4. Mathematical modeling of a round elastic channel with a longitudinal-radial size identical to that of the human aorta has proved that the possibility of generation of a tornado-like swirling jet significantly depends on the distribution of elasticity along the flow channel [47].

5. MRI 4D-Flow visualization of a flow inside the aorta demonstrates that the degree of jet swirl changes significantly depending on the phase dynamics of

the aortic valve. The degree of jet swirl significantly increases when the valve is closed [44].

6. Mapping and analysis of the velocity field in the aorta, measured by phase-contrast MRI velocimetry, revealed the following features of the flow: (a) the velocity vectors predominantly rotate clockwise; (b) in each aortic cross-section, there are at least two oppositely charged circulation centers corresponding to the dominant jet and secondary reversed jets with the same structure; (c) the axis of the injected swirling axis in the aortic lumen (precession) rotates clockwise during the entire cardiac cycle (the jet is "rolling" along the aortic wall); (d) jet circulation along the aorta is reduced (both for positive and negative circulation); (e) the frequency parameter of the jet C_0 along the aorta is reduced; and (f) circulation Γ_0 during the cardiac cycle is reduced (rotation decay). A conclusion has been drawn that the pulsatile mode of blood ejection into the aorta is needed for twisting the medium and maintaining continuous rotation of the jet [35].

Having summarized the effects mentioned above, it seems fair to say that the geometric conditions required for maintaining the structure of a tornado-like jet are met during the entire cardiac cycle and within the entire section of the circulatory bed between the left atrium and the aorta. The deterministic distribution of blood over aortic branches is ensured by a radial shift of the secondary and reversed flows, with allowance for the local diffuser segments of the flow channel of the aorta.

THE PROPOSED MECHANISM OF GENERATION AND MAINTENANCE OF THE SWIRLING FLOW STRUCTURE IN THE HEART AND AORTA

According to our own data and the facts known from the studies conducted by other researchers, the concept of tornado-like swirling flows allows one to describe the mechanism of generation and evolution of a swirling, tornado-like blood jet in the left heart and aorta.

This mechanism acts continuously and is reproduced for every next cardiac contraction in all the flow channel segments under analysis. This process can be conveniently classified into several stages:

1. Filling of the left atrium. The blood masses are primarily swirled on the concave streamlined surface of the LA, between the PVs ostia at a sufficiently high velocity of the incident flow. As soon as the medium gets swirled in the LA cavity, the LA is filled via two mechanisms: the ongoing blood inflow through the pulmonary veins and suction of the medium as a result of the dynamic pressure gradient in the axial zone of the swirling flow in the LA cavity.

2. The phase of rapid LV filling (the mitral valve is open; P_{LV} is minimal; P_{LA} is maximal; the jet is limited in its origin by the curvilinear surface of the LA, the converging LA walls and mitral valve leaflets that together form a converging channel; the trabeculae of the free walls are exposed to the flow in the LV; the cavity radius and the azimuthal velocity increase.) The mitral valve is open due to a drop in pressure in the LV cavity (caused by the active diastolic phase), and the swirling tornado-like jet is forced from the LA into the LV along the converging channel formed by the LA walls and mitral valve leaflets. Jet circulation ensures maximal blood evacuation of the LA (the origination zone) due to dynamic pressure gradient in the axial jet zone.

3. The phase of slow LV filling. (The mitral valve is open; $P_{LV} = P_{LA}$; a large vortex in the LV cavity ensures suction from the LA cavity.) LAA systole ensures circulation of the residual blood volume in the LA cavity and suction from the pulmonary veins before the mitral valve closes.

4. Beginning of the isometric phase. (Contraction of the papillary muscles and trabeculae of the anterior septal angle, elevation of LV pressure, and mitral valve closure.) After the mitral valve closure, a dominant vortex is formed in the LV cavity: its axis is oriented towards the aortic valve and its base is oriented with respect to the LV free wall curved like a generating surface. Vortex circulation is maintained by free wall trabeculae. This circulation ensures a drop in pressure in the jet center due to which the jet gets "sucked" into the LV free wall. The mechanism through which the jet orientation (expressed by a vector with respect to the LA cavity) changes to the orientation of a dominant vortex in the LV cavity (whose vector field is built with respect to the LV cavity) still requires explanation.

5. The LV systole. In the beginning of the mechanical systole, a large dominant vortex (oriented with respect to the curvature of the LV free wall so that its axis was directed towards the aortic valve) has already taken form in the LV cavity. The papillary muscles and long trabeculae of the anterior septal angle of the LV act as guidance for this vortex. The aortic valve opens as soon as pressure in the LV cavity exceeds the pressure in the aorta. At that instant, the structure of the vortical motion extends (at the velocity of sound in the blood medium) to the entire available length of the aorta to form the so-called "vortex filament" along which the dominant jet is filled with the medium supplied from its base.

6. Rapid ejection. As the jet is filled, its radius and the azimuthal component of the velocity increase. As it interacts with the jet, but does not exchange medi-

um with it, the residual blood in the aorta acquires a swirling jet structure due to viscous interactions and localizes in the space between the dominant jet and the aortic walls. These jets are the secondary and reversed flows; they are a source of the flows running into the branches of the aorta.

7. Slow ejection. A swirling jet in the aorta continues to rotate due to inertance, thus maintaining the dynamic pressure gradient between the axis and the jet boundary. This gradient ensures the ejection of an additional volume of the medium from the LV cavity. However, the jet energy decreases because of the lack of blood inflow and the jet gets broken down into several oppositely directed swirling flows. The ones with retrograde direction ensure aortic valve closure.

8. Aortic valve closure and getting ready for the next cycle. After aortic valve closure, the residual volume in the LV cavity, which also retains a swirling flow structure due to rotational inertia, changes its localization and orientation to be indentified and linked with the next jet supplied from the mitral valve.

The proposed cyclically reproducible mechanism reveals that blood flow swirl is the key property of blood circulation, since it ensures blood motion with minimal energy expenditure for the drag, minimizes the interactions inside the jet and at its boundaries (including the walls), ensures maximum evacuation of the medium from the jet formation zone, provides for an axial model of jet injection into each next cavity without coming into contact with the channel walls and re-orientation of the flow's direction, determines the organization of the secondary and reversed flows and a strictly determined blood distribution over the aortic branches. Meanwhile, the formation of detached flows or congestion zones along the flow is normally impossible.

This mechanism has no apparent contradictions; however, many evolution stages of the swirling flow in the heart and great vessels require additional research. Thus, a more detailed phase study of blood inflow through the pulmonary veins and a study focusing on the dynamics of LA contraction and a refining of the role played by LAA contraction in the formation of the primary swirling jet are needed. It is also important to refine the contraction sequence of the blood-flow's intracardiac muscular elements. The type of interaction between a jet injected into the LV cavity and the residual blood volume, as well as the kinetics of the vortical structures that form simultaneously, needs to be additionally studied. The process related to blood injection into the aorta and the detailed mapping of the velocities of the injected jet and the secondary jets it interacts with is an important question. The mechanisms of blood flow distribution over the main aortic branches, with allowance for the geometric polymorphicity of branching, need to be additionally studied. The main problem still in need of clarification is the one related to the energy balance of the heart: how much energy is produced due to the metabolic processes occurring in the myocardium and how much energy is consumed to maintain the pumping function of the heart.

The answers to these questions can be obtained only partially from experimental and clinical studies. The central role in solving the problems listed above should belong to methods of mathematical modeling of flows based on the proposed conception and exact solutions to the hydrodynamics equations for the analyzed class of flows.

The swirling potential flow pattern can be easily distorted and even destroyed. The disturbances may be caused by distortion of coordinated contraction of the heart, changes in the geometric configuration of the flow channel or the dynamics of functioning of the cardiac valvular apparatus, reduced elasticity or altered distribution of elasticity along the aorta, as well as changes in blood rheology. Since a swirling jet is submerged at all its evolutionary stages and comes into contact with the channel walls only at critical points, it is highly adaptable. However, energy loss is inevitable and mainly consists in interaction with secondary and residual jets. Therefore, the local increase in the volume of the flow channel as the jet evolves causes a loss of its intensity. Jet properties also can be critically altered if any hindrance to the azimuthal rotation of the jet occurs. These and other disturbances to the normal physiological parameters of the analyzed segment of the circulatory system inevitably reduce the cardiac output, increase the load on the myocardium, and disrupt the normal functioning of the cardiovascular system.

CONCLUSIONS: SIGNIFICANCE OF THE CONDUCTED STUDIES AND THEIR RESULTS, PROMISING RESEARCH TRENDS UNDER THE CONCEPT OFA TORNADO-LIKE STRUCTURE OF THE BLOOD FLOW

The proposed conception of the blood flow based on the idea that the flow swirl plays a crucial role in the blood flow significantly contributes to our general understanding of physiological processes and applied fields in clinical and engineering research.

For fundamental physiology and medicine:

· the proposed mechanism allows one to perform comprehensive studies to establish how a pulsatile blood flow (which is formed in the LA and retains its structure at least until it passes the end of the aorta) is generated and evolves.

For blood flow modeling:

· the exact solutions allow one to single out the specific signs of the initial and boundary conditions that are important upon blood flow simulation.

For pathophysiology:

· the proposed mechanism allows one to explain how to perform compensatory correction of the flow channel configuration because of the plastic processes occurring in the places where flow detachment or congestion zones emerge (geometrical remodeling of the heart and aorta.)

For cardiology:

· the use of exact solutions allows one to formulate new quantitative diagnostic criteria and elaborate novel diagnostic systems and software for assessing the state of a blood flow.

For cardiac surgery:

· the use of exact solutions and modeling based on them allows one to choose the optimal approach for reconstructing the geometric configuration of the flow channel when conducting reconstruction surgeries of the heart and great vessels.

For designing organ-replacement prosthetic devices for cardiac surgery:

· the use of exact solutions allows one to design prosthetic devices taking into account the features of the blood flow: that was how the full-flow mechanical aortic valve prosthesis was created. A model of the prosthetic mitral valve has been proposed, and an elastic vascular prosthesis has been designed.

For physical modeling of blood flow:

· the exact solutions offer the key for producing research test benches that simulate the real-world hydrodynamic conditions under which the components of the cardiovascular system function.

In order to solve the problem of a totally implantable artificial heart:

· this problem could be solved by designing a pump that can generate a structured swirling blood flow.

The following directions in research based on the conception of a tornado-like self-organization of the blood flow in the heart and great vessels:

– developing novel approaches to the mathematical modeling of the blood flow;

– elaborating new diagnostic principles based on an assessment of the blood flow quality;

– studying the mechanisms of generation and maintenance of a swirling blood flow in the right heart segments and the pulmonary vascular bed. Analyzing the role played by the blood flow in the pathogenesis of pulmonary hypertension;

– studying the remodeling mechanisms and elaborating new approaches to the correction of acquired pathological disruptions in the dynamic geometry of the heart flow channel and great vessels (valves, the geometric configuration of cavities, and the biomechanical characteristics of streamlined surfaces);

– studying the remodeling and elaborating new approaches to the correction of disruptions in the heart rhythm (surgical isolation of ectopic foci, atrial fibrillation, modes of cardiac pacing, and isolated stimulation of the LAA);

– analyzing the compensation mechanisms and elaborating new approaches to the correction of complex congenital heart defects;

– elaborating physical blood circulation models that reproduce the hydrodynamic features of the blood flow;

– elaborating new configurations and operation modes for paracorporeal devices for circulatory assistance (artificial blood circulation machines, hemodialysis and plasmapheresis equipment); and

– designing novel configurations of prosthetic segments of the circulatory system (valves, vessels, auxiliary pumps, and fully implantable artificial hearts) that take into account the hydrodynamic features of the blood flow, and designing novel test systems for assessing the functional characteristics of implants for cardiac surgery.

CONCLUSIONS

Hence, a novel, promising line in research is taking shape. It is of fundamental importance for understanding the physiological mechanisms of circulation and of applied significance for the diagnosis and treatment of patients with various circulatory disorders. It is likewise crucial for designing new organ replacement devices that can be used in cardiovascular surgery. ●

This study was supported by the Russian Science Foundation (grant No. 16-15-00109).

REFERENCES

1. Bremer J. // Amer. J. Anatomy. 1932. V. 49. P. 409–440.
2. Markl M., Kilner P.J., Ebbers T. // J. Cardiovasc. Magn. Reson. 2011. V. 13. P. 7. doi: 10.1186/1532-429X-13-7
3. Buonocore M.H. // Magn. Reson. Med. 1998. V. 40(2). P. 210–226. doi: 10.1002/mrm.1910400207
4. Kilner P.J., Yang G.Z., Mohiaddin R.H., Firmin D.N., Longmore D.B. // Circulation. 1993. V. 88. № 5. P. 2235–2247. doi: 10.1161/01.cir.88.5.2235
5. Frazin L.J., Vonesh M.J., Chandran K.B., Shipkowitz T.,

Yaacoub A.S., McPherson D.D. // ASAIO J. 1996. V. 42(6). P. 951–956. doi: 10.1097/00002480-199642060-00006
6. Bagaev S.N., Zakharov V.N., Orlov V.A. // Russian Journal of Biomechanics. 2002. V. 6. № 4. P. 30–50. (in Russian)
7. Kirsanov R.I., Kulikov V.P. // Uspekhi Fiziologicheskih nauk. 2013. V. 44. № 2. P. 62–78. (in Russian)
8. Gallo D., Isu G., Massai D., Pennella F., Deriu M. A., Ponzini R., Bignardi C., Audenino A., Rizzo G. Morbiducci U. Visualization and simulation of complex flows in biomedical engineering: Lecture notes in computational vision and biomechanics / Eds Lima R., Imai Y., Ishikawa T., Oliveira M. Dordrecht: Springer, 2014. V. 12.
9. De Nisco G., Kok A.M., Chiastra C., Gallo D., Hoogendoorn A., Migliavacca F., Wentzel J.J., Morbiducci U. // Ann. Biomed. Eng. 2019. V. 47(2). P. 425–438. doi: 10.1007/s10439-018-02169-x
10. Bockeria L.A., Gorodkov A.J., Dorofeev A.V., Alshibaya M.D. // Eur. J. Cardiothorac. Surg. and the RESTORE Group. 2006. V. 29. P. 251–258. doi: 10.1016/j.ejcts.2006.02.057
11. Pedley T.G. The fluid mechanics of large blood vessels. Cambridge: University Press, 1980.
12. Caro C.G., Watkins N.W., Sherwin S.J., Pitt R., Giordana S., Franke P.T., Peiro J., Doorly D.J., Papaharilaou Y., Chesire N., Jackson M., Bicknall C. Swirling circulatory and respiratory flow: Biological/pathological implications. IFMBE Proc. EMBEC, 2002. P. 8–16.
13. Gataulin Y.A., Yukhnev A.D., Zaitsev D.K., Smirnov E.M., Kulikov V.P., Kirsanov R.I. Structure of the secondary flow in the bifurcation of a blood vessel: patientspecific modeling and clinical Doppler measurements. Proceedings of the International Conference PhysicA.SPb. 23–25 October 2018. St. Petersburg: A.F. Ioffe Physico-Technical Institute. 2018. P. 270–271. (in Russian)
14. Pedrizzetti G., La Canna G., Alfieri O., Tonti G. // Nat. Rev. Cardiol. 2014. V. 11. P. 545–553. doi: 10.1038/nrcardio.2014.75
15. Pasipoularides A. // Hellenic J. Cardiol. 2012. V. 53. P. 458–469.
16. Burakovskiy V.I., Dobrova N.B., Kuzmina N.B., Agafonov A.V., Roeva L.A., Drogaytsev A.D. // Experimental Surgery and Anaesthesiology. 1976. № 3. P. 13–16. (in Russian)
17. Varaksin A.Y., Romash M.E., Kopeytsev V.N. Tornado. M.: PhysMathLit, 2011. 344 p. (in Russian)
18. Rotunno R. // Annu. Rev. Fluid Mechanics. 2013. V. 45. P. 59–84.
19. Goldshshtick M.A. Vortical Flows. Novosybirsk: Nauka, 1981. 367 p. (in Russian)
20. Escudier M. // Annu. Rev. Fluid Mechanics. 1987. V. 19. № 1. P. 27–52.
21. Piralishvili Sh.A. Vortical Effect. V. 1. Physical Phenomenon, Experiment, Theoretical Modeling. M.: NauchTechLitIzdat, 2013. 343 p. (in Russian)
22. Biriuk V.V., Veretennikov S.V., Gurianov A.I., Piralishvili Sh.A. Vortical Effect. Technical Applications. M.: NauchTechLitIzdat, 2014. V. 2(1). 288 p. (in Russian)
23. Piralishvili Sh.A., Pisarevskiy A.S. // Izvestiya Rossiyskoy Academii Nauk. Fluid and Gas Mechanics. 2013. № 3. P. 138–147. (in Russian)
24. Kiknadze G.I., Krasnov Yu.K. // Sov. Phys. Dokl. 1986. V. 290. № 6. P. 1315–1319. (in Russian)
25. Kiknadze G.I., Krasnov Yu.K., Podymaka N.F., Khabenskiy V.B. // Sov. Phys. Dokl. 1986. V. 291. № 6. P. 1315–1318. (in Russian)
26. Andreev V.K., Kaptsov O.V., Pukhnachiov V.V., Rodionov A.A. Application of group-theoretical methods in hydrodynamics. Novosybirsk: VO Nauka, 1994. 319 p. (in Russian)
27. Goldshtik M.A. // Annu. Rev. Fluid Mechanics. 1990. T. 22. № 1. P. 441–472.
28. Shtern V., Hussain F. // Annu. Rev. Fluid Mechanics. 1999. V. 31. № 1. P. 537–566.
29. Kiknadze G.I., Gachechiladze I.A., Gorodkov A.Yu. Self-Organization of Tornado-Like Jets in Flows of Gases and Liquids and the Technologies Utilizing This Phenomenon. Proc. ASME 2009 Heat Transfer Summer Conference. San Francisco, California, USA. July 19–23 2009. P. 547–560. doi:10.1115/HT2009-88644
30. Kiknadze G.I., Gachechiladze I.P., Alekseev V.V. Self-Organization of Tornado-Like Jets in Flows of Viscous Continua and Enhancement of Heat Transfer which Accompanies This Phenomenon. M.: MEI Publ. House, 2005. 83 p. (in Russian)
31. Burgers J.M. // Adv. Appl. Mechanics. 1948. V. 1. P. 171–199.
32. Kiknadze G.I., Olejnikov V.G., Gachechiladze I.A., Gorodkov A.Y., Dobrova N.B., Baquey C., Barat J.-L. // Doklady Akademii nauk. 1996. V. 351. P. 119–122. (in Russian)
33. Gorodkov A.Y. // Bulleten of NCSSKh im. Bakuleva RAMN. 2003. № 9. P. 61–66. (in Russian)
34. Gorodkov A.Y., Nikolaev D.A. // Bulleten of NCSSKh im. Bakuleva RAMN. 2003. № 9. P. 67–69. (in Russian)
35. Bockeria L.A., Gorodkov A.Y., Nikolaev D.A, Kiknadze G.I., Gachechiladze I.A. // Bulleten NCSSKh im. Bakuleva RAMN. 2003. № 9. P. 70–74. (in Russian)
36. Bockeria L.A., Kiknadze G.I., Gachechiladze I.A., Gorodkov A.Y. Application of Tornado-flow Fundamental Hydrodynamic Theory to the Study of Blood Flow in the Heart and Main Vessels – Further Development of Tornado-like Jet Technology. Proc. ASME 2011 International Mechanical Engineering Congress & Exposition ASME2011, November 11–17, 2011. Denver, Colorado, USA. IMECE2011-63769. doi: 10.1115/IMECE2011-63769
37. Bockeria L.A., Kiknadze G.I., Gachechiladze I.A., Gabidullina R.F., Makarenko V.N. // Cardiometry. 2013. № 3. P. 5–29. doi: 10.12710/cardiometry.2013.3.530
38. Talygin E.A., Zazybo N.A., Zhorzholiany S.T., Krestinich I.M., Mironov A.A., Kiknadze G.I., Bokeriya L.A., Gorodkov A.Yu., Makarenko V.N., Aleksandrova S.A. // Uspekhi Fiziologicheskikh Nauk. 2016. V. 47. № 1. P. 48–68. (in Russian)
39. Schlichting H. Boundary-Layer Theory. M.: Nauka,1969. (in Russian)
40. Zhorzholiani Sh.T., Mironov A.A., Talygin E.A., Cygankov Yu.M., Agafonov A.V., Kiknadze G.I., Gorodkov A.Yu., Bokeriya L.A. // Byul. eksp. biol. med. 2017. V. 164. № 10. P. 519–524.
41. Tkhagapsova M.M., Talygin E.A., Zhorzholiani Sh.T., Agafonov A.V., Dorofeev A.V., Gorodkov A.Yu., Kiknadze G.I., Bokeriya L.A. // Biophysics. 2020. V. 65 № 1. P. 165–174. doi: 10.31857/S0006302920010184
42. Talygin E., Kiknadze G., Agafonov A., Gorodkov A. Application of the tornado-like flow theory to the study of blood flow in the heart and main vessels: Study of the potential swirling jets structure in an arbitrary viscous medium. Proceedings of the ASME 2019 International Mechanical Engineering Congress and Exposition. V. 3: Biomedical and Biotechnology Engineering. Salt Lake City, Utah, USA. November 11–14, 2019. V003T04A032. ASME. https://doi.org/10.1115/IMECE2019-11298
43. Talygin E.A., Zhorzholiani Sh.T., Tkhagapsova M.M., Tsygankov Y.M., Agafonov A.V., Gorodkov A.Y., Kiknadze G.I.,

Bockeria L.A. Reconstruction of Swirling Blood Flow in the Heart and Aorta on the Basis of Measurements of Dynamic Geometry and Elastic Properties of the Flow Channel. 2019. IMECE2018-87680, V003T04A052; 7 pages. doi: 10.1115/IMECE2018-87680
44. Gorodkov A.Yu. Using the concept of tornado-like viscous fluid flows to explain the phenomenon of blood movement in the heart and great vessels. "Physiology and pathology of blood circulation". VII All-Russian school-conference with international participation. February 3–6 2020. M.: Moscow State University. M.V. Lomonosov. Faculty of Fundamental Medicine. 2020. P. 17–19.
45. Pedrizzetti G., Domenichini F. // Ann. Biomed. Eng. 2015. V. 43. № 1. P. 26–40. doi: 10.1007/s10439-014-1101-x
46. Zhorzholiani Sh.T., Talygin E.A., Krasheninnikov S.V., Cygankov Yu.M., Agafonov A.V., Gorodkov A.Yu., Kiknadze G.I., Chvalun S.N., Bokeriya L.A. // Human Physiology. 2018. V. 44. № 5. P. 47–56. doi: 10.1134/S013116461805017X
47. Talygin E.A., Zhorzholiani Sh.T., Agafonov A.V., Kiknadze G.I., Gorodkov A.Yu., Bockeria L.A. // Human Physiol. 2019. V. 45. № 5. *P.* 527–535. doi: 10.1134/S0362119719050190

Molecular Tools for Targeted Control of Nerve Cell Electrical Activity. Part II

D. V. Kolesov, E. L. Sokolinskaya, K. A. Lukyanov, A. M. Bogdanov*
Shemyakin-Ovchinnikov Institute of Bioorganic Chemistry, Moscow, 117997 Russia
*E-mail: noobissat@ya.ru
Received August 24, 2020; in final form, May 14, 2021
DOI: 10.32607/actanaturae.11415

ABSTRACT **In modern life sciences, the issue of a specific, exogenously directed manipulation of a cell's biochemistry is a highly topical one. In the case of electrically excitable cells, the aim of the manipulation is to control the cells' electrical activity, with the result being either excitation with subsequent generation of an action potential or inhibition and suppression of the excitatory currents. The techniques of electrical activity stimulation are of particular significance in tackling the most challenging basic problem: figuring out how the nervous system of higher multicellular organisms functions. At this juncture, when neuroscience is gradually abandoning the reductionist approach in favor of the direct investigation of complex neuronal systems, minimally invasive methods for brain tissue stimulation are becoming the basic element in the toolbox of those involved in the field. In this review, we describe three approaches that are based on the delivery of exogenous, genetically encoded molecules sensitive to external stimuli into the nervous tissue. These approaches include optogenetics (overviewed in Part I), as well as chemogenetics and thermogenetics (described here, in Part II), which is significantly different not only in the nature of the stimuli and structure of the appropriate effector proteins, but also in the details of experimental applications. The latter circumstance is an indication that these are rather complementary than competing techniques.**
KEYWORDS **optogenetics, chemogenetics, thermogenetics, action potential, membrane voltage, neurointerface, ion channels, channelrhodopsin, chemoreceptors, GPCR, neural activity stimulation, neural excitation, neural inhibition.**
ABBREVIATIONS **ADPR – adenosine diphosphate ribose; ATP – adenosine triphosphate; BL-OG – bioluminescent optogenetics; CHO – Chinese hamster ovary cells; CID – chemically induced dimerization; CNO – clozapine N-oxide; DAAO – *D*-amino acid oxidase; DHFR – dihydrofolate reductase; DREADDs – designer receptors exclusively activated by designer drugs; FAST – fluorescence-activating and absorption shifting tag; FLIRT – fast local infrared thermogenetics; FKBP – FK506 binding protein; FlyMAD – fly mind-altering device; FRB – FKBP12-rapamycin binding domain; GABA – gamma-aminobutyric acid; GFP – green fluorescent protein; GPCR – G-protein-coupled receptor; GR – gustatory receptors; *hsp* – heat shock protein; HEK293 – human embryonic kidney 293 cells; IPD – ion pore domain; IR – infrared or ionotropic receptor (context-sensitive); IR-LEGO – infrared-laser evoked gene operator; KOR – kappa-opioid receptor; LBD – ligand-binding domain; PhoCl – photo-cleavable; PSAM – pharmacologically selective actuator module; PSEM – pharmacologically selective effector molecule; PYP – photoactive yellow protein; RASSL – receptors activated solely by synthetic ligands; RNAT – RNA thermometer; TeNT – tetanus toxin; TRP – transient receptor potential.**

INTRODUCTION

Minimally invasive methods of selective stimulation of the activity of nerve cells and brain structures hold a prominent place in the neuroscience toolkit. Part I of this review has focused on the most developed one, optogenetics, while Part II discusses the promising orthogonal approaches, thermogenetics and chemogenetics.

THERMOGENETICS

Similarly to visible light, thermal energy propagates as electromagnetic oscillations and temperature is one of the key environmental factors interacting with biological organisms. The relatively narrow range of temperatures at which most cellular life-forms can function is determined by the thermodynamic and kinetic features of biochemical processes and facilitates

the development of various evolutionary adaptations (such as thermotaxis, maintenance of a constant body temperature in homoiothermic animals, etc.) that are related to how temperature is perceived at the cellular and molecular levels [1, 2]. Thermoreceptors and other molecules that specifically capture temperature changes are typical of almost all living organisms [3]. This fact represents the foundation for the development of genetically engineered approaches to the manipulation of cell physiology and biochemistry using heating or cooling.

Thermogenetics is a relatively young group of methods where thermally sensitive, genetically encoded effector macromolecules are used to manipulate various physiological and biochemical processes in living cells. The thermogenetic approach can be viewed as an approach that is alternative or even orthogonal with respect to the one designated as optogenetic [4], but only with allowance for the fact that the former is significantly less commonly used. Thus, there currently exist less than a few hundred academic publications describing the application of thermogenetic methods.

An interesting difference between thermogenetics and optogenetics consists in the technological diversity of the methods used to activate effector molecules. The first method to appear, which remains the most commonly used, is heating of the entire model organism (this usually refers to heating insects in a special thermostat) [5, 6]. The second method to appear is the performance of local heating of tissues using magnetic nanoparticles that dissipate heat upon excitation by external fields. Thermal activation of the TRPV1 receptor by iron oxide nanoparticles induced by radio-wave irradiation is described in at least three studies [7–9]. The first of these publications demonstrated the principle underlying the method: Huang *et al.* [7] performed the excitation of cultured neurons expressing the TRPV1 receptor by radiofrequency radiation of ferrite nanoparticles placed on the cell surface. In the second study, Stanley *et al.* [8] successfully manipulated the blood plasma glucose level in mice with grafted tumors expressing the bioengineered insulin gene under the control of the Ca^{2+}-sensitive promoter. The promoter was induced by calcium flux through the temperature-sensitive TRPV1 channel, whose molecule was labeled with nanoparticles using histidine tag antibodies [8]. In the third study, Chen *et al.* [9] stimulated neurons transiently expressing TRPV1 deep inside the brain tissue of living mice in a similar manner. More detailed information about the application of magnetic nanoparticles in thermogenetics has been provided in the topical review by Tay and Di Carlo [10]. Finally, the third method of thermogenetic stimulation involves infrared laser irradiation [11–13]. Bath *et al.* [12] developed an instrumental setup ensuring precise activation of *Drosophila* neurons and gave it an original name: FlyMAD (the fly mind-altering device). It is noteworthy that the nature of thermogenetic stimulation is responsible for both the fundamental limitations of the method and its potential advantages over optogenetics. On the one hand, the need to locally alter the temperature noticeably reduces the temporal resolution of the stimulation (this problem is partially solved using powerful IR lasers), while the approach involving overall heating of the object possesses such a drawback as virtual loss of spatial resolution. On the other hand, both infrared laser stimulation and radio-frequency excitation of nanoparticles are characterized by a high degree of stimulus penetration into the tissue (up to several millimeters), which makes thermogenetics noticeably advantageous over optogenetics in experiments aimed at studying such organs as the heart and the brain [4, 9, 10].

Although the thermogenetic approach is used relatively rarely as things stand, the repertoire of effector molecules and model systems associated with it is rather diverse and continues to grow. Thus, so-called RNA thermometers (RNATs) have been used as a tool for studying and modulating temperature-dependent gene expression in bacteria parasitizing homoiothermic animals [14]. The 3D structure of these wild-type sequences found in the 5' untranslated regions of the mRNAs of some bacterial genes changes depending on the temperature. At low temperatures, the RNA thermometer inhibits mRNA translation by limiting the probability of ribosomal landing; contrariwise, translation is induced at higher temperatures. Another approach for the thermogenetic control of transcription is called IR-LEGO [15]. In this case, a living nematode *C. elegans* was exposed to IR laser irradiation to attain local activation of transgene (the *GFP* gene) transcription controlled by the heat-shock promoter *hsp16-2*. A similar irradiation scheme for the same model system has recently been used to demonstrate the FLIRT (fast local infrared thermogenetics) method [16]. In this case, the thermogenetic experiment was aimed at controlling protein activity, and the temperature-sensitive variants of myosin II, Delta and cyk-4 acted as targets.

Mutant GTPase dynamin, an expression product of the temperature-sensitive allele of the *Drosophila shibire* (shi^{ts1}) gene, historically became the first thermogenetic effector in neurobiology [17]. Dynamin plays a crucial role in endocytosis regulation and, in particular, in synaptic vesicle recycling, while expression of its Shibire (G273D) variant inhibits vesicle

activity due to depletion of the synaptic vesicular pool and blocking of synaptic transmission [18]. Reversible motor paralysis in animals in response to temperature elevation to 30°C was successfully demonstrated using targeted shi^{ts1} expression in *Drosophila* neurons [17]. Today, the shi^{ts1} allelic variant is a standard inhibitory effector in neurobiological studies focusing on *Drosophila* [19–24].

Interestingly, chemoreceptors belonging to the IR and GR families are involved in thermoreception in insects [25, 26]. These molecules are ligand-specific, non-selective cation channels, while the molecular mechanisms that allow them to take part in the development of avoidance behavior in response to cooling or heating remain understudied. Nonetheless, one of the GR family receptors, Gr28bD, has become a progenitor of a fundamentally new class of thermogenetic actuators [26]. It has been found that thermostimulation of *Xenopus* oocytes and *Drosophila* motor neurons expressing *Gr28bD* results in the generation of a transmembrane cationic current that induces an action potential in neurons. Gr28bD was used as an activator of dopaminergic neurons when studying learning and memory in *Drosophila* [27]. Transient receptor potential channels (TRP channels) are the most important class of effector molecules used in modern thermogenetics, especially in relation to neurobiological problems [5, 28, 29].

TRP channels

TRP channels constitute a superfamily of ion channels residing on the plasma membrane of many types of animal cells. Approximately 30 types of TRP channels are currently known; they are clustered into seven families and share common structural properties (*Fig. 1*). All TRP channels consist of six transmembrane segments, show significant sequence homology within the family, and are characterized by nonselective cation permeation [30]. TRPs differ from other ion channels by an incredible diversity of cation selectivity and activation mechanisms. These proteins are involved in the functioning of all sensory systems (vision, gustation, olfaction, hearing, tactile perception, thermal sensitivity, and osmotic sensitivity). Hence, TRP channels mediate the cellular response to all the key classes of external stimuli, including light, sound, chemical substances, temperature, and mechanical force. Furthermore, TRP channels allow cells to sense changes in their immediate environment, such as changes in the osmolarity of a solution [30].

TRP channels are found in many multicellular organisms, including worms, insects, and vertebrates. According to the genetic organization and topology of their molecules, the entire superfamily of TRP channels can be divided into two large groups that include seven families (*Fig. 1*).

Nonselective permeation of cations (including Na^+, Ca^{2+}, and Mg^{2+}) through the TRP channels becomes possible after activation. Ions entering nerve cells alter the membrane voltage and cause action potential generation. Interestingly, the conductance of TRP channels is three orders of magnitude higher than that of the channelrhodopsins involved in optogenetics [31].

TRP channels can be activated by various plant-derived substances, including those found in spices, e.g., in garlic (allicin), chili pepper (capsaicin), and wasabi (allyl isothiocyanate), as well as by menthol, camphor, peppermint, etc. TRP channels sensitive to temperature variation, or the so-called thermo-TRPs (*Fig. 1*), represent a highly relevant protein group to be used in thermogenetics. These channels are activated once a certain temperature threshold is attained. Thermo-TRPs are expressed in thermosensitive neurons and constitute the molecular basis for the organism's response to thermal stimuli [30].

Four types of thermo-TRP channels activated by heating (TRPV1–4) and two thermo-TRP channels activated by cooling (TRPM8 and TRPA1, see *Fig. 1*) have been described. Upon heterologous expression (in HEK293 cells, CHO cells, and *Xenopus* oocytes), all six TRPs share the unique property of rendering cells temperature-sensitive. Each type of thermo-TRP channel has its unique temperature threshold of activation [30, 32]. The thermal sensitivity makes it possible for a neuron expressing thermo-TRP to be activated when the temperature is changed by 1–2°C [5, 33]. High ionic conductance makes these receptors particularly efficient neurobiological tools. Even at a lower expression level, thermo-TRPs cause a more stable depolarization compared to channelrhodopsins. The ability of thermo-TRPs to ensure reliable activation at moderate expression levels means that relatively "weak" promoters can be used in genetic vectors. Furthermore, low expression levels minimize the potential toxicity associated with the expression of exogenous proteins. Two tools based on thermo-TRP, rat TRPM8 (rTRPM8) [34], and the endogenous *Drosophila* receptor TRPA1 (dTRPA1) [5] (see details in the "Thermogenetics in Neurogiology" section) are currently used in *Drosophila* neurobiology. rTRPM8 is the "cold" channel activated at temperatures less than 25°C that is also sensitive to menthol [28, 35]. In routine experimentation, reliable activation of fly neurons using heterologously expressed rTRPM8 requires cooling down the animals to $\leqslant$ 18°C [34]. dTRPA1 is the *Drosophila* thermoreceptor that responds to heating and is involved in the induction

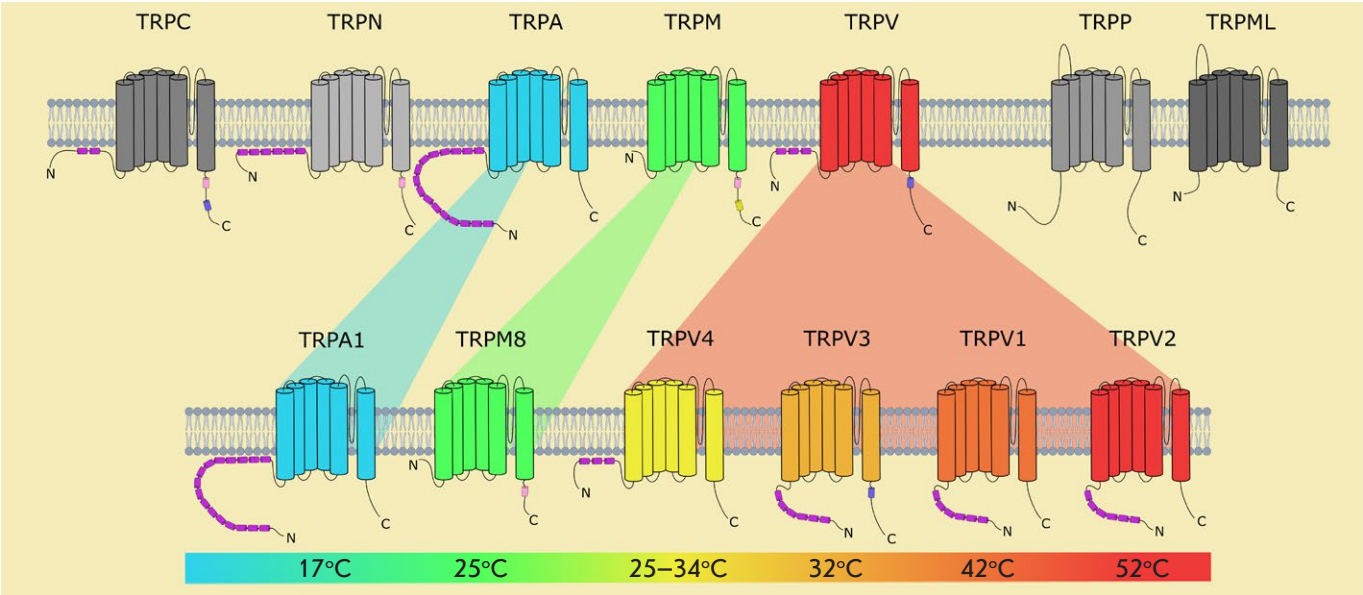

Fig. 1. The TRP superfamily and temperature sensitivity of its chosen members. The top of the figure shows seven TRP-receptor families subdivided into two groups. In the bottom row, there are thermogenetically relevant molecules originating from three TRP families. The color scheme depicts the temperatures needed for the activation of the corresponding TRPs

of avoidance behavior at elevated temperatures in fly larvae [5]. Contrariwise, homologs of this receptor in mammals are sensitive to cold temperatures [36]. dTRPA1 is activated by moderate heating within a temperature range of 25–29°C or slightly higher [5, 36–38]. The temperature modes of rTRPM8 and dTRPA1 activation make these receptors poorly suitable for experiments with homoiothermic animals (and even their neuronal cultures). To date, most thermogenetic experiments with mammalian cells and tissues have been conducted using the "hot" vanilloid channel TRPV1 [7–9, 39], which is sensitive to capsaicin and is activated at appreciably high temperatures (> 42°C) [31, 40]. A few studies have reported on the use of other thermo-TRPs (TRPV2 and 3 in HEK293 cells [41], TRPV4 in a rat primary neuronal culture [11], and TRPA1 from the rattlesnake thermosensory apparatus in a murine primary neuronal culture [13]) as thermoeffectors.

Thermogenetics in neurobiology

While neurobiological optogenetics employs mice as the main model organism, neurobiological thermogenetics is almost exclusively the "territory" of *Drosophila* fruit fly [20, 42]. Over the past decade, researchers have achieved a real breakthrough in understanding how the nervous system of fruit fly functions by using a kit consisting of two thermo-TRP channels (rTRPM8 and dTRPA1 neuronal activators) and temperature-sensitive dynamin (Shibire^{ts} neuronal inhibitor). The thermogenetic approach was used for studying memory [21–23, 37], motor activity [19, 24, 34, 43], biological rhythms [38, 44], feeding [45, 46] and sexual [6, 47] behaviors, the connectome, and learning mechanisms in *Drosophila* [48]. Temperature-sensitive effectors were used in the original studies focused on the effect of microRNA expression [49] and the gut microbiome composition [50] on the behavior of fruit flies. A study kit for demonstrating 60 different types of thermogentically induced *Drosophila* behaviors has been designed based on the dTRPA1 thermoreceptor [51].

The application of the thermogenetic approach in vertebrate neurobiology has not been systematic thus far. *In vivo* activation of thermo-TRP in the neurons of the zebrafish *Danio rerio* [13, 52] and mice [8, 9] has been reported. As mentioned above, the principle of the thermogenetic activation method has been demonstrated for the culture of mammalian neurons *in cellulo* [7, 11, 13] and for acute slices of the mouse brain *ex vivo* [39].

Limitations and perspectives of the method

Modern thermogenetics is substantially inferior to optogenetics in terms of the spatial and temporal resolution of stimulation. Thus, thermo-TRPs activate neurons during several seconds [5, 33], which is probably indicative of the kinetics of tissue heating and cooling.

When planning an *in vivo* thermogenetic experiment, it is necessary to bring the temperature mode of effector activation in line with the temperature optimum of the experimental animal. Going beyond the temperature optimum may induce the activation of the animal's endogenous thermoreceptors and sometimes even cause thermal shock. This is especially challenging when working with homoiothermic animals, since the difference between normal body temperature and the temperature at which tissue destruction begins can be as small as 6–7°C. Heating (or cooling) of tissue with a high spatial resolution poses a much greater challenge than irradiation with visible light. On the other hand, when it becomes necessary to manipulate deep-brain structures or the nervous system in general, the thermogenetic approach can be preferable to the optogenetic one (as has been confirmed by its successful application in insect neurobiology).

Further advances in thermogenetics have been largely associated with the discovery of new effector molecules that are characterized in particular by rapid activation/inactivation kinetics and/or function within a temperature range of 38–42°C (in other words, well-compatible with the physiology of homoiothermal animals). The possibility of using thermogenetic neurostimulation for therapeutic purposes (e.g., for the functioning of cochlear implants) has been discussed in [53].

CHEMOGENETICS

Chemogenetics is a family of methods involving the chemical stimulation of biological systems by small molecules mediated by actuators genetically incorporated into these systems. Chemogenetical actuators are characterized by (a) specific sensitivity to ligands acting as stimuli and (b) the ability to initiate physiologically/biochemically significant activity in response to ligand binding. Among the three approaches discussed in this review, chemogenetics is the one witnessing the most rapid development today. Thus, while in 2013 only about twenty studies employing chemogenetic tools (with few studies focusing on neurobiology) were published, at least 300 chemogenetic publications appeared in 2019 (they mainly involved *in vivo* experiments focusing on neurobiology). An explosion in interest towards tools for specific chemical stimulation started to register approximately in 2014–2015 and seems poised to increase in the near future. This boom in chemogenetics, partially caused by overall neuroscience "mobilization" (happening due to the advances in optogenetics, among other factors), is also substantially related to the enormous diversity of the mechanisms of small molecule stimulation.

The term "chemogenetics" *per se* can be interpreted widely. Below, we list the main chemogenetic approaches; from the ones less significant for neurobiology to the more significant ones.

Broch and Gautier [54] classify proteins/RNA fluorogens and small molecules acting as exogenous chromophores for these macromolecules as chemogenetic tools. Here, the dye-in-box principle of fluorescent labeling is implemented, when a non-fluorescent dye molecule that is capable of penetrating the cell binds noncovalently and highly specifically to a macromolecule genetically incorporated into the cell, thus acquiring fluorescent properties [55, 56]. A vivid example of the implementation of this concept is the FAST (fluorescence-activating and absorption shifting tag) system, whose initial form is represented by a monomeric, genetically engineered variant of the apoform of the photoactive yellow protein (PYP) from a halophilic proteobacterium, *Halorhodospira halophila*, which forms fluorescent complexes with 4-hydroxybenzylidene rhodamine derivatives [57]. Chemogenetic tools for multicolor labeling [58], including far-red fluorophores [59], have been developed as part of FAST. As fluorescent tags, fluorogenic pairs have a number of advantages over both single-component, genetically encoded dyes (GFP and similar) and small-molecule organic fluorophores. In particular, they are typically characterized by high photostability and photo-fatigue resistance, which are critical in the context of advanced microscopy methods [60, 61].

Some researchers consider that chemogenetic methods include the design of artificial enzymes (mostly metalloenzymes) and control of their activity by biotin-(strept)avidin targeting [62–65]. The principle implies delivery of biotinylated organometallic catalysts to a molecule of streptavidin or its variants. Chemogenetic optimization of the catalytic activity of such hybrid molecules can be achieved by combining the library of biotinylated catalysts with the library of streptavidin mutants [65].

A similar but more biologically relevant principle has been implemented in chemogenetics (or even chemogenomics) as a tool used for screening small-molecule libraries [66–69]. This method usually implies that the biological model system is subjected to an impact from the target compounds, selection being performed with respect to a functionally significant parameter (e.g., phenotypic manifestation of enzyme activity). It allows one to identify the most active substance within the chemical library and, vice versa, the protein (or genotype) variant most sensitive to a selected individual substance. Yeast chemogenetic screening has made it possible to identify novel protein kinase inhibitors [66], histone acetyl transferase

inhibitors [69], and fungicides [70]. The recent large-scale project [71] has characterized the resistome (i.e., a set of genes and their allelic variants associated with resistance to a certain substance) for the causative agent of malaria, relative to several dozen antimalarial drugs. Genetic determinants of multiple drug resistance have been identified.

The application of small molecules to control protein–protein interactions also conceptually refers to chemogenetic approaches. The chemically induced dimerization (CID) systems [72], which allow one to induce interaction between the target proteins fused to ligand-activated dimerization domains, are especially important here. CID systems based on homodimerization of the FKBP protein [73], heterodimerization of FKBP/FRB proteins [74], and their derivatives have shown good performance [75, 76]. These CID systems are used in neurobiology for reversible inactivation of synaptic transmission *in vivo* (in transgenic mice) by inhibiting the coalescence of synaptic vesicles [77]. The dihydrofolate reductase (DHFR) enzyme and its synthetic inhibitors (methotrexate and trimethoprim) are used in another family of chemically induced dimerization systems. For heterodimerizing targets, DHFR is combined with other ligand-binding proteins [78, 79]. Nanoantibodies (also known as nanobodies) based on this CID system, with their affinity to the target controlled chemically, are of significant interest [80, 81]. In particular, an antibody whose binding to GFP is switched on and off by NADPH and TMP ligands, respectively, has been reported [80]. This technology ensures chemically controlled reversible fluorescent labeling. Techniques for the computational design of protein molecules, which are expressed as two complementary fragments and can thus be associated upon ligand binding, are currently being developed [82].

The interaction between FKBP and its partner FRB, as well as the modulation of the activity of these proteins by small molecules (rapamycin, etc.), is applied not only in dimerization systems, but also in the chemogenetic regulation of the stability of the target proteins [83–85]. An interesting system for controlling the stability of the protein based on hepatitis C virus protease has been designed [86, 87]. When integrated into a chimeric protein, the viral polypeptide exhibits a default autoproteolytic activity, which is suppressed by the introduction of an inhibitor molecule into the system. Therefore, the chimeric protein retains its integrity and activity, as long as there is an inhibitor in the cell and it is degraded after the inhibitor is removed. Various pharmaceuticals have been successfully adapted to proteolysis inhibition, and this protein destabilization system has been shown to be promising in experiments involving transcriptional regulation, genome editing, and apoptosis.

Chemogenetic generators of small molecules come into general use. A vivid example is D-amino acid oxidase (DAAO), used to generate hydrogen peroxide in cells [88]. This yeast enzyme catalyzes the conversion of D-amino acids into the respective α-keto derivatives, accompanied by the release of a peroxide molecule [89]. Hence, almost any D-amino acid can be used to activate the H_2O_2 generator. DAAO is used as a chemogenetic effector in studies focusing on the activity of antioxidant systems [90] and cellular signaling [91] in cell cultures, as well as the effect of peroxide on cardiac activity *in vivo* [92]. In the aforelisted studies, DAAO was activated simultaneously with the monitoring of the peroxide level using fluorescent indicators.

Chemogenetic principles are used when designing fluorescent indicators of the membrane voltage. In some cases, voltage-sensitive dyes are targeted to the cell membrane using protein molecules (usually those binding covalently to these molecules) [93, 94] or even fluorogenically activated by membrane-bound enzymes [95]. In other cases, a plasma-membrane-anchored fluorescent protein acts as a FRET donor for organic fluorophore that migrates in the lipid bilayer in response to changes in the electrical potential [96]. Third, contrariwise, a microbial rhodopsin molecule acts as a voltage-sensitive unit, while its fluorescent signal is amplified due to resonance energy transfer from a bright fluorescent dye exogenously added to the cells [97, 98]. Such indicators are promising neurobiological tools; they are already being used today to monitor the electrical activity of neurons *in vivo* [98].

Chemical induction of gene transcription of bacterial enzymes is probably one of the first prototypes of chemogenetic methods [99, 100]. In turn, heterologous expression of bacterial enzymes acts as a basis for chemogenetic systems where pharmacologically relevant compounds modulate the activity of endogenous proteins in specific cell types. Thus, exposure of eukaryotic cells expressing bacterial β-galactosidase to daunomycin (daun02, a galactose derivative) was used as a model tool in tumor therapy [101]. The enzyme activity of β-galactosidase converts the pharmacologically inert daun02 into the daunorubicin antibiotic, which causes apoptosis. Experiments in the cells of a transgenic rat line where β-galactosidase is expressed under the control of the *c-fos* promoter are quite noteworthy in the context of neurosciences. Researchers employed the differential amplification of Fos (which is the endogenous transcriptional transactivator) expression in cocaine-susceptible neurons to selectively block calcium signaling in those cells.

Therefore, infusion of daunomycin into the rat brain blocked ion channels (and, therefore, transmission of motor signals) only in cocaine-sensitized neurons [102]. Some natural neurotoxins show good potential for neurobiological application in chemically inducible expression systems. In particular, the tetanus toxin (TeNT) light chain inhibiting synaptic transmission by proteolytic cleavage of synaptic vesicle proteins [103], which is expressed in neurons under the control of tetracycline-sensitive regulatory elements, is used (together with tetracycline transactivator) as a reversible chemogenetic inhibitor [104–106].

Finally, there is a large group of chemogenetic effectors that is rather heterogeneous in terms of their structure and functions that is used almost exclusively in neurobiological research. We thoroughly characterized this group in the section below.

Chemogenetic effectors for neurobiology

All the effector molecules used in neurobiological chemogenetics can be subdivided into two types: ligand-gated ion channels and chemically activated G protein-coupled receptors [107]. The evolution of both types of molecular tools is most often achieved by using wild-type receptors towards the engineering of chimeric molecules optimized to address specific research issues.

Among wild-type ligand-gated cation channels, the TRP receptors already mentioned in the Thermogenetics section are used as chemogenetic effectors. We would like to remind the reader that these cationic channels are sensitive not only to temperature, but also to chemical agents. When establishing the role played by the TRPM2 endogenous receptor expressed in the mammalian hypothalamic cells in central control of body temperature, this protein was activated by a wild-type agonist, adenosine diphosphate ribose (ADPR), and its activity was modulated by a sensitizer, hydrogen peroxide [108]. Activation of the vanilloid receptor TRPV1 by capsaicin was used for neuronal excitation in the cell culture [109] and in the brain of transgenic mice *in vivo* [110, 111] (including studies on feeding behavior [112] and pain [113]). Menthol stimulation of neurons expressing the cold receptor TRPM8 was also described [109]. A substantial drawback of TRP channels as chemogenetic actuators consists in their presence in mammalian brain tissue as endogenous receptors, which can elicit a nonspecific response to stimulation. In that context, *TRP* knockout mouse lines are used for *in vivo* studies [107].

Cys-loop receptors constitute the most important family of chemically gated ion channels used in neurobiology [107, 114]. This family of pentameric molecules carrying a typical cysteine-rich structural unit that controls ion-pore permeability includes nicotine, glycine, serotonin, and GABA receptors, as well as glutamate-gated chloride channels [107]. Although wild-type Cys-loop receptors (in particular, GABA(C) and its agonist *cis*-4-aminocrotonic acid [115], as well as GluCl and ivermectin [116]), have also been used in single studies to control neuronal activity, their artificial variants, characterized by higher sensitivity [117, 118] and modified ligand specificity [119], as well as altered ionic selectivity [120], are used more commonly as neuromodulators. However, the family of PSAM chimeric module ion channels and their ligands (PSEM) is the most in-demand chemogenetic tool designed on the basis of Cys-loop receptors [107, 120, 121]. The first variant of a pharmacologically selective actuator module (PSAM) is the product of a genetic modification of the ligand-binding domain (LBD) of the α7 nicotinic acetyl choline receptor (nAchR), with the aim to reduce its affinity for acetylcholine and develop specificity to synthetic compounds that do not activate wild-type nAchR. These compounds are called pharmacologically selective effector modules (PSEMs) [122]. The features of Cys-loop receptors' molecular organization (including structural independence of the ligand-binding domain (LBD) and the ion pore domain (IPD) [123]) have made it possible to perform the module engineering of PSAM-based receptors. Thus, the LBD selective to PSEM ligands was combined with the ion pore domains of other Cys-loop receptors [122]. In combination with the IPD of the serotonin 5HT3 receptor, the activated PSAM provides Na^+/K^+ fluxes into the cell, membrane depolarization, and neuronal excitation; in combination with the IPD of the nAchr receptor, it provides calcium flux into the cell; while in combination with the IPD of the glycine or GABA receptor, it ensures a Cl^- influx accompanied by membrane hyperpolarization and silencing of neuronal activity (*Fig. 2*). Each of the chemogenetic modules (PSAM, IPD, and PSEM) can be subjected to further modifications with the aim to broaden the range of available ligands, increase specificity and ligand affinity, as well as ion pore conductance [107, 121]. The results of a large-scale study that focused on the rational design of a new $PSAM^4$ activator specific to the anti-smoking drug varenicline, as well as a new family of uPSEM ligands characterized by subnanomodular affinity for $PSAM^4$, were published in 2019 [124] (*Fig. 2*). The potential of these tools was demonstrated in *in vivo* experiments for the activation and inhibition of neuronal activity in the brains of mice and monkeys.

The PSAM/PSEM-based system of chemogenetic neuromodulation was used in a number of important studies that focused on the mechanisms of memory

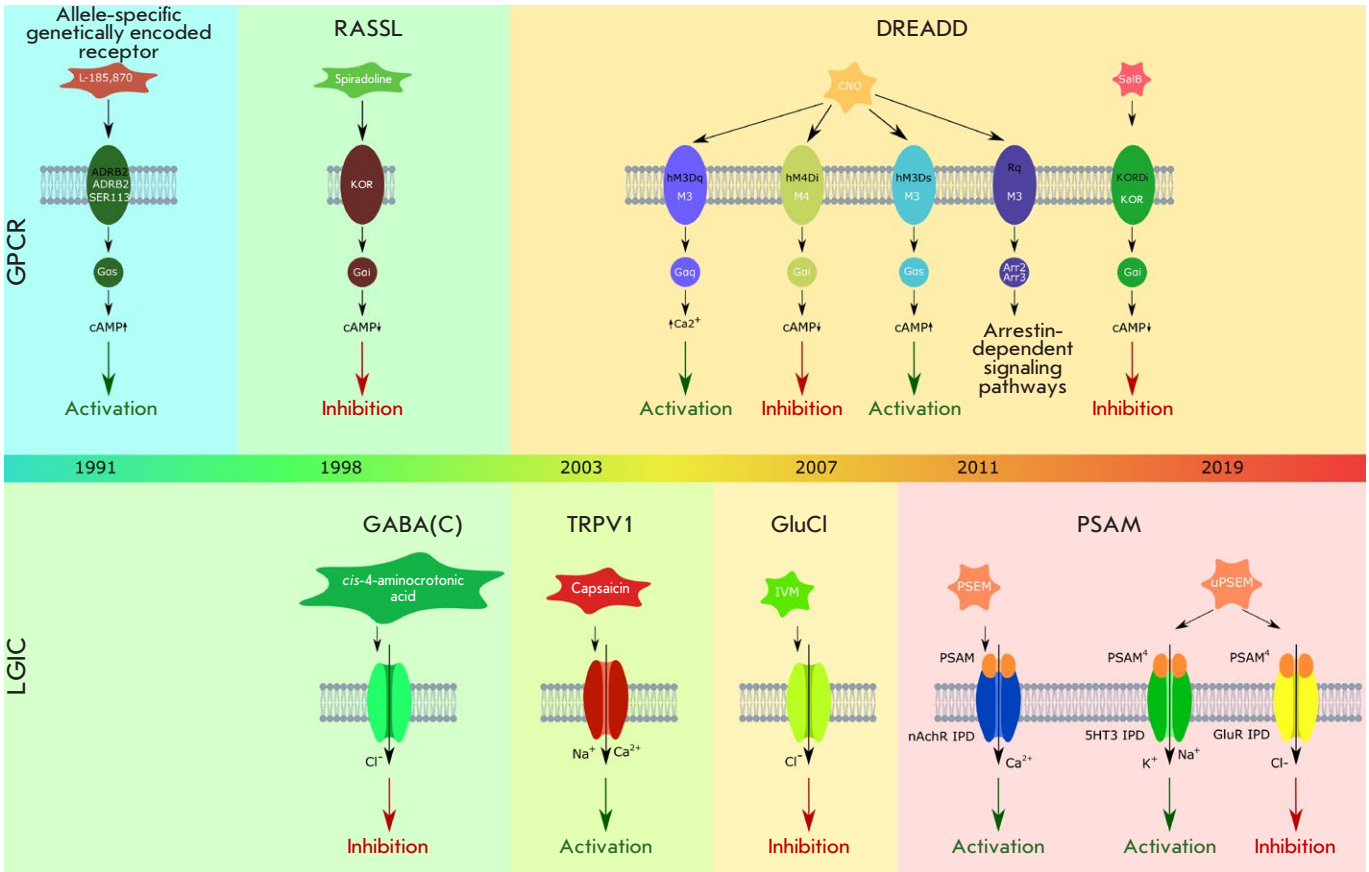

Fig. 2. The timeline showing the emergence of diverse chemogenetic approaches. The main types of chemogenetic actuators, their wild-type predecessors (top panel: GPCR-based ones; bottom panel: the ones based on ligand-gated ion channels (LGICs)), and the molecular mechanisms providing their activation are shown

and learning [125–129], pain [68], the motivational effects of hunger and thirst [130], as well as motor and behavioral activity [131, 132] *in vivo*. The clinical and therapeutic potential of this approach was discussed in [133].

Identically to optogenetic tools based on microbial rhodopsins, ligand-gated ion channels (TRPs, Cys-loop) have an ionotropic mechanism of neuromodulation; i.e., they generate transmembrane ion currents that alter the polarization of the neuronal membrane. However, receptors with a metabotropic mechanism of activation (chemically activated G protein-coupled receptors, GPCRs) are used in chemogenetics much more widely than in optogenetics. It took approximately 20 years to create a pool of chemogenetic GPCRs suitable for *in vivo* neurobiological experiments, and several stages of their evolution can be distinguished (*Fig. 2*). The key amino acid positions associated with the specificity of adrenalin binding have been identified in the study of the molecular mechanisms of ligand recognition by β-adrenergic metabotropic receptors, and the resulting data were used to design receptor variants activated by synthetic catechol derivatives [134, 135]. That was how the first allele-specific, genetically encoded receptors appeared [121, 134]. Modified β-adrenergic receptors have not found application in neurobiology; however, altering ligand specificity by rational design has become a key concept in the engineering of the RASSL family of receptors that are activated solely by synthetic ligands [136, 137]. The first RASSLs were obtained by mutagenesis of the κ-opioid receptor (KOR) [136]. The modified KOR has lost sensitivity to endogenous peptide ligands but has become activatable by its synthetic agonist, spiradoline. The *in vivo* chemogenetic experiments with the early RASSL variants made it possible to modulate cardiac activity in mice [138]. Specific stimulation of gustatory neurons by RASSLs was later used to study the mechanism of sensation of the sweet, umami, and bitter tastes [139, 140]. The application of RASSLs in neurobiology is limited, mostly because of the sensitivity of

endogenous opioid receptors to the RASSLs ligand spiradoline [107].

The drawbacks typical of RASSLs have been mostly eliminated in the next-generation chimeric GPCRs that became known as DREADDs (designer receptors exclusively activated by designer drugs, *Fig. 2*) [141]. These molecules are currently the most in-demand chemogenetic tools.

DREADDs

Systematic research into the molecular structure and activation mechanisms of wild-type GPCRs [142] has laid the conceptual foundation for designing chimeric molecules that can be activated by a pharmacologically inert substance [143]. The muscarinic acetylcholine receptor hM3 has been chosen as a pilot target for mutagenesis. After modification, hM3 has become highly selective to clozapine N-oxide (CNO) and has almost lost its affinity to the wild-type agonist acetylcholine [143]. This receptor has become the first member of the DREADD family and is known as hM3Dq, as it binds to Gq-type G proteins. CNO was chosen as a ligand, because this substance has favorable pharmacokinetics in both mice and humans; furthermore, it hardly activates endogenous GPCRs. The potential of hM3Dq was soon after demonstrated in *in vivo* experiments, where the receptor selectively activated mouse hippocampal neurons [144]. The mechanism of neuronal excitation caused by GPCR activation is much more complex than that for ionotropic receptors. Thus, hM3Dq activation induces phosphoinositol signaling, which enhances neuronal excitability, as well as the release of calcium cations from the intracellular depots, which in turn facilitates the driving of the Na^+/Ca^{2+} antiport system depolarizing the membrane [107]. Like in the case of Cys-loop receptors, the "modular design" of GPCR molecules facilitates the design of new variants of the molecule. Thus, hM3Ds [145], a DREADD activating cAMP production in response to binding to CNO, was obtained on the basis of the aforementioned hM3Dq by replacing the intracellular G protein-binding module with the Gs-coupled module from the β-adrenergic receptor [146]. By analogy with hM3, other muscarinic receptors have been modified: so, the family of CNO-sensitive DREADDs has been extended. Along with hM3Dq/hM3Ds, it includes hM1Dq, hM2Di, hM4Di, and hM5Dq; some of them are now widely used in neurobiology [121, 143, 147]. In particular, hM4Di is an inhibitory effector that reduces cAMP production and ensures hyperpolarization of neuronal membranes mediated by potassium channel opening [143]. It was further demonstrated that hM4Di is also a potent inhibitor of synaptic transmission [148, 149]. Therefore, the DREADD family comprises both effectors activating neuronal activity and the ones inhibiting it, which influence the cell physiology via the three canonical G-protein signaling pathways (Gαs, Gαq, and Gαi). Furthermore, introducing an additional mutation to hM3Dq gave rise to DREADD[Rq(R165L)] that does not interact with G proteins but selectively triggers β-arrestin signaling [150]. The molecular design principles of DREADD have been used in the engineering of other GPCRs. Thus, modification of the κ-opioid receptor (KOR) made it possible to alter ligand specificity: instead of the wild-type agonist, psychoactive salvinorin A, its mutant variant KORDi functioning as a silencer of neuronal activity is activated by pharmacologically inert salvinorin B [151].

The strategies used to deliver the DREADD genes into target cells are generally similar to those used for delivering channelrhodopsins and other optogenetic effectors (see Part I of the review) and include transient expression using viral vectors and transgenesis [107]. DREADDs are activated solely by a target-specific chemical ligand (CNO), which is not found in the cells being stimulated and exhibits extremely weak activity against endogenous receptors. The advantages of using DREADDs for neurostimulation are as follows [121]:

(a) CNO can be delivered into an animal's brain using both invasive techniques (injections) and via oral administration (with food or drinking water); no special technical facilities or manipulations (such as implantation of an optical fiber or the placing of an implant into the experimental animal's brain) are required for DREADD activation;

(b) According to its pharmacokinetics, CNO exhibits sustained action on nerve cells (lasting from several minutes to several hours); so, experiments involving long-term stimulation can be performed. Furthermore, when being introduced into the animal's organism, a DREADD ligand is appreciably uniformly distributed over tissues and reaches the deepest brain regions; so, the challenges related to the stimulation of large neuronal populations and difficultly accessible areas of the nervous tissue, which are typical of optogenetics, are ruled out in this case.

Therefore, while lacking a high spatial and temporal resolution and being barely suitable for the analysis of fast physiological processes, chemogenetic stimulation is an excellent tool for studying the effect of various chronic effects on cells or mimicking prolonged biological cycles (e.g., circadian rhythms).

Some difficulties related to the application of DREADDs are caused by the high doses of CNO required to attain sufficient stimulation intensity [152], the side effects associated with them [153], as well as

a gap in our understanding of the molecular mechanisms of CNO penetration into the brain tissue. In 2017, it was demonstrated that DREADDs in rat brain are activated by clozapine formed metabolically rather than by CNO (which cannot easily penetrate the blood–brain barrier) [154]. These facts have driven researchers to design novel DREADD agonists characterized by better penetration characteristics into the brain and possessing a higher affinity for chimeric receptors [155, 156]. Advanced techniques for ligand delivery facilitating local penetration through the blood–brain barrier have also been proposed, in particular acoustic targeting [157] and chemomagnetic modulation using heat-dissipating nanoparticles [158].

Neurobiological applications and the outlook for the method

As we mentioned earlier, the past 4–5 years have witnessed a real boom in neurobiological chemogenetics. Most of the new studies employ DREADD-family receptors, *in vivo* experiments are performed, and the range of model systems used is as broad as that in optogenetics (from mice to monkeys). Interestingly, it took almost a decade for the approach related to designer chemoreceptors to become widespread in neurosciences. We attribute this to the complexity of the molecular mechanisms of neuronal stimulation using exogenous GPCRs. We will provide only some vivid examples of chemogenetic studies, as it is impossible to cover them all in a review.

The chemogenetic approach has allowed us to gain insight into the mechanisms of axonal regeneration [159], connectome organization and interaction between large neuronal populations [160–162], as well as to study the neurophysiological foundations of cognitive dysfunction on genetic models of schizophrenia [163, 164] and autism [165, 166]. In a number of studies, selective stimulation of neurons expressing DREADDs was used to investigate the behavioral effects of cocaine [167] and alcohol [168], as well as disruptions in the brain function in the offspring caused by alcohol consumption by a pregnant female [169]. Most of the "chemogenetic" publications have focused on deciphering the mechanisms of memory [170–174] and sleep [175–178]. Some large studies have discussed the unusual associations between the functioning of the nervous and digestive systems: the role played by specific neuronal populations in the development of obesity [179], the gastroneural pathways of developing sweet taste preferences [180], and the effect of gut microbiota on the activity of sympathetic neurons [181]. In a recent elegant study, DREADD receptors helped to uncover an association between stress and the graying of hair [182]. The largest and most significant cluster of research projects employing the chemogenetic toolkit is related to the study of the neurophysiological determinants of animal behavior. These projects cover the traditional topics (such as feeding [183] and defensive [184] behavior and attention [185]), as well as specific behavioral patterns such as parental care [186] and mother–infant vocalization [187]. The chemogenetic tools have found application even in the study of the mechanisms of cat odor perception by mice [188, 189].

The question related to the clinical and therapeutic use of chemogenetics is being pondered. This refers to both the GPCR-based receptor–ligand systems [178, 190] and ligand-gated ion channels [133].

The incredible diversity of wild-type chemoreceptors (both their chemical specificity and activation mechanisms) opens up broad prospects for further development of the chemogenetic approach.

COMBINATIONS OF THE APPROACHES

Thus, we have discussed the three modern approaches to controlling biochemical processes (while placing emphasis on control over the activity of nerve cells), as well as the molecular tools related to the implementation of these approaches. Each of them (the optogenetic, thermogenetic, and chemogenetic approaches) has its own merits and flaws, and the merits of one approach are often complementary to the flaws of another. This allows one to use a more efficient and relevant tool in each specific case and even combine different principles of cell manipulation in a single model system. Here, a role is played by the orthogonality of stimulation mechanisms; (e.g., the short-term optical stimulation through ion channels and prolonged chemical stimulation through G-protein signaling can obviously be mutually complementary.)

Indeed, some examples of complementary use of opto- and chemogenetics can be found in many neurobiological experiments. Thus, simultaneous *in vivo* optogenetic and chemogenetic stimulation is used to study the mechanisms of motivation [191] and behavioral adaptations [192, 193], to identify the role played by the sodium cation in circadian rhythm regulation [194] and the role of microglia in the regulation of myelination [195], as well as to study epilepsy [196], sleep physiology [197], regulation of feeding behavior [198], and pain perception [199].

Meanwhile, there are systems where the principles of optical and chemical stimulation are intertwined at the molecular level to give rise to actual hybrid molecular tools, rather than individual ones.

The first example of this kind might date back to the early days of neurobiological optogenetics, when hippocampal neurons expressing the ligand-gated

ion channels TRPV1 and P2X2 were successfully stimulated by photoreleaseable ligands (capsaicin and ATP, respectively) in 2003 [109]. Later, hybrid photochemical stimulation of the P2X2 channel was used *in vivo* to control *Drosophila* behavior [200]. Several systems of reversible optochemical stimulation based on covalent protein modification by a small molecule linked by a photoisomerizable (azobenzene) group have been described. In one case, photoisomerization made it possible to open (using long-wavelength light) and close (using short-wavelength light) potassium channels [201], while in the other case, it allowed reversible ligand presentation to the ionotropic glutamate receptor (iGluR) [202]. Further development of this approach involved a modification of endogenous potassium channels and photochemical stimulation of the rat neurons mediated by them *in cellulo* and *ex vivo* [203], as well as the emergence of new "designer" potassium channels [204], acetylcholine [205] and glutamate [206] receptors with the same principle of activation. The latter receptors (belonging to the LiGluR family) were used in *in vivo* experiments [206, 207]. In 2020, a photochemically activated GPCR, the endogenous metabotropic glutamate receptor (mGluR2) capable of reversibly stimulating neurons, was first reported [208].

The Mito-FAP fluorogen activating peptide delivering the MG-2I photosensitizer into mitochondria also belongs to chemo-optogenetic effectors [209].

Finally, the BL-OG (BioLuminescent OptoGenetics) system, where the effector is a fusion protein (luminopsin) consisting of luciferase and channelrhodopsin, is the most "elegant" implementation of the hybrid photochemical approach to the control of cell activity [210–214]. A rhodopsin molecule is activated by luciferase luminescence; in turn, its induction and emission intensity can be adjusted by composition and the amount of cofactors (luciferin and its transporter) added to the system. The BL-OG system can be metaphorically characterized as a system for brain-targeted delivery of light.

CONCLUSIONS AND OUTLOOK

Optogenetics is a mature and extremely efficient method that has been widely recognized throughout the academic community. Thus, in 2010, *Nature Methods* recognized optogenetics as the Method of the Year [215], and *Science* included the technique into its "Breakthroughs of the Decade" collection [216]. In 2013, the exceptional significance of the optogenetic approach for neurobiological research was acknowledged by the prestigious Brain Prize awarded to six researchers who have made consequential contribution to the elaboration and development of optogenetic tools. Optogenetics has been included in the list of fundamental approaches to the implementation of the large research program BRAIN initiative (https://braininitiative.nih.gov/) supervised by the National Institutes of Health. Furthermore, we believe that the success of optogenetics has had a global impact on the development of scientific methodology, as it has become a potent catalyst for the development of diverse genetically encoded tools. The several hundred breakthrough studies that have been published over the past decade and demonstrated the flexibility and efficiency of the new approaches (chemogenetics, thermogenetics, and hybrid photochemical methods) serve as the best evidence to support this assertion. In addition to these well-proven methods, fundamentally new approaches continue to appear, such as ultrasound neuronal stimulation mediated by cation activation (sonogenetics) [217] and single-component magnetic stimulation by iron-containing proteins (magnetogenetics) [218]. We wish these methods every success. ●

This work was supported by the Russian Foundation for Basic Research (project No. 19-14-50116).

REFERENCES

1. Abram P.K., Boivin G., Moiroux J., Brodeur J. // Biol. Rev. Camb. Philos. Soc. 2017. V. 92. № 4. P. 1859–1876.
2. Garrity P.A., Goodman M.B., Samuel A.D., Sengupta P. // Genes Dev. 2010. V. 24. № 21. P. 2365–2382.
3. McKemy D.D. // Pflugers Arch. 2007. V. 454. № 5. P. 777–791.
4. Bernstein J.G., Garrity P.A., Boyden E.S. // Curr. Opin. Neurobiol. 2012. V. 22. № 1. P. 61–71.
5. Hamada F.N., Rosenzweig M., Kang K., Pulver S.R., Ghezzi A., Jegla T.J., Garrity P.A. // Nature. 2008. V. 454. № 7201. P. 217–220.
6. Kohatsu S., Koganezawa M., Yamamoto D. // Neuron. 2011. V. 69. № 3. P. 498–508.
7. Huang H., Delikanli S., Zeng H., Ferkey D.M., Pralle A. // Nat. Nanotechnol. 2010. V. 5. № 8. P. 602–606.
8. Stanley S.A., Gagner J.E., Damanpour S., Yoshida M., Dordick J.S., Friedman J.M. // Science. 2012. V. 336. № 6081. P. 604–608.
9. Chen R., Romero G., Christiansen M.G., Mohr A., Anikeeva P. // Science. 2015. V. 347. № 6229. P. 1477–1480.
10. Tay A., Di Carlo D. // Curr. Med. Chem. 2017. V. 24. № 5. P. 537–548.
11. Albert E.S., Bec J.M., Desmadryl G., Chekroud K., Travo

C., Gaboyard S., Bardin F., Marc I., Dumas M., Lenaers G., et al. // J. Neurophysiol. 2012. V. 107. № 12. P. 3227–3234.
12. Bath D.E., Stowers J.R., Hörmann D., Poehlmann A., Dickson B.J., Straw A.D. // Nat. Methods. 2014. V. 11. № 7. P. 756–762.
13. Ermakova Y.G., Lanin A.A., Fedotov I.V., Roshchin M., Kelmanson I.V., Kulik D., Bogdanova Y.A., Shokhina A.G., Bilan D.S., Staroverov D.B., et al. // Nat. Commun. 2017. V. 8. P. 15362.
14. Klinkert B., Cimdins A., Gaubig L.C., Roßmanith J., Aschke-Sonnenborn U., Narberhaus F. // J. Biotechnol. 2012. V. 160. № 1–2. P. 55–63.
15. Kamei Y., Suzuki M., Watanabe K., Fujimori K., Kawasaki T., Deguchi T., Yoneda Y., Todo T., Takagi S., Funatsu T., et al. // Nat. Methods. 2009. V. 6. № 1. P. 79–81.
16. Hirsch S.M., Sundaramoorthy S., Davies T., Zhuravlev Y., Waters J.C., Shirasu-Hiza M., Dumont J., Canman J.C. // Nat. Methods. 2018. V. 15. № 11. P. 921–923.
17. Kitamoto T. // J. Neurobiol. 2001. V. 47. № 2. P. 81–92.
18. Kawasaki F., Hazen M., Ordway R.W. // Nat. Neurosci. 2000. V. 3. № 9. P. 859–860.
19. Scaplen K.M., Mei N.J., Bounds H.A., Song S.L., Azanchi R., Kaun K.R. // Sci. Rep. 2019. V. 9. № 1. P. 4427.
20. Luo L., Callaway E.M., Svoboda K. // Neuron. 2018. V. 98. № 2. P. 256–281.
21. Felsenberg J., Jacob P.F., Walker T., Barnstedt O., Edmondson-Stait A.J., Pleijzier M.W., Otto N., Schlegel P., Sharifi N., Perisse E., et al. // Cell. 2018. V. 175. № 3. P. 709–722.e15.
22. Senapati B., Tsao C.-H., Juan Y.-A., Chiu T.-H., Wu C.-L., Waddell S., Lin S. // Nat. Neurosci. 2019. V. 22. № 12. P. 2029–2039.
23. Zhao B., Sun J., Zhang X., Mo H., Niu Y., Li Q., Wang L., Zhong Y. // Nat. Commun. 2019. V. 10. № 1. P. 4550.
24. Kohsaka H., Zwart M.F., Fushiki A., Fetter R.D., Truman J.W., Cardona A., Nose A. // Nat. Commun. 2019. V. 10. № 1. P. 2654.
25. Ni L., Klein M., Svec K.V., Budelli G., Chang E.C., Ferrer A.J., Benton R., Samuel A.D., Garrity P.A. // Elife. 2016. V. 5. P. e13254.
26. Mishra A., Salari A., Berigan B.R., Miguel K.C., Amirshenava M., Robinson A., Zars B.C., Lin J.L., Milescu L.S., Milescu M., et al. // Sci. Rep. 2018. V. 8. № 1. P. 901.
27. Mishra A., Cronley P., Ganesan M., Schulz D.J., Zars T. // J. Neurogenet. 2020. V. 34. № 1. P. 115–122.
28. McKemy D.D., Neuhausser W.M., Julius D. // Nature. 2002. V. 416. № 6876. P. 52–58.
29. Dhaka A., Viswanath V., Patapoutian A. // Annu. Rev. Neurosci. 2006. V. 29. P. 135–161.
30. Venkatachalam K., Montell C. // Annu. Rev. Biochem. 2007. V. 76. P. 387–417.
31. Tominaga M., Caterina M.J. // J. Neurobiol. 2004. V. 61. № 1. P. 3–12.
32. Jordt S.-E., McKemy D.D., Julius D. // Curr. Opin. Neurobiol. 2003. V. 13. № 4. P. 487–492.
33. Pulver S.R., Pashkovski S.L., Hornstein N.J., Garrity P.A., Griffith L.C. // J. Neurophysiol. 2009. V. 101. № 6. P. 3075–3088.
34. Peabody N.C., Pohl J.B., Diao F., Vreede A.P., Sandstrom D.J., Wang H., Zelensky P.K., White B.H. // J. Neurosci. 2009. V. 29. № 11. P. 3343–3353.
35. Peier A.M., Moqrich A., Hergarden A.C., Reeve A.J., Andersson D.A., Story G.M., Earley T.J., Dragoni I., McIntyre P., Bevan S., et al. // Cell. 2002. V. 108. № 5. P. 705–715.
36. Viswanath V., Story G.M., Peier A.M., Petrus M.J., Lee V.M., Hwang S.W., Patapoutian A., Jegla T. // Nature. 2003. V. 423. № 6942. P. 822–823.
37. Krashes M.J., DasGupta S., Vreede A., White B., Armstrong J.D., Waddell S. // Cell. 2009. V. 139. № 2. P. 416–427.
38. Parisky K.M., Agosto J., Pulver S.R., Shang Y., Kuklin E., Hodge J.J.L., Kang K., Kang K., Liu X., Garrity P.A., et al. // Neuron. 2008. V. 60. № 4. P. 672–682.
39. Roshchin M., Ermakova Y.G., Lanin A.A., Chebotarev A.S., Kelmanson I.V., Balaban P.M., Zheltikov A.M., Belousov V.V., Nikitin E.S. // Neurosci. Lett. 2018. V. 687. P. 153–157.
40. Tominaga M., Caterina M.J., Malmberg A.B., Rosen T.A., Gilbert H., Skinner K., Raumann B.E., Basbaum A.I., Julius D. // Neuron. 1998. V. 21. № 3. P. 531–543.
41. Yao J., Liu B., Qin F. // Biophys. J. 2009. V. 96. № 9. P. 3611–3619.
42. Guo C., Pan Y., Gong Z. // Neurosci. Bull. 2019. V. 35. № 6. P. 1058–1072.
43. Park J., Kondo S., Tanimoto H., Kohsaka H., Nose A. // Sci. Rep. 2018. V. 8. № 1. P. 10307.
44. Dreyer A.P., Martin M.M., Fulgham C.V., Jabr D.A., Bai L., Beshel J., Cavanaugh D.J. // PLoS Genet. 2019. V. 15. № 11. P. e1008478.
45. Youn H., Kirkhart C., Chia J., Scott K. // PLoS One. 2018. V. 13. № 6. P. e0198362.
46. Poças G.M., Domingos P.M., Mirth C.K. // J. Vis. Exp. 2020. № 160. P. e61323.
47. Agrawal S., Dickinson M.H. // J. Exp. Biol. 2019. V. 222. № 16. P. jeb203414.
48. Warth Pérez Arias C.C., Frosch P., Fiala A., Riemensperger T.D. // Front. Physiol. 2020. V. 11. P. 53.
49. Picao-Osorio J., Johnston J., Landgraf M., Berni J., Alonso C.R. // Science. 2015. V. 350. № 6262. P. 815–820.
50. Schretter C.E., Vielmetter J., Bartos I., Marka Z., Marka S., Argade S., Mazmanian S.K. // Nature. 2018. V. 563. № 7731. P. 402–406.
51. McKellar C.E., Wyttenbach R.A. // J. Undergrad. Neurosci. Edu. 2017. V. 15. № 2. P. A110–A116.
52. Chen S., Chiu C.N., McArthur K.L., Fetcho J.R., Prober D.A. // Nat. Methods. 2016. V. 13. № 2. P. 147–150.
53. Richter C.-P., Rajguru S., Bendett M. // Proc. SPIE–the Int. Soc. Opt. Eng. 2013. V. 8565. P. 85651Y.
54. Broch F., Gautier A. // Chempluschem. 2020. V. 85. № 7. P. 1487–1497.
55. Szent-Gyorgyi C., Schmidt B.F., Schmidt B.A., Creeger Y., Fisher G.W., Zakel K.L., Adler S., Fitzpatrick J.A.J., Woolford C.A., Yan Q., et al. // Nat. Biotechnol. 2008. V. 26. № 2. P. 235–240.
56. Gallo E. // Bioconjug. Chem. 2020. V. 31. № 1. P. 16–27.
57. Plamont M.-A., Billon-Denis E., Maurin S., Gauron C., Pimenta F.M., Specht C.G., Shi J., Quérard J., Pan B., Rossignol J., et al. // Proc. Natl. Acad. Sci. USA. 2016. V. 113. № 3. P. 497–502.
58. Tebo A.G., Moeyaert B., Thauvin M., Carlon-Andres I., Böken D., Volovitch M., Padilla-Parra S., Dedecker P., Vriz S., Gautier A. // Nat. Chem. Biol. 2020. V. 17. № 1. P. 30–38.
59. Li C., Tebo A.G., Thauvin M., Plamont M.-A., Volovitch M., Morin X., Vriz S., Gautier A. // Angew. Chem. Int. Ed. Engl. 2020. V. 59. № 41. P. 17917–17923.
60. Li H., Vaughan J.C. // Chem. Rev. 2018. V. 118. № 18. P. 9412–9454.
61. Kiuchi T., Higuchi M., Takamura A., Maruoka M., Watanabe N. // Nat. Methods. 2015. V. 12. № 8. P. 743–746.
62. Collot J., Gradinaru J., Humbert N., Skander M., Zocchi A., Ward T.R. // J. Am. Chem. Soc. 2003. V. 125. № 30. P. 9030–9031.

63. Klein G., Humbert N., Gradinaru J., Ivanova A., Gilardoni F., Rusbandi U.E., Ward T.R. // Angew. Chem. Int. Ed. Engl. 2005. V. 44. № 47. P. 7764–7767.
64. Zimbron J.M., Sardo A., Heinisch T., Wohlschlager T., Gradinaru J., Massa C., Schirmer T., Creus M., Ward T.R. // Chemistry. 2010. V. 16. № 43. P. 12883–12889.
65. Heinisch T., Ward T.R. // Acc. Chem. Res. 2016. V. 49. № 9. P. 1711–1721.
66. Bishop A.C., Ubersax J.A., Petsch D.T., Matheos D.P., Gray N.S., Blethrow J., Shimizu E., Tsien J.Z., Schultz P.G., Rose M.D., et al. // Nature. 2000. V. 407. № 6802. P. 395–401.
67. Deb Roy A., Grüschow S., Cairns N., Goss R.J.M. // J. Am. Chem. Soc. 2010. V. 132. № 35. P. 12243–12245.
68. Ren W., Centeno M.V., Berger S., Wu Y., Na X., Liu X., Kondapalli J., Apkarian A.V., Martina M., Surmeier D.J. // Nat. Neurosci. 2016. V. 19. № 2. P. 220–222.
69. Secci D., Carradori S., Bizzarri B., Bolasco A., Ballario P., Patramani Z., Fragapane P., Vernarecci S., Canzonetta C., Filetici P. // Bioorg. Med. Chem. 2014. V. 22. № 5. P. 1680–1689.
70. Chaillot J., Tebbji F., García C., Wurtele H., Pelletier R., Sellam A. // Front. Microbiol. 2017. V. 8. P. 1956.
71. Cowell A.N., Istvan E.S., Lukens A.K., Gomez-Lorenzo M.G., Vanaerschot M., Sakata-Kato T., Flannery E.L., Magistrado P., Owen E., Abraham M., et al. // Science. 2018. V. 359. № 6372. P. 191–199.
72. Voß S., Klewer L., Wu Y.-W. // Curr. Opin. Chem. Biol. 2015. V. 28. P. 194–201.
73. Spencer D.M., Wandless T.J., Schreiber S.L., Crabtree G.R. // Science. 1993. V. 262. № 5136. P. 1019–1024.
74. Ho S.N., Biggar S.R., Spencer D.M., Schreiber S.L., Crabtree G.R. // Nature. 1996. V. 382. № 6594. P. 822–826.
75. Liberles S.D., Diver S.T., Austin D.J., Schreiber S.L. // Proc. Natl. Acad. Sci. USA. 1997. V. 94. № 15. P. 7825–7830.
76. Wu H.D., Kikuchi M., Dagliyan O., Aragaki A.K., Nakamura H., Dokholyan N.V., Umehara T., Inoue T. // Nat. Methods. 2020. V. 17. № 9. P. 928–936.
77. Karpova A.Y., Tervo D.G.R., Gray N.W., Svoboda K. // Neuron. 2005. V. 48. № 5. P. 727–735.
78. Lin H., Abida W.M., Sauer R.T., Cornish V.W. // J. Am. Chem. Soc. 2000. V. 122. № 17. P. 4247–4248.
79. Czlapinski J.L., Schelle M.W., Miller L.W., Laughlin S.T., Kohler J.J., Cornish V.W., Bertozzi C.R. // J. Am. Chem. Soc. 2008. V. 130. № 40. P. 13186–13187.
80. Farrants H., Tarnawski M., Müller T.G., Otsuka S., Hiblot J., Koch B., Kueblbeck M., Kräusslich H.-G., Ellenberg J., Johnsson K. // Nat. Methods. 2020. V. 17. № 3. P. 279–282.
81. Marzilli A.M., McMahan J.B., Ngo J.T. // Nat. Methods. 2020. V. 17. № 3. P. 259–260.
82. Dagliyan O., Krokhotin A., Ozkan-Dagliyan I., Deiters A., Der C.J., Hahn K.M., Dokholyan N.V. // Nat. Commun. 2018. V. 9. № 1. P. 4042.
83. Banaszynski L.A., Chen L.-C., Maynard-Smith L.A., Ooi A.G.L., Wandless T.J. // Cell. 2006. V. 126. № 5. P. 995–1004.
84. Banaszynski L.A., Sellmyer M.A., Contag C.H., Wandless T.J., Thorne S.H. // Nat. Med. 2008. V. 14. № 10. P. 1123–1127.
85. Glass M., Busche A., Wagner K., Messerle M., Borst E.M. // Nat. Methods. 2009. V. 6. № 8. P. 577–579.
86. Tague E.P., Dotson H.L., Tunney S.N., Sloas D.C., Ngo J.T. // Nat. Methods. 2018. V. 15. № 7. P. 519–522.
87. Jacobs C.L., Badiee R.K., Lin M.Z. // Nat. Methods. 2018. V. 15. № 7. P. 523–526.
88. Stein K.T., Moon S.J., Sikes H.D. // ACS Synth. Biol. 2018. V. 7. № 9. P. 2037–2044.
89. Pollegioni L., Langkau B., Tischer W., Ghisla S., Pilone M.S. // J. Biol. Chem. 1993. V. 268. № 19. P. 13850–13857.
90. Mishina N.M., Bogdanova Y.A., Ermakova Y.G., Panova A.S., Kotova D.A., Bilan D.S., Steinhorn B., Arnér E.S.J., Michel T., Belousov V.V. // Antioxid. Redox Signal. 2019. V. 31. № 9. P. 664–670.
91. Saeedi Saravi S.S., Eroglu E., Waldeck-Weiermair M., Sorrentino A., Steinhorn B., Belousov V., Michel T. // Redox Biol. 2020. V. 36. P. 101605.
92. Steinhorn B., Sorrentino A., Badole S., Bogdanova Y., Belousov V., Michel T. // Nat. Commun. 2018. V. 9. № 1. P. 4044.
93. Sundukova M., Prifti E., Bucci A., Kirillova K., Serrao J., Reymond L., Umebayashi M., Hovius R., Riezman H., Johnsson K., et al. // Angew. Chem. Int. Ed. Engl. 2019. V. 58. № 8. P. 2341–2344.
94. Grenier V., Daws B.R., Liu P., Miller E.W. // J. Am. Chem. Soc. 2019. V. 141. № 3. P. 1349–1358.
95. Liu P., Grenier V., Hong W., Muller V.R., Miller E.W. // J. Am. Chem. Soc. 2017. V. 139. № 48. P. 17334–17340.
96. Chanda B., Blunck R., Faria L.C., Schweizer F.E., Mody I., Bezanilla F. // Nat. Neurosci. 2005. V. 8. № 11. P. 1619–1626.
97. Xu Y., Peng L., Wang S., Wang A., Ma R., Zhou Y., Yang J., Sun D.-E., Lin W., Chen X., et al. // Angew. Chem. Int. Ed. Engl. 2018. V. 57. № 15. P. 3949–3953.
98. Abdelfattah A.S., Kawashima T., Singh A., Novak O., Liu H., Shuai Y., Huang Y.-C., Campagnola L., Seeman S.C., Yu J., et al. // Science. 2019. V. 365. № 6454. P. 699–704.
99. Pardee A.B., Jacob F., Monod J. // J. Mol. Biol. 1959. V. 1. № 2. P. 165–178.
100. Jacob F., Monod J. // J. Mol. Biol. 1961. V. 3. P. 318–356.
101. Farquhar D., Pan B.F., Sakurai M., Ghosh A., Mullen C.A., Nelson J.A. // Cancer Chemother. Pharmacol. 2002. V. 50. № 1. P. 65–70.
102. Koya E., Golden S.A., Harvey B.K., Guez-Barber D.H., Berkow A., Simmons D.E., Bossert J.M., Nair S.G., Uejima J.L., Marin M.T., et al. // Nat. Neurosci. 2009. V. 12. № 8. P. 1069–1073.
103. Link E., Edelmann L., Chou J.H., Binz T., Yamasaki S., Eisel U., Baumert M., Südhof T.C., Niemann H., Jahn R. // Biochem. Biophys. Res. Commun. 1992. V. 189. № 2. P. 1017–1023.
104. Nakashiba T., Young J.Z., McHugh T.J., Buhl D.L., Tonegawa S. // Science. 2008. V. 319. № 5867. P. 1260–1264.
105. Wahl A.S., Omlor W., Rubio J.C., Chen J.L., Zheng H., Schröter A., Gullo M., Weinmann O., Kobayashi K., Helmchen F., et al. // Science. 2014. V. 344. № 6189. P. 1250–1255.
106. Kinoshita M., Matsui R., Kato S., Hasegawa T., Kasahara H., Isa K., Watakabe A., Yamamori T., Nishimura Y., Alstermark B., et al. // Nature. 2012. V. 487. № 7406. P. 235–238.
107. Atasoy D., Sternson S.M. // Physiol. Rev. 2018. V. 98. № 1. P. 391–418.
108. Song K., Wang H., Kamm G.B., Pohle J., Reis F. de C., Heppenstall P., Wende H., Siemens J. // Science. 2016. V. 353. № 6306. P. 1393–1398.
109. Zemelman B.V., Nesnas N., Lee G.A., Miesenbock G. // Proc. Natl. Acad. Sci. USA. 2003. V. 100. № 3. P. 1352–1357.
110. Arenkiel B.R., Klein M.E., Davison I.G., Katz L.C., Ehlers M.D. // Nat. Methods. 2008. V. 5. № 4. P. 299–302.
111. Güler A.D., Rainwater A., Parker J.G., Jones G.L., Argilli E., Arenkiel B.R., Ehlers M.D., Bonci A., Zweifel L.S., Palmiter R.D. // Nat. Commun. 2012. V. 3. P. 746.
112. Dietrich M.O., Zimmer M.R., Bober J., Horvath T.L. // Cell. 2015. V. 160. № 6. P. 1222–1232.
113. Wang S., Bian C., Yang J., Arora V., Gao Y., Wei F., Chung M.-K. // eNeuro. V. 7. № 3. P. ENEURO.0118-20.2020.

114. Sine S.M., Engel A.G. // Nature. 2006. V. 440. № 7083. P. 448–455.
115. Cheng Q., Kulli J.C., Yang J. // J. Neurosci. 2001. V. 21. № 10. P. 3419–3428.
116. Slimko E.M., McKinney S., Anderson D.J., Davidson N., Lester H.A. // J. Neurosci. 2002. V. 22. № 17. P. 7373–7379.
117. Lerchner W., Xiao C., Nashmi R., Slimko E.M., van Trigt L., Lester H.A., Anderson D.J. // Neuron. 2007. V. 54. № 1. P. 35–49.
118. Lin D., Boyle M.P., Dollar P., Lee H., Lein E.S., Perona P., Anderson D.J. // Nature. 2011. V. 470. № 7333. P. 221–226.
119. Obenhaus H.A., Rozov A., Bertocchi I., Tang W., Kirsch J., Betz H., Sprengel R. // Front. Mol. Neurosci. 2016. V. 9. P. 75.
120. Islam R., Keramidas A., Xu L., Durisic N., Sah P., Lynch J.W. // ACS Chem. Neurosci. 2016. V. 7. № 12. P. 1647–1657.
121. Sternson S.M., Roth B.L. // Annu. Rev. Neurosci. 2014. V. 37. P. 387–407.
122. Magnus C.J., Lee P.H., Atasoy D., Su H.H., Looger L.L., Sternson S.M. // Science. 2011. V. 333. № 6047. P. 1292–1296.
123. Eiselé J.L., Bertrand S., Galzi J.L., Devillers-Thiéry A., Changeux J.P., Bertrand D. // Nature. 1993. V. 366. № 6454. P. 479–483.
124. Magnus C.J., Lee P.H., Bonaventura J., Zemla R., Gomez J.L., Ramirez M.H., Hu X., Galvan A., Basu J., Michaelides M., et al. // Science. 2019. V. 364. № 6436. P. eaav5282.
125. Donato F., Rompani S.B., Caroni P. // Nature. 2013. V. 504. № 7479. P. 272–276.
126. Lovett-Barron M., Kaifosh P., Kheirbek M.A., Danielson N., Zaremba J.D., Reardon T.R., Turi G.F., Hen R., Zemelman B.V., Losonczy A. // Science. 2014. V. 343. № 6173. P. 857–863.
127. Donato F., Chowdhury A., Lahr M., Caroni P. // Neuron. 2015. V. 85. № 4. P. 770–786.
128. Basu J., Zaremba J.D., Cheung S.K., Hitti F.L., Zemelman B.V., Losonczy A., Siegelbaum S.A. // Science. 2016. V. 351. № 6269. P. aaa5694.
129. Karunakaran S., Chowdhury A., Donato F., Quairiaux C., Michel C.M., Caroni P. // Nat. Neurosci. 2016. V. 19. № 3. P. 454–464.
130. Betley J.N., Xu S., Cao Z.F.H., Gong R., Magnus C.J., Yu Y., Sternson S.M. // Nature. 2015. V. 521. № 7551. P. 180–185.
131. Esposito M.S., Capelli P., Arber S. // Nature. 2014. V. 508. № 7496. P. 351–356.
132. Muñoz W., Tremblay R., Levenstein D., Rudy B. // Science. 2017. V. 355. № 6328. P. 954–959.
133. Vogt N. // Nat. Methods. 2019. V. 16. № 5. P. 363.
134. Strader C.D., Gaffney T., Sugg E.E., Candelore M.R., Keys R., Patchett A.A., Dixon R.A. // J. Biol. Chem. 1991. V. 266. № 1. P. 5–8.
135. Small K.M., Brown K.M., Forbes S.L., Liggett S.B. // J. Biol. Chem. 2001. V. 276. № 34. P. 31596–31601.
136. Coward P., Wada H.G., Falk M.S., Chan S.D., Meng F., Akil H., Conklin B.R. // Proc. Natl. Acad. Sci. USA. 1998. V. 95. № 1. P. 352–357.
137. Conklin B.R., Hsiao E.C., Claeysen S., Dumuis A., Srinivasan S., Forsayeth J.R., Guettier J.-M., Chang W.C., Pei Y., McCarthy K.D., et al. // Nat. Methods. 2008. V. 5. № 8. P. 673–678.
138. Redfern C.H., Coward P., Degtyarev M.Y., Lee E.K., Kwa A.T., Hennighausen L., Bujard H., Fishman G.I., Conklin B.R. // Nat. Biotechnol. 1999. V. 17. № 2. P. 165–169.
139. Zhao G.Q., Zhang Y., Hoon M.A., Chandrashekar J., Erlenbach I., Ryba N.J.P., Zuker C.S. // Cell. 2003. V. 115. № 3. P. 255–266.
140. Mueller K.L., Hoon M.A., Erlenbach I., Chandrashekar J., Zuker C.S., Ryba N.J.P. // Nature. 2005. V. 434. № 7030. P. 225–229.
141. Zhu H., Roth B.L. // Int. J. Neuropsychopharmacol. 2014. V. 18. № 1. P. pyu007.
142. Armbruster B.N., Roth B.L. // J. Biol. Chem. 2005. V. 280. № 7. P. 5129–5132.
143. Armbruster B.N., Li X., Pausch M.H., Herlitze S., Roth B.L. // Proc. Natl. Acad. Sci. USA. 2007. V. 104. № 12. P. 5163–5168.
144. Alexander G.M., Rogan S.C., Abbas A.I., Armbruster B.N., Pei Y., Allen J.A., Nonneman R.J., Hartmann J., Moy S.S., Nicolelis M.A., et al. // Neuron. 2009. V. 63. № 1. P. 27–39.
145. Guettier J.-M., Gautam D., Scarselli M., Ruiz de Azua I., Li J.H., Rosemond E., Ma X., Gonzalez F.J., Armbruster B.N., Lu H., et al. // Proc. Natl. Acad. Sci. USA. 2009. V. 106. № 45. P. 19197–19202.
146. Farrell M.S., Pei Y., Wan Y., Yadav P.N., Daigle T.L., Urban D.J., Lee H.-M., Sciaky N., Simmons A., Nonneman R.J., et al. // Neuropsychopharmacology. 2013. V. 38. № 5. P. 854–862.
147. Whissell P.D., Tohyama S., Martin L.J. // Front. Genet. 2016. V. 7. P. 70.
148. Mahler S.V., Vazey E.M., Beckley J.T., Keistler C.R., McGlinchey E.M., Kaufling J., Wilson S.P., Deisseroth K., Woodward J.J., Aston-Jones G. // Nat. Neurosci. 2014. V. 17. № 4. P. 577–585.
149. Stachniak T.J., Ghosh A., Sternson S.M. // Neuron. 2014. V. 82. № 4. P. 797–808.
150. Nakajima K., Wess J. // Mol. Pharmacol. 2012. V. 82. № 4. P. 575–582.
151. Vardy E., Robinson J.E., Li C., Olsen R.H.J., DiBerto J.F., Giguere P.M., Sassano F.M., Huang X.-P., Zhu H., Urban D.J., et al. // Neuron. 2015. V. 86. № 4. P. 936–946.
152. Roth B.L. // Neuron. 2016. V. 89. № 4. P. 683–694.
153. MacLaren D.A.A., Browne R.W., Shaw J.K., Krishnan Radhakrishnan S., Khare P., España R.A., Clark S.D. // eNeuro. V. 3. № 5. P. ENEURO.0219-16.2016.
154. Gomez J.L., Bonaventura J., Lesniak W., Mathews W.B., Sysa-Shah P., Rodriguez L.A., Ellis R.J., Richie C.T., Harvey B.K., Dannals R.F., et al. // Science. 2017. V. 357. № 6350. P. 503–507.
155. Bonaventura J., Eldridge M.A.G., Hu F., Gomez J.L., Sanchez-Soto M., Abramyan A.M., Lam S., Boehm M.A., Ruiz C., Farrell M.R., et al. // Nat. Commun. 2019. V. 10. № 1. P. 4627.
156. Nagai Y., Miyakawa N., Takuwa H., Hori Y., Oyama K., Ji B., Takahashi M., Huang X.-P., Slocum S.T., DiBerto J.F., et al. // Nat. Neurosci. 2020. V. 23. № 9. P. 1157–1167.
157. Szablowski J.O., Lee-Gosselin A., Lue B., Malounda D., Shapiro M.G. // Nat. Biomed. Eng. 2018. V. 2. № 7. P. 475–484.
158. Rao S., Chen R., LaRocca A.A., Christiansen M.G., Senko A.W., Shi C.H., Chiang P.-H., Varnavides G., Xue J., Zhou Y., et al. // Nat. Nanotechnol. 2019. V. 14. № 10. P. 967–973.
159. Jaiswal P.B., Mistretta O.C., Ward P.J., English A.W. // Brain Sci. 2018. V. 8. № 5. P. 93.
160. Wall N.R., Neumann P.A., Beier K.T., Mokhtari A.K., Luo L., Malenka R.C. // Neuron. 2019. V. 104. № 5. P. 916–930.e5.
161. Zhang D., Yan X., She L., Wen Y., Poo M.-M. // Proc. Natl. Acad. Sci. USA. 2020. V. 117. № 33. P. 20254–20264.
162. Peeters L.M., Hinz R., Detrez J.R., Missault S., De Vos W.H., Verhoye M., van der Linden A., Keliris G.A. // Neuroimage. 2020. V. 220. P. 117088.

163. Marissal T., Salazar R.F., Bertollini C., Mutel S., De Roo M., Rodriguez I., Müller D., Carleton A. // Nat. Neurosci. 2018. V. 21. № 10. P. 1412–1420.
164. Mukherjee A., Carvalho F., Eliez S., Caroni P. // Cell. 2019. V. 178. № 6. P. 1387–1402.e14.
165. Krishnan V., Stoppel D.C., Nong Y., Johnson M.A., Nadler M.J.S., Ozkaynak E., Teng B.L., Nagakura I., Mohammad F., Silva M.A., et al. // Nature. 2017. V. 543. № 7646. P. 507–512.
166. Trakoshis S., Martínez-Cañada P., Rocchi F., Canella C., You W., Chakrabarti B., Ruigrok A.N., Bullmore E.T., Suckling J., Markicevic M., et al. // Elife. 2020. V. 9. P. e55684.
167. Bariselli S., Miyazaki N.L., Creed M.C., Kravitz A.V. // Nat. Commun. 2020. V. 11. № 1. P. 3996.
168. Valyear M.D., Glovaci I., Zaari A., Lahlou S., Trujillo-Pisanty I., Andrew Chapman C., Chaudhri N. // Nat. Commun. 2020. V. 11. № 1. P. 3764.
169. Cuzon Carlson V.C., Gremel C.M., Lovinger D.M. // Nat. Commun. 2020. V. 11. № 1. P. 2555.
170. Adamsky A., Kol A., Kreisel T., Doron A., Ozeri-Engelhard N., Melcer T., Refaeli R., Horn H., Regev L., Groysman M., et al. // Cell. 2018. V. 174. № 1. P. 59–71.e14.
171. Khalaf O., Resch S., Dixsaut L., Gorden V., Glauser L., Gräff J. // Science. 2018. V. 360. № 6394. P. 1239–1242.
172. Zhu B., Eom J., Hunt R.F. // Nat. Commun. 2019. V. 10. № 1. P. 5156.
173. Shrestha P., Ayata P., Herrero-Vidal P., Longo F., Gastone A., LeDoux J.E., Heintz N., Klann E. // Nat. Neurosci. 2020. V. 23. № 2. P. 281–292.
174. Keinath A.T., Nieto-Posadas A., Robinson J.C., Brandon M.P. // Nat. Commun. 2020. V. 11. № 1. P. 3026.
175. Eban-Rothschild A., Rothschild G., Giardino W.J., Jones J.R., de Lecea L. // Nat. Neurosci. 2016. V. 19. № 10. P. 1356–1366.
176. Holth J.K., Fritschi S.K., Wang C., Pedersen N.P., Cirrito J.R., Mahan T.E., Finn M.B., Manis M., Geerling J.C., Fuller P.M., et al. // Science. 2019. V. 363. № 6429. P. 880–884.
177. Feng H., Wen S.-Y., Qiao Q.-C., Pang Y.-J., Wang S.-Y., Li H.-Y., Cai J., Zhang K.-X., Chen J., Hu Z.-A., et al. // Nat. Commun. 2020. V. 11. № 1. P. 3661.
178. Fleury Curado T., Pho H., Freire C., Amorim M.R., Bonaventura J., Kim L.J., Lee R., Cabassa M.E., Streeter S.R., Branco L.G., et al. // Am. J. Respir. Crit. Care Med. 2020. V. 203. № 1. P. 102–110.
179. Ewbank S.N., Campos C.A., Chen J.Y., Bowen A.J., Padilla S.L., Dempsey J.L., Cui J.Y., Palmiter R.D. // Proc. Natl. Acad. Sci. USA. 2020. V. 117. № 34. P. 20874–20880.
180. Tan H.-E., Sisti A.C., Jin H., Vignovich M., Villavicencio M., Tsang K.S., Goffer Y., Zuker C.S. // Nature. 2020. V. 580. № 7804. P. 511–516.
181. Muller P.A., Schneeberger M., Matheis F., Wang P., Kerner Z., Ilanges A., Pellegrino K., Del Mármol J., Castro T.B.R., Furuichi M., et al. // Nature. 2020. V. 583. № 7816. P. 441–446.
182. Zhang B., Ma S., Rachmin I., He M., Baral P., Choi S., Gonçalves W.A., Shwartz Y., Fast E.M., Su Y., et al. // Nature. 2020. V. 577. № 7792. P. 676–681.
183. Barbier M., Chometton S., Pautrat A., Miguet-Alfonsi C., Datiche F., Gascuel J., Fellmann D., Peterschmitt Y., Coizet V., Risold P.-Y. // Proc. Natl. Acad. Sci. USA. 2020. V. 117. № 27. P. 15967–15976.
184. Barbano M.F., Wang H.-L., Zhang S., Miranda-Barrientos J., Estrin D.J., Figueroa-González A., Liu B., Barker D.J., Morales M. // Neuron. 2020. V. 107. № 2. P. 368–382.e8.
185. Nabel E.M., Garkun Y., Koike H., Sadahiro M., Liang A., Norman K.J., Taccheri G., Demars M.P., Im S., Caro K., et al. // Nat. Commun. 2020. V. 11. № 1. P. 3983.
186. Bendesky A., Kwon Y.-M., Lassance J.-M., Lewarch C.L., Yao S., Peterson B.K., He M.X., Dulac C., Hoekstra H.E. // Nature. 2017. V. 544. № 7651. P. 434–439.
187. Tasaka G.-I., Feigin L., Maor I., Groysman M., DeNardo L.A., Schiavo J.K., Froemke R.C., Luo L., Mizrahi A. // Neuron. 2020. V. 107. № 3. P. 566–579.e7.
188. Kondoh K., Lu Z., Ye X., Olson D.P., Lowell B.B., Buck L.B. // Nature. 2016. V. 532. № 7597. P. 103–106.
189. Tong W.H., Abdulai-Saiku S., Vyas A. // Neuroendocrinology. 2020. V. 111. № 6. P. 505–520.
190. Shchepinova M.M., Hanyaloglu A.C., Frost G.S., Tate E.W. // Curr. Opin. Chem. Biol. 2020. V. 56. P. 98–110.
191. Parker K.E., Pedersen C.E., Gomez A.M., Spangler S.M., Walicki M.C., Feng S.Y., Stewart S.L., Otis J.M., Al-Hasani R., McCall J.G., et al. // Cell. 2019. V. 178. № 3. P. 653–671.e19.
192. Han W., Tellez L.A., Rangel M.J., Motta S.C., Zhang X., Perez I.O., Canteras N.S., Shammah-Lagnado S.J., van den Pol A.N., de Araujo I.E. // Cell. 2017. V. 168. № 1–2. P. 311–324.e18.
193. Mu Y., Bennett D.V., Rubinov M., Narayan S., Yang C.-T., Tanimoto M., Mensh B.D., Looger L.L., Ahrens M.B. // Cell. 2019. V. 178. № 1. P. 27–43.e19.
194. Gizowski C., Bourque C.W. // Nature. 2020. V. 583. № 7816. P. 421–424.
195. Hughes A.N., Appel B. // Nat. Neurosci. 2020. V. 23. № 9. P. 1055–1066.
196. Chen B., Xu C., Wang Y., Lin W., Wang Y., Chen L., Cheng H., Xu L., Hu T., Zhao J., et al. // Nat. Commun. 2020. V. 11. № 1. P. 923.
197. Zhong P., Zhang Z., Barger Z., Ma C., Liu D., Ding X., Dan Y. // Neuron. 2019. V. 104. № 4. P. 795–809.e6.
198. Bai L., Mesgarzadeh S., Ramesh K.S., Huey E.L., Liu Y., Gray L.A., Aitken T.J., Chen Y., Beutler L.R., Ahn J.S., et al. // Cell. 2019. V. 179. № 5. P. 1129–1143.e23.
199. Yin L., Li L., Deng J., Wang D., Guo Y., Zhang X., Li H., Zhao S., Zhong H., Dong H. // Front. Neural Circuits. 2019. V. 13. P. 73.
200. Lima S.Q., Miesenböck G. // Cell. 2005. V. 121. № 1. P. 141–152.
201. Banghart M., Borges K., Isacoff E., Trauner D., Kramer R.H. // Nat. Neurosci. 2004. V. 7. № 12. P. 1381–1386.
202. Volgraf M., Gorostiza P., Numano R., Kramer R.H., Isacoff E.Y., Trauner D. // Nat. Chem. Biol. 2006. V. 2. № 1. P. 47–52.
203. Fortin D.L., Banghart M.R., Dunn T.W., Borges K., Wagenaar D.A., Gaudry Q., Karakossian M.H., Otis T.S., Kristan W.B., Trauner D., et al. // Nat. Methods. 2008. V. 5. № 4. P. 331–338.
204. Fortin D.L., Dunn T.W., Fedorchak A., Allen D., Montpetit R., Banghart M.R., Trauner D., Adelman J.P., Kramer R.H. // J. Neurophysiol. 2011. V. 106. № 1. P. 488–496.
205. Tochitsky I., Banghart M.R., Mourot A., Yao J.Z., Gaub B., Kramer R.H., Trauner D. // Nat. Chem. 2012. V. 4. № 2. P. 105–111.
206. Szobota S., Gorostiza P., Del Bene F., Wyart C., Fortin D.L., Kolstad K.D., Tulyathan O., Volgraf M., Numano R., Aaron H.L., et al. // Neuron. 2007. V. 54. № 4. P. 535–545.
207. Wyart C., Del Bene F., Warp E., Scott E.K., Trauner D., Baier H., Isacoff E.Y. // Nature. 2009. V. 461. № 7262. P. 407–410.
208. Donthamsetti P.C., Broichhagen J., Vyklicky V., Stanley C., Fu Z., Visel M., Levitz J.L., Javitch J.A., Trauner

D., Isacoff E.Y. // J. Am. Chem. Soc. 2019. V. 141. № 29. P. 11522–11530.
209. Qian W., Kumar N., Roginskaya V., Fouquerel E., Opresko P.L., Shiva S., Watkins S.C., Kolodieznyi D., Bruchez M.P., van Houten B. // Proc. Natl. Acad. Sci. USA. 2019. V. 116. № 37. P. 18435–18444.
210. Berglund K., Clissold K., Li H.E., Wen L., Park S.Y., Gleixner J., Klein M.E., Lu D., Barter J.W., Rossi M.A., et al. // Proc. Natl. Acad. Sci. USA. 2016. V. 113. № 3. P. E358–E367.
211. Park S.Y., Song S.-H., Palmateer B., Pal A., Petersen E.D., Shall G.P., Welchko R.M., Ibata K., Miyawaki A., Augustine G.J., et al. // J. Neurosci. Res. 2020. V. 98. № 3. P. 410–421.
212. Zenchak J.R., Palmateer B., Dorka N., Brown T.M., Wagner L.-M., Medendorp W.E., Petersen E.D., Prakash M., Hochgeschwender U. // J. Neurosci. Res. 2020. V. 98. № 3. P. 458–468.
213. Berglund K., Fernandez A.M., Gutekunst C.-A.N., Hochgeschwender U., Gross R.E. // J. Neurosci. Res. 2020. V. 98. № 3. P. 422–436.
214. Gomez-Ramirez M., More A.I., Friedman N.G., Hochgeschwender U., Moore C.I. // J. Neurosci. Res. 2020. V. 98. № 3. P. 471–480.
215. Method of the Year 2010. // Nat. Methods. 2011. V. 8. № 1. P. 1. doi: 10.1038/nmeth.f.321.
216. News Staff. // Science. 2010. V. 330. № 6011. P. 1612–1613.
217. Ibsen S., Tong A., Schutt C., Esener S., Chalasani S.H. // Nat. Commun. 2015. V. 6. P. 8264.
218. Wheeler M.A., Smith C.J., Ottolini M., Barker B.S., Purohit A.M., Grippo R.M., Gaykema R.P., Spano A.J., Beenhakker M.P., Kucenas S., et al. // Nat. Neurosci. 2016. V. 19. № 5. P. 756–761.

Development of Neutralizing Nanobodies to the Hemagglutinin Stem Domain of Influenza A Viruses

D. V. Voronina*, D. V. Shcheblyakov, I. B. Esmagambetov, A. A. Derkaev, O. Popova, D. N. Shcherbinin
FSBI "National Research Centre for Epidemiology and Microbiology named after Honorary Academician N.F. Gamaleya" of the Ministry of Health of Russia, Moscow, 123098 Russia
*E-mail: daryavoronin2009@yandex.ru
Received June 18, 202l; in final form August 5, 2021
DOI: 10.32607/actanaturae.11495

ABSTRACT **The influenza virus infection claims ~650,000 lives annually. Taking into account the evolving resistance of the pathogen to antiviral drugs and the waning effectiveness of vaccination among certain populations, new approaches to the treatment of influenza are needed. The current study is aimed at obtaining single-domain antibodies (Nanobodies®) to the highly conserved stem domain of influenza A virus hemagglutinin by phage display. Two high-affinity neutralizing clones of Nanobodies® with a particular specificity were selected; they ensured 100% neutralization of the H1N1 and H5N2 influenza viruses *in vivo*. The obtained data demonstrate that it is possible to develop highly effective VHH-based drugs for the treatment of influenza.**
KEYWORDS **Nanobodies®, VHH, phage display, influenza virus.**
ABBREVIATIONS **HA – hemagglutinin; SD – stem domain of HA; HcAb – camelid heavy-chain-only antibody; VHH – variable domain of a HcAb; PCR – polymerase chain reaction; ELISA – enzyme-linked immunosorbent assay; PBMC – peripheral blood mononuclear cell; PAGE – polyacrylamide gel electrophoresis; HRP – horseradish peroxidase; EC_{50} – half maximal effective concentration; SPR – surface plasmon resonance; LD_{50} – median lethal dose; mAb – monoclonal antibody.**

INTRODUCTION

Influenza remains a serious public health risk despite the large number of vaccines and etiopathogenetic approaches to its treatment developed every year. Vaccination remains the most surefire strategy against the influenza infection to date. Antiviral drugs targeting both seasonal and pandemic influenza strains complement existing prevention strategies against the virus. However, given the increasing drug resistance, reduced vaccination efficacy in certain populations, and the short therapeutic window for the available antiviral drugs, there is an urgent need for a new type of drugs against the influenza virus infection.

Production of antibodies against highly conserved regions of viral proteins can be an effective strategy to treat influenza. Hemagglutinin (HA) is one of the major proteins of the influenza virus envelope; it forms trimers on the virion surface. HA monomers consist of two subunits: HA1 and HA2. HA contains the following spatial elements: the globular head domain, which includes the central part of the HA1 subunit, and the distal stem (stalk) domain (SD) formed by the HA2 subunit and the N- and C-terminal regions of the HA1 subunit [1]. The overwhelming majority of antibodies are directed against the highly immunogenic region around the receptor-binding site located in the globular domain, thereby simultaneously providing virus neutralization and exerting immunological pressure, leading to the emergence of escape mutants [2]. These antibodies are almost always either strain- or subtype-specific. SD is, on the other hand, less immunogenic; however, antibodies against it often recognize several HA subtypes due to its highly conserved sequence [2]. Thus, the development of anti-SD antibodies is considered a promising strategy in the pursuit of new antiviral drugs.

Currently available monoclonal antibodies (mAbs) against SD have a wide spectrum of reactivity: from binding HA subtypes within one phylogenetic group [3–10] to recognizing HA of both groups [11–21], and even exerting cross-reactivity between type A and B HA proteins [22]. Most of these antibodies recognize

the conserved conformational epitopes in SD. In addition to conventional antibodies, single-domain anti-SD antibodies (nanobodies, VHH) have been obtained [23, 24]. All reported nanobodies are cross-reactive and either neutralize viruses of the same HA phylogenetic group or, as in the case of multispecific antibodies, acquire the ability to neutralize both type A and B influenza viruses.

VHH is a variable domain of heavy-chain immunoglobulins (HcAbs) found in *Camelidae* [25]. Despite their small size (12–15 kDa), VHHs are not inferior to conventional antibodies in affinity and specificity. Due to their unique stability in a wide temperature range, resistance to the action of various detergents and proteolytic cleavage, single-domain antibodies can be delivered in the body orally and by inhalation [26, 27]. Nanobodies are used to treat oncological, hematological, infectious, and autoimmune diseases; such drugs are either undergoing clinical trials or have been approved for use in European countries and the United States [28, 29].

In this study, we obtained a stabilized SD trimer with preserved conformational epitopes of the neutralizing antibodies and selected virus-neutralizing anti-SD VHHs by phage display. We selected two high-affinity clones exhibiting 100% neutralization of the H1N1 and H5N2 influenza viruses in a model of lethal infection *in vivo*. The possibility of developing highly effective VHH-based drugs for the treatment of influenza has been demonstrated.

EXPERIMENTAL

Biological materials

The following highly purified preparations of recombinant proteins were used in the study: full-length HAs of the influenza A viruses H3N2 (A/Switzerland/9715293/2013) and H1N1 (A/California/04/2009) (Sino Biological, China). Restriction endonucleases, T4 DNA ligase, and alkaline phosphatase (FastAP) were obtained from NEB (USA) and Thermo Fisher Scientific (USA). The trivalent inactivated polymer-subunit influenza vaccine Grippol® plus (NPO Petrovax Pharm LLC, Russia) was used for alpaca immunization.

HA SD synthesis

The nucleotide sequence corresponding to the amino acid sequence of the influenza H1N1 strain SD (A/Brisbane/59/2007) (HA stem) #4900 reported by Impagliazzo A. *et al.* [30] was obtained from Evrogen JSC (Russia) and cloned into the pShuttle-CMV plasmid (Stratagene, USA) to obtain the pShuttle-CMV-HAstem plasmid. Next, CHO-S cells (Thermo Fisher Scientific, USA) were transiently transfected with pShuttle-CMV-HAstem using a CHOgro Expression System (Mirus Bio, USA) according to the manufacturer's instructions. The cells were cultured in Erlenmeyer flasks at 125 rpm, 5% CO_2, 80% humidity, and 37°C; the temperature was lowered to 32°C after 24 h, and the cells were incubated for another 10 days. Starting from day three, Cell boosts 7a (2%) and 7b (0.2%) (HyClone, USA) and 0.5% CHO Bioreactor Feed Supplement (Sigma, USA) were added once a day. After 10 days, the culture medium was clarified by centrifugation at 5,000 *g*. HA SD was purified by affinity chromatography on a AKTA Start Protein Purification System (Cytiva, Sweden) using 1-ml HisTrap HP columns (Cytiva, Sweden) according to the manufacturer's instructions. Additional purification and buffer exchange for 20 mM sodium phosphate and 150 mM sodium chloride were performed on a XK 26/100 column (Cytiva) packed with 200 pg of the Superdex sorbent (Cytiva).

Animal immunization

An alpaca (*Vicugna pacos*) was immunized five times with a 14-day interval between the first and the second injection and a 10-day interval between the subsequent ones. For primary immunization, the animal was injected subcutaneously with a preparation containing 100 μg of Grippol® plus vaccine and Freund's complete adjuvant (FCA; Sigma) mixed in a 1 : 1 ratio until a homogeneous suspension was obtained. The next four injections contained a combination of Grippol® plus and Freund's incomplete adjuvant (FIA; Sigma). Before immunization and seven days after the fifth injection, a small amount of blood (5–10 ml) was taken from the animal as a control to determine the level of specific antibodies. One week after the last injection, 50 ml of venous blood were collected into a sterile container with lithium heparin anticoagulant. The peripheral blood mononuclear cell (PBMC) fraction was obtained using the standard protocol by centrifugation with a Ficoll solution at a density of 1.077 g/ml (PanEco, Russia).

Phage library construction and selection of individual clones

Messenger RNA isolation, polymerase chain reaction (PCR) of the target DNA fragments, and library construction were performed according to the standard protocols [31, 32]. The variable domains of HcAbs from the peripheral B lymphocytes of immunized alpaca were cloned into the phagemid vector pHEN1. Specific two-step PCR primers contained the SfiI and NotI restriction sites at the 5' and 3' end, respectively. Amplified VHH sequences were cloned

into the restriction sites using endonucleases SfiI and NotI and T4 DNA ligase. Electrocompetent *Escherichia coli* TG1 cells were transformed with the recombinant plasmid DNA. As a result, a basic library of nanobodies, which included 3×10^6 individual clones, was obtained.

Phages carrying anti-SD nanobodies were obtained after three rounds of selection (panning). A total of 5 and 1 μg of HA SD of H1N1 (A/Brisbane/59/2007) were used as an antigen in the first and next two rounds of selection. Plasmid DNA was isolated from individual selected clones, and VHHs were sequenced.

Nanobody expression and purification

In order to express candidate nanobodies, recombinant phagemid DNA isolated from the selected individual clones of TG1 cells was transformed into *E. coli* BL21 cells. Bacterial cells were grown in a liquid medium at 30°C overnight, pelleted by centrifugation, and lysed with the BugBuster Protein Extraction Reagent (Novagen, USA) according to the manufacturer's instructions. The nanobodies were purified using TALON Superflow cobalt-charged resin (GE Healthcare Bio-Sciences AB, Sweden); the eluted fraction was dissolved in phosphate-buffered saline (PBS). The expression level was evaluated by denaturing 12% polyacrylamide gel electrophoresis (PAGE).

Protein electrophoresis

The proteins were separated by 12% SDS-PAGE (Bio-Rad, USA) according to Laemmli. For non-reducing non-denaturing electrophoresis, samples were mixed with a loading buffer without 2-mercaptoethanol and loaded into gel wells without preliminary heating. Precision Plus Protein™ (Bio-Rad, USA) was used as the molecular weight standard.

Enzyme-linked immunosorbent assay (ELISA)

To evaluate the serum levels of the antibodies in alpaca, serum samples were added to the plate wells containing either recombinant HA or recombinant SD (1 μg/ml each) immobilized in standard 0.05 M carbonate-bicarbonate buffer (pH 9.6) and then treated with IgG Goat anti-Llama IgG Heavy and Light Chain antibodies conjugated with horseradish peroxidase (HRP) (Bethyl Laboratories, USA). Library enrichment was estimated using HRP-conjugated Anti-M13 antibodies (Sino Biological, China). For the indirect analysis of the nanobodies, Rabbit Polyclonal c-Myc antibodies conjugated to HRP (Abcam, UK) were used. A 3,3',5,5'-tetramethylbenzidine solution (Bio-Rad, USA) was used as the HRP substrate. The optical density was measured at 450 nm using a Varioskan LUX Multimode Microplate Reader (Thermo Fisher Scientific, USA).

Surface plasmon resonance (SPR)

The affinity and kinetics of the nanobody–antigen (HA SD) interaction were determined using a Biacore 3000 four-channel optical biosensor (GE Healthcare Bio-Sciences AB, Sweden). The recombinant SD protein (20 μg/ml solution in 10 mM acetate buffer; pH 4.5) was covalently immobilized on the surface of a CM5 sensor chip using an Amine Coupling Kit (GE Healthcare Bio-Sciences AB, Sweden). The level of immobilized ligand in the test channel of the optical biosensor was 1,800 RU.

Kinetic parameters were analyzed by injecting fivefold dilutions of nanobody samples in the concentration range of 0–267 nM through the control (without the immobilized ligand) and test channels for 3 min at a constant flow rate of 15 μL/min. HBS-EP (0.01 M HEPES, pH 7.4; 0.15 M NaCl; 3 mM EDTA; and 0.005% Surfactant P20) was used as the working buffer. The dissociation time after sample loading was 10 min. After each measurement, the chip surface was regenerated by injecting 100 mM Tris-HCl buffer (pH 1.3) for 30 s at a flow rate of 30 μL/min. All measurements were carried out at 25°C in at least two replicates.

The equilibrium dissociation and association constants (K_d and K_a) and the rate constants of formation (k_{on}) and decay (k_{off}) of the molecular complexes were calculated using the BIAEvaluation software (GE Healthcare Bio-Sciences AB, Sweden).

Evaluation of VHH neutralizing activity *in vivo*

The studies were performed on 6-week-old female BALB/c mice weighing 18–20 g. Mouse-adapted influenza viruses H1N1 (A/Duck/mallard/Moscow/4970/2018) and H5N2 (A/Mallard duck/Pennsylvania/10218/84) kindly provided by the Laboratory of Molecular Biotechnology of the N.F. Gamaleya National Research Center for Epidemiology and Microbiology of the Ministry of Health of the Russian Federation were used to infect the animals.

The animals were divided into groups (test and control) of five animals each and infected intranasally with a mixture of 200 μg of antibody and 15 LD_{50} of virus pre-incubated at 37°C for 1 h either in a volume of 50 μL/mouse (test groups) or with the virus at a dose of 15 LD_{50} in PBS (control groups). The mice were observed for 14 days after infection; they were examined and weighed on a daily basis. Agonizing animals and animals that had lost more than 25% of their initial weight were euthanized by cervical dislocation. The neutralizing effect of the nanobodies was

assessed by the survival rate and changes in the body weight of the mice.

Statistical data analysis

The statistical data was analyzed using the Microsoft Excel and GraphPad Prism 7 software.

RESULTS

Stabilized HA SD trimer

We used the amino acid sequence of the stabilized SD trimer from the H1N1 strain (A/Brisbane/59/2007) reported by Impagliazzo A. et al. [30]. In order to increase the level of HA SD expression, the HA signal peptide sequence was replaced with the signal peptide sequence of SEAP alkaline phosphatase. HA SD was produced in CHO-S cells, which provide a high level of recombinant protein expression [33]. An SD preparation of optimal purity was obtained after two purification stages: affinity chromatography and gel filtration. SD trimerization was confirmed by reducing denaturing (to visualize the monomeric structure; molecular weight, 37 kDa) and non-reducing non-denaturing (to visualize the trimeric structure; molecular weight, ~110 kDa) electrophoresis (*Fig. 1*).

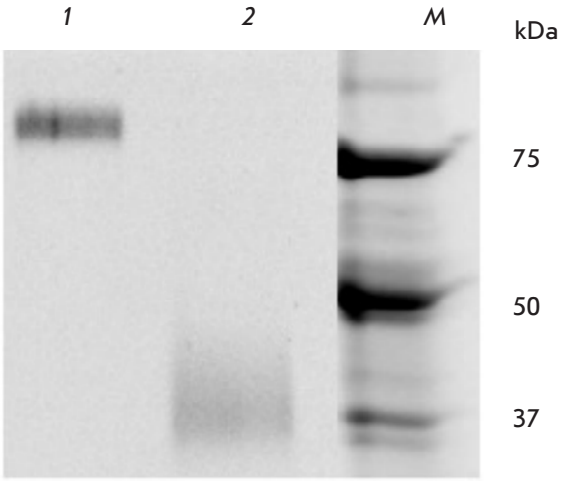

Fig. 1. 12% PAGE analysis of SD. *1* – Non-reducing non-denaturing conditions. *2* – Reducing denaturing conditions. *M* – molecular weight ladder

Production of anti-SD nanobodies

A panel of anti-SD nanobodies was obtained by immunizing alpaca (*V. pacos)* according to the scheme presented in *Fig. 2A*. On day seven after the last injection, 50 ml of blood were collected from the animal. The PBMC fraction was separated for total RNA isolation and immune library preparation.

The serum was also collected to assess the induction of the humoral immune response. The serum levels of antibodies in alpaca were determined for both HA SD and recombinant HAs (*Fig. 2B*). The titer of anti-SD antibodies was 1 : 12,500. A high titer of anti-H1 (A/California/04/2009) and anti-H3 (A/Switzerland/9715293/2013) antibodies was revealed: 1 : 204,800 and 1 : 409,600, respectively. These results indicate a strong humoral response after five cycles of alpaca immunization with the influenza vaccine, both against full-length HAs and SD.

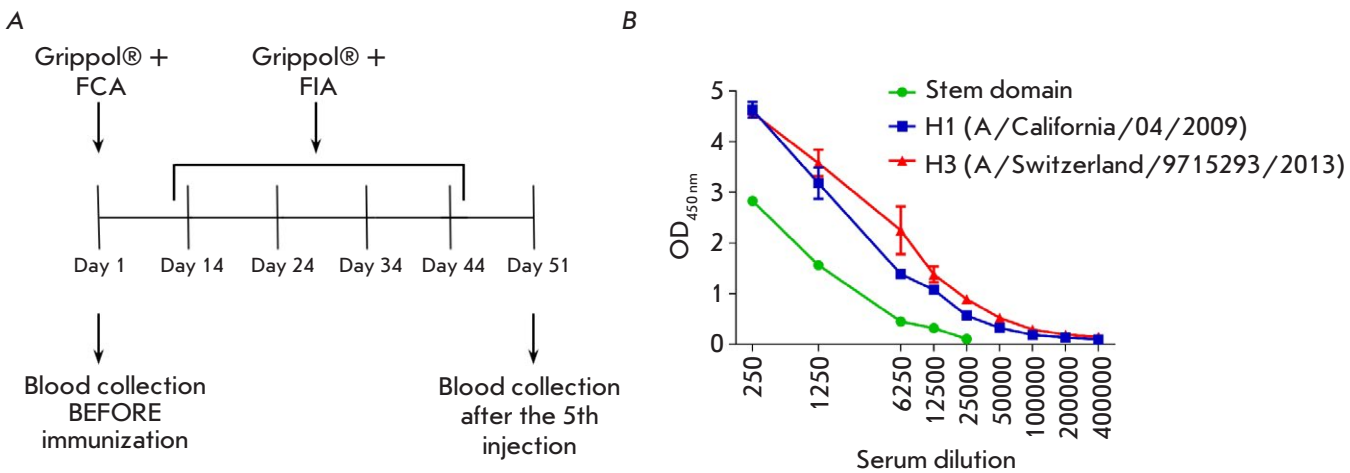

Fig. 2. (*A*) – Schematic representation of alpaca immunization with the Grippol® plus vaccine in combination with either Freund's complete adjuvant (FCA) or Freund's incomplete adjuvant (FIA). (*B*) – serum levels of antibodies to SD and full-length HAs in alpaca after five immunizations

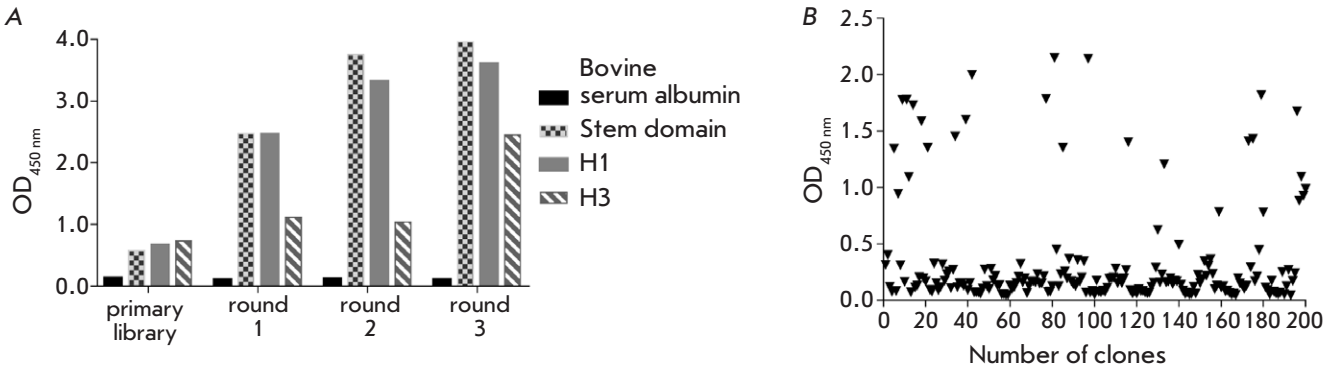

Fig. 3. (*A*) – Polyclonal phage ELISA: phage binding after different rounds of selection using SD and full-length HAs. (*B*) – Screening of randomly selected monoclones by phage ELISA

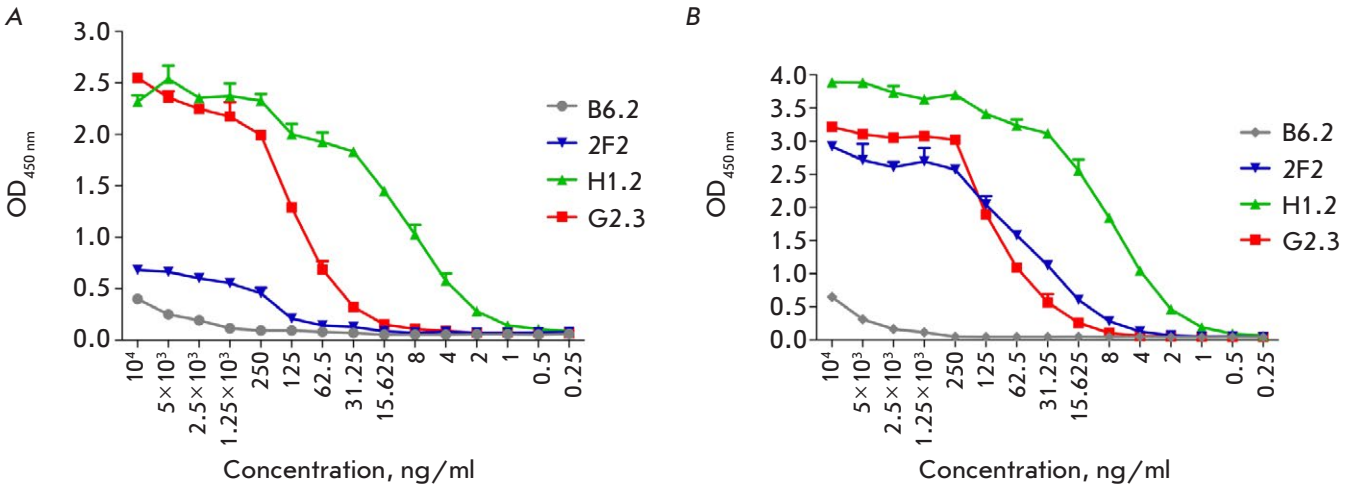

Fig. 4. Titration of selected VHH clones by ELISA using SD (*A*) and full-length HA of the H1N1 influenza virus (A/California/04/2009) (*B*)

Kinetic parameters of the interaction between VHH and SD determined by SPR

Clone	k_{on} (1/Ms)	k_{off} (1/s)	R_{max} (RU)	K_a (1/M)	K_d (M)	Chi^2
2F2	3.95×10^5	6.17×10^{-3}	51.7	6.38×10^7	1.57×10^{-8}	1.53
H1.2	9.87×10^5	3.6×10^{-4}	139	2.74×10^9	3.65×10^{-10}	1.59
G2.3	3.68×10^5	2.04×10^{-4}	154	1.8×10^9	5.54×10^{-10}	1.39

Construction of a nanobody library and subsequent selection by phage display were performed as described previously [34]. The library size was 3×10^6 individual clones. All 30 colonies, randomly selected and analyzed by PCR for the presence of the VHH gene fragment, contained an insert. The phage library was subjected to three rounds of selection, and the results of each round were monitored by polyclonal phage ELISA (*Fig. 3A*). At the end of panning, 66 individual clones with an ELISA OD_{450} value above 0.25 were sequenced by Sanger (*Fig. 3B*). Based on the results of the CDR3 region analysis, these clones were combined into eight groups. Of these, four clones were selected for further study (B6.2, 2F2, H1.2, and G2.3) based on the specific activity in monoclonal phage ELISA and the protein expression level.

In vitro characterization of nanobodies

The specific activity of nanobodies was confirmed by indirect ELISA, and the kinetics of interaction with SD and affinity were assessed by SPR. Full-length HAs of influenza viruses H1N1 (A/California/04/2009)

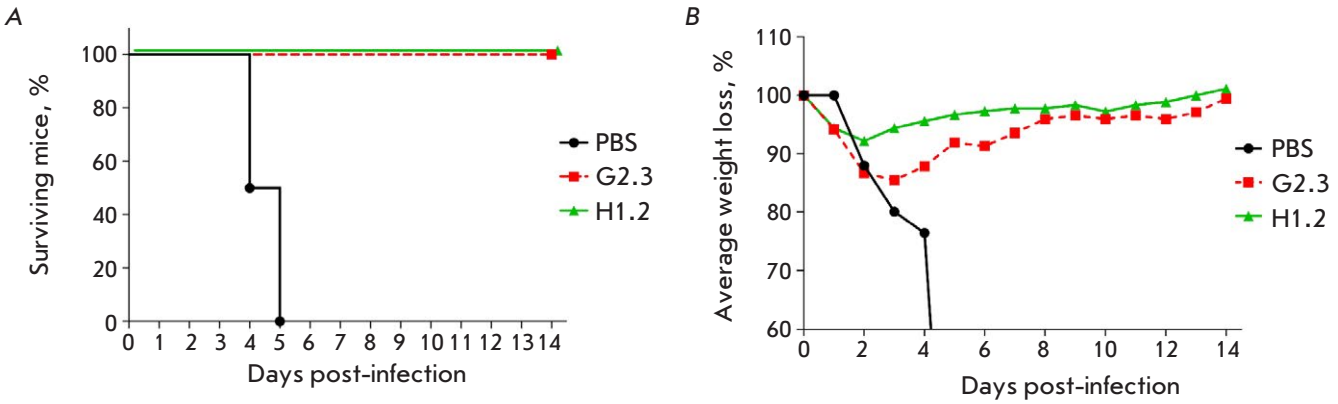

Fig. 5. Changes in the survival rate (*A*) and body weight (*B*) of mice after intranasal infection with 15 LD_{50} of H1N1 (A/Duck: mallard/Moscow/4970/2018) pre-incubated with VHH. The differences in the survival rate between the experimental and control groups are statistically significant ($p < 0.0005$)

and H3N2 (A/Switzerland/9715293/2013), as well as HA SD (*Fig. 4*), were used as the antigen in ELISA; HRP-conjugated polyclonal c-Myc antibodies were used for VHH detection. Calibration curves were constructed, and EC_{50} values were determined for the clones 2F2, H1.2, and G2.3, based on the OD dependence on the antibody concentration. The EC_{50} values were 0.7, 7.4, and 13.8 nM for the interaction of SD with the clones H1.2, G2.3, and 2F2, respectively, and 0.6, 5.9, and 3.0 nM for the interaction of H1 HA with the same clones, respectively. There was no significant signal for the interaction between the antibodies and HA H3.

The affinity between SD and the clones 2F2, H1.2, and G2.3 was studied by SPR using the Biacore 3000. For this, the recombinant protein was covalently immobilized on the surface of a CM5 sensor chip. Association and dissociation constants were determined by analyzing sensograms in the BIAEvaluation software. The results are shown in the *Table*.

Neutralization in *in vivo* experiments

The neutralizing activity of nanobodies was studied using the mouse-adapted influenza virus H1N1 (A/Duck/mallard/Moscow/4970/2018). For that purpose, the mice were infected intranasally with high lethal doses (15 LD_{50}) of the virulent H1N1 strain pre-incubated with either VHH H1.2 or G2.3. The animal survival rate in the test groups was 100% at 100% mouse death in the control group (*Fig. 5A*), which indicates effective neutralization of the H1N1 virus by both nanobodies. The neutralizing effect of the antibodies *in vivo* is further confirmed by a slight decrease in mouse body weight and its rapid recovery in the test groups compared to the control (*Fig. 5B*).

An *in vivo* study of H5N2 (A/Mallard duck/Pennsylvania/10218/84) neutralization was carried out similarly to H1N1 neutralization. The obtained data indicate 100% neutralization of the H5N2 virus by nanobodies (*Fig. 6*).

DISCUSSION

The advantages of nanobodies over conventional mAbs make them an attractive platform for the development of therapeutic agents, including antiviral agents. Because of the unique structure of its variable domain, VHHs can interact with difficult-to-reach epitopes on the viral surface [35, 36]. The smaller VHH footprint compared to conventional mAbs, which bind to larger and flatter epitopes, may constitute a greater genetic barrier for the emergence of escape mutations. In addition, the high stability and solubility of nanobodies are extremely important when creating an effective drug that can be delivered directly to the site of the infection: the lungs.

Most mAbs capable of neutralizing different subtypes of influenza viruses recognize conserved conformational epitopes in HA SD; however, they are difficult to access in a natural infection and immunization with full-length HA due to predominant exposure of variable epitopes of the HA globular domain. For this reason, what is necessary is SD with an optimal stabilized conformation, with preserved mAb-neutralizing epitopes. Impagliazzo A. *et al.* [30] obtained several variants of the stabilized HA SD trimer, of which #4900 can induce antibody production and provide protection against various influenza A subtypes in mice. Using the SD #4900 sequence, we obtained a preparation whose trimeric structure was confirmed by electrophoresis and that

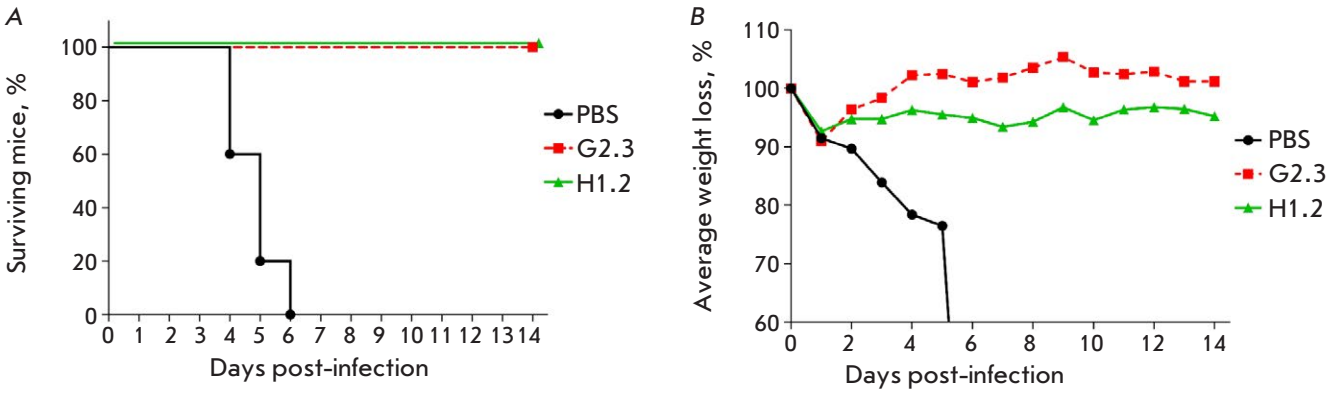

Fig. 6. Changes in the survival rate (*A*) and body weight (*B*) of mice after intranasal infection with 15 LD_{50} of H5N2 (A/Mallard duck/Pennsylvania/10218/84) pre-incubated with VHH. The differences in the survival rate between the experimental and control groups are statistically significant ($p < 0.0002$)

was further used to select high-affinity antibodies capable of protecting mice from various subtypes of influenza A.

We have obtained nanobodies against HA SD that potentially recognize conserved conformational epitopes and exhibit neutralizing activity against different subtypes of the influenza A virus. Four individual clones – B6.2, 2F2, H1.2, and G2.3 – were obtained after selection; they were characterized by the level of specific activity against SD and full-length HA of the subtypes H1 and H3 in indirect ELISA, affinity in SPR analysis, and in *in vivo* neutralization tests.

An ELISA analysis showed that the clones H1.2 and G2.3 establish the strongest interaction with SD and full-length H1 HA. A similar signal was observed for the interaction between the clone 2F2 and H1 HA; however, in the case of SD, it was lower for 2F2 compared to H1.2 and G2.3. Clone B6.2, even at high concentrations, weakly reacted with the antigens (*Fig. 4*). At this stage, clone B6.2, which exhibited the lowest titer in ELISA and, presumably, had the lowest affinity, was excluded from further study. According to the ELISA data, the clones we selected do not bind to H3 HA; however, many available broad-spectrum mAbs neutralize HA only within one phylogenetic group. In addition to evolutionary similarity, these groups share common conserved epitopes of cross-neutralizing antibodies in the SD hydrophobic pocket [4]. Monoclonal Abs binding this antigenic site preferentially neutralize HA of the same group and either do not neutralize the subtypes of the other one or neutralize them with less efficiency.

The K_d values correlate with those obtained in indirect ELISA: the lowest dissociation constants (nanomolar range) are characteristic of the antibodies H1.2 and G2.3. Despite a EC_{50} similar to those of the clones in ELISA for H1N1, 2F2 exhibited significantly lower specificity and affinity for SD. The *in vitro* experiments allowed us to select the clones H1.2 and G2.3 with the highest affinity (K_d 3.65×10^{-10} and 5.54×10^{-10} M, respectively) for *in vivo* characterization of antibodies.

Validation of the neutralizing activity of the nanobodies H1.2 and G2.3 against a lethal dose of a mouse-adapted H1N1 virus (A/Duck: mallard/Moscow/4970/2018) ensured 100% protection to mouse.

Based on the phylogenetic proximity of the viruses of the HA subtypes H1 and H5 and the conservation of their SD amino acid sequence, we assumed that the selected antibodies can bind and neutralize influenza virus strains with the HA subtype H5 *in vivo* [37]. The adapted H5N2 influenza virus (A/Mallard duck/Pennsylvania/10218/84) was selected for animal experiments. The HA SD sequences of the influenza viruses used in our animal experiments were first analyzed in the Geneious Prime software. There was an 83% homology between the sequences. Both nanobodies H1.2 and G2.3 were shown to display 100% neutralizing activity against an influenza virus with the HA subtype H5. This may be due to the high degree of homology between the HA SDs of the selected strains and, as a consequence, preservation of the VHH binding sites in G2.3 and H1.2.

The new single-domain antibodies we obtained have an extremely high affinity, they bind and effectively neutralize viruses with the HA subtypes H1 and H5; however, it is possible to further increase the binding and neutralizing ability of VHH by

creating bivalent and bispecific constructs with the Fc fragment. Thus, affinity is enhanced thanks to the increased avidity, and effector functions such as antibody-dependent cellular cytotoxicity, antibody-dependent phagocytosis, and antibody-mediated complement-dependent cytotoxicity are gained; all of them are critical in terminating an influenza infection.

Antibodies capable of neutralizing HA of the first phylogenetic group are highly important, since this group also includes viruses with pandemic potential. The VHHs obtained by us ensured neutralizing activity against viruses carrying the HA subtypes H1 and H5. The presence/absence of neutralizing activity against other influenza strains will be the subject of further study.

CONCLUSIONS

We have obtained a stabilized SD trimer of H1 HA (A/Brisbane/59/2007) containing conformational mAb epitopes with a broad spectrum of neutralizing activity.

The new nanobodies H1.2 and G2.3 identified by us specifically bind SD with dissociation constants exceeding those of many known monomeric VHHs and also effectively neutralize the influenza viruses H1N1 and H5N2 belonging to the first phylogenetic group of HA. We obtained constructs of these antibodies with the Fc fragment which will be used for *in vivo* study of protection against various influenza A virus strains. ●

This study was supported by the State Assignment of the Ministry of Health of the Russian Federation No. 121031800132-4.

REFERENCES

1. Gamblin S.J., Skehel J.J. // J. Biol. Chem. 2010. V. 285. № 37. P. 28403–28409.
2. Krammer F., Palese P. // Nat. Rev. Drug Discov. 2015. V. 14. № 3. P. 167–182.
3. Ekiert D.C., Friesen R.H.E., Bhabha G., Kwaks T., Jongeneelen M., Yu W., Ophorst C., Cox F., Korse H.J., Brandenburg B., et al. // Science. 2011. V. 333. № 6044. P. 843–850.
4. Throsby M., van den Brink E., Jongeneelen M., Poon L.L.M., Alard P., Cornelissen L., Bakker A., Cox F., van Deventer E., Guan Y., Cinatl J., et al. // PLoS One. 2008. V. 3. № 12. P. e3942.
5. Sui J., Hwang W.C., Perez S., Wei G., Aird D., Chen L.M., Santelli E., Stec B., Cadwell G., Ali M., et al. // Nat. Struct. Mol. Biol. 2009. V. 16. № 3. P. 265–273.
6. Wyrzucki A., Dreyfus C., Kohler I., Steck M., Wilson I.A., Hangartner L. // J. Virol. 2014. V. 88. № 12. P. 7083–7092.
7. Corti D., Suguitan A.L., Pinna D., Silacci C., Fernandez-Rodriguez B.M., Vanzetta F., Santos C., Luke C.J., Torres-Velez F.J., Temperton N.J., et al. // J. Clin. Invest. 2010. V. 120. № 5. P. 1663–1673.
8. de Marco D., Clementi N., Mancini N., Solforosi L., Moreno G.J., Sun X., Tumpey T.M., Gubareva L.V., Mishin V., Clementi M., et al. // PLoS One. 2012. V. 7. № 4. P. 1–9.
9. Kashyap A.K., Steel J., Rubrum A., Estelles A., Briante R., Ilyushina N.A., Xu L., Swale R.E., Faynboym A.M., Foreman P.K., et al. // PLoS Pathog. 2010. V. 6. № 7. P. 1–7.
10. Friesen R.H.E., Lee P.S., Stoop E.J.M., Hoffman R.M.B., Ekiert D.C., Bhabha G., Yu W., Juraszek J., Koudstaal W., Jongeneelen M., et al. // Proc. Natl. Acad. Sci. USA. 2014. V. 111. № 1. P. 445–450.
11. Corti D., Voss J., Gamblin S.J., Codoni G., Macagno A., Jarrossay D., Vachieri S.G., Pinna D., Minola A., Vanzetta F., et al. // Science. 2011. V. 333. № 6044. P. 850–856.
12. Nakamura G., Chai N., Park S., Chiang N., Lin Z., Chiu H.., Fong R, Yan D., Kim J., Zhang J., et al. // Cell Host Microbe. 2013. V. 14. № 1. P. 93–103.
13. Wu Y., Cho M., Shore D., Song M., Choi J., Jiang T., Deng Y.Q., Bourgeois M., Almli L., Yang H., et al. // Nat. Commun. 2015. V. 6. P. 7708.
14. Tharakaraman K., Subramanian V., Viswanathan K., Sloan S., Yen H.L., Barnard D.L., Leung Y.H., Szretter K.J., Koch T.J., Delaney J.C., et al. // Proc. Natl. Acad. Sci. USA. 2015. V. 112. № 35. P. 10890–10895.
15. Wyrzucki A., Bianchi M., Kohler I., Steck M., Hangartner L. // J. Virol. 2015. V. 89. № 6. P. 3136–3144.
16. Hu W., Chen A., Miao Y., Xia S., Ling Z., Xu K., Wang T., Xu Y., Cui J., Wu H., et al. // Virology. 2013. V. 435. № 2. P. 320–328.
17. Li G.M., Chiu C., Wrammert J., McCausland M., Andrews S.F., Zheng N.Y., Lee J.H., Huang M., Qu X., Edupuganti S., et al. // Proc. Natl. Acad. Sci. USA. 2012. V. 109. № 23. P. 9047–9052.
18. Henry Dunand C.J., Leon P.E., Kaur K., Tan G.S., Zheng N.Y., Andrews S., Huang M., Qu X., Huang Y., Salgado-Ferrer M., et al. // J. Clin. Invest. 2015. V. 125. № 3. P. 1255–1268.
19. Clementi N., de Marco D., Mancini N., Solforosi L., Moreno G.J., Gubareva L.V., et al. // PLoS One. 2011. V. 6. № 12. P. e28001.
20. Kallewaard N.L., Corti D., Collins P.J., Neu U., McAuliffe J.M., Benjamin E., Wachter-Rosati L., Palmer-Hill F.J., Yuan A.Q., Walker P.A., et al. // Cell. 2016. V. 166. № 3. P. 596–608.
21. Joyce M.G., Wheatley A.K., Thomas P.V., Chuang G.Y., Soto C., Bailer R.T., Druz A., Georgiev I.S., Gillespie R.A., Kanekiyo M., et al. // Cell. 2016. V. 166. № 3. P. 609–623.
22. Dreyfus C., Laursen N.S., Kwaks T., Zuijdgeest D., Khayat R., Ekiert D.C., Lee J.H., Metlagel Z., Bujny M.V., Jongeneelen M., et al. // Science. 2012. V. 337. № 6100. P. 1343–1348.
23. Laursen N.S., Friesen R.H.E., Zhu X., Jongeneelen M., Blokland S., Vermond J., van Eijgen A., Tang C., van Diepen H., Obmolova G., et al. // Science. 2018. V. 362. № 6414. P. 598–602.
24. Gaiotto T., Hufton S.E. // PLoS One. 2016. V. 11. № 10. P. 1–27.
25. Hamers-Casterman C., Atarhouch T., Muyldermans S., Robinson G., Hamers C., Songa E.B., Bendahman N., Hamers R. // Nature. 1993. V. 363. № 6428. P. 446–448.
26. Harmsen M.M., van Solt C.B., van Zijderveld-Van Bemmel A.M., Niewold T.A., van Zijderveld F.G. // Appl. Microbiol. Biotechnol. 2006. V. 72. № 3. P. 544–551.
27. van Heeke G., Allosery K., De Brabandere V., De Smedt

T., Detalle L., de Fougerolles A. // Pharmacol. Ther. 2017. V. 169. P. 47–56.
28. Arbabi-Ghahroudi M. // Front. Immunol. 2017. V. 8. P. 1589.
29. Jovčevska I., Muyldermans S. // BioDrugs. 2020. V. 34. № 1. P. 11–26.
30. Impagliazzo A., Milder F., Kuipers H., Wagner M.V., Zhu X., Hoffman R.M., van Meersbergen R., Huizingh J., Wanningen P., Verspuij J., et al. // Science. 2015. V. 349. № 6254. P. 1301–1306.
31. Arbabi Ghahroudi M., Desmyter A., Wyns L., Hamers R., Muyldermans S. // FEBS Lett. 1997. V. 414. № 3. P. 521–526.
32. Ledsgaard L., Kilstrup M., Karatt-Vellatt A., McCafferty J., Laustsen AH. // Toxins (Basel). 2018. V. 10. № 6. P. 236.
33. Fischer S., Handrick R., Otte K. // Biotechnol. Adv. 2015. V. 33. № 8. P. 1878–1896.
34. Godakova S.A., Noskov A.N., Vinogradova I.D., Ugriumova G.A., Solovyev A.I., Esmagambetov I.B., Tukhvatulin A.I., Logunov D.Y., Naroditsky B.S., Shcheblyakov D.V., et al. // Toxins (Basel). 2019. V. 11. № 8. P. 464.
35. De Genst E., Silence K., Decanniere K., Conrath K., Loris R., Kinne J., Muyldermans S., Wyns L. // Proc. Natl. Acad. Sci. USA. 2006. V. 103. № 12. P. 4586–4591.
36. Stijlemans B., Conrath K., Cortez-Retamozo V., van Xong H., Wyns L., Senter P., Revets H., De Baetselier P., Muyldermans S., Magez S. // J. Biol. Chem. 2004. V. 279. № 2. P. 1256–1261.
37. Nobusawa E., Aoyama T., Kato H., Suzuki Y., Tateno Y., Nakajima K. // Virology. 1991. V. 182. № 2. P. 475–485.

The rs1800470 Polymorphism of the *TGFB1* Gene Is Associated with Myocardial Fibrosis in Heart Transplant Recipients

O. E. Gichkun[1,2*], O. P. Shevchenko[1,2], R. M. Kurabekova[1], N. P. Mozheiko[1], A. O. Shevchenko[1,2]
[1]Shumakov National Medical Research Center of Transplantology and Artificial Organs, Moscow, 123182 Russia
[2]I.M. Sechenov First Moscow State Medical University (Sechenov University), Moscow, 119435 Russia
*E-mail: gichkunoe@yandex.ru
Received June 16, 2021; in final form, September 27, 2021
DOI: 10.32607/actanaturae.11469

ABSTRACT **The transforming growth factor β1 (TGFβ1), whose level may depend on the polymorphism of the *TGFB1* gene, is involved in the formation of myocardial fibrosis. Myocardial fibrosis in a cardiac allograft may lead to a heart's structural and functional remodeling and subsequent dysfunction. The frequency of occurrence of alleles and genotypes of the *TGFB1* gene polymorphic regions rs1800469, rs1800470, and rs1800471 in heart transplant recipients and their association with graft myocardial fibrosis were analyzed. Carriers of the CC genotype (p = 0.023, OR = 0.12, 95% CI: 0.017–1.0), and more often the G allele of rs1800471 (p = 0.023, OR = 7.76, 95% CI: 1.0–60.20), were found among heart transplant recipients less frequently than among healthy individuals. In patients with ischemic heart disease (IHD), the GG genotype was less common (p = 0.035, OR = 2.68, 95% CI: 1.061–6.793), while the A allele of rs1800469 was found more frequently (p = 0.035, OR = 0.37 95% CI: 0.148–0.942) than in patients with dilated cardiomyopathy (DCM). In heart transplant recipients with the AA genotype of rs1800470, myocardial fibrosis, verified by endomyocardial biopsy, was detected more often than in carriers of the G allele (OR = 10.4, 95% CI: 1.152–94.538, p = 0.013). The revealed differences suggest a relationship between *TGFB1* gene polymorphism and graft myocardial fibrosis. Studies on a larger group of patients would make it possible to characterize the influence of genetic factors on the formation of myocardial fibrosis in heart transplant recipients.**
KEYWORDS **transforming growth factor β1 gene, single nucleotide polymorphisms, myocardial fibrosis, cardiac allograft.**
ABBREVIATIONS **TGFβ1 – transforming growth factor β1; TGFB1 – the gene encoding TGF β1; DCM – dilated cardiomyopathy; IHD – ischemic heart disease; SNP – single nucleotide polymorphism; OR – odds ratio; PCR – polymerase chain reaction.**

INTRODUCTION

The number of patients with heart failure is constantly on the rise as the mean life expectancy increases, while mortality due to acute medical conditions in young and middle-aged individuals declines. Heart transplantation is an efficient method for treating end-stage heart failure that improves the prognosis and quality of life of patients. The recently observed increase in the longevity of heart transplant recipients has been achieved mainly thanks to a reduction in the mortality rate during the early posttransplant period. Myocardial fibrosis, whose development is accompanied by structural and functional remodeling of the cardiac graft, is among the factors with an unfavorable impact on the long-term outcome of heart transplantation [1].

Graft myocardial fibrosis is a multifactorial process, with a number of cellular and molecular factors predisposing one to it [2]. Recent studies have shown that transforming growth factor β1 (TGFβ1), a profibrotic mediator involved in the production of the extracellular matrix, is among the pathogenetic factors of fibrosis [3].

The finding that the TGFβ1 level in the peripheral blood is genetically determined is now a fact. Some genetic polymorphisms of the *TGFB1* gene were

shown to be associated with the severity of coronary artery atherosclerosis and genetic predisposition to myocardial infarction; this association varies for different ethnic groups [4, 5].

The TGFβ1 protein is encoded by the *TGFB1* gene residing on chromosome 19. Eight single nucleotide polymorphisms and a deletion/insertion polymorphism affecting the expression and activity of TGFβ1 have been identified thus far [6]. Researchers put particular focus on three *TGFB1* gene polymorphisms associated with cardiovascular diseases: rs1800469 is localized in the promoter region, and rs1800470 (leucine-to-proline substitution in codon 10) and rs1800471 (arginine-to-proline substitution in codon 25) are localized in the coding region. Data on the effect of *TGFB1* gene polymorphisms on the long-term outcomes of heart transplantation and genetic predisposition to developing post-transplant complications – acute and chronic (cardiac allograft vasculopathy) transplant rejection – are scarce and far from definitive [7–9].

This study aims at uncovering any association between the rs1800469, rs1800470, and rs1800471 polymorphisms of the *TGFB1* gene and myocardial fibrosis in cardiac allograft in heart transplant recipients.

EXPERIMENTAL

A total of 110 randomly selected heart transplant recipients who had undergone cardiac allograft transplantation at the Shumakov National Medical Research Center of Transplantology and Artificial Organs in 2017–2019 were enrolled in the study. All study participants were ethnic Russians; of those, 99 (84%) patients were males: the recipients' mean age was 44 ± 14 (range: 16–70) years. The reason for the development of the end-stage heart failure responsible for the indications to transplantation was dilated cardiomyopathy (DCM) in 57 patients and ischemic heart disease (IHD) in 53 patients. The duration of the follow-up period after heart transplantation extended up to 4 (2.3 ± 1.3) years.

The patients were examined and treated in compliance with the clinical guidelines of the Russian Transplant Society. Endomyocardial biopsy for heart transplant recipients was performed according to the protocol during scheduled clinical laboratory examination or if there were respective indications. Endomyocardial biopsy specimens were assessed based on the histological and immunohistochemical data. Thin sections of endomyocardial tissue were subjected to Masson's trichrome staining to confirm fibrosis in a cardiac allograft [10].

Genomic DNA was isolated from peripheral blood in accordance with the protocol, using a commercial QIAamp DNA Blood Mini Kit on a QIAcube™ automated analyzer (Qiagen, Germany). The rs1800469, rs1800470, and rs1800471 polymorphisms of the *TGFB1* gene were analyzed by real-time polymerase chain reaction using TaqMan probes (Applied Biosystems, USA) on a CFX96™ amplification system (Bio-Rad, USA). The probes fluorescently labeled using VIC (allele 1)/FAM (allele 2) channels were detected at each amplification cycle. The resulting data were analyzed using the BioRad CFX manager 3.0 software.

Table 1. Data analysis for compliance with the Hardy–Weinberg equilibrium

Groups \ SNP	rs1800469	rs1800470	rs1800471
Healthy individuals	$\chi^2 = 1.0$ $p = 0.31$	$\chi^2 = 0.02$ $p = 0.81$	$\chi^2 = 0.006$ $p = 0.93$
Heart transplant recipients	$\chi^2 = 4.32$ $p = 0.03$*	$\chi^2 = 9.3$ $p = 0.002$*	$\chi^2 = 5.73$ $p = 0.01$*

*$p < 0.05$ – does not comply with the Hardy–Weinberg equilibrium. SNP – single nucleotide polymorphism.

The statistical analysis was carried out using the suite of applied software for research and engineering computations IBM SPSS STATISTICS 20 (IBM SPSS Inc., USA). In order to prove an independent distribution of alleles in the analyzed polymorphisms, their compliance to the Hardy–Weinberg Equilibrium was tested [11]. The frequencies of the genotypes or individual alleles in different groups were compared using the Pearson's χ^2 test. The potential effect of the genotype on a trait was assessed by determining the odds ratio and 95% confidence intervals. The critical value for the significance level was assumed to be 0.05.

RESULTS

Genomic typing of the rs1800469, rs1800470, and rs1800471 polymorphisms of the *TGFB1* gene in heart transplant recipients was conducted. No deviations in the distribution of the alleles and genotypes from the Hardy–Weinberg Equilibrium were revealed in the sex- and age-matched control group, consisting of healthy individuals (43). Compliance with the Hardy–Weinberg Equilibrium was detected in none of the heart transplant recipients for all three polymorphisms (*Table 1*).

The deviation from the Hardy–Weinberg Equilibrium in the heart transplant recipient group can be associated with a cardiovascular pathology, although the effect of a small sample size should not be ruled out; so, a larger sample is needed for testing.

Table 2. Distribution of genotypes and alleles of the polymorphic regions of the *TGFB1* gene in heart transplant recipients and healthy individuals

Genotype/allele	Heart transplant recipients, *n* (%)	Healthy individuals, n (%)	*p*
rs1800469			
AA	22 (20)	6 (14)	0.38
AG	42 (38)	16 (37)	0.91
GG	46 (42)	21 (49)	0.43
A	64 (58)	22 (51)	0.43
G	88 (80)	37 (86)	0.38
rs1800470			
AA	91 (83)	40 (93)	0.12
AG	14 (13)	3 (7)	0.30
GG	4 (4)	-	0.20
A	105 (96)	43 (100)	0.20
G	18 (17)	3 (7)	0.12
rs1800471			
GG	3 (3)	-	0.27
GC	14 (13)	1 (2)	0.051
CC	92 (84)	42 (98)	0.023*
G	17 (16)	1 (2)	0.023*
C	106 (97)	43 (100)	0.27

*$p < 0.05$.

Table 2 shows the distribution of alleles and genotypes of the *TGFB1* gene in heart transplant recipients and in the control group.

A comparative analysis of the distribution of the genotypes and alleles of the rs1800469 and rs1800470 polymorphisms of the *TGFB1* gene detected no differences between healthy individuals and heart transplant recipients. However, some differences in the distribution of the alleles and genotypes of the rs1800471 polymorphism of the *TGFB1* gene were found (*Fig. 1*).

Carriers of the CC genotype of the rs1800471 polymorphism of the *TGFB1* gene were found among heart transplant recipients less frequently than among healthy individuals ($p = 0.023$; OR = 0.12; 95% CI, 0.017–1.0), while carriers of the G allele were found more often (within the GG and GC genotypes) ($p = 0.023$; OR = 7.76; 95% CI, 1.0–60.2).

An analysis of the association between the frequencies of distribution of the studied polymorphisms and the demographic and clinical characteristics of the heart transplant recipients revealed statistically significant associations with sex, diagnosis, and myocardial fibrosis in a cardiac allograft.

The distribution of the alleles and genotypes of the rs1800470 polymorphism of the *TGFB1* gene differed significantly among male and female heart transplant recipients (*Fig. 2*).

Male heart transplant recipients were less likely to carry the GG genotype than females ($p \leqslant 0.05$).

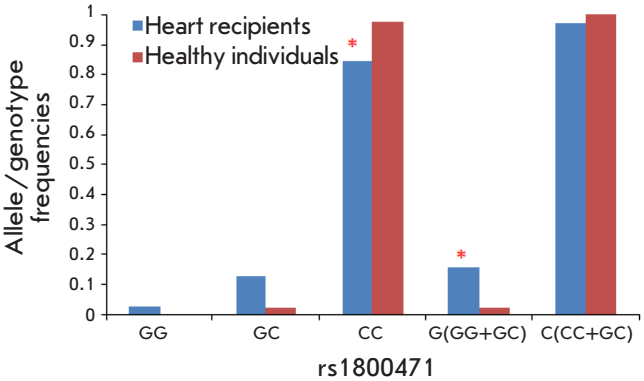

Fig. 1. Frequency distribution of the alleles and genotypes of the rs1800471 polymorphism of the *TGFB1* gene in heart transplant recipients and healthy individuals . *$p < 0.05$ compared to healthy individuals

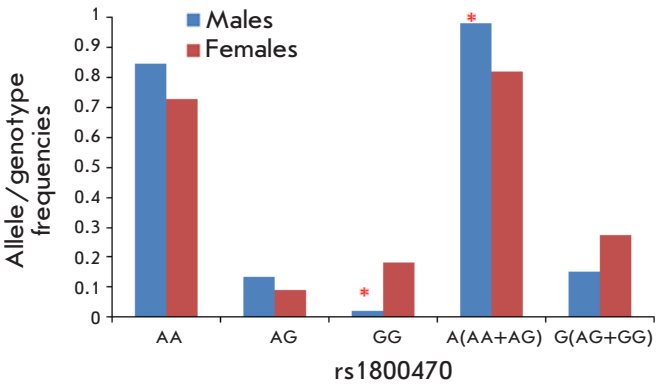

Fig. 2. Frequency distribution of the alleles and genotypes of the rs1800470 polymorphism of the *TGFB1* gene in males and females, *$p < 0.05$ compared to females

A comparison of the frequencies of individual alleles showed that the frequency of the A rs1800470 allele of the *TGFB1* gene is higher in males ($p = 0.007$; OR = 10.6; 95% CI, 1.34–85.01). No differences in the distribution of the genotypes and alleles of the rs1800469 and rs1800471 polymorphisms of the *TGFB1* gene among males and females were revealed.

A comparison analysis of the frequencies of the alleles and genotypes of the polymorphisms in the *TGFB1* gene depending on the disease responsible for the heart failure and subsequent cardiac allograft transplantation revealed that patients with DCM carried the GG genotype of rs1800469 more frequently than patients with IHD did ($p = 0.03$; OR = 2.68; 95% CI, 1.061–6.793) (*Fig. 3*).

The frequency of the A allele among patients with IHD was higher than that among patients with DCM ($p = 0.01$, OR = 0.37; 95% CI, 0.148–0.942).

Examination of the endomyocardial biopsy specimens showed that myocardial interstitial fibrosis in cardiac allografts was verified in 49 out of 110 transplant recipients. Staining made it possible to clearly discern the connective tissue, which was colored in various shades of blue (depending on its maturation state) and differed from other cardiac muscle tissues. All fibrosis types (diffuse, focal, and diffuse/focal) were taken into account during the analysis.

Figure 4 shows the histological preparations of cardiac allograft biopsy specimens with fibrotic changes.

A comparative analysis of the frequency and genotype distribution revealed differences in the frequency of the AA genotype of the rs1800470 polymorphism of the *TGFB1* gene in heart transplant recipients with and without myocardial fibrosis (*Fig. 5*).

Heart transplant recipients carrying the AA genotype of the rs1800470 polymorphism of the *TGFB1* gene were more likely to have fibrosis than those carrying the G allele (OR = 10.4; 95% CI, 1.152–94.538, $p = 0.013$).

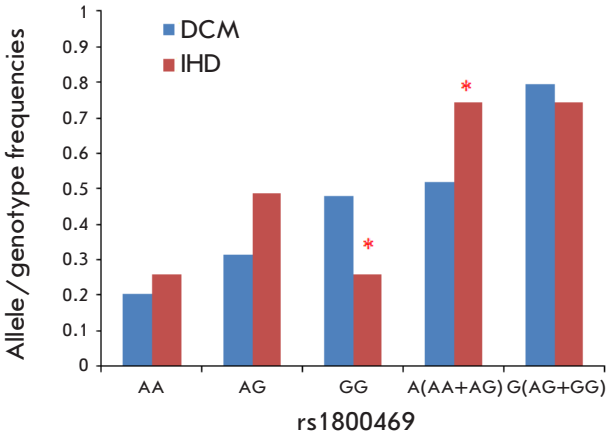

Fig. 3. Frequency distribution of the alleles and genotypes of the rs1800469 polymorphism of the *TGFB1* gene in patients with DCM and IHD, *$p < 0.05$ compared to DCM

DISCUSSION

This study has analyzed the distribution of the alleles and genotypes of three functionally significant polymorphisms of the *TGFB1* gene in heart transplant recipients. In heart transplant recipients, differences in the frequency of occurrence of genotypes and alleles of the rs1800471 polymorphism of the *TGFB1* gene were found in comparison with healthy individuals. A number of studies have shown that the G allele of the rs1800471 polymorphism is associated with a higher level of gene expression and elevated blood level of TGFβ1. Dysregulation of the TGFβ1 signaling pathway caused by a mutation can be associated with an increased risk of cardiovascular diseases [12, 13].

When analyzing the genetic predisposition to the primary disease that had been responsible for the end-stage heart failure and had made it necessary to perform heart transplantation, we observed a significant association between ischemic heart disease and the rs1800469 single nucleotide polymorphism. Similar data were obtained by Barsova *et al.* [4], who found a positive association between the *TGFB1**-509T (rs1800469) allele and genetic predisposition to early myocardial infarction (in patients younger than 50 years). It still remains unclear what are the mechanisms underlying the association between the polymorphism and the development of end-stage heart failure. It is possible that the rs1800469 polymorphism alters promoter affinity for the transcription factors and inhibits TGFβ

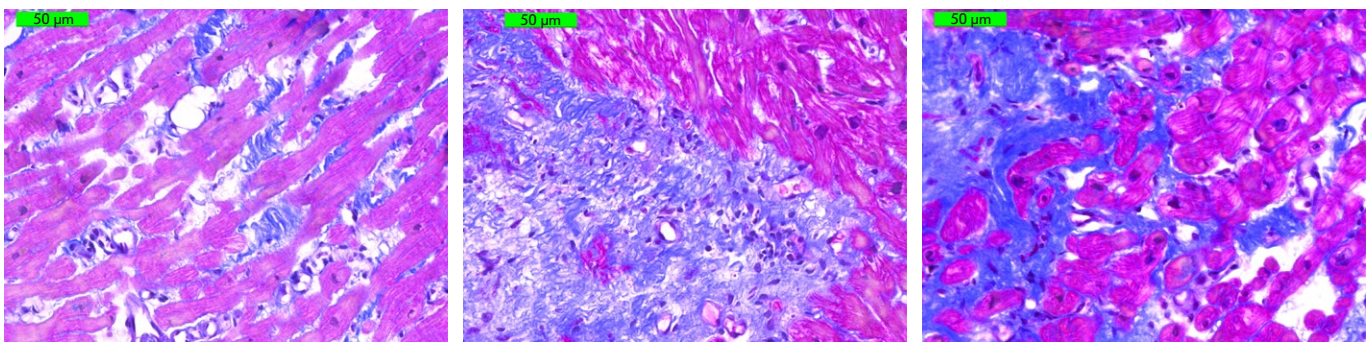

Fig. 4. Histological preparations of endomyocardial biopsy specimens. Masson's trichrome staining 400× (connective tissue is stained blue; cardiomyocytes are stained pink). (*A*) – diffuse overgrowth of loose fibrous connective tissue with single fibroplastic cells, focal granular proteinaceous degeneration of cardiomyocytes. (*B*) – focal overgrowth of non-mature connective tissue with single connective tissue cells, moderate proteinaceous degeneration of cardiomyocytes. (*C*) – diffuse/focal overgrowth of loose fibrous connective tissue, where proliferation of connective tissue cells is detected. Focal proteinaceous degeneration of cardiomyocytes

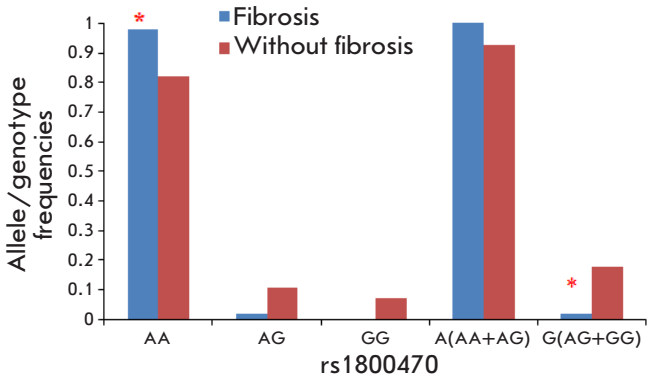

Fig. 5. Frequency distribution of the alleles and genotypes of the rs1800470 polymorphism of the *TGFB1* gene in heart transplant recipients with and without graft myocardial fibrosis, $*p < 0.05$ compared to heart transplant recipients without fibrosis

expression, thus activating proinflammatory cytokines (tumor necrosis factor α and interleukin-1), which may contribute to the progression of IHD [4]. Inconclusive data have been obtained in a number of studies: thus, no association between the 509C/T polymorphism and IHD was detected in a group of German patients [14]. Liu *et al.* [15] performed a meta-analysis of eight studies and showed a statistically significant association between the rs1800469 (TT) polymorphism and an increased risk of IHD.

Having analyzed the genetic predisposition to myocardial fibrosis in heart transplant recipients, we found significant associations between this trait and the rs1800470 polymorphism. The A allele of this polymorphism is known to be associated with a high level of TGFβ1 in peripheral blood. TGFβ1 is a potent stimulator of extracellular matrix production; its hyperproduction is associated with fibrotic disorders and the development of myocardial fibrosis. Leask [16] showed that TGFβ added to a fibroblast culture *in vitro* induces the expression of the genes related to extracellular matrix production and thus increases matrix accumulation and contributes to a concomitant suppression of matrix metalloproteinase production by raising the level of inhibitors of the gene encoding its expression.

CONCLUSIONS

This study has revealed the differences in occurrence of the alleles and genotypes of the *TGFB1* gene: the rs1800471 polymorphism in heart transplant recipients and healthy individuals, the rs1800469 polymorphism in patients with DCM and IHD, and the rs1800470 polymorphism in patients with and without myocardial fibrosis in a cardiac allograft. The findings give grounds for assuming that the *TGFB1* gene and its polymorphic variants are involved in the formation of genetic predisposition to myocardial fibrosis in heart transplant recipients. Further studies using a larger cohort of patients would provide more specific characteristics of the impact of single nucleotide polymorphisms on the development of fibrosis in a cardiac allograft. ●

The authors have no conflict of interest to declare.
This study was partially supported by the Russian Federation Presidential Grant (grant No. NSh-2598-2020.7) for state support of the leading research schools.

REFERENCES

1. Gautier S.V., Zacharevich V.M., Khalilulin T.A., Shevchenko A.O., Poptsov V.N., Ahmadzai R.L., Goltz A.M., Zakiryanov A.R., Koloskova N.N., Zacharevich N.Y. et al. // Russian Journal of Transplantology and Artificial Organs. 2019. V. 21. № 2. P. 7–15.
2. Wynn T.A. // J. Pathol. 2008. V. 214. № 2. P. 199–210.
3. Akdis M., Aab A., Altunbulakli C., Azkur K., Costa R., Crameri R., Duan S., Eiwegger T., Eljaszewicz A., Ferstl R., et al. // J. Allergy Clin. Immunol. 2016. V. 138. № 4. P. 984–1010.
4. Barsova R.M., Titov B.V., Matveeva N.A., Favorov A.V., Sukhinina T.S., Shahnovich R.M., Ruda M.Ia., Favorova O.O. // Acta Naturae. 2012. V. 4. № 2. P. 74–79.
5. Brusentsov D.A., Nikulina S.Yu., Shesternya P.A., Chernova A.A. // Rus. J. Cardiology. 2018. V. 23. № 10. P. 43–47.
6. Martelossi Cebinelli G.C., Paiva Trugilo K., Badaró Garcia S., Brajão de Oliveira K. // Eur. Cytokine Netw. 2016. V. 27. № 4. P. 81–89.
7. van Setten J., Warmerdam E.G., Groot O.Q., De Jonge N., Keating B., Asselbergs F.W. // Transplant. Direct. 2019. V. 5. № 2. P. 1–6.
8. Densem C.G., Hutchinson I.V., Yonan N., Brooks N.H. // Transplant. Immunol. 2004. V. 13. № 3. P. 211–217.
9. Ge Y.Z., Wu R., Lu T.Z., Jia R.P., Li M.H., Gao X.F., Jiang X.M., Zhu X.B., Li L.P., Tan S.J., et al. // PLoS One. 2014. V. 9. № 4. P. e93938.
10. Got'ye S.V., Shevchenko A.O., Poptsov V.N. Patsiyent s transplantirovannym serdtsem. Rukovodstvo dlya vrachey po vedeniyu patsiyentov, perenesshikh transplantatsiyu serdtsa. M.–Tver': Izdatel'stvo «Triada», 2014. 144 s.
11 Namipashaki A., Razaghi-Moghadam Z., Ansari-Pour N. // Cell J. 2015. V. 17. № 2. P. 187.
12. Rao M., Guo D., Jaber B.L., Tighiouart H., Pereira B.J., Balakrishnan V.S. // Kidney Int. 2004. V. 66. P. 419–427. [PubMed: 15200451].
13. Nikolova P.N., Ivanova M.I., Mihailova S.M., Myhailova A.P., Baltadjieva D.N., Simeonov P.L., Paskalev E.K., Naumova E.J. // Transplant. Immunol. 2008. V. 18. № 4. P. 344–348.
14. Koch W., Hoppmann P., Mueller J., Schömig A., Kastrati A. // Arterioscler. Thromb. Vasc. Biol. 2006. V. 26. № 5. P. 1114–1119.
15. Liu K., Liu X., Gu S., Sun Q., Wang Y., Meng J., Xu Z. // Oncotarget. 2017. V. 8. № 37. P. 62463–62469.
16. Leask A. // Circ. Res. 2010. V. 106. P. 1675–1680.

A Sorbent with Synthetic Ligand for Removing Pro-atherogenic and Pro-inflammatory Components from Human Blood Plasma

O. A. Dmitrieva[1*], E. D. Ovchinnikova[1], E. A. Utkina[1], P. A. Levashov[2], O. I. Afanasieva[1], I. Y. Adamova[1], S. N. Pokrovsky[1]

[1]Federal State Budgetary Institution «National Medical Research Center of Cardiology» Ministry of Health of the Russian Federation, Moscow, 121552 Russia

[2]Lomonosov Moscow State University, Moscow, 119991 Russia

*E-mail: dmitrievaoksan@rambler.ru

Received March 22, 2021; in final form, July 20, 2021

DOI: 10.32607/actanaturae.11292

ABSTRACT **Elevated levels of apoB-100 containing lipoproteins and markers of systemic inflammation are often observed in patients with cardiovascular diseases. The concentrations can be reduced by pharmacotherapy or extracorporeal treatment. The sorbent, which removes CRP and atherogenic lipoproteins, simultaneously reduces the bloodstream concentration of these components. The efficacy and selectivity of the designed sorbent were studied, desorption constants of CRP (K_d = 4.2 × 10^{-8} M) and LDL (K_d = 7.7 × 10^{-7} M) were distribution coefficients of CRP (K_c = 101) and Lp(a) (K_c = 38) were calculated, and the ability to bind large amounts of atherogenic lipoproteins (up to 32 mg of TC per mL of the sorbent gel) was demonstrated. Our sorbent can be recommended for performing complex removal of CRP and atherogenic lipoproteins from the blood plasma in patients with refractory hyperlipidemia and CVD that are accompanied by elevated levels of CRP.**

KEYWORDS **C-reactive protein, atherogenic lipoproteins, lipoprotein (a), atherosclerosis, therapeutic apheresis.**

ABBREVIATIONS **CRP – C-reactive protein; mCRP – the monomeric form of CRP; nCRP – the pentameric form of CRP; Lp(a) – lipoprotein(a); apoB-100 – apolipoprotein B-100; LDL – low-density lipoprotein; HDL – high-density lipoprotein; oxLDL – oxidized LDL; TC – total cholesterol; TG – triglyceride; HSA – human serum albumin; IgG – immunoglobulin G; LDL-C – low-density lipoprotein cholesterol; HDL-C – high-density lipoprotein cholesterol; CVD – cardiovascular diseases.**

INTRODUCTION

Despite the existing advanced lipid-lowering drugs and high-technology invasive methods for their diagnosis and treatment, cardiovascular diseases (CVDs) stubbornly remain the leading cause of death in developed countries. Lipid metabolism disorders are the main factors behind the development and progression of the atherosclerosis underlying CVD, while the C-reactive protein (CRP) is a marker of systemic inflammation. Available data increasingly suggest that CRP is not only an inflammatory marker, but that it can be also regarded as one of the pathogenic components of CVD [1]. The monomeric form of CRP (mCRP) originates from a dissociation of the native pentameric form (nCRP) on the surface of activated platelets and damaged cells [2, 3] and can be found in the necrotic zones after acute myocardial infarction and in atherosclerotic plaques [4]. The high CRP level detected after a myocardial infarction is associated with the risk of later myocardial dysfunction and heart failure [5, 6]. The plasma concentration of CRP is related to the prognosis of disease progression in atherosclerosis, chronic heart failure, atrial fibrillation, myocarditis, aortic regurgitation, and the prognosis after heart transplantation [7]. The CANTOS trial, which involves high-risk patients with an elevated nCRP level (median, 4.1 mg/L), has reliably shown that inflammation suppression without any effect on the low-density lipoprotein cholesterol (LDL-C) concentration significantly reduces the risk of cardiovascular complications, thereby being a new therapeutic strategy for cardiovascular patients [8].

The link between an elevated nCRP concentration and atherogenic apoB-100 containing lipoproteins was

demonstrated in several studies. Elevated levels of nCRP and oxidized low-density lipoproteins (oxLDLs) were found in patients with CAD. It was established in an augmentation of atherosclerosis severity that is estimated by the number of affected coronary arteries [9]. High levels of nCRP and lipoprotein(a) (Lp(a)) were observed in a group of patients younger than 45 years with a history of myocardial infarction [10]. M. Gronholdt *et al.* established that an elevated concentration of acute inflammatory markers is strongly related to an elevated level of triglyceride-rich lipoprotein particles, a larger volume of atheroma, and a higher echogenicity of the plaques located in the carotid arteries, an indication of the role of inflammatory markers as possible predictors of lesion severity and formation of an unstable atherosclerotic plaque [11].

The capabilities to pharmacologically correct the CRP level are currently confined to drugs that affect its synthesis in the liver [12]; meanwhile, means to directly influence the concentration of this protein are being actively sought. Elimination of CRP from a patient's bloodstream using the extracorporeal methods of therapeutic apheresis is one of the potential solutions. The methods based on adsorption technologies are considered the most effective and selective. Active ingredients of adsorption columns include specific antibodies or synthetic mimetics of natural ligands and the binding sites of CRP molecules.

CRP elimination significantly reduced the necrotic zone in animal models of acute myocardial infarction [13]. A PentraSorb CRP column (Pentracor, Germany) applied in patients with acute myocardial infarction showed a CRP level decreased by 50% within a single procedure [14]. Trials to collect data on the clinical efficacy of such procedures are currently underway.

We have previously elaborated a sorbent containing a synthetic mimetic ligand capable of simultaneously binding CRP and atherogenic lipoproteins [15]. Synchronous reduction of the concentration in the bloodstream of these components allows one to reduce their proinflammatory and proatherogenic activity, and, thereby, influence both major components of the pathogenesis of atherosclerosis.

The aim of this study was to investigate the efficiency and selectivity of the binding proinflammatory and proatherogenic components of human blood plasma using the synthesized sorbent.

MATERIALS AND METHODS

The research was conducted using purified solutions of low-density lipoproteins (LDL), human serum albumin (HSA), immunoglobulin G (IgG), CRP, and blood plasma or serum (to be more specific, plasma from healthy volunteers stabilized with citrate phosphate dextrose anticoagulant; heparin-containing plasma obtained after plasma exchange; and the serum of patients with CAD). LDL solutions with total cholesterol (TC) concentrations of 500 and 800 mg/dL were obtained from the blood plasma of healthy individuals by ultracentrifugation in the neutral NaBr density gradient [16]. A HSA solution (29 mg/mL) was prepared using a lyophilized sample (Calbiochem, United States). The CRP solution (1 mg/mL) contained 1% HSA as a stabilizer (Imtek, Russia). The IgG solution was a sample of human IgG for intravenous administration (Octapharm, Switzerland) with a concentration of 50 mg/mL.

A comparative analysis was performed using immune sorbents with immobilized polyclonal antibodies against LDL (LDL–Lipopak®), against IgG (Ig Adsopak®, both LTD sorbents manufactured by POCARD, Russia), and against nCRP. The sorbent with a synthetic ligand was obtained by immobilization of aromatic aldehyde on a cross-linked agarose matrix using a molecular spacer according to the method described earlier [17], albeit modified. The synthesis was carried out without glutaraldehyde.

Batch chromatography was applied in all chromatographic studies at room temperature with a 1 : 10 volume ratio between the sorbent gel and the studied sample (i.e., protein solution, plasma, or serum), unless agreed otherwise. To construct the adsorption isotherms, chromatography was performed in a buffer solution containing 10 mM NaH_2PO_4, 140 mM NaCl (pH 7.0) for 1 h. The maximum adsorption capacity (S_{max}) and desorption constant (K_d) were calculated according to the isotherms. Permanent load and a plasma dilution from 1 to 5 times were used to estimate the distribution of plasma components during chromatography, which is characterized by the ratio between the concentrations of substances bound to the sorbent and free ones, or the distribution coefficient (K_c). Chromatography with the concentrated LDL solutions (300–500 mg/dL) was performed to determine the maximum LDL-binding capacity; the amount of free cholesterol was controlled for a period extending from 30 min to 20 h.

The plasma levels of TC, high-density lipoprotein cholesterol (HDL-C), HSA, and triglycerides (TG) were measured using kits manufactured by Analiticon Biotechnologies AG (Germany) and Vector Best (Russia). The IgG and HSA concentrations in the solutions were determined by spectrophotometric methods using molar extinction coefficients of 1.4 and 0.6, respectively. Enzyme immunoassay (Vector Best, Russia) was applied to measure the CRP and

IgG concentrations. TheLp(a) concentration was measured using monospecific sheep polyclonal antibodies against human Lp(a) [18]. The LDL-C concentration was calculated using the Friedewald formula: LDL-C = TC – HDL-C – TG/5 [19]. The concentration of the corrected LDL-C (LDL-C_{corr}) that allows for a concentration of Lp(a) cholesterol (Lp(a)-C) was calculated using the Friedewald formula with Dahlen's modification: LDL-C_{corr} = LDL-C – 0.33 × Lp(a), where Lp(a) is the Lp(a) concentration in mg/dL [20].

The adsorptions of CRP, IgG, HSA, and LDL onto the sorbent are adequately described with the Langmuir equation: $S = S_{max} \times [C_{sol}]/(K_d+[C_{sol}])$, where S is the amount of bound component, S_{max} is the maximum adsorption capacity, $[C_{sol}]$ is the concentration of free component in the solution, and K_d is the desorption constant. When recalculating K_d into the desorption constants expressed as a particle count (K_d M), we used the corresponding molecular weights. Recalculation of the LDL-C concentration into the LDL concentration was performed considering the percentage of cholesterol in the corresponding lipoprotein.

RESULTS AND DISCUSSION

The synthesized sorbent is a polymeric agarose matrix with a synthetic ligand containing an aromatic group covalently attached via a molecular spacer. The sorbent is characterized by a significantly specific surface and well-developed pores available for all the plasma components studied in this work. The granule size of the matrix varies from 40 to 180 μm; the pore size – or the limit of molecular weight exclusion – is 6.3 × 10^5 kDa [21].

Hydroxyl radicals of monosaccharide agarose residuals, primary and secondary amine groups of the spacer, and phenyl groups of the ligand are the functional groups possible on the surface of the synthesized sorbent (*Fig. 1A*). Adsorption of plasma components can be performed using an ion exchange, aromatic, and hydrophobic interactions.

When studying peptides that inhibit interaction between the CRP and U937 cell lines, Q. Zen et al found that TKPLK**AFTV**CLH amino acids are of critical significance for the interaction between CRP and the CRP-binding site of the receptor to take place [22]. This sequence contains a section with three hydrophobic amino acids, including a single aromatic group (*Fig. 1B*). An assumption was made that the sorbent would bind to the ligand according to the principle of complementarity and hydrophobic interactions. Since an investigation of its properties revealed an ability to sorb atherogenic lipoproteins, it is not unlikely that the designed sorbent is a LOX-1 receptor mimetic [23].

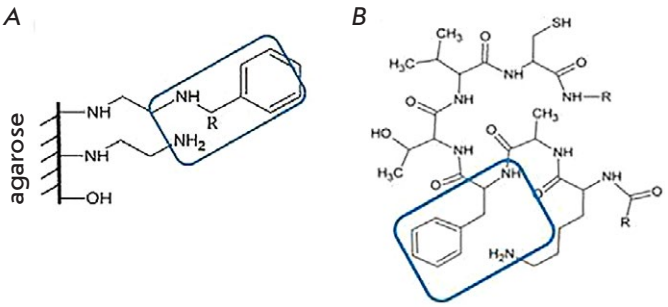

Fig. 1. Structural components of the synthesized sorbent (*A*) and the epitope of CRP (**AFTV**) for binding to leukocyte receptor (*B*) [22]

Table 1. The parameters of adsorption isotherms of human blood plasma proteins such as CRP, IgG, and HSA

	Plasma proteins		
	CRP	IgG	HSA
Molecular weight, kDa	115	146	64
Adsorption characteristics			
Desorption constant, K_d, M			
Synthetic sorbent	4.2 × 10^{-8}	2.9 × 10^{-5}	1.4 × 10^{-5}
Immunosorbent*	1.3 × 10^{-8}	7.5 × 10^{-7}	um#
Adsorption capacity, S_{max}, mg/mL of gel			
Synthetic sorbent	34.4	45.2	46.6
Immunosorbent*	0.9	16.1	um#

*the sorbent with an immobilized sulfate fraction of polyclonal goat antibodies against human nCRP was used for CRP adsorption; IgG–Adsopak® sorbent with immobilized polyclonal sheep antibodies against human IgG was used for IgG adsorption;
#um – unmeasured.

Table 1 shows the adsorption characteristics, and the maximum adsorption capacity (S_{max}) and desorption constant (K_d) in particular, in comparison with the corresponding parameters of the IgG–Adsopak® immunosorbent and the sorbent with immobilized polyclonal antibodies against human nCRP. The desorption constant of 4.2 × 10^{-8} M is an indication of the specific binding of the synthetic sorbent to CRP, suggesting that the functional groups of sorbents can act as mimetics of the CRP-binding site. Interaction between the synthetic sorbent and major protein components of the human blood plasma such as IgG and HSA is substantially less specific (K_d for IgG and HSA were 2.9 × 10^{-5} and 1.4 × 10^{-5} M, respectively). Interaction with LDL is characterized by a desorption constant of (7.7 ± 3.6) × 10^{-7} M, similar to that for the

Table 2. The distribution coefficients (K_c) of the human blood plasma components Lp(a), TG, and HSA

Sorbent	Distribution coefficients (K_c)		
	Lp(a)	TG	HSA
Synthetic sorbent	38 ± 7	7 ± 1	6 ± 5
LDL–Lipopak®	23 ± 6	6 ± 1	5 ± 4

LDL–Lipopak immunosorbent ((8.0 ± 2.2) × 10^{-7} M). The large amount of active functional groups in the synthetic sorbent results in the high S_{max} values seen in *in vitro* experiments with blood plasma or serum.

Plasma lipoproteins serve as ligands for various receptors of the endothelial and smooth muscle surface, as well as for macrophages and platelets. These numerous receptors, capable of binding native and modified LDL, participate not only in cholesterol transport, but also in multiple physiological and pathophysiological processes, including inflammation, repair, and atherosclerosis [24]. Scavenger receptors can bind to a wide range of ligands, including apoB-100 containing modified lipoproteins, Lp(a), and CRP [25, 26], suggesting possible common epitopes for the interaction.

Lp(a) is an LDL-like particle where the apoB-100 molecule is covalently bound to a high-molecular-weight glycosylated apoprotein (a). Although Lp(a) is an independent genetic risk factor of various CVDs, there are no ways to manage it pharmacologically [27, 28]. Therapeutic antisense oligonucleotides designed for these purposes are currently undergoing clinical trials [29].

The adsorption of Lp(a), TG, and LDL-C_{corr} was investigated using chromatography of human blood plasma with varied concentrations of the studied components (dilution 1 to 5 times) and a permanent load of 1 mL of plasma per 0.1 mL of synthetic or immune sorbents. The distribution coefficients (K_c) are shown in *Table 2*; adsorption capacity and adsorption efficacy (% of removal) are shown in *Fig. 2*. Adsorption of Lp(a) was more pronounced compared to that of TG and HSA; the largest differences in the K_c values were recorded for the synthetic sorbent. The LDL–Lipopak immune sorbent was characterized by a better interaction with LDL, as shown by high values of the adsorption efficacy.

Adsorption of CRP was studied *in vitro* in a human blood serum with an extremely high CRP concentration (1330 mg/L). The specificity of the interaction between the synthetic sorbent and CRP was convincingly proved by a high binding efficiency (101), while HSA and IgG were characterized by a K_c value amounting to 2. Based on the results of this experiment, the adsorption capacity of the synthetic sorbent reached 12 mg of CRP per mL of gel.

Incubation of the synthetic sorbent with concentrated LDL solutions (300 and 500 mg/dL) for a long period of time showed that maximum LDL-binding capacity was not attained until the 6th hour of incubation, which was apparently associated with the steric peculiarities of the interaction between the active functional groups of the sorbents and such a large supramolecular complex as LDL. The adsorption capacity after 6 h of incubation with a higher load was 32 mg of TC per mL of gel, with 64% binding efficiency. The adsorption capacity was lower (26 mg of TC per mL of gel) under a lower load after 20 h of incubation, although the binding efficiency appeared to be higher (86%). *Figure 3* shows the adsorption capacity of the synthetic sorbent as a function of the load and chromatography duration.

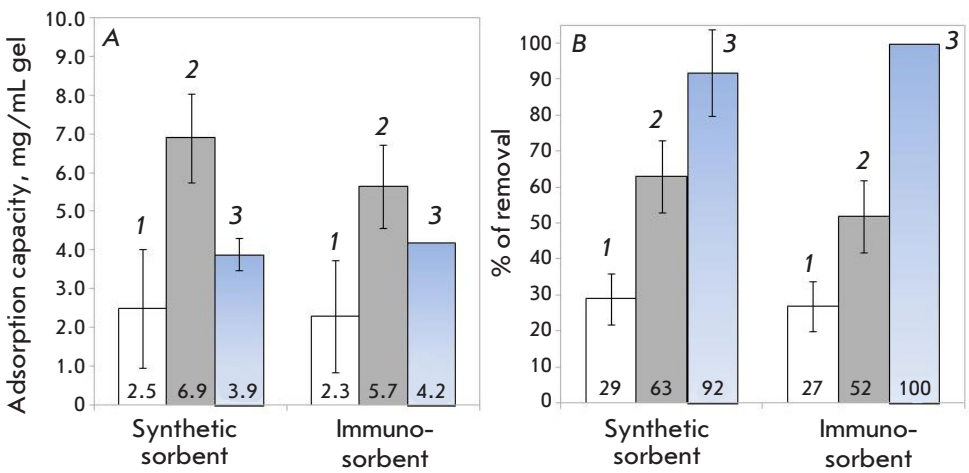

Fig. 2. The values of (*A*) adsorption capacity, (*B*) adsorption efficiency (% of removal) of the studied plasma components for the synthetic sorbent and the LDL–Lipopak® immunosorbent. The studied plasma components: (*1*) TG, (*2*) Lp(a), and (*3*) LDL-C_{corr}. The initial plasma concentrations were 149 mg/dL for TC, 48 mg/dL for HDL-C, 108 mg/dL for TG, 109 mg/dL for Lp(a), and 42 mg/dL for LDL-C_{corr} (the estimated value)

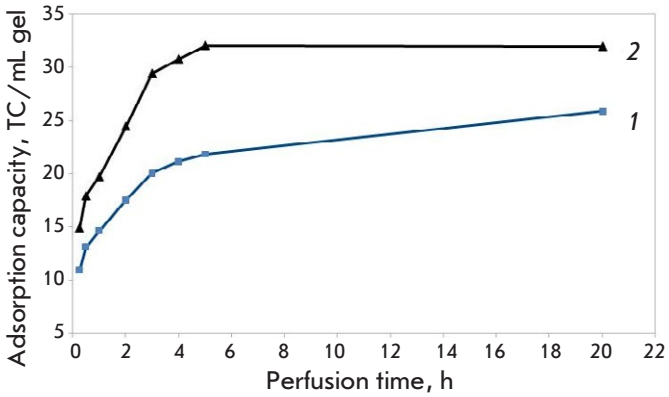

Fig. 3. Adsorption capacity of the synthetic as a function of load and chromatography duration (from 30 min to 20 h). *1* – 30 mg of TC per mL of gel, *2* – 50 mg of TC per mL of gel

CONCLUSIONS

Our experimental data point to a high specificity of the interaction between the synthetic sorbent and CRP. The desorption constant (K_d) (4.2 × 10^{-8} M) was 1000 times higher than that of major plasma proteins, such as HSA and IgG, while the distribution coefficient (K_c), equal to 101, was 50 times higher than those of HSA and IgG. The ability to bind to the majority of atherogenic lipoproteins was demonstrated; the maximal adsorption capacity in a LDL solution is 32 mg of TC per mL of gel sorbent. This sorbent can be recommended for a complex elimination of CRP and atherogenic lipoproteins from the blood plasma of patients with refractory hyperlipidemia and CVD that are accompanied by elevated CRP levels.

LIMITATIONS

The adsorption isotherm of CRP was constructed using a solution containing CRP (1 mg/mL) and HSA (10 mg/mL). The distribution coefficient of LDL-C (LDL-C_{corr}) was not calculated because of the low initial LDL concentration in the blood plasma. The duration of the chromatography (1 h) was shorter than that required for the saturation of the synthetic sorbent at high LDL concentrations. ●

This study was financially supported through;. State Assignment AAAA-A18-118030690076-7 on "Elaboration of next-generation affine sorbents for the therapeutic apheresis procedures in treating patients with drug-resistant cardiovascular and other diseases."
The authors claim that they have no conflict of interests. This article does not contain the descriptions of experiments involving humans or animals as subjects.

REFERENCES

1. Avan A., Tavakoly Sany S.B., Ghayour-Mobarhan M., Rahimi H.R., Tajfard M., Ferns G. // J. Cell. Physiol. 2018. V. 233. № 11. P. 8508–8525. doi:10.1002/jcp.26791.
2. Sproston N.R., Ashworth J.J. // Front. Immunol. 2018. V. 9. P. 754. doi:10.3389/fimmu.2018.00754.
3. Thiele J.R., Habersberger J., Braig D., Schmidt Y., Goerendt K., Maurer V., Bannasch H., Scheichl A., Woollard K.J., von Dobschütz E. // Circulation. 2014. V. 130. № 1. P. 35–50. doi:10.1161/CIRCULATIONAHA.113.007124.
4. Meuwissen M., van der Wal A.C., Niessen H.W., Koch K.T., de Winter R.J., van der Loos C.M., Rittersma S.Z., Chamuleau S.A., Tijssen J.G., Becker A.E. // J. Clin. Pathol. 2006. V. 59. № 2. P. 196–201. doi:10.1136/jcp.2005.027235.
5. Al Aseri Z.A., Habib S.S., Marzouk A. // Vasc. Health Risk Manag. 2019. V. 15. P. 221–227. doi:10.2147/VHRM.S198452.
6. Wang J., Tang B., Liu X., Wu X., Wang H., Xu D., Guo Y. // Atherosclerosis. 2015. V. 239. № 2. P. 343–349. doi:10.1016/j.atherosclerosis.2015.01.024.
7. Osman R., L'Allier P.L., Elgharib N., Tardif J.C. // Vasc. Health Risk Manag. 2006. V. 2. № 3. P. 221–237. doi:10.2147/vhrm.2006.2.3.221.
8. Koenig W. // Eur. Cardiol. 2017. V. 12. № 2. P. 89–91. doi:10.15420/ecr.2017:18:1.
9. Abolhasani S., Shahbazloo S.V., Saadati H.M., Mahmoodi N., Khanbabaei N. // Arq. Bras. Cardiol. 2019. V. 113. № 4. P. 667–674. doi:10.5935/abc.20190159.
10. Wadhwa A., Avasthi R., Ghambhir J.K., Dwivedi S. // J. Assoc. Physicians India. 2013. V. 61. № 6. P. 384–386.
11. Grønholdt M.L., Sillesen H., Wiebe B.M., Laursen H., Nordestgaard B.G. // Eur. J. Vasc. Endovasc. Surg. 2001. V. 21. № 3. P. 227–234. doi:10.1053/ejvs.2001.1321.
12. McFadyen J.D., Kiefer J., Braig D., Loseff-Silver J., Potempa L.A., Eisenhardt S.U., Peter K. // Front Immunol. 2018. V. 9. P. 1351. doi:10.3389/fimmu.2018.01351.
13. Sheriff A., Schindler R., Vogt B., Abdel-Aty H., Unger J.K., Bock C., Gebauer F., Slagman A., Jerichow T., Mans D. // J. Clin. Apher. 2015. V. 30. № 1. P. 15–21. doi:10.1002/jca.21344.
14. Ries W., Heigl F., Garlichs C., Sheriff A., Torzewski J. // Ther. Apher. Dial. 2019. V. 23. № 6. P. 570–574. doi:10.1111/1744-9987.12804.
15. Levashov P.A., Dmitrieva O.A., Afanasieva M.I., Ovchinnikova E.D., Utkina E.A., Afanasieva O.I., Adamova I.Y., Pokrovsky S.N. // Patent RF № 2700605. B01J 20/26 (2006.01). B01J 20/32 (2006.01). 2019.
16. Patsch J.R., Sailer S., Kostner G., Sandhofer F., Holasek A., Braunsteiner H. // J. Lipid. Res. 1974. V. 15. № 4. P. 356–366.
17. Levashov P.A., Ovchinnikova E.D., Frid D.A., Azmuko A.A., Afanasieva M.I., Kotkina T.I., Afanasieva O.I., Adamova I.Y., Pokrovsky S.N. // J. Bioorg. Chem. 2015. V. 41. № 5. P. 553–558. doi:10.7868/S0132342315040089.
18. Afanasieva O.I., Adamova I.Y., Benevolenskaya G.F., Pokrovsky S.N. // B. Exp. Biol. Med. 1995. V. 120. № 10. P. 398–401.
19. Friedewald W.T., Levy R.I., Fredrickson D.S. // Clin. Chem. 1972. V. 18. № 6. P. 499–502.

20. Dahlen G.H. // Lipoprotein(a). / Ed. Scanu A.M. New York: Acad. Press, 1990. P. 151–173.
21. Afanasieva M.I., Dmitrieva O.A., Afanasieva O.I., Adamova I.Y., Levashov P.A., Ovchinnikova E.D., Pokrovsky S.N. // Kardiologicheskij Vestnik. 2019. V. 14 № 3. P. 26–32. doi:10.36396/MS.2019.14.03.004.
22. Zen Q., Zhong W., Mortensen R.F. // J. Cell. Biochem. 1997. V. 64. № 1. P. 140–151. doi:10.1002/(sici)1097-4644(199701)64:1<140::aid-jcb16>3.0.co;2-p.
23. Stancel N., Chen C.C., Ke L.Y., Chu C.S., Lu J., Sawamura T., Chen C.H. // Clin. Chem. 2016. V. 62. № 2. P. 320–327. doi:10.1373/clinchem.2015.243923
24. Mineo C. // Cardiovasc. Res. 2020. V. 116. № 7. P. 1254–1274. doi:10.1093/cvr/cvz338.
25. Pirillo A., Norata G.D., Catapano A.L. // Mediators Inflamm. 2013. V. 2013. P. 152786. doi:10.1155/2013/152786.
26. McCormick S.P.A., Schneider W.J. // Pathology. 2019. V. 51. № 2. P. 155–164. doi:10.1016/j.pathol.2018.11.003.
27. Pokrovsky S.N., Afanasieva O.I., Ezhov M.V. // Curr. Opin. Lipidol. 2016. V. 27. № 4. P. 351–358. doi:10.1097/MOL.0000000000000319.
28. Afanasieva O.I., Pokrovsky S.N. // Russ. J. Cardiol. 2019. V. 24. № 5. P. 101–108. doi:10.15829/1560-4071-2019-5-101-108.
29. Afanasieva O.I., Ezhov M.V., Pokrovsky S.N. // Russ. J. Cardiol. 2018. V. 23. № 8. P. 99–109. doi:10.15829/1560-4071-2018-8-99-109.

Nanobodies Are Potential Therapeutic Agents for the Ebola Virus Infection

I. B. Esmagambetov[1*], D. V. Shcheblyakov[1], D. A. Egorova[1], O. L. Voronina[1], A. A. Derkaev[1], D. V. Voronina[1], O. Popova[1], E. I. Ryabova[1], D. N. Shcherbinin[1], E. I. Aksenova[1], A. N. Semenov[1], M. S. Kunda[1], N. N. Ryzhova[1], O. V. Zubkova[1], A. I. Tukhvatulin[1], D. Yu. Logunov[1], B. S. Naroditsky[1], S. V. Borisevich[2], A. L. Gintsburg[1]

[1]Federal State Budgetary Institution "National Research Centre for Epidemiology and Microbiology named after the Honorary Academician N. F. Gamaleya" of the Ministry of Health of the Russian Federation, Moscow, 123098 Russia

[2]48 Central Research Institute, Ministry of Defense, Sergiev Posad-6, 141306 Russia

[*]E-mail: esmagambetovib@gmail.com

Received June 18, 2021; in final form, July 14, 2021

DOI: 10.32607/actanaturae.11487

ABSTRACT **Ebola fever is an acute, highly contagious viral disease with a mortality rate that can reach 90%. There are currently no licensed therapeutic agents specific to Ebola in the world. Monoclonal antibodies (MAbs) with viral-neutralizing activity and high specificity to the Ebola virus glycoprotein (EBOV GP) are considered as highly effective potential antiviral drugs. Over the past decade, nanobodies (single-domain antibodies, non-canonical camelid antibodies) have found wide use in the diagnosis and treatment of various infectious and non-infectious diseases. In this study, a panel of nanobodies specifically binding to EBOV GP was obtained using recombinant human adenovirus 5, expressing GP (Ad5-GP) for alpaca (*Vicugna pacos*) immunization, for the first time. Based on specific activity assay results, affinity constants, and the virus-neutralizing activity against the recombinant vesicular stomatitis virus pseudotyped with EBOV GP (rVSV-GP), the most promising clone (aEv6) was selected. The aEv6 clone was then modified with the human IgG1 Fc fragment to improve its pharmacokinetic and immunologic properties. To assess the protective activity of the chimeric molecule aEv6–Fc, a lethal model of murine rVSV-GP infection was developed by using immunosuppression. The results obtained in lethal model mice have demonstrated the protective effect of aEv6–Fc. Thus, the nanobody and its modified derivative obtained in this study have shown potential protective value against Ebola virus.**

KEYWORDS **Ebola virus, nanobody, recombinant adenoviral vector, recombinant vesicular stomatitis virus.**

ABBREVIATIONS **EVD – Ebola virus disease; EBOV GP – Ebola virus glycoprotein; MAb – monoclonal antibody; PFU – plaque-forming unit; ELISA – enzyme-linked immunosorbent assay; TMB – 3,3',5,5'-tetramethylbenzidine; PBST – phosphate buffered saline with polysorbate 20; HRP – horseradish peroxidase; PBMC – peripheral blood mononuclear cell; PRNT – plaque reduction neutralization test; PRNT50 – 50% neutralization titer.**

INTRODUCTION

Ebola virus, a member of the Filoviridae family, genus *Ebolavirus*, is a causative agent of hemorrhagic fever in humans and non-human primates [1]. The genus *Ebolavirus* consists of six species: Zaire ebolavirus (EBOV), Sudan ebolavirus (SUDV), Bundibugyo ebolavirus (BDBV), Tai Forest ebolavirus (TAFV), Reston ebolavirus (RESTV), and Bombali ebolavirus (BOMV) [2]. The mortality rate of the disease caused by the Ebola virus (EVD) can top 60–90% [3, 4]. Recent EVD outbreaks were reported in the Congo in 2018, Uganda in 2019, and Congo and Guinea in 2021 [5].

Monoclonal antibody cocktails specific to EBOV GP can provide complete protection against EVD in non-human primates; some of them (Zmapp, MAb114, REGN-EB3, and GamEMab) are currently undergoing clinical trials [6–8]. In our previous study [9], we immunized mice with Ad5-GP (component B of the GamEvac-Combi vaccine [10]) and managed to obtain two mouse monoclonal antibodies (2c8 and 6g3) that are protective against EVD.

In addition to monoclonal antibodies, the possibility of using nanobodies (non-canonical forms of camelid monoclonal antibodies) and their modified derivatives in the treatment of infectious diseases has been an area of interest for the past 20 years [11, 12]. However, there are only a few studies on the development of anti-EVD nanobody drugs [13–15]. The main advantages of nanobodies are a relatively straightforward technology of production and their ability to bind to hidden antigenic epitopes [13–15]. The disadvantages of nanobodies are associated with their rapid excretion by kidneys and the fact that the Fc fragment lacks an independent effector function. The Fc fragment of IgG requires some modification to improve the pharmacokinetic and effector properties of nanobodies [12] and increase their avidity due to molecule dimerization.

We have obtained a nanobody with protective activity against the recombinant vesicular stomatitis virus pseudotyped with the Ebola virus glycoprotein (rVSV-GP). For this, we used a technology that included the following steps: (1) immunization of alpaca with Ad5-GP, (2) generation of a panel of nanobodies specific to EBOV GP, (3) selection of a clone with optimal activity *in vitro*, (4) modification of the selected clone to improve its pharmacokinetic and immunological properties, and (5) *in vivo* assessment of the protective effect of the selected clone.

We selected and characterized the most promising nanobody: aEv6. The protective activity of a modified form of this clone (aEv6–Fc) was evaluated in a lethal model of rVSV-GP infection in immunosuppressive mice. Mice were injected with dexamethasone and cyclophosphamide to induce immunosuppression. This approach has been previously used to assess the activity of antiviral drugs and study the factors of Ebola virus pathogenesis [16, 17]. Our study established the ability of the aEv6–Fc antibody to protect mice from a lethal rVSV-GP infection, which may indicate its potential antiviral activity against the Ebola virus.

EXPERIMENTAL PROCEDURES

Viruses and antigens

The following viruses were used in the study: Ad5-GP, a recombinant replication-defective adenovirus expressing the GP Zaire ebola virus gene (*Ebola virus/H. sapiens-wt/SLE/2014/Makona-G3735.1* isolate; GenBank Accession No. KM233056) obtained as previously described [10, 18] and rVSV-GP, a recombinant vesicular stomatitis virus expressing the GP Zaire ebolavirus gene (*Ebola virus/H. sapiens-wt/SLE/2014/Makona-G3735.1* isolate, GenBank Accession No. KM233056) obtained as previously described [10].

The antigens used in the study are as follows: recombinant protein GP Zaire ebolavirus (*H. sapiens-wt/GIN/2014/Kissidougou-C15* strain; Sino Biological, China, Cat No. 40442-V02H) and helper phage M13 Hyperphage M13 K07ΔpIII (Progen, Germany, Cat No. PRHYPE).

Cell lines

The following cell lines were used in the study: CHO-S cells (Thermo Fisher Scientific, USA, Cat No. R80007); Vero E6 (ATCC CRL 1586) and GMK-AH-1(D) (CVCL_L878) cells were received from the Russian collection of cell cultures of vertebrates (St. Petersburg, Russia, https://www.incras.ru/institut/struktura/ckp/rossijskaja-kollekcija-kletochnyh-kultur/).

Alpaca immunization, immune library construction, nanobody expression and purification

A healthy four-year old male alpaca (*Vicugna pacos*) was used for immunization and blood sampling. The animal was provided by the Russian Alpaca Farm (Pokhodkino, Russia).

Triple injections of Ad5-GP (10^8 PFU), without adjuvants, were administered intramuscularly at three-week intervals. The recombinant EBOV GP protein (200 μg) with an incomplete Freund's adjuvant was injected intramuscularly three weeks after the last injection of Ad5-GP.

A total of 150 ml of blood was sampled five days after the last immunization; blood samples were collected in sterile vacuum tubes containing lithium heparin.

Isolation of mRNA, PCR, library construction, and specific screening were performed according to [19] using the recombinant EBOV GP protein as an antigen.

Expression and purification of the nanobodies were carried out as previously described [19].

Next-Generation Sequencing of nanobody genes

Nanobody gene amplicons were generated using specific primers [19] and purified by the MinElute PCR Purification Kit (QiaGen, Netherlands). Libraries were prepared according to the random priming protocol (Roche, Switzerland). Library sizing and quantitation were performed using the High Sensitivity DNA Kit (Agilent, USA). Sequencing was performed using the GS Junior Titanium Sequencing Kit and GS Junior + Series XL + Kit GS Junior + Series XL (Roche), according to the manufacturer's instructions.

Amplicons were analyzed using 454 Sequencing System Software v. 3.0 and our own software.

Determination of nanobody affinity constants

The affinity constants of the nanobodies were determined using the recombinant EBOV GP protein by surface plasmon resonance (SPR) on a Biacore 3000 instrument (GE Healthcare Bio-Sciences AB, Sweden) as previously described [19].

Production of the modified nanobody aEv6–Fc

The nucleotide sequence of aEv6–Fc (synthesized at ZAO Evrogen, Russia) was cloned into the pShuttle-CMV plasmid (Stratagene, USA) to obtain the plasmid pShuttle-CMV-aEv6Fc.

CHO-S cells (Thermo Fisher Scientific, USA) were transiently transfected with plasmid pShuttle-CMV-aEv6Fc using the CHOgro Expression System (Mirus Bio, USA) according to the manufacturer's instructions. Cells were cultured in Erlenmeyer flasks in a 5% CO_2 and 80% humidity at 32°C and 125 rpm; the temperature was reduced to 32°C after 24 h, and the cells were cultured for up to 10 days. Starting from day 3, the following supplements were added: Cell boosts 7a (2%) and 7b (0.2%) (HyClone, USA) and 0.5% CHO Feed Bioreactor Supplement (Sigma, USA) once a day. After 10 days of cultivation, the cell culture medium was clarified by centrifugation at 5,000 g. The antibody was purified by affinity chromatography on the AKTA Start Protein Purification System (Cytiva, Sweden) using 1-ml MAbSelect SuRe columns (Cytiva, Sweden) according to the manufacturer's instructions. Additional purification and buffer exchange were performed on a XK 26/100 column (Cytiva) using a Superdex 200 prep grade resin (Cytiva).

Production of the control antibody MAb114

The amino acid sequence published by Corti D. *et al.* was used to obtain the control antibody MAb114 [7]. Nucleotide sequences encoding the heavy and light chains of MAb114 were synthesized at ZAO Evrogen and cloned into the pShuttle-CMV plasmid (Stratagene). The resulting plasmids pShuttle-CMV-Mab-114HC and pShuttle-CMV-Mab114LC were used to transfect CHO-S cells. Cell transfection and antibody purification were performed as described in the previous section.

Indirect ELISA

Indirect ELISA was carried out according to [9]. Anti-human IgG (Sigma, Cat No. A8667), Anti-Myc Tag (Abcam, Cat No. 1326), and anti-Llama IgG Heavy, and Light Chain (Bethyl, Cat No. A160-100P) antibodies conjugated to horseradish peroxidase (HRP) were used to detect nanobodies and antibodies (aEv6–Fc and MAb114) in alpaca serum.

Virus neutralization assay

Virus neutralization assay was performed as described in [9] using Vero E6 cells infected with the rVSV-GP virus as the model.

Study of aEv6–Fc pharmacokinetics

Three healthy rhesus macaques (*Macaca mulatta*) received from the Research Institute of Medical Primatology (Veseloye, Russia) were injected with 10 mg/kg aEv6–Fc intravenously with an infusion rate of 10 ml/h. Blood samples were collected before infusion and 1, 4, 8, 16, 24, 48, and 96 h and 7, 14, and 21 days after infusion. Indirect ELISA using various dilutions of aEv6–Fc as standards was used to assess the blood concentration of aEv6–Fc. Pharmacokinetic parameters were calculated using the Microsoft Excel and PKSolver software.

Passive immunization and evaluation of protective activity

Female BALB/c mice aged 4–6 weeks (weight, 18–20 g) were provided by the Pushchino Branch of the Institute of Bioorganic Chemistry, Russian Academy of Sciences (Pushchino, Russia). The mice were injected with dexamethasone (daily intraperitoneal injection of 10 mg/kg/day 10 days before virus injection) [17] and cyclophosphamide (single intraperitoneal injection of 150 mg/kg 5 days before virus injection) to induce immunosuppression. Recombinant VSV-GP was administered intravenously at a dose of 10^9 PFU/mouse; the aEv6–Fc antibody was injected intravenously at a dose of 50 mg/kg. The experimental animals were observed and weighed every day during the experiment. The results are presented as the animal survival rate (%) at different time points.

The experimental scheme is described in more detail in the Results section.

Determination of rVSV-GP titers in the organs and tissues of infected mice

Organs and tissues of infected mice were isolated under sterile conditions. Organ samples (20 mg each) were homogenized in 1 ml of DMEM. The suspension was clarified by centrifugation at 2,000 rpm for 10 min. The supernatant was collected to determine the virus-neutralizing titers of rVSV-GP.

Statistical data analysis

Data were analyzed using EXCEL 2010 and the STATISTICA v. 7.0 software. The Mann–Whitney U test and the Gehan–Wilcoxon test with a significance level of 0.05 were used to assess intergroup differences in the antibody titers and animal survival.

Table 1. NGS analysis of nanobody libraries

Clone	Read frequency, %		Amplification factor	CDR3 (amino acid sequence)
	Primary library	Library after selection		
aEv1	0.33	18.89	57.79024	NVQLGRFGILE
aEv2	0.31	7.81	24.89199	KSRRYGVDYW
aEv3	0.01	3.70	282.6006	AAVNSWAVYSLSRNYDY
aEv4	0.05	2.01	38.44366	AMRRGGVSYTYW
aEv5	0,01	3.71	283.5078	AVRSERYTRRYDH
aEv6	0.01	0.42	31.75288	YVDARYGALHTYRS
aEv7	0.08	1.60	20.41256	NAHYWSRD
aEv8	0.01	3.38	258.5591	KVTRGDFLGRRTDY
aEv9	0.01	0.20	14.96921	AARPGSYSRDARRYD
aEv10	0.03	2.08	79.609	NAQLSRSVLWGRY
aEv11	0.01	1.29	98.88753	QQKYAGRLY
aEv12	0.05	0.97	18.59811	AADRVLTSSSRNWDY
aEv13	0.01	1.54	117.9393	YARRRTYLAAY
aEv14	0.01	0.61	46.72209	AAGRSSMGLLDATDWRH
aEv15	0.01	0.85	65.3202	NSRGRHDWNRYN
aEv16	0.01	0.42	32.20649	AASPRTSMLVVGNVDH
aEv17	0.01	1.39	106.5989	NAQSHFFGSNY
aEv18	0.05	0.14	2.721675	AARPEYYSGTASYVSTSYDY
The remaining	98.954	48.99	0.494915	

Compliance with animal use regulations

Experimental procedures were carried out in accordance with the Guide for the Care and Use of Laboratory Animals published by the National Institutes of Health (NIH Publication No. 85–23, revised in 1996) and the National Standard of the Russian Federation GOST R 53434–2009. All experiments were approved by the ethical committee of the N. F. Gamaleya National Research Center for Epidemiology and Microbiology (Minutes No. 27 of 2020). All individuals who worked with the animals and took care of them during the study received annual training in accordance with the IACUC requirements.

RESULTS

Production of a panel of nanobodies specific to EBOV GP

A panel of nanobodies specific to EBOV GP was obtained by immunizing alpaca (*V. pacos*) with the recombinant Ad5-GP adenovirus and recombinant GP protein, according to the scheme presented in *Fig. 1A*.

On day 5 after booster immunization, 150 ml of alpaca blood was collected; serum was isolated to evaluate the titer of antibodies specific to EBOV GP to confirm the effectiveness of immunization. The titer of antibodies against EBOV-GP was determined at a dilution of 1 : 16,000, which indicates that the immunized animal has a high immune response (*Fig. 1B*).

Peripheral blood mononuclear cells (PBMCs) were isolated to create an immune library of nanobodies. Nucleotide sequences encoding variable fragments of nanobodies obtained from alpaca's PBMCs were cloned into the phagemid vector pHEN1. Specific antibodies were selected by phage display as described in [19].

The selection results were analyzed using polyclonal phage ELISA (*Fig. 1C*). The library obtained after the second round of selection was used in further studies to prevent a decrease in nanobody diversity. Nucleotide sequences of nanobodies were identified by Next Generation Sequencing (NGS).

A total of 18 clones (aE1–18) were identified (*Table 1*). The amplification factor of 16 clones after two rounds of selection exceeded 20, which was an indication of their specific accumulation through EBOV GP binding. A library analysis also showed that the selected clones constituted about 51% of all amplicons in the library after selection, while the percentage of these clones in the primary library was < 1% (*Fig. 2A,B*).

As a result of indirect ELISA using EBOV GP, the clones aEv2, aEv3, aEv6, and aEv7 were selected as the most specific ones (*Fig. 2C*).

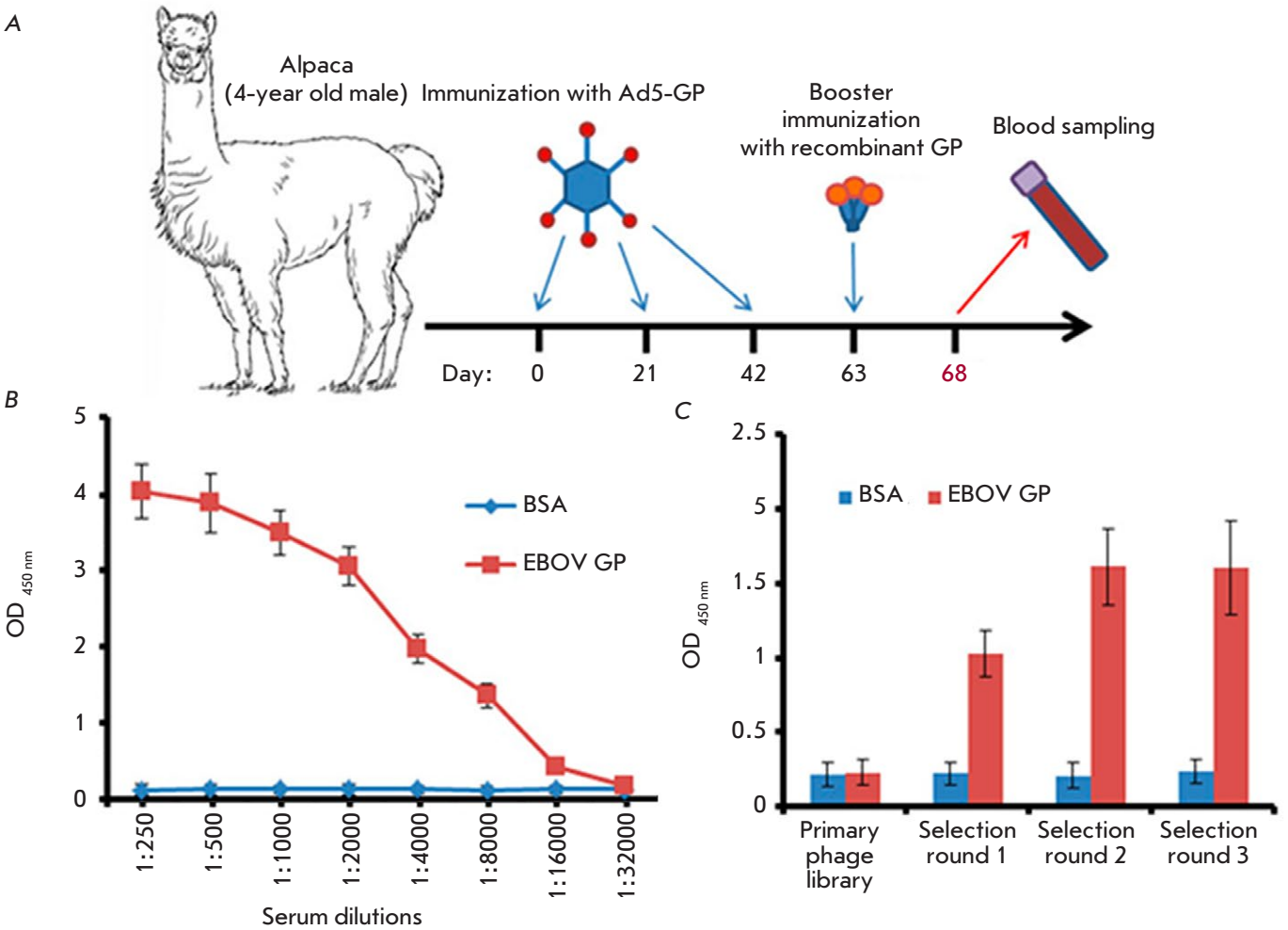

Fig. 1. Schematic representation of alpaca (*Vicugna pacos*) immunization to obtain a library of nanobodies (*A*), anti-EBOV GP antibody titers in the serum of immunized alpaca (*B*), and polyclonal phage ELISA (*C*). (*B*) – High-binding Polystyrene Microtiter plates were coated with 100 µl (1 µg/ml) of EBOV GP (*H. sapiens-wt/GIN/2014/Kissidougou-C15*). On the next day, the wells were washed with 0.1% PBST five times and blocked with 5% non-fat skim milk in PBST. Different dilutions of the serum in PBST were added, and the samples were incubated at 37°C for 1 h. The wells were washed five times, and Anti-Llama IgG Heavy- and Light-Chain antibodies (Bethyl, USA, A160-100P) in blocking buffer (1 : 5,000) were added for incubation at 37°C for 1 h. The wells were washed five times, TMB was added, and the results were evaluated. (*C*) – High-binding Polystyrene Microtiter Plates were coated with 100 µl of EBOV GP (*H.sapiens-wt/GIN/2014/Kissidougou-C15*). On the next day, the wells were washed with 0.1% PBST five times and then blocked with 5% non-fat skim milk in PBST. A total of 10^{11} phages from each stage of the selection were added in PBST and incubated at 37°C for 1 h. The wells were washed five times to remove unbound phages, and HRP-conjugated Anti-M13 antibodies (Abcam, UK, B62-FE2) in blocking buffer (1 : 5,000) were added for incubation at 37°C for 1 h. The wells were washed five times, TMB was added, and the results were evaluated

Wells were coated with 100 µl (1 µg/ml) of EBOV GP (*H. sapiens-wt/GIN/2014/Kissidougou-C15*). On the next day, the wells were washed with 0.1% PBST five times and blocked with 5% non-fat skim milk in PBST. Samples of the selected clones (10 µg/ml) were added to the wells and incubated in blocking buffer at 37°C for 1 h. The wells were washed five times, HRP-conjugated Anti-Myc Tag antibodies in blocking buffer (1 : 5,000) were added, with further incubation at 37°C for 1 h. The wells were washed five times, TMB was added, and the results were evaluated.

Analysis of the selected clones by indirect ELISA, SPR, and virus neutralization assay

The immunological properties of the selected clones aEv2, aEv3, aEv6, and aEv7 were studied by ELISA,

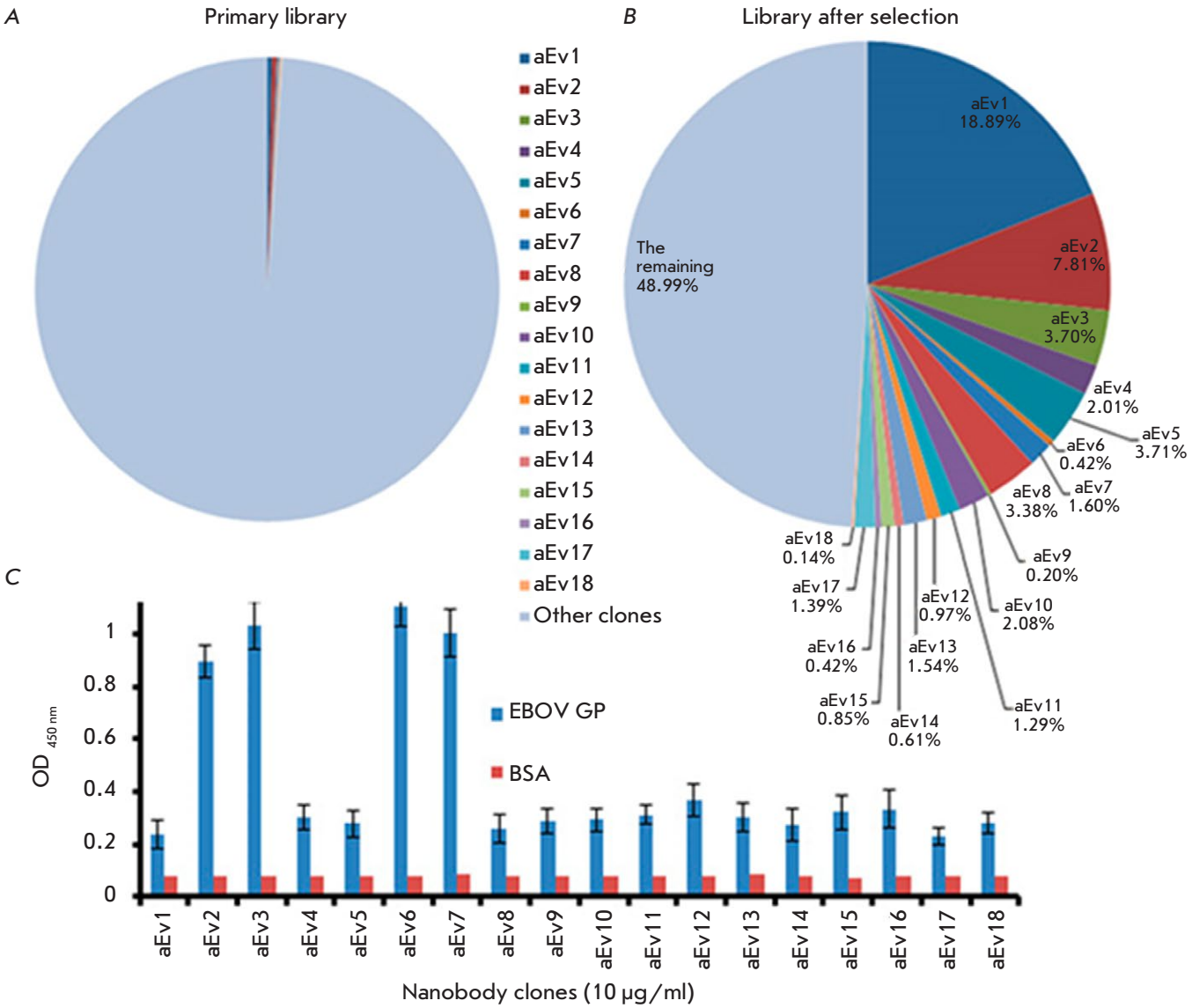

Fig. 2. Comparative analysis of the percentage of nanobodies in the primary library before and after selection. (*A*) – percentage of nanobodies in the primary library. (*B*) – percentage of nanobodies in the library after selection. (*C*) – Screening of 18 nanobody clones by indirect ELISA. aEv1–18 – nanobody clones, EBOV GP – recombinant EBOV GP, BSA – bovine serum albumin (negative control)

SPR (determination of affinity constants, K_D), and virus neutralization assay *in vitro*; the main results are shown in *Fig. 3*.

Indirect ELISA showed the following optimal titers for the clones aEv2, aEv3, aEv7, and aEv6: ⩾ 1 μg/ml, 500 ng/ ml, 500 ng/ ml, and 50 ng/ml, respectively (*Fig. 3A*). Clone aEv6 had the lowest K_D value (1.87×10^{-10} M), followed by clones aEv3 and aEv7: 5.53×10^{-8} and 2.4×10^{-8} M, respectively. Clone aEv2 had the lowest K_D value: 7.13×10^{-7} M. As shown in *Fig. 3B*, aEv2, aEv3, and aEv7 did not exhibit any significant neutralizing activity against rVSV-GP, while aEv6 showed 50% neutralizing activity starting at a concentration of 400 ng/ml. Based on the obtained results, aEv6, which had the highest affinity for EBOV GP and the highest virus-neutralizing potential against rVSV-GP, was selected for further study.

Production of the aEv6 clone modified with the Fc fragment of human IgG1 and analysis of its properties

The selected aEv6 clone was modified with a human IgG1 Fc fragment to improve its immunological and pharmacokinetic properties. The resulting antibody

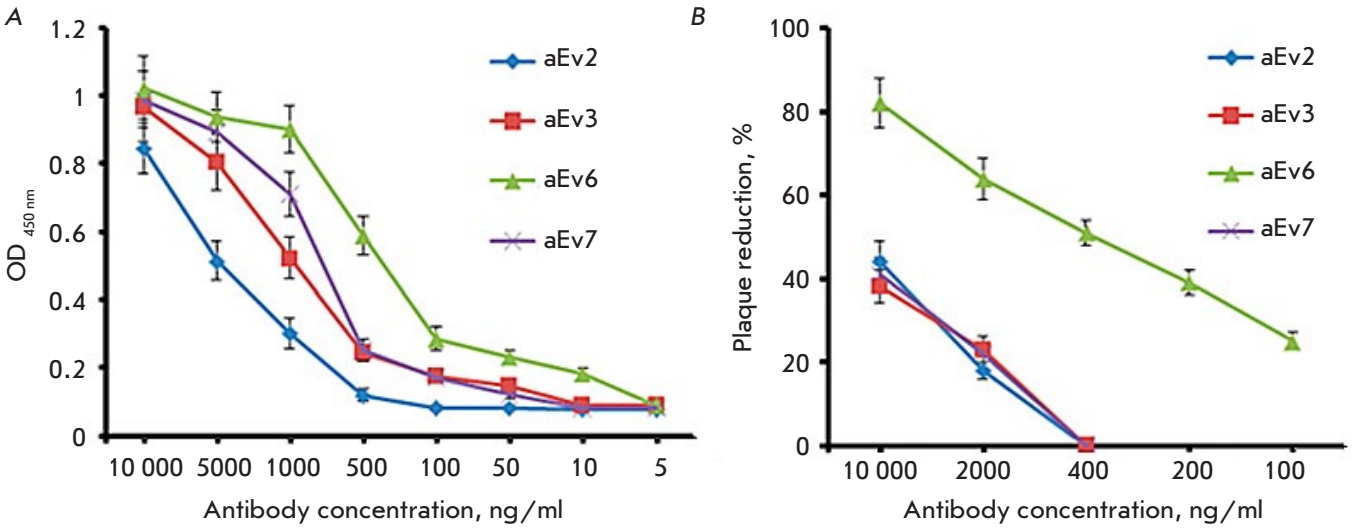

Fig. 3. The activity of the selected nanobody clones evaluated by indirect ELISA (*A*) and the virus-neutralizing activity assessed using rVSV-GP (*B*). (*A*) – High-binding Polystyrene Microtiter plates were coated with 100 µl (1 µg/ml) of EBOV GP (*H. sapiens-wt/GIN/2014/Kissidougou-C15*). On the next day, the wells were washed with 0.1% PBST five times and blocked with 5% non-fat skim milk in PBST. Different dilutions of the nanobodies in blocking buffer were added to the plates and incubated at 37°C for 1 h. The wells were washed five times, and HRP-conjugated Anti-Myc Tag antibodies (Abcam, UK, ab1326) in blocking buffer (1 : 5,000) were added for incubation at 37°C for 1 h. The wells were washed five times, TMB was added, and the results were evaluated. (*B*) – Dilutions of rVSV-GP (*H. sapiens-wt/SLE/2014/Makona-G3735.1*) in buffer (10 mM Tris-HCl, pH 7.5; 1mM EDTA, 10% sucrose) were prepared. A mixture of equal volumes of the nanobodies and virus stocks was incubated at 37°C for 1 h and then transferred to Vero E6 cell monolayers. After cell incubation with the nanobody + virus complex at 37°C for 2 h, the cells were coated with agar. The plates were incubated in 5% CO_2 atmosphere at 37°C for 48 h. The results were evaluated by counting the number of plaques under the microscope. The assay was performed in triplicate. The following formula was used to determine the plaque-forming units (PFU) per milliliter: PFU/ml = (mean PFU count/0.2 ml) × dilution factor

aEv6–Fc showed specific activity against EBOV GP of the *H. sapiens-wt/GIN/2014/Kissidougou-C15* strain, which was similar to the activity of the MAb114 used as a control (*Fig. 4A*).

Then, the virus was neutralized using rVSV-GP to compare the antibodies aEv6–Fc and MAb114. The aEv6–Fc antibody had a significantly higher neutralizing activity than MAb114 (*Fig. 4B*).

The study of the pharmacokinetic properties of aEv6–Fc in rhesus macaques showed that the average circulation time of the antibodies in the blood after injection is at least 7 days (data not shown), which is much higher than that of unmodified low-molecular-weight nanobodies [20, 21].

Evaluation of aEv6–Fc protective activity in a lethal model of murine rVSV-GP infection

At the last stage, the protective effect of aEv6–Fc was evaluated in a lethal rVSV-GP infection model in mice. While the non-human primate model is the most representative, financial and ethical considerations drive the development of new, small animal models [22]. In addition, all studies involving filoviruses require a biosafety level 4 [22]. All of this makes it reasonable to replace the natural Ebola virus with a recombinant analogue that is safer for humans. An example of such an analogue is the recombinant vesicular stomatitis virus pseudotyped with the EBOV GP protein (rVSV-GP). Since rVSV-GP is non-pathogenic in mice, the latter were injected with dexamethasone and cyclophosphamide prior to virus administration to induce immunosuppression [17]. The experiment was performed as follows: five groups of six mice each were selected. All groups were subjected to immunosuppressive therapy for 10 days. After that, the mice of the first group received virus injections, while other groups received virus+antibody injections.

On day 11, mice were injected intravenously with 10^9 PFU of rVSV-GP in both the absence and presence of aEv6–Fc either pre-incubated with the virus at 37°C for 1 h, mixed with the virus immediately before injection, administered intravenously 2 h after infection, or administered intravenously 5 h after

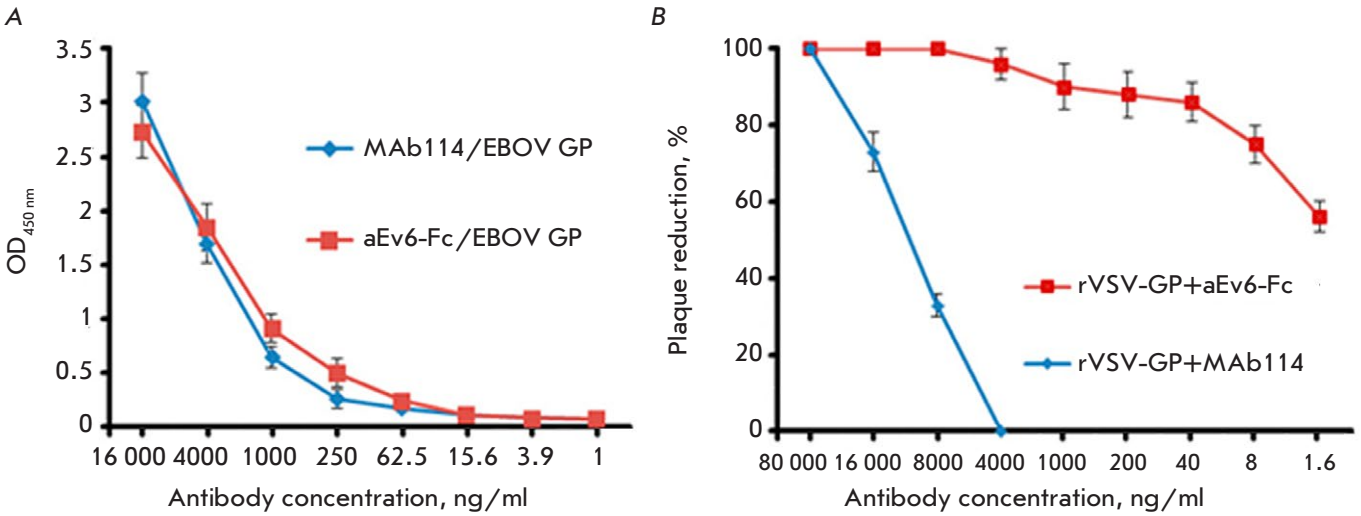

Fig. 4. Comparison of the specific activity of aEv6–Fc and MAb114 against EBOV GP of the *H.sapiens-wt/GIN/2014/Kissidougou-C15* strain (*A*) and the virus-neutralizing activity of aEv6–Fc and MAb114 against rVSV-GP (*B*). (*A*) – High-binding Polystyrene Microtiter plates were coated with 100 µl (1 µg/ml) of EBOV GP (*H. sapiens-wt/GIN/2014/Kissidougou-C15*). On the next day, the wells were washed with 0.1% PBST five times and blocked with 5% non-fat skim milk in PBST. Different dilutions of aEv6–Fc and MAb114 in blocking buffer were added to plates and incubated at 37°C for 1 h. The wells were washed five times, HRP-conjugated Anti-Human IgG antibodies (Sigma, USA) in blocking buffer (1 : 5,000) were added for incubation at 37°C for 1 h. The wells were washed five times, TMB was added, and the results were evaluated. (*B*) – Dilutions of rVSV-GP in buffer (10 mM Tris-HCl, pH 7.5; 1mM EDTA, 10% sucrose) were prepared. A mixture of equal volumes of the antibodies and virus stocks was incubated at 37°C for 1 h and then transferred to Vero E6 cell monolayers. After cell incubation with the antibody + virus complex at 37°C for 2 h, the cells were coated with agar. The plates were incubated in 5% CO_2 atmosphere at 37°C for 48 h. The results were evaluated by counting the number of plaques under the microscope. The assay was performed in triplicate. The following formula was used to determine the plaque-forming units (PFU) per milliliter: PFU/ml = (mean PFU count/0.2 ml) × dilution factor

infection. The experimental scheme is presented in *Fig. 5A*.

The mice were observed for 5 days after infection. The control mice that did not receive aEv6–Fc died on day 2 after infection. Administration of aEv6–Fc 5 h after infection also failed to either prevent or delay animal death. Introduction of antibodies 2 h after infection resulted in the survival of two out of six mice. Pre-incubation and mixing of aEv6–Fc with rVSV-GP fully protected the animals. The experimental results are shown in *Fig. 5B*.

For a more detailed assessment of the protective properties of aEv6–Fc against rVSV-GP in a mouse infection model, PFU was determined in the blood and organs of infected mice. Mice were divided into three groups of four animals each. The first group of immunosuppressed mice remained intact. The mice of the second group were infected with rVSV-GP. The third group was challenged with rVSV-GP that had been previously neutralized with aEv6–Fc (900 µg). The presence of rVSV-GP in the brain, liver, kidney, spleen, intestine, and blood of infected mice was determined using VeroE6 cells 1 and 2 days after. The experiment results are shown in *Table 2*. No signs of viral presence were noted in the tissues and organs of immunosuppressed mice free of the rVSV-GP infection (negative control). The virus was detected in the blood, liver, kidneys, and spleen of the animals in the second group (immunosuppressed mice infected with rVSV-GP) on the first day after its administration. Significantly higher titers of rVSV-GP were observed in the blood and liver on day 2, while no virus was detected in the organs and tissues of mice receiving rVSV-GP + aEv6–Fc injections (group 3).

Thus, experimental data confirm that aEv6–Fc has a virus-neutralizing and protective effect against a lethal rVSV-GP infection in immunosuppressed mice.

DISCUSSION

In this study, the possibility of producing a nanobody fused to the Fc fragment of human IgG1, which has a neutralizing and protective activity against the vesicular stomatitis virus pseudotyped with the GP protein of the Ebola virus, was shown for the first time. In addition, a panel of nanobodies specific to EBOV GP was obtained for the first time by immunizing

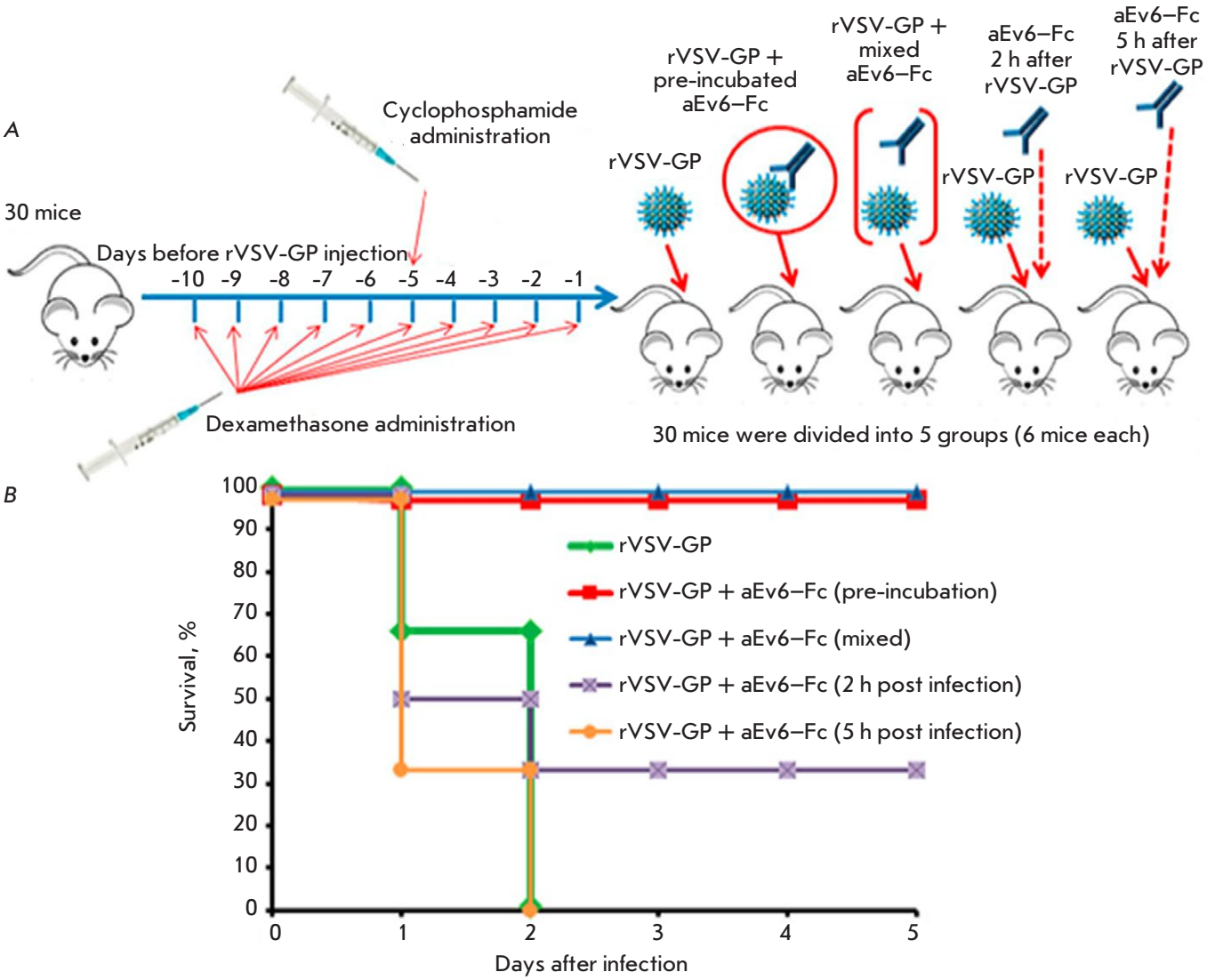

Fig. 5. Protective activity of the aEv6–Fc antibody. Experimental scheme (*A*) and results of the experiment (*B*). (*A*) – rVSV-GP – recombinant live-attenuated vesicular stomatitis virus expressing EBOV GP (*H. sapiens-wt/SLE/2014/Makona-G3735.1*); aEv6–Fc – nanobody clone fused to the human IgG Fc fragment. (*B*) – rVSV-GP – mice challenged with rVSV-GP (10^9 PFU/mice); rVSV-GP+aEv6–Fc (pre-incubation) – mice receiving rVSV-GP (10^9 PFU/mice) that has been previously mixed and incubated with 300 µl of aEv6–Fc (3 mg/ml); rVSV-GP+aEv6–Fc (mixed) – mice injected with rVSV-GP (10^9 PFU/mice) that has been previously mixed with 300 µl of aEv6–Fc (3 mg/ml); rVSV-GP+aEv6–Fc (2 h post infection) – mice challenged with rVSV-GP (10^9 PFU/mice) and treated with 300 µl of aEv6–Fc (3 mg/ml) after 2 h; rVSV-GP+aEv6–Fc (5 h post infection) – mice receiving rVSV-GP (10^9 PFU/mice) and treated with 300 µl of aEv6–Fc (3 mg/ml) after 5 h

Table 2. Titers of rVSV-GP in the organs of infected mice

Group	Day after injection	Average rVSV-GP titers (two mice), PFU/20 µg of organ					
		blood	brain	liver	kidney	spleen	intestine
Intact immunosuppressed mice	1	–	–	–	–	–	–
	2	–	–	–	–	–	–
Immunosuppressed mice infected with rVSV-GP	1	4.44×10^5	–	6.67×10^4	4.14×10^4	3.65×10^4	–
	2	1.7×10^7	–	1.27×10^5	2.44×10^4	3.44×10^4	–
Immunosuppressed mice receiving rVSV-GP+aEv6–Fc	1	–	–	–	–	–	–
	2	–	–	–	–	–	–

Table 3. Immunogenic characteristics of the clones aEv2, aEv3, aEv6, and aEv7

Clone	Titers for EBOV GP, ng/ml	Affinity constant (K_D) for EBOV GP, M	Virus-neutralizing activity against rVSV-GP (PRNT50)
aEv2	⩾ 1,000	7.13×10^{-7}	No virus-neutralizing activity
aEv3	⩾ 500	5.53×10^{-8}	⩾ 400 ng/ml
aEv6	⩾ 50	1.87×10^{-10}	No virus-neutralizing activity
aEv7	⩾ 500	2.4×10^{-8}	No virus-neutralizing activity

alpaca with the recombinant adenovirus Ad5-GP. This immunization strategy has previously been used successfully to obtain monoclonal antibodies with a protective activity against the Ebola virus [9]. Thus, four nanobody clones (aEv2, aEv3, aEv6, and aEv7) were obtained; their characteristics are presented in *Table 3*.

Our analysis of the data presented in *Table 3* allows us to conclude that the results of three independent experiments completely correlated with each other. Based on the data we obtained, the aEv6 clone showed both the highest affinity for EBOV GP and virus-neutralizing activity against rVSV-GP. Therefore, this clone was selected for further study.

The aEv6 clone was further modified with the human IgG1 Fc fragment, resulting in a 40–45 kDa nanobody; the Fc fragment dimerizes the molecule and enables its interaction with the Fc receptors on the cell surface [21]. This modification increased the circulation duration of the aEv6–Fc antibody in the blood of non-human primates for up to 7 days, considering that the circulation of primary nanobodies usually lasts only several hours [20, 23, 24]. We used non-human primates, because their immune system and Fc receptors are highly homologous to those in humans. Improving antibody pharmacokinetics is an important aspect that can significantly reduce the dose and number of drug injections in the treatment of viral diseases. ELISA showed that the modified antibody aEv6–Fc had specific activity similar to that of MAb114 (*Fig. 4A*), which has a protective activity against the Ebola virus [25], and a stronger virus-neutralizing activity than both MAb114 and an unmodified antibody lacking the Fc fragment (*Fig. 4B*).

The last stage of the study was the assessment of the protective activity of aEv6–Fc in a mouse model of lethal infection with the vesicular stomatitis virus pseudotyped with EBOV GP. We developed this model to avoid the need for a wild-type Ebola virus and non-human primates in the study (due to the high cost and ethical considerations [22]). The drug dose (50 mg/kg) was selected based on published data [25]. Our experiments have shown that aEv6–Fc completely protects mice from infection when either pre-incubated or mixed with the virus prior to injection and, in our case, had a 30%-protection level when administered no later than 2 h after infection with the virus. Thus, aEv6–Fc can be used as a protective agent for both prevention and treatment immediately after suspected contact with the pathogen. A detailed analysis of rVSV-GP accumulation in the organs and tissues of the infected mice revealed the highest virus titer in the blood, liver, kidneys, and spleen, while no rVSV-GP was found in the brain and intestine. The obtained results may have to do with the pseudotyping of the vesicular stomatitis virus with EBOV GP, which apparently alters the tropism of the virus. Changes in rVSV tropism, in turn, may explain the virus accumulation in the kidneys, spleen, and especially in the liver and blood, which apparently causes multiple organ failure and animal death on the second day of infection. It is important to note that no virus was found in the organs and tissues of mice infected with rVSV-GP pre-incubated with aEv6–Fc, which once again confirms the virus-neutralizing and protective capacity of the antibody.

CONCLUSION

In this study, the possibility of producing nanobodies and modified derivatives from them specific to the Ebola virus surface glycoprotein and exhibiting strong antiviral activity in a lethal model of mice infected with a pseudotyped vesicular stomatitis virus was shown for the first time. ●

We thank A.I. Smirnov (owner of the Russian Alpaca Farm) for providing alpacas for our study.

REFERENCES

1. Siragam V., Wong G., Qiu X. // Zool. Res. 2018. V. 39. № 1. P. 15–24.
2. Zhu W., Banadyga L., Emeterio K., Wong G., Qiu X. // Viruses. 2019. V. 11. № 11. e999.
3. Qiu X., Fernando L., Melito P.L., Audet J., Feldmann H.,

Kobinger G., Alimonti J.B., Jones S.M. // PLoS Neglected Tropical Diseases. 2012. V. 6. № 3. e1575
4. Qiu X., Audet J., Wong G., Pillet S., Bello A., Cabral T., Strong J.E., Plummer F., Corbett C.R., Alimonti J.B., et al. // Sci. Transl. Med. 2012. V. 4. № 138. P. 138ra81.
5. ECDC. Ebola outbreak in the Democratic Republic of the Congo – ongoing. URL: https://ecdc.europa.eu/en/ebola-virus-disease-outbreak-democratic-republic-congo-ongoing (accessed August 9, 2019).
6. Moekotte A.L., Huson M.A., van der Ende A.J., Agnandji S.T., Huizenga E., Goorhuis A., Grobusch M.P. // Expert Opin. Investigat. Drugs. 2016. V. 25. № 11. P 1325–1335.
7. Corti D., Misasi J., Mulangu S., Stanley D.A., Kanekiyo M., Wollen S., Ploquin A., Doria-Rose N.A., Staupe R.P., Bailey M., et al. // Science. 2016. V. 351. P. 1339–1342. Suppl. Materials.
8. Hoenen T., Groseth A., Feldmann H. // Nat. Rev. Microbiol. 2019. V. 17. № 10. P. 593–606.
9. Shcheblyakov D., Esmagambetov I., Simakin P., Kostina L., Kozlov A., Tsibezov V., Grebennikova T., Chifanov D., Rumyantseva I., Boyarskaya N., et al. // Antiviral Res. 2019. V. 172. e104617.
10. Dolzhikova I.V., Zubkova O.V., Tukhvatulin A.I., Dzharullaeva A.S., Tukhvatulina N.M., Shcheblyakov D.V., Shmarov M., Tokarskaya E., Simakova Y., Egorova D., et al. // Human Vaccines Immunotherapeutics. 2017. V. 13. № 3. P. 613–620.
11. Wu Y., Jiang S., Ying T. // Front. Immunol. 2017. V. 8. P. e1802.
12. De Vlieger D., Ballegeer M., Rossey I., Schepens B., Saelens X. // Antibodies (Basel). 2018. V. 8. № 1. e1.
13. Liu J.L., Shriver-Lake L.C, Anderson G.P., Zabetakis D., Goldman E.R. // Microbial Cell Factories. 2017. V. 16. № 1. e223.
14. Darling T.L., Sherwood L.J., Hayhurst A. // Front. Immunol. 2017. V. 8. e1197.
15. Sherwood L.J., Hayhurst A. // PLoS One. 2013. V. 8. № 4. e61232.
16. Brunton B., Rogers K., Phillips E.K., Brouillette R.B., Bouls R., Butler N.S., Maury W. // PLoS Neglected Tropical Diseases. 2019. V. 13. № 6. e0006983.
17. Marathe B.M., Mostafa H.H., Vogel P., Pascua P.N.Q., Jones J.C., Russell C.J., Webby R.J., Govorkova E.A. // Antiviral Res. 2017. V. 148. P. 20–31.
18. Shcherbinin D.N., Esmagambetov I.B., Noskov A.N., Selyaninov Y.O., Tutykhina I.L., Shmarov M.M., Logunov D.Yu., Naroditsky B.S., Gintsburg A.L., et al. // Acta Naturae. 2014. V. 6. № 1. P. 76–84.
19. Godakova S.A., Noskov A.N., Vinogradova I.D., Ugriumova G.A., Solovyev A.I., Esmagambetov I.B., Tukhvatulin A.I., Logunov D.Y., Naroditsky B.S., Shcheblyakov D.V. // Toxins (Basel). 2019. V. 11. № 8. e464.
20. Cortez-Retamozo V., Lauwereys M., Hassanzadeh Gh.G., Gobert M., Conrath K., Muyldermans S., De Baetselier P., Revets H. // Internat. J. Cancer. 2002. V. 98. № 3. P. 456–462.
21. Harmsen M.M., van Solt C.B., Fijten H.P., van Setten M.C. // Vaccine. 2005. V. 23. № 41. P. 4926–4934.
22. St Claire M., Ragland D., Bollinger L., Jahrling P. // Comp. Med. 2017. V. 67. № 3. P. 253–262.
23. Huston J.S., George A.J., Adams G.P., Stafford W.F., Jamar F., Tai M.S., McCartney J.E., Oppermann H., Heelan B.T., Peters A.M., et. al. // Quarterly J. Nucl. Med. Mol. Imaging. 1996. V. 40. P. 320–333.
24. Batra S.K., Jain M., Wittel U.A., Chauhan S.C., Colcher D. // Curr. Opin. Biotechnol. 2002. V. 13. P. 603–608.
25. WHO. WHO R&D Blueprint – Ad-hoc Expert Consultation on clinical trials for Ebola Therapeutics. Appendix 4. URL: https://www.who.int/ebola/drc-2018/treatments-approved-for-compassionate-use-update/en/ (accessed January, 2020).

Circulating Actin-Binding Proteins in Laryngeal Cancer: Its Relationship with Circulating Tumor Cells and Cells of the Immune System

G. V. Kakurina*, M. N. Stakheeva, I. A. Bakhronov, E. E. Sereda, O. V. Cheremisina, E. L. Choynzonov, I. V. Kondakova
Cancer Research Institute, Tomsk National Research Medical Center, Russian Academy of Sciences, Tomsk, 634050 Russia
*E-mail: kakurinagv@oncology.tomsk.ru
Received April 13, 2021; in final form, July 30, 2021
DOI: 10.32607/actanaturae.11413

ABSTRACT **We previously exposed the role of actin-binding proteins (ABPs) in cancer development and progression. In this paper, we studied the relationship between circulating ABPs and the number of ABP-expressing leukocytes and circulating tumor cells (CTCs) in patients with highly aggressive laryngeal squamous cell carcinoma (LSCC). The levels of cofilin (CFL1), profilin (PFN1), ezrin (EZR), fascin (FSCN1), and adenylate cyclase-associated protein 1 (CAP1) were determined using enzyme immunoassay. The ABP expression by the cellular pools was analyzed by flow cytometry. The highest levels of FSCN1 and EZR were found in the blood serum of LSCC patients. There was a difference in ABP expression between the pools of leukocytes and CTCs. Leukocytes were mainly represented by CAP1+ and FSCN1+ pools, and CTCs contained CAP1+, FSCN1+, and EZR+ cells. The serum FSCN1 level correlated with the number of FSCN1-containing and CFL1-containing leukocytes. Thus, the level of circulating EZR is likely related to its expression in CTCs. The levels of CFL1 and PFN1 are likely to be supported by the expression of these proteins by leukocytes. Both CTCs and leukocytes can be a source of FSCN1 and CAP1 in blood serum. The results suggest that serum proteins can be produced by various cells, thus indicating both cancer development and the response of the immune system to this process.**
KEYWORDS **actin-binding proteins, circulating tumor cells, leukocytes, laryngeal squamous cell carcinoma.**
ABBREVIATIONS **LSCC – laryngeal squamous cell carcinoma; ABPs – actin-binding proteins; CTCs – circulating tumor cells; CAP1 – adenylyl cyclase-associated protein 1; CFL1 – cofilin; PFN1 – profilin 1; EZR – ezrin; FSCN1 – fascin.**

INTRODUCTION

Metastases are considered to be the major cause of death in cancer patients. It is important to study metastasis-related biological processes in order to attempt to identify prognostic markers of tumor progression [1]. Research focusing on blood serum/plasma proteome profiling of cancer patients using mass spectrometry is ongoing. Laryngeal squamous cell cancer (LSCC) is one of the aggressive cancers, which makes it a good model for studying the metastasis mechanisms [2–4]. Earlier, we uncovered the differences in the blood serum proteome of LSCC patients and healthy volunteers, as well as the correlation between several functionally different proteins (including actin-binding protein CAP1 (adenylyl cyclase-associated protein 1)) [4] and metastases of LSCC. Actin-binding proteins (ABPs) coordinate the rearrangement of the actin cytoskeleton, which is closely linked to metastasis development. The ABP level in tumors has been investigated rather thoroughly [5–7], while systemic circulating ABPs (cABPs) have been insufficiently studied. Previously, the serum levels of CAP1, profilin 1, and fascin 1 in T3-4N0–1M0 LSCC patients were found to differ from those in patients with T1N0M0 LSCC [8]. It is possible that the cABP level in systemic circulation can be maintained by several sources, including immune circulating tumor cells (CTCs). The correlation between cABPs and their potential cellular sources in systemic circulation is virtually unstudied. Therefore, in this work, the serum level of cABP was compared to cABP expression in populations of leukocytes and CTCs in systemic circulation in order to

identify any relationship between these parameters. Peripheral blood samples from LSCC patients were used as a model of aggressive cancer with a high probability of metastasis.

EXPERIMENTAL

Material and characterization of patient groups

The study involved 13 LSCC patients (stage T2-4N0-2M0) (four patients, T2-4N0M0; nine patients, T2-4N1-2M0) with a morphologically verified diagnosis, who were not receiving antitumor therapy. The patients' mean age was 57 (52–63) years. Blood serum for ELISA was collected in accordance with an approved protocol and stored at -80°C. Freshly collected blood samples were used for flow cytometry. All the manipulations were conducted after the patients had provided informed consent, and patients' confidentiality was maintained in compliance with the World Medical Association's Declaration of Helsinki "Ethical Principles for Medical Research Involving Human Subjects" (as amended in 2000). The study was approved by the Ethics Committee of the Cancer Research Institute, Tomsk National Research Medical Center. All study subjects had signed informed consent forms.

Study methods

The analysis of cABPs in peripheral blood was performed by enzyme-linked immunosorbent assay on a Multiscan FC microplate reader (Thermo Fisher Scientific, USA) according to the instructions in the kit. The following ELISA kits (Cloud-Clone Corp.) were used: CAP1 (SEB349Hu), PFN1 (SEC233Hu), CFL1 (SEB559Hu), FSCN1 (EB757Hu), and EZR (SEB297Hu).

ABP expression in leukocytes and CTCs was analyzed by flow cytometry on a BD FACS Canto II cytometer (BD, USA). The total leukocyte pool and CTC populations were identified using blood cell labeling with the specific fluorescent tags CD45 (AF700 (BD)) and EpCAM (PerCPCy5.5 (BD)), respectively. ABP expression in the cell pools was assessed using AF488-conjugated mouse monoclonal antibodies against human ezrin (pY353) (BD); APC-conjugated rabbit polyclonal antibodies against human CFL1 (Cloud-Clone Corp); AF647-conjugated rabbit polyclonal antibodies against human PFL1 (Cloud-Clone Corp); PE-conjugated rabbit polyclonal antibodies against human FSCN1 (Biorbyt); unconjugated rabbit monoclonal antibodies against human CAP1 (Abcam, UK); and goat anti-rabbit antibodies conjugated to AF488 (Abcam) as secondary anti-CAP1 antibodies. The gating strategy involved the separation of blood cells into CD45+ cells (leukocytes) and CD45- cells. Gates of CAP1+, EZR+, PFL1+, CFL1+, and FSCN1+ cells were isolated from the gate of CD45+ leukocytes, and their percentage in the total leukocyte pool was determined. CD326 (EpCAM)+ cells were isolated from the gate of CD45- cells by regarding them as circulating tumor cells; the aforelisted populations were sequentially isolated from CTCs CD326 (EpCAM)+, and their percentage in the pool of CTCs was assessed. The results were presented as a percentage of CD45+ and EpCAM+ cells expressing these ABPs.

Statistical analysis

The data were analyzed using the IBM SPSS Statistics 22.0 software. The existence of correlation and its strength were evaluated using the Spearman's rank correlation coefficient (r). The results were presented as Me (Q1; Q3), where Me is the median value; Q1 and Q3 are the upper and lower quartiles, respectively. Differences at $p \leqslant 0.05$ were considered statistically significant.

RESULTS AND DISCUSSION

We determined the serum levels of cABP in LSCC patients by ELISA. The FSCN1 and EZR levels were the highest: the median levels were 1.8 (0.43–8.1) and 2.1 (1.69–2.56) ng/mL, respectively. The CAP1 level was the lowest (median value = 0.11 (0.08–1.15)), followed by the levels of PFN1 and CFL1 (median values: 0.28 (0.23–0.38) and 0.78 (0.63–1.14) ng/mL, respectively). *Figure 1* shows the dispersion of the serum levels of each protein in LSSC patients.

The ABP levels in the pools of CTCs (CD45-CD326+) and leukocytes (CD45+CD326-) in the whole blood of LSCC patients were then determined. It was shown for the presented sample of LSCC patients that the median level of CTCs CD45-CD326+ was 0.006 (0.00–0.1) % of all cellular components of the blood (per 50,000 blood cells). Differences in the relative content of all ABPs in the populations of CD45-CD326+ CTCs and CD45+ leukocytes were revealed (*Figs. 2, 3*).

Table shows the relative number of CD45-CD326+ CTCs and CD45+ leukocytes expressing ABPs in LSCC patients. CD45-CD326+ CTCs in LSCC patients predominantly consist of FSCN1+ and CAP1+ subpopulations whose median percentage was 91.8 (87.2–100) % and 87.0 (61.5–100) %, respectively. The percentage of CD45-CD326+ CTCs expressing PFN1 and CFL1 was reduced: 0.2 (0.0–0.5) % and 0.3 (0.0–0.5) %, respectively. The population of CD45+ leukocytes is mainly represented by CAP1+ and FSCN1+ cells: 45.3 (4.6–55.3) % and 34.5 (31.3–72.1) %, respectively. The percentage of the EZR+ CD45+ leukocyte subpopula-

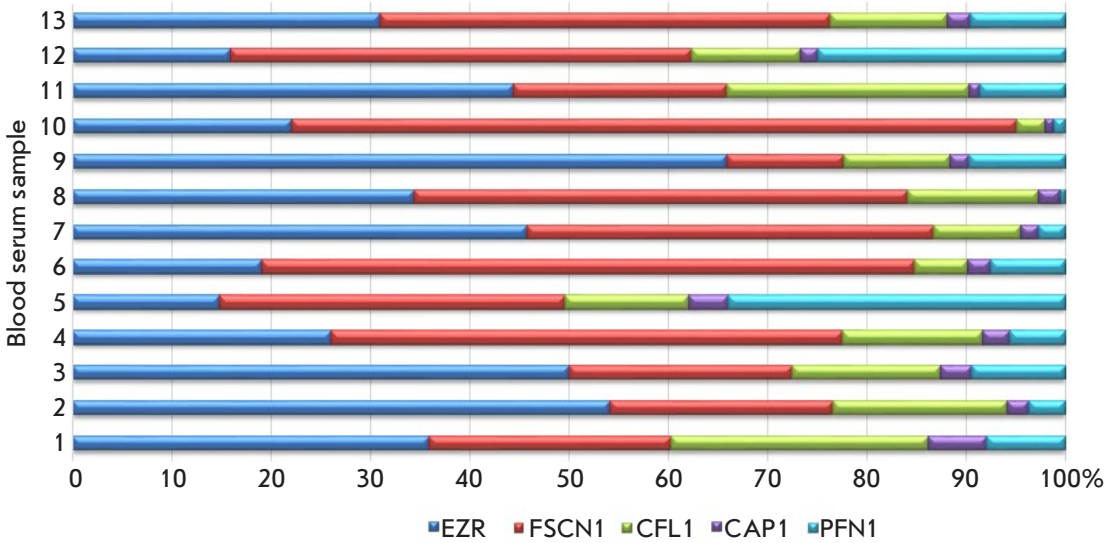

Fig. 1. The serum levels of circulating actin-binding proteins in LSCC patients. The Y axis shows patients with LSCC, and the X axis shows the percentage concentration of serum ABPs, % of the total cABP content (assumed to be 100%)

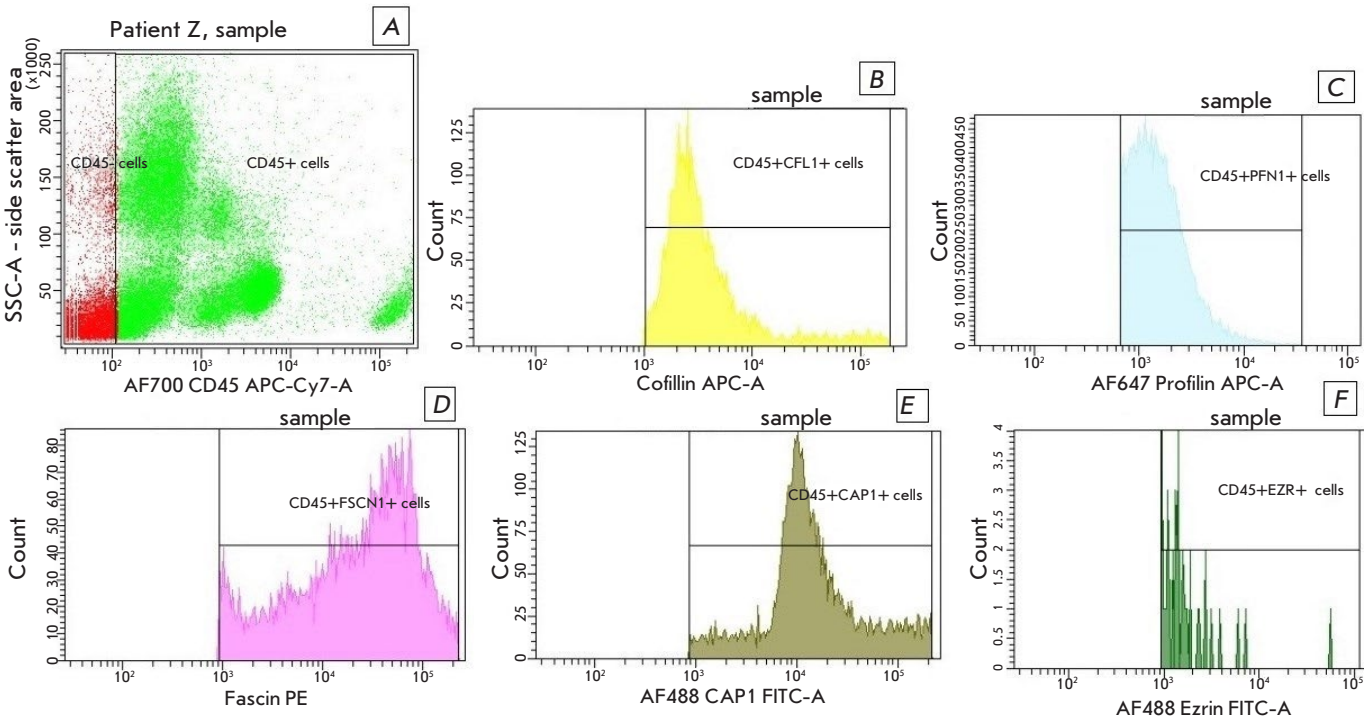

Fig. 2. The relative number of CD45+ cells expressing actin-binding proteins in patients with laryngeal cancer. (*A*) – Gates of CD45- and CD45+ peripheral blood cells. Histograms representing the content of actin-binding proteins in CD45+ cells are shown in the figures: (*B*) – the count of CD45+ cells containing CFL1; (*C*) – the count of PFN1-containing CD45+ cells; (*D*) – the count of FSCN1-containing CD45+ cells; (*E*) – the count of CAP1-expressing and (*F*) – the count of EZR-containing CD45+ cells

tion was reduced (0.3 (0.14–0.91) %). EZR was mainly expressed by CTCs (51.5 (39.3–85.4) %).

An analysis of the correlations between the cABP level and the number of cell subpopulations expressing the respective protein revealed medium-strength correlations. Thus, the level of circulating FSCN1 correlated with the percentage of FSCN+ and CFL1+ subpopulations of CD45+ leukocytes (r = 0.7; p = 0.03). Correlations between the analyzed pools expressing ABPs were also revealed in the blood circulation of LSSC patients. The pool of CD45-CD326+ leukocytes containing FSCN+ was found to negatively

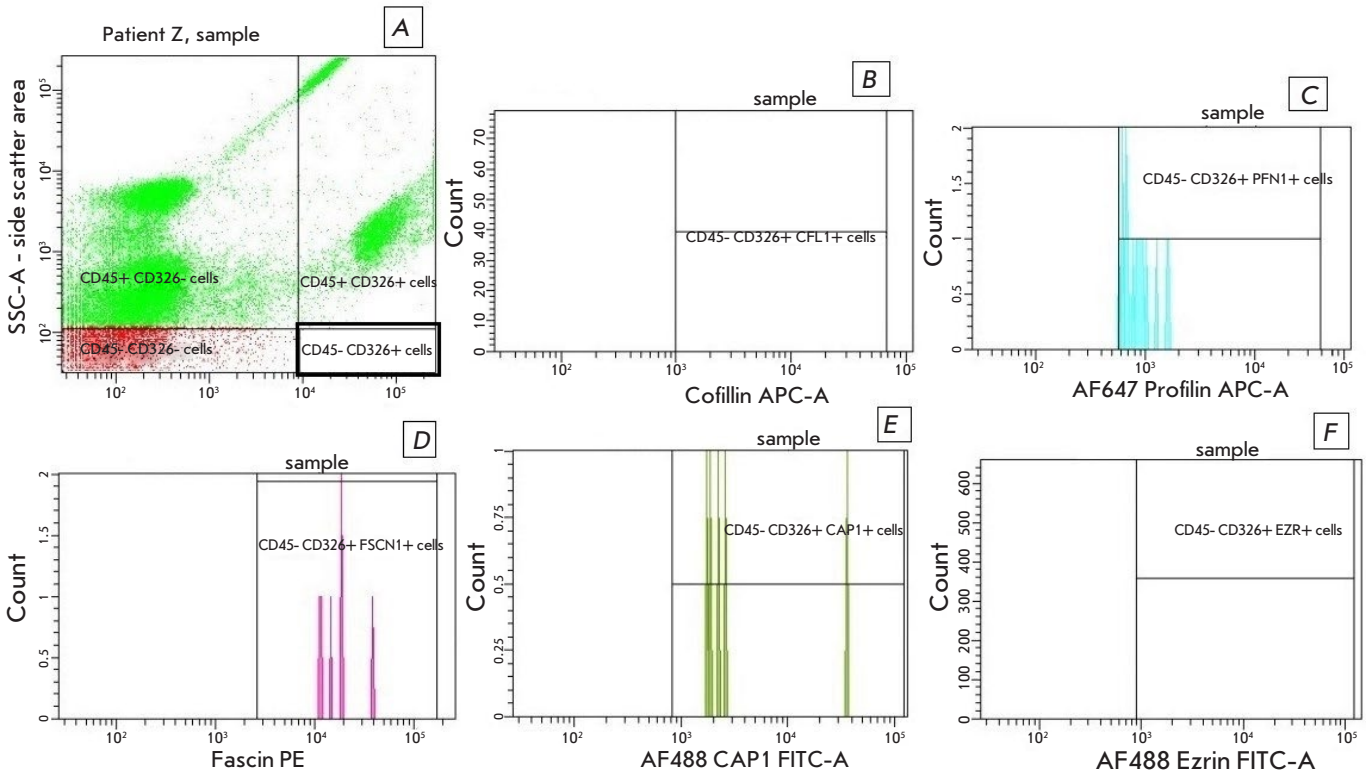

Fig. 3. The relative number of circulating tumor cells (CD45-CD326+) containing actin-binding proteins in peripheral blood in patients with laryngeal cancer. (*A*) – Gate of CD45-CD326+ cells (CSCs) in peripheral blood. Histograms showing the contents of actin-binding proteins in CTCs are shown in the figures: (*B*) – the level of CTCs containing CFL1; (*C*) – the level of PFN1-containing CSCs; (*D*) – the level of fascin-containing CTCs; (*E*) – the level of CAP1-expressing; and (*F*) – the level of EZR-containing CTCs

correlate with CD45+ leukocytes containing FSCN+ (r= -0.7; p = 0.01) and CFL1+ (r = -0.7; p = 0.03). A positive correlation was revealed between CAP1+ CD326+ and CAP1+ CD45+ (r = 0.7; p = 0.02). A correlation between EZR+ and CFL1+ CD45+ leukocytes was revealed at the level of the leukocyte pool.

This study showed that the levels of the FSCN1 and EZR proteins in the systemic circulation of LSCC patients were higher compared to the levels of other cABPs. Peripheral blood leukocytes and CTCs were found to differ in ABP expression. A correlation between the serum level of FSCN1 and the percentage of FSCN+ and CFL1+ CD45+ leukocytes was revealed. CAP1 and FSCN1 expressions were increased in both cell populations. However, significant differences in the levels of these proteins in CTCs and leukocytes were detected. Whereas almost all CTCs contained CAP1 and FSCN1, the percentages of CAP1+ and FSCN1+ leukocytes were lower by two- and threefold, respectively. The population of CD45+ leukocytes had almost no EZR+ cells, while the percentage of EZR+ CD326+ was 51.5% of the pool of CTCs. CFL1 and PFN1 were found in leukocytes but

The serum level of actin-binding proteins (ABPs), the relative number of CD45-CD326+ circulating tumor cells and CD45+ leukocytes expressing actin-binding proteins in patients with laryngeal squamous cell carcinoma

cABP	Leukocytes, CD45+, %	CTCs, CD45-CD326+, %	Blood serum, ng/mL
EZR	0.6 (0.3–1.0)	51.5 (39.3–85.4)	1.2 (0.9–1.7)
FSCN1	34.5 (31.3–72.1)	91.8 (87.2–100)	1.5 (0.8–2.2)
CFL1	12.0 (8.5–39.1)	0.3 (0.0–0.5)	0.5 (0.3–0.6)
CAP1	45.3 (4.6–55.3)	87.0 (61.5–100)	0.10 (0.06–0.14)
PFN1	5.7 (4.0–13.2)	0.2 (0.0–0.5)	0.2 (0.1–0.4)

were almost totally absent in CTCs. Therefore, the tumor cells circulating in the bloodstream of LSCC patients can express several ABPs: EZR, CAP1, and FSCN1.

By comparing the flow cytometry and ELISA data, one can suggest that the presence of EZR in the blood

flow is associated with its presence in CTCs. The level of CFL1 and PFN1 circulating in the blood is probably maintained by the expression of these proteins by leukocytes. The serum level of FSCN1 and CAP1 can be related both to CTCs and to leukocytes.

The involvement of ABPs in the pathogenesis of cancer has been, for the most part, studied based on the results of a determination of their tissue levels [7, 9, 10]. It has been suggested that the fascin levels in the tissues of head and neck tumors can be used as prognostic markers of tumors of this localization [https://www.proteinatlas.org; 11]. The results of the study of ABPs in neoplasm tissues (tumor cells being the most plausible and the main source of these proteins) have been reported. The role played by cABPs in patients with pathological conditions, including cancer, has been very poorly studied. For example, it has been shown that extracellular gelsolin (pGSN) cleaves actin, which can be released upon cell injury [12]. The ABPs studied in this publication also may be functionally active in blood serum, which can become the subject of further research.

CONCLUSIONS

Data on a correlation between functionally different systemically circulating ABPs and populations of CTCs and immune cells expressing the respective proteins in patients with laryngeal cancer were obtained for the first time in this study. The revealed correlations and differences in the ABP level in CTCs and leukocytes can be attributed both to the specificity of a tumor of this localization and/or be indicative of the body's overall immune response to tumor growth. To draw any definitive conclusions, the research needs to be continued, with a larger number of LSCC patients and an assessment of additional clinical and morphological parameters. ●

This work was supported by the Russian Foundation for Basic Research (grant No. 20-015-00151).

REFERENCES

1. Gaponova A.V., Rodin S., Mazina A.A., Volchkov P.V. // Acta Naturae. 2020. V. 12. № 3(46). P. 4–23. doi: 10.32607/actanaturae.11010
2. Bhawal R., Oberg A.L., Zhang S., Kohli M. // Cancers (Basel). 2020. V. 12. № 9. P. 2428. doi:10.3390/cancers12092428
3. Gasparri R., Sedda G., Noberini R., Bonaldi T., Spaggiari L. // Proteomics Clin. Appl. 2020. V. 14. № 5. P. 1900138. doi: 10.1002/prca.201900138
4. Kakurina G.V., Kondakova I.V., Cheremisina O.V., Shishkin D.A., Choinzonov E.L.// Bull Exp Biol Med. 2015. V. 160. № 11. P. 648–651.
5. Gross S.R. // Cell Adh Migr. 2013. V. 7. № 2. P. 199–213. doi: 10.4161/cam.23176
6. Liu H., Cui J., Zhang Y., Niu M., Xue X., Yin H., Tang Y., Dai L., Dai F., Guo Y., et al.// IUBMB Life. 2019. V. 71. № 11. P. 1771–1784. doi: 10.1002/iub.2121
7. Kakurina G.V., Kolegova E.S., Kondakova I.V. // Biochemistry (Moscow). 2018. V. 83. № 1. P. 45–53.
8. Kakurina G.V., Shashova E.E., Cheremisina O.V., Choinzonov E.L., Kondakova I.V. // Siberian Journal of Oncology. 2020. V. 19. № 4. P. 88–93.
9. Coumans J.V.F., Davey R.J., Moens P.D.J. // Biophys. Rev. 2018. V. 10. № 5. P. 1323–1335.
10. Izdebska M., Zielińska W., Grzanka D., Gagat M. // BioMed. Res. Int. 2018. V. 2018. P. 4578373. doi: 10.1155/2018/4578373
11. Papaspyrou K., Brochhausen C., Schmidtmann I., Fruth K., Gouveris H., Kirckpatrick J., Mann W., Brieger J.// Oncol Lett. 2014. V. 7(6). P. 2041–2046.
12. Piktel E., Levental I., Durnaś B., Janmey P.A., Bucki R. // Int. J. Mol. Sci. 2018. V. 19. № 9. P. 2516.

The Different Impact of ERK Inhibition on Neuroblastoma, Astrocytoma, and Rhabdomyosarcoma Cell Differentiation

T. D. Lebedev*, E. R. Vagapova, V. S. Prassolov
Engelhardt Institute of Molecular Biology, Russian Academy of Sciences, Moscow, 119991 Russia
*E-mail: lebedevtd@gmail.com
Received May 24, 2021; in final form, August 02, 2021
DOI: 10.32607/actanaturae.11461

ABSTRACT **Aberrant ERK activity can lead to uncontrolled cell proliferation, immortalization, and impaired cell differentiation. Impairment of normal cell differentiation is one of the critical stages in malignant cell transformation. In this study, we investigated a relationship between ERK tyrosine kinase activity and the main differentiation features (changes in cell morphology and expression of genes encoding differentiation markers and growth factor receptors) in SH-SY5Y neuroblastoma, U-251 astrocytoma, and TE-671 rhabdomyosarcoma cells. ERK activity was assessed using a reporter system that enabled live measurements of ERK activity in single cells. We demonstrated that suppression of ERK activity by selective ERK inhibitors, in contrast to a commonly used differentiation inducer, retinoic acid, leads to significant changes in TE-671 cell morphology and expression of the myogenic differentiation marker genes *PROM1*, *MYOG*, and *PAX7*. There was a relationship between ERK activity and morphological changes at an individual cell level. In this case, SH-SY5Y cell differentiation induced by retinoic acid was ERK-independent. We showed that ERK inhibition increases the sensitivity of TE-671 cells to the EGF, IGF-1, and NGF growth factors, presumably by reducing basal ERK activity, and to the BDNF growth factor, by increasing expression of the TrkB receptor.**
KEYWORDS **cell differentiation, malignant tumors, ERK inhibitors, growth factors, fluorescent reporter.**
ABBREVIATIONS **ATRA – *all-trans* retinoic acid (tretinoin); ERK – extracellular signal-regulated kinase; NGF – nerve growth factor; BDNF – brain-derived neurothropic factor; EGF – epidermal growth factor; IGF-1 – insulin-like growth factor 1; EGFR – epidermal growth factor receptor; IGF1R – insulin-like growth factor 1 receptor; TrkA – tropomyosin receptor kinase A; TrkB – tropomyosin receptor kinase B; MYOG – myogenin; FBS – fetal bovine serum.**

INTRODUCTION

Extracellular signal-regulated kinases 1/2 (ERK1/2) play a key role in important processes such as cell proliferation, survival, and differentiation [1, 2]. In this case, the effect of ERK activation on these processes often depends on the cell type, activation signal and its duration, and the dynamics of ERK activity, which significantly complicates the identification of the specific role of ERK in cellular processes. Usually, ERK activation is associated with cell survival and proliferation signals [3]. However, depending on the cell type, ERK inhibition can both stimulate and prevent cell death [4].

The emergence of various reporter systems to monitor ERK activity in living cells has stimulated research in this area [5–9]. However, there is no generally accepted model describing the effect of ERK on cell differentiation. ERK is known to directly inhibit the activity of pluripotency-associated transcription factors, such as NANOG, OCT4, KLF2, and KLF4 [10, 11]. Downregulation of ERK activity, e.g., by MEK inhibitors, stimulates the self-renewal of embryonic stem cells via the inhibition of ERK-dependent differentiation [12]. However, in some cases, ERK inhibition stimulates cell differentiation, in particular in neuroectoderm cells or bone marrow mesenchymal stem cells [13, 14]. Many growth factors, such as FGF, NGF, PDGF, BDNF, EGF, and IGF-1, play an important role in cell differentiation [15, 16]. Certain growth factors controlling survival of differentiated cells are often essential in the late stages of differentiation. In this case, many growth factors act through ERK activation. Therefore, ERK activation can differently affect differentiation, depending on the stage and cell type.

ERK activity is upregulated in most malignant tumors, in particular due to activating mutations in the MAPK signaling cascade. In this case, activating mutations in the *RAS* genes inhibit epidermal

cell differentiation [17–19]. Investigation of malignant cell differentiation is required to understand malignant cell transformation and develop approaches to tumor therapy. For example, approaches based on retinoic acid-stimulated cell differentiation are used in the therapy of neuroblastomas [20] and some types of leukemia [21]. In addition, inhibition of the RAS-MEK-ERK signaling cascade is considered a promising approach to the treatment of rhabdomyosarcomas, astrocytomas, and neuroblastomas [22–24].

When testing the effectiveness of ERK inhibitors in various cells, we noticed morphological changes in some cell types, which were similar to the changes associated with differentiation. In this study, we used a reporter system enabling measurements of ERK activity in live single cells to quantify the relationship between ERK activity and differentiation of various malignant cells.

EXPERIMENTAL

Cell cultures and reagents

Continuous TE-671 rhabdomyosarcoma and U-251 astrocytoma cells as well as HEK293T embryonic kidney cells were cultured in a DMEM medium (Gibco, USA). SH-SY5Y neuroblastoma cells were cultured in a RPMI-1640 medium (Gibco) containing 10% fetal bovine serum (FBS), 100 U/mL penicillin, 100 μg/mL streptomycin, 1 mM sodium pyruvate, and 2 mM *L*-glutamine at 37°C and 5% CO_2. All cell lines were donated by the Heinrich-Pette Institute – Leibniz Institute for Experimental Virology (Hamburg, Germany). We used *all-trans* retinoic acid (R2625) and Hoechst 33342 DNA dye (14533) (Sigma-Aldrich, USA). We used SCH772984 (S7101), Ulixertinib (S7854), and VX-11e (S7709) (Selleckchem, USA) ERK inhibitors. All reagents were initially diluted in DMSO. We also used recombinant human growth factors EGF (ab179628), IGF-1 (ab9573), NGF (ab179616), and BDNF (ab206642) (Abcam, UK).

Production of ERK-KTR reporter cell lines

Lentiviral particles directing expression of the gene encoding the ERK-KTR reporter protein were prepared by calcium phosphate transfection of HEK293T cells using a ProFection® Mammalian Transfection System kit (Promega, USA, E1200). We used pMDLg/pRRE and pRSV-Rev third-generation packaging plasmids and a plasmid encoding the VSV-G coat protein. The pLentiCMV Puro DEST ERKKTRClover lentiviral vector was received from Addgene (#59150). After lentiviral transduction, TE-671, SH-SY5Y, and U-251 cells were selected with puromycin (Sigma-Aldrich, P7255) until more than 80% of the cells were positive for the reporter protein. After lentiviral transduction, the TE-671, SH-SY5Y, and U-251 cells were selected on media containing puromycin (0.5–2 μg/mL), which provided a population where more than 80% of the cells were reporter-protein positive.

Processing of cell images and calculations of ERK activity and cell length

Cell Images were acquired using a Leica DMI8 automated fluorescence microscope (Germany). Images were processed using the CellProfiler 4 software. Segmentation of Hoechst 33342-stained nuclei was assessed using the Otsu image thresholding algorithm. Cytoplasmic boundaries were determined based on the fluorescent ERK-KTR reporter signal using the position of nuclei to evaluate cell boundaries by the Sauvola image thresholding algorithm. To calculate the lengths of the cytoskeleton and cell processes, the cell body was first defined (a 3- to 5-pixel radius around the nucleus), and then the cytoskeleton was binarized based on a fluorescent reporter signal. Binarization parameters were selected for each cell type at all stages. Incorrectly recognized cells, elimination of outliers and artifacts, and subsequent data processing were performed using original algorithms in Python 3.8. The protocols used for CellProfiler are available at: https://github.com/CancerCellBiology/ActaNaturae-2021.

Assessment of gene expression

Total RNA was isolated by chloroform-trizol extraction using the TRIzol reagent (Thermo Scientific, USA, 15596018) according to the manufacturer's protocol. Total RNA (1 μg) was used to prepare cDNA using a RevertAid First Strand cDNA Synthesis Kit (Thermo Scientific, K1622), according to the manufacturer's protocol. Expression was analyzed by real-time PCR using a qPCRmix-HS SYBR kit (Evrogen, Russia, PK147L) on a Bio-Rad CFX96 device (USA). Results were processed using the Bio-Rad CFX Manager 3.1 and GraphPad Prism 9.1 software. A list of primers is shown in the *Table*.

RESULTS

Creation of ERK-KTR reporter expressing cell lines

The role of ERK in cell differentiation was studied in three lines of malignant cells capable of *in vitro* differentiation: SH-SY5Y neuroblastoma, U-251 MG astrocytoma, and TE-671 rhabdomyosarcoma cells. Lentiviral transduction of cells of these lines resulted in cells expressing the ERK activity reporter, ERK-KTR, a chimeric protein composed of the

Primers used in real-time PCR

Primer	Nucleotide sequence 5'→3'
GAPDH pr1	GAGCCCGCAGCCTCCCGCT
GAPDH pr2	GCGCCCAATACGACCAAATC
PROM1 pr1	CCTGGTCCAACAGGGCTATC
PROM1 pr2	TCGTGGTTTGGCGTTGTACT
RBFOX3 pr1	CAGACAGTGCCGCAGACAG
RBFOX3 pr2	TTCTCTGTAGGGTCGGAGGG
TUBB3 pr1	ATGAGCATGGCATCGACCC
TUBB3 pr2	AGGCACGTACTTGTGAGAAGA
MYOG pr1	TCAGCTCCCTCAACCAGGAG
MYOG pr2	CCGTGAGCAGATGATCCCC
PAX7 pr1	CACTGTGACCGAAGCACTGT
PAX7 pr2	TCCAGCCGGTTCCCTTTGT
EGFR pr1	AGGAGAGGAGAACTGCCAGAA
EGFR pr2	TCTCGGAATTTGCGGCAGAC
IGF1R pr1	CATCCGACGGGGGAATAACA
IGF1R pr2	GCTGCAAGTTCTGGTTGTCG
NTRK1 pr1	CCATCCCTGACACTAACAGCA
NTRK1 pr2	GCACAAGGAGCAGCGTAGAA
NTRK2 pr1	CTGAACCAAGCACGGTTTCC
NTRK2 pr2	CAGGGGCAGAAACTCCAGAA

ERK1/2 docking site of the ELK1 protein, nuclear localization signal (NLS), nuclear export signal (NES), and green fluorescent protein mClover [25]. In contrast to NES, NLS in the chimeric protein is activated, which ensures predominantly nuclear localization of the reporter protein. Activated ERK1/2 kinases occur in the cell nucleus, where they bind to the ELK1 docking site and phosphorylate the NLS and NES regions. This activates the nuclear export signal and deactivates the nuclear localization signal, which leads to translocation of the reporter protein from the nucleus to the cytoplasm. In the cytoplasm, the reporter protein is dephosphorylated by cellular phosphatases and transferred back to the nucleus. The reporter protein distribution between the nucleus and cytoplasm is established depending on an ERK activity level. The fluorescent protein in the reporter enables an evaluation of ERK activity by the ratio of the fluorescent protein signal intensity in the cytoplasm and the nucleus. Thus, the ERK-KTR reporter provides an evaluation of ERK activity in live individual cells using a fluorescence microscope.

Next, we treated ERK-KTR expressing cells with ERK inhibitors and *all-trans* retinoic acid (ATRA) that is widely used for induction of differentiation of various cell types and for neuroblastoma therapy. For the initial test, we selected three ERK inhibitors that had been effective in clinical trials: SCH772984, Ulixertinib, and VX-11e. Cells were treated with ERK inhibitors (250 nM) or ATRA (10 μM) for 72 h, and images were acquired on a fluorescence microscope. All inhibitors significantly reduced the ERK activity, which is evident from the changes in the fluorescent signal distribution in the nucleus and the cytoplasm (*Fig. 1A*). We also noticed morphological changes in SH-SY5Y cells induced by ATRA, as well as in TE-671 and U-251 cells induced by ERK inhibitors. The most pronounced changes were caused by SCH772984 (*Fig. 1A*). The observed morphological changes included elongation of the cell processes and the entire cytoskeleton, especially in TE-671 cells. These changes are similar to the previously reported morphological changes characteristic of cell differentiation. To quantify the observed changes, we developed algorithms for the CellProfiler 4 software to identify the nuclei (pre-stained with Hoechst 33342) and cytoplasm of each cell based on the fluorescence of the mClover protein (*Fig. 1B*). ERK activity in individual cells was calculated based on median mClover intensities in the nucleus and cytoplasm, and the cytoplasmic shape was used to measure the length of the cytoskeleton, including processes. This algorithm enabled the assessment of the changes in the mean ERK activity and the length of the cytoskeleton at each exposure, as well as a comparison of the ERK activity and changes in the cytoskeleton length in individual cells.

ERK activity is associated with cell differentiation

Exposure to retinoic acid led to a decrease in ERK activity in all three cell lines, SH-SY5Y, U-251, and TE-671. However, this decrease was less pronounced compared to the effect of the ERK inhibitors SCH772984, Ulixertinib, and VX-11e (*Fig. 2A*). In this case, retinoic acid induced process extension only in SH-SY5Y neuroblastoma cells. Induction of differentiation and, as a result, extension of cell processes are a well-known effect of retinoic acid on neuroblastoma cells. In turn, ERK inhibitors did not cause extension of the cytoskeleton in SH-SY5Y cells (*Fig. 2B*). Interestingly, we observed opposite effects in U-251 and TE-671 cells. For example, retinoic acid did not affect the length of TE-671 cells and even reduced the length of U-251 cells. In this case, ERK inhibitors, especially SCH772984, significantly increased the length of TE-671 and U-251 cells, in particular due to the extension of cell processes (*Fig. 2B*). It is also worth noting that SCH772984 was the most potent

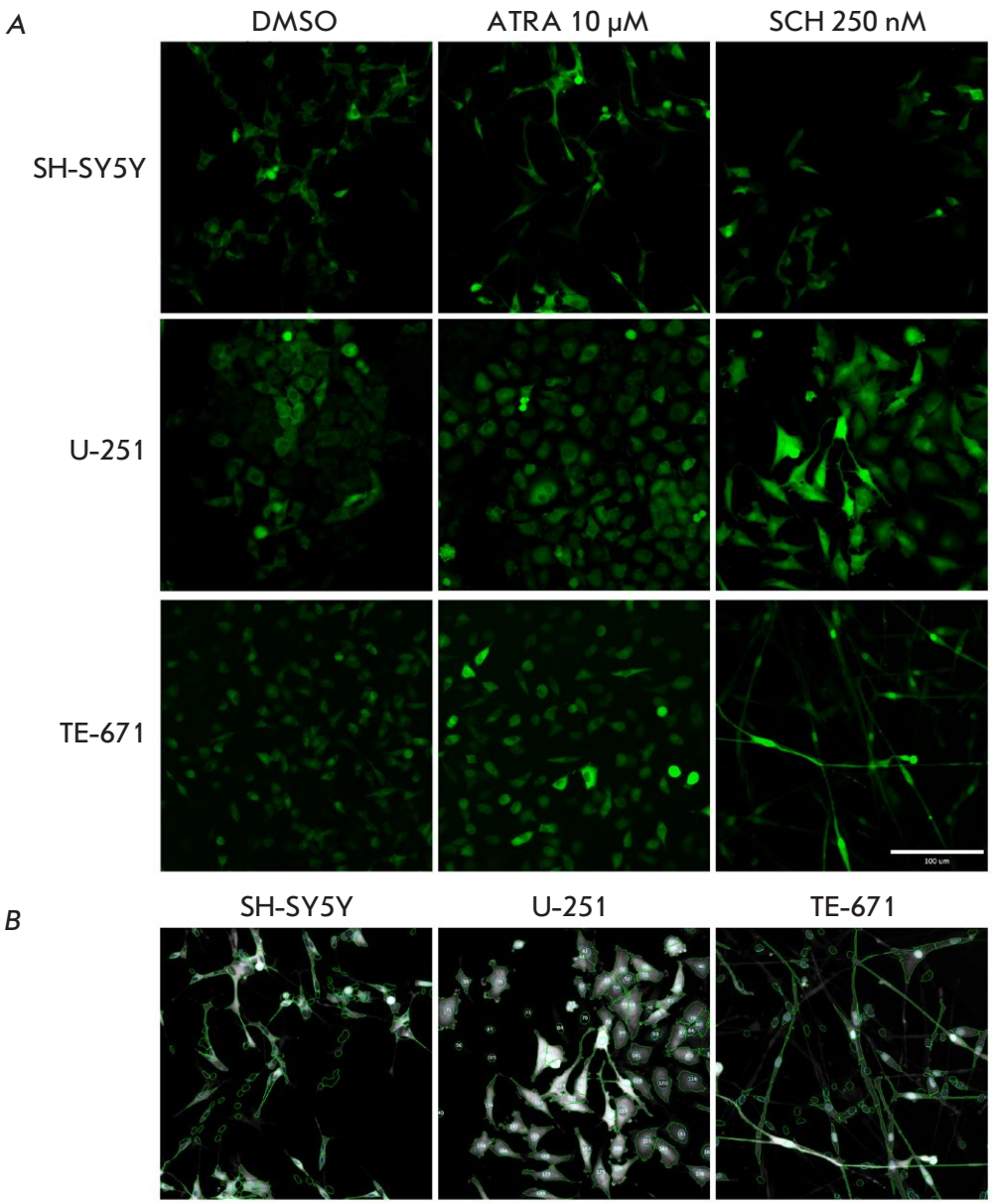

Fig. 1. SH-SY5Y, U-251, and TE671 cells with ERK-KTR reporter expression. (*A*) – Images of SH-SY5Y, U-251, and TE671 cells with ERK-KTR reporter expression 72 h after addition of 10 μM retinoic acid (ATRA) or 250 nM of the ERK inhibitor SCH772984 (SCH). (*B*) – Examples of cell images processed using the CellProfiler 4 software. Images are shown in a gray gradient. The cytoplasm boundaries are marked in green. The nuclei are marked in blue; the nuclei were identified by staining with the Hoechst 33342 DNA dye

ERK inhibitor (*Fig. 2A*) and most strongly affected the length of U-251 and TE-671 cells.

To test whether the observed morphological changes were associated with cell differentiation, we measured the mRNA expression of the genes encoding differentiation markers (*Fig. 2C*). We measured the expression of the *PROM1* gene, which encodes the CD133 protein, in all cells. Expression of this gene is characteristic of undifferentiated cells, in particular malignant neuroblastoma and glioblastoma stem cells and undifferentiated rhabdomyosarcoma cells. We also selected genes whose expression changes during neural cell differentiation: the *RBFOX3* gene encoding the NeuN protein [26, 27] and the *TUBB3* gene encoding β3-tubulin [27]. Because TE-671 rhabdomyosarcoma cells are known to be capable of differentiating into muscle cells, we chose the myogenin gene *MYOG* and the transcription factor gene *PAX7* to analyze the dif-

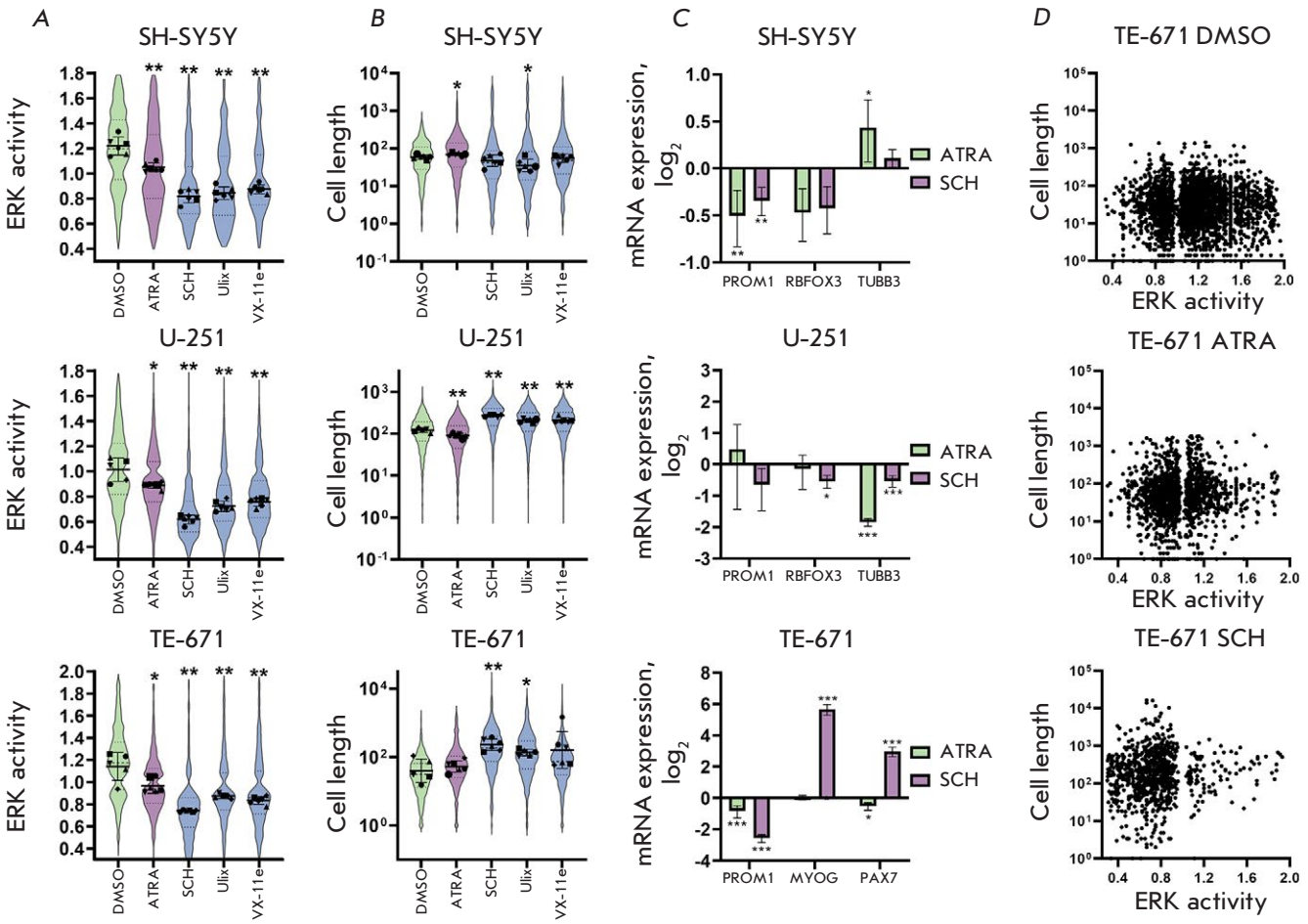

Fig. 2. Changes in the ERK activity and cell length induced by retinoic acid and ERK inhibitors.
(*A*) – Distributions of ERK activity (violin plots) in SH-SY5Y, U-251, and TE-671 cells 72 h after the addition of 10 μM retinoic acid (ATRA) or 250 nM of the ERK inhibitors SCH772982 (SCH), Ulixertinib (Ulix), and VX-11e. In controls, cells were added with DMSO because all agents were dissolved in DMSO. Each measurement included images of 6 independent, randomly selected fields (median values for each field are marked with dots).
(*B*) – Cell length distributions (violin plots) in pixels 72 h after the addition of agents. Violin plots are based on the results of measuring ERK activity in at least 300 unique cells. Dots indicate median values for each of the 6 analyzed independent, randomly selected fields. Standard deviations (SDs) are shown in violin plots. The statistical significance is determined using the nonparametric Mann–Whitney U-test.
(*C*) – Expression of the *PROM1* (CD133), *RBFOX3* (NeuN), *TUBB3* (β3-tubulin), *MYOG* (myogenin), and *PAX7* genes measured by real-time PCR 72 h after addition of agents. PCR data are normalized to the expression of the *GAPDH* gene in each sample; the results are presented as a logarithm of the change in gene expression relative to the control (DMSO-treated cells). Gene expression measurements were performed in triplicate. Plots show the mean expression change and 95% confidence interval. Statistical significance was determined using the Student's t-test.
(*D*) – ERK activity and cell length distributions in individual TE-671 cells 72 h after the addition of agents.
$^{*}p$-value < 0.05; $^{**}p$-value < 0.01; $^{***}p$-value < 0.001

ferentiation of these cells [28]. Myogenin is one of the main markers of muscle cell differentiation, and PAX7 is an important regulator of early differentiation of these cells. We found a significant increase in the expression of the *MYOG* and *PAX7* genes and a decrease in the expression of *PROM1* in TE-671 cells exposed to SCH772984. Retinoic acid did not cause noticeable changes in the expression of these genes. There was also a slight decrease in *PROM1* expression in U-251 cells treated with SCH772984 and a decrease in *TUBB3* expression after exposure to retinoic acid. There were no significant changes in gene expression in SH-SY5Y cells. Interestingly, TE-671 cells, whose length increased most substantially

by SCH772984, had low ERK activity (*Fig. 2D*). These data indicate a relationship between ERK tyrosine kinase activity and differentiation of TE-671 cells at the level of both the entire population and individual cells.

ERK inhibition alters the expression of growth factor receptors

How do the ERK inhibitor SCH772984 and retinoic acid affect cell sensitivity to growth factors? To understand this, we treated cells with the agents for 72 h, washed them from a culture medium containing the agents, and added a serum-free medium because the growth factors present in the serum could strongly affect ERK activity. Twelve hours after changing the medium, growth factors at a concentration of 100 ng/mL were added to the cells. We selected growth factors that are able to activate ERK in various cells, involved in neural or myogenic differentiation, and able to stimulate cell survival: epidermal growth factor (EGF) [29], insulin-like growth factor 1 (IGF-1) [30], neural growth factor (NGF) [15, 31], and brain-derived neurotrophic factor (BDNF) [15]. All growth factors significantly activated ERK in SH-SY5Y neuroblastoma cells, in particular after induction of cell differentiation with retinoic acid and treatment of cells with the ERK inhibitor SCH772984 (*Fig. 3A*). The growth factors also activated ERK in the control U-251 astrocytoma cells (treated with DMSO only) and SCH772984-treated cells (*Fig. 3A*). However, treatment of U-251 cells with retinoic acid resulted in less pronounced effects of EGF, IGF-1, and BDNF. There was no statistically significant effect of the growth factors on the control TE-671 cells and retinoic acid-treated cells. SCH772984-induced differentiation of TE-671 cells rendered the cells sensitive to all growth factors. It is important to note that undifferentiated TE-671 cells in the serum-free medium had high ERK activity comparable with that in the presence of serum, whereas basal ERK activity after treatment with the ERK inhibitor for 72 h was significantly lower. Probably, the initially high basal ERK activity of TE-671 cells prevents the detection of significant changes in the ERK activity induced by growth factors. However, even after prolonged exposure to the ERK inhibitor SCH772984, all cells either retained or acquired the ability to respond to growth factors (*Fig. 3A*).

Because the effect of growth factors can depend on both basal ERK activity and changes in the abundance of growth factor receptors during differentiation, we measured changes in the receptor mRNA expression. For this purpose, we chose the *NTRK1* and *NTRK2* genes encoding the main receptors of the used growth factors NGF and BDNF (TrkA and TrkB), IGF1R encoding the IGF-1 receptor, and *EGFR* encoding the EGF receptor. Expression of the *NTRK2* gene, one of the main markers of neuroblastoma cell differentiation, was significantly upregulated in SH-SY5Y cells exposed to retinoic acid (*Fig. 3B*). We found similar changes in *NTRK2* expression in TE-671 cells treated with SCH772984. Retinoic acid caused a slight increase in *NTRK1* expression in TE-671 and SH-SY5Y cells. In U-251 cells, *NTRK1* expression was significantly downregulated after treatment with retinoic acid, whereas *NTRK2* expression was downregulated after treatment with both retinoic acid and SCH772984 (*Fig. 3B*). There were no significant changes in the *EGFR* and *IGF1R* expression. These data indicate that increased sensitivity of TE-671 cells to growth factors may be associated with both a decrease in the basal level of ERK activity and an increase in the expression of receptors; e.g., in the case of TrkA and TrkB.

DISCUSSION

In this study, we investigated the effect of retinoic acid on the ERK activity and the effect of ERK inhibition on the differentiation of three types of malignant cells. We found a direct relationship between a decrease in the ERK activity in U-251 astrocytoma and TE-671 rhabdomyosarcoma cells and differentiation-associated morphological changes in these cells. Exposure of TE-671 cells to the ERK inhibitor SCH772984 for 72 h resulted in a significant increase in the expression of the myogenin gene *MYOG*. Increased myogenin expression is considered the main marker of skeletal muscle differentiation [32]. There was a decrease in the expression of the *PROM1* gene that is typical of malignant stem cells. Changes in the expression of the *PROM1* and *MYOG* genes and significant morphological changes in SCH772984-treated TE-671 cells indicate induction of myogenic differentiation. Our results are consistent with reported data holding that MEK inhibitors initiate the differentiation of rhabdomyosarcoma cells [22]. In this case, inhibition of MEK for 72 h led to a decrease in the expression of the *PAX7* gene [28], whereas direct inhibition of ERK caused a significant increase in *PAX7* expression. PAX7 is believed to be necessary for the initiation of myogenic differentiation, and its expression level is upregulated in early skeletal muscle progenitor cells [33]. At the later stages of differentiation, PAX7 expression usually decreases; however, there are no unambiguous data on the effect of changes in the PAX7 expression on cell differentiation upon suppression of ERK. The observed differences in *PAX7* expression are possibly related to differences in

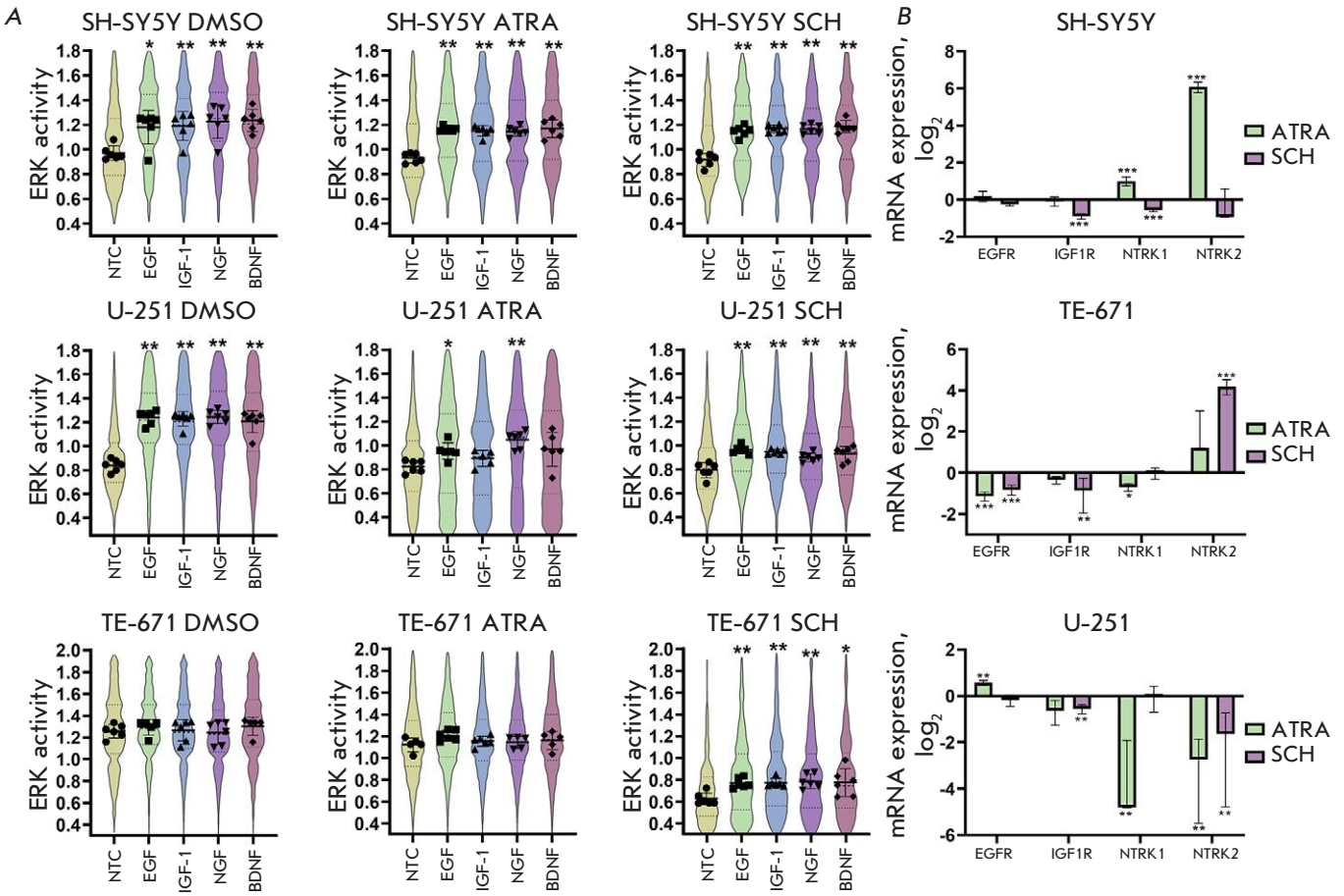

Fig. 3. Effect of ERK inhibition and retinoic acid on growth factor activity. (*A*) – Distributions of ERK activity (violin plots) 30 min after addition of the growth factors EGF, IGF-1, NGF, and BDNF (100 ng/mL each) to SH-SY5Y, U-251, and TE-671 cells pretreated with 10 μM retinoic acid (ATRA) or 250 nM of the ERK inhibitor SCH772982 (SCH) for 72 h. DMSO-treated cells were used as the control. A non-treated control (NTC) is a cell added with the culture medium without growth factors. Dots indicate median values for each of 6 analyzed independent, randomly selected fields. Standard deviations (SDs) are shown in violin plots. Statistical significance is determined using the nonparametric Mann–Whitney U-test. (*B*) – Expression of the *EGFR*, *IGF-1R*, *NTRK1* (*TrkA*), and *NTRK2* (*TrkB*) genes by real-time PCR 72 h after the addition of agents. PCR data are normalized to the expression of the *GAPDH* gene in each sample; the results are presented as a logarithm of the change in gene expression relative to the control (DMSO-treated cells). Gene expression measurements were performed in triplicate. Plots show the mean expression change and a 95% confidence interval. Statistical significance is determined using the Student's t-test. $^{*}p$-value < 0.05; $^{**}p$-value < 0.01; $^{***}p$-value < 0.001

MEK and ERK inhibition. There were no significant changes in the expression of the neural differentiation markers NeuN and β3-tubulin at the mRNA level in SH-SY5Y and U-251 cells treated with retinoic acid or the ERK inhibitor SCH772984. However, in SH-SY5Y cells, retinoic acid caused a significant increase in the expression of TrkB, the main differentiation marker in these cells. Interestingly, ERK inhibition-induced differentiation of TE-671 cells resulted in increased TrkB expression. This indicates a potential similarity in the regulation of TrkB expression in these cell types during differentiation. In the case of U-251 astrocytoma cells, differentiation markers suitable for a PCR analysis should be selected.

Using the ERK-KTR reporter system, we have shown that the length of TE-671 cells depends on a decrease in ERK activity both in the entire population and in individual cells. This indicates a direct relationship between ERK activity and cell differentiation. Similar results were obtained for U-251 astrocytoma cells. Retinoic acid-induced differentiation of SH-SY5Y neuroblastoma cells also led to a decrease

in ERK activity. However, direct ERK inhibition in SH-SY5Y cells does not cause initiation of differentiation, which indicates a secondary role of the retinoic acid-induced decrease in ERK activity. Several studies have shown that ERK activation in neural stem cells or early progenitors initiates differentiation into neurons and suppresses differentiation into glial cells [34, 35]. It should be noted that astrocytomas [36] and rhabdomyosarcomas [37, 38] are characterized by mutations directly in the MAPK signaling cascade, which lead to ERK hyperactivation, whereas these mutations are relatively rare in neuroblastomas. TE-671 cells contain a mutation in the *NRAS* gene (Q61H) [39, 40], which leads to ERK hyperactivation, and U-251 cells contain a deletion in the *NF1* gene [41] that encodes neurofibromin, a negative regulator of RAS proteins and the RAS-MEK-ERK signaling cascade [42]. The F1174L mutation in ALK receptor tyrosine kinase also leads to ERK activation in SH-SY5Y cells, but it does not directly regulate the RAS-MEK-ERK signaling cascade. Probably, mutations in the RAS-MEK-ERK cascade are responsible for the initiation of the differentiation induced by ERK inhibition in TE-671 and U-251 cells [40].

Our study has several limitations. Although we see morphological changes and changes in gene expression, which are induced by ERK inhibitors, we cannot identify the stage to which cell differentiation proceeds. In addition, it is not known whether TE-671 cells can differentiate into normal muscle cells upon ERK inhibition. However, ERK inhibition can be at least an initiating event that does not suppress the activity of growth factors. Also, it cannot be unambiguously asserted that the observed morphological changes in U-251 cells are differentiation. Therefore, additional experiments are required, in particular a search for reliable markers of differentiation.

CONCLUSION

In this study, we have established a relationship between morphological changes associated with the differentiation of TE-671, U-251, and SH-SY5Y cells and the activity of ERK kinases, in particular at the level of individual cells. We have demonstrated that ERK inhibition in TE-671 rhabdomyosarcoma cells initiates their myogenic differentiation. Differentiation renders TE-671 cells more sensitive to growth factors, potentially by reducing basal ERK activity and increasing TrkB expression. Our findings can be used to develop new protocols for cell differentiation: in particular, for basic research and the development of new approaches to the therapy of malignant diseases. ●

The study was supported by a grant from the Russian Science Foundation (project No. 19-74-00120).

REFERENCES

1. Lavoie H., Gagnon J., Therrien M. // Nat. Rev. Mol. Cell. Biol. 2020. V. 21. № 10. P. 607–632.
2. Orlova N.N., Lebedev T.D., Spirin P.V., Prassolov V.S. // Mol. Biol. (Moskow). 2016. V. 50. № 3. P. 395–405.
3. Bonni A., Brunet A., West A.E., Datta S.R., Takasu M.A., Greenberg M.E. // Science. 1999. V. 286. № 5443. P. 1358–1362.
4. Spirin P., Lebedev T., Orlova N., Morozov A., Poymenova N., Dmitriev S.E., Buzdin A., Stocking C., Kovalchuk O., Prassolov V. // Oncotarget. 2017. V. 8. № 34. P. 56991–57002.
5. Ma M., Bordignon P., Dotto G.P., Pelet S. // Heliyon. 2020. V. 6. № 12. P. e05574.
6. Simon C.S., Rahman S., Raina D., Schroter C., Hadjantonakis A.K. // Dev. Cell. 2020. V. 55. № 3. P. 341–353 e345.
7. Pokrass M.J., Ryan K.A., Xin T., Pielstick B., Timp W., Greco V., Regot S. // Dev. Cell. 2020. V. 55. № 3. P. 328–340 e325.
8. Ogura Y., Sami M.M., Wada H., Hayashi S. // Genes Cells. 2019. V. 24. № 4. P. 297–306.
9. Maryu G., Matsuda M., Aoki K. // Cell Struct. Funct. 2016. V. 41. № 2. P. 81–92.
10. Hamilton W.B., Mosesson Y., Monteiro R.S., Emdal K.B., Knudsen T.E., Francavilla C., Barkai N., Olsen J.V., Brickman J.M. // Nature. 2019. V. 575. № 7782. P. 355–360.
11. Spelat R., Ferro F., Curcio F. // J. Biol. Chem. 2012. V. 287. № 45. P. 38279–38288.
12. Ying Q.L., Wray J., Nichols J., Batlle-Morera L., Doble B., Woodgett J., Cohen P., Smith A. // Nature. 2008. V. 453. № 7194. P. 519–523.
13. Tamama K., Sen C.K., Wells A. // Stem Cells Dev. 2008. V. 17. № 5. P. 897–908.
14. Yu Y., Wang X., Zhang X., Zhai Y., Lu X., Ma H., Zhu K., Zhao T., Jiao J., Zhao Z.A., et al. // Stem Cell Res. Ther. 2018. V. 9. № 1. P. 2.
15. Liu F., Xuan A., Chen Y., Zhang J., Xu L., Yan Q., Long D. // Mol. Med. Rep. 2014. V. 10. № 4. P. 1739–1745.
16. Yan L., Zhou L., Yan B., Zhang L., Du W., Liu F., Yuan Q., Tong P., Shan L., Efferth T. // Cell Death Dis. 2020. V. 11. № 10. P. 857.
17. Khavari T.A., Rinn J. // Cell Cycle. 2007. V. 6. № 23. P. 2928–2931.
18. Kern F., Niault T., Baccarini M. // Br. J. Cancer. 2011. V. 104. № 2. P. 229–234.
19. Olson E.N., Spizz G., Tainsky M.A. // Mol. Cell. Biol. 1987. V. 7. № 6. P. 2104–2111.
20. Reynolds C.P., Matthay K.K., Villablanca J.G., Maurer B.J. // Cancer Lett. 2003. V. 197. № 1–2. P. 185–192.
21. Tallman M.S., Andersen J.W., Schiffer C.A., Appelbaum F.R., Feusner J.H., Ogden A., Shepherd L., Willman C., Bloomfield C.D., Rowe J.M., et al. // N. Engl. J. Med. 1997. V. 337. № 15. P. 1021–1028.
22. Yohe M.E., Gryder B.E., Shern J.F., Song Y.K., Chou H.C., Sindiri S., Mendoza A., Patidar R., Zhang X., Guha R., et al. // Sci. Transl. Med. 2018. V. 10. № 448. P. eaan4470.

23. Forshew T., Tatevossian R.G., Lawson A.R., Ma J., Neale G., Ogunkolade B.W., Jones T.A., Aarum J., Dalton J., Bailey S., et al. // J. Pathol. 2009. V. 218. № 2. P. 172–181.
24. Tanaka T., Higashi M., Kimura K., Wakao J., Fumino S., Iehara T., Hosoi H., Sakai T., Tajiri T. // J. Pediatr. Surg. 2016. V. 51. № 12. P. 2074–2079.
25. Regot S., Hughey J.J., Bajar B.T., Carrasco S., Covert M.W. // Cell. 2014. V. 157. № 7. P. 1724–1734.
26. Gusel'nikova V.V., Korzhevskiy D.E. // Acta Naturae. 2015. V. 7. № 2. P. 42–47.
27. Constantinescu R., Constantinescu A.T., Reichmann H., Janetzky B. // J. Neural. Transm. Suppl. 2007. № 72. P. 17–28.
28. De Luna N., Suarez-Calvet X., Garicano M., Fernandez-Simon E., Rojas-Garcia R., Diaz-Manera J., Querol L., Illa I., Gallardo E. // J. Neuropathol. Exp. Neurol. 2018. V. 77. № 10. P. 964–972.
29. Garcez R.C., Teixeira B.L., Schmitt Sdos S., Alvarez-Silva M., Trentin A.G. // Cell Mol. Neurobiol. 2009. V. 29. № 8. P. 1087–1091.
30. Galvin C.D., Hardiman O., Nolan C.M. // Mol. Cell. Endocrinol. 2003. V. 200. № 1–2. P. 19–29.
31. Lebedev T.D., Vagapova E.R., Popenko V.I., Leonova O.G., Spirin P.V., Prassolov V.S. // Front. Oncol. 2019. V. 9. P. 1046.
32. Bentzinger C.F., Wang Y.X., Rudnicki M.A. // Cold Spring Harb. Perspect. Biol. 2012. V. 4. № 2. P. a008342.
33. Florkowska A., Meszka I., Zawada M., Legutko D., Proszynski T.J., Janczyk-Ilach K., Streminska W., Ciemerych M.A., Grabowska I. // Stem Cell Res. Ther. 2020. V. 11. № 1. P. 238.
34. Paquin A., Barnabe-Heider F., Kageyama R., Miller F.D. // J. Neurosci. 2005. V. 25. № 46. P. 10747–10758.
35. Samuels I.S., Karlo J.C., Faruzzi A.N., Pickering K., Herrup K., Sweatt J.D., Saitta S.C., Landreth G.E. // J. Neurosci. 2008. V. 28. № 27. P. 6983–6995.
36. Jones D.T., Gronych J., Lichter P., Witt O., Pfister S.M. // Cell Mol. Life Sci. 2012. V. 69. № 11. P. 1799–1811.
37. Marampon F., Bossi G., Ciccarelli C., Di Rocco A., Sacchi A., Pestell R.G., Zani B.M. // Mol. Cancer Ther. 2009. V. 8. № 3. P. 543–551.
38. Ciccarelli C., Vulcano F., Milazzo L., Gravina G.L., Marampon F., Macioce G., Giampaolo A., Tombolini V., Di Paolo V., Hassan H.J., et al // Mol. Cancer. 2016. V. 15. P. 16.
39. Stratton M.R., Darling J., Pilkington G.J., Lantos P.L., Reeves B.R., Cooper C.S. // Carcinogenesis. 1989. V. 10. № 5. P. 899–905.
40. Dolgikh N., Hugle M., Vogler M., Fulda S. // Cancer Res. 2018. V. 78. № 8. P. 2000–2013.
41. McGillicuddy L.T., Fromm J.A., Hollstein P.E., Kubek S., Beroukhim R., De Raedt T., Johnson B.W., Williams S.M., Nghiemphu P., Liau L.M., et al. // Cancer Cell. 2009. V. 16. № 1. P. 44–54.
42. Cichowski K., Jacks T. // Cell. 2001. V. 104. № 4. P. 593–604.

Evaluation of the Antiviral Potential of Modified Heterocyclic Base and 5′-Norcarbocyclic Nucleoside Analogs Against SARS-CoV-2

E. S. Matyugina[1], M. S. Novikov[2], L. I. Kozlovskaya[3,4], V. P. Volok[3], E. Y. Shustova[3], A. A. Ishmukhametov[3,4], S. N. Kochetkov[1], A. L. Khandazhinskaya[1*]
[1]Engelhardt Institute of Molecular Biology, Moscow, 119991 Russia
[2]Volgograd State Medical University, Volgograd, 400131 Russia
[3]FSBSI "Chumakov Federal Scientific Center for Research and Development of Immune and Biological Products of the Russian Academy of Sciences", Moscow, 108819 Russia
[4]Sechenov Moscow State Medical University, Moscow, 119991 Russia
*E-mail: khandazhinskaya@bk.ru
Received October 20, 202l; in final form December 10, 2021
DOI: 10.32607/actanaturae.11479

ABSTRACT **The pandemic caused by the novel betacoronavirus SARS-CoV-2 has already claimed more than 3.5 million lives. Despite the development and use of anti-COVID-19 vaccines, the disease remains a major public health challenge throughout the world. Large-scale screening of the drugs already approved for the treatment of other viral, bacterial, and parasitic infections, as well as autoimmune, oncological, and other diseases is currently underway as part of their repurposing for development of effective therapeutic agents against SARS-CoV-2. In this work, we present the results of a phenotypic screening of libraries of modified heterocyclic bases and 5'-norcarbocyclic nucleoside analogs previously synthesized by us. We identified two leading compounds with apparent potential to inhibit SARS-CoV-2 replication and EC_{50} values in a range of 20–70 μM. The structures of these compounds can be further optimized to develop an antiviral drug.**
KEYWORDS **SARS-CoV-2, antiviral drugs, nucleosides, nucleoside analogs.**
ABBREVIATIONS **EC_{50} – 50% effective concentration, i.e. the compound concentration that inhibits viral replication by 50%; NHC – N(4)-hydroxycytidine; SARS-CoV-2 – Severe Acute Respiratory Syndrome Coronavirus 2; HIV – Human Immunodeficiency Virus; DMSO – dimethyl sulfoxide; COVID-19 – coronavirus disease 2019; $TCID_{50}$ – 50% tissue culture infective dose, i.e. the viral dose that causes cytopathic effects in 50% of tissue culture cells.**

INTRODUCTION

Coronaviridae is a viral family that comprises two subfamilies: Orthocoronavirinae and Letovirinae. The Orthocoronavirinae subfamily includes dangerous human pathogens. Human coronaviruses (HCoVs) HCoV-OC43 (OC43) and HCoV-229E (229E) were first identified in the 1960s [1]. Later, other human coronaviruses were discovered: HCoV-NL63 (NL63) in 2004, and HCoV-HKU1 (HKU1) in 2005 [1]. These four viruses usually cause acute diseases of the upper and (less often) lower respiratory tract, but a severe coronavirus infection is diagnosed rarely and is usually considered to be due to a concomitant pathology and/or immunological aging. Two more pathogenic human coronaviruses, SARS-CoV (2003) and MERS-CoV (2012), cause atypical symptoms of the upper and lower respiratory tract, which are especially severe in people over 65 years of age and patients with comorbidities [1].

SARS-CoV-2, which was identified in Wuhan city (China) in December 2019, is seventh in the group of human coronaviruses. The infection caused by this virus, which is called COVID-19, spread rapidly around the world. The World Health Organization announced the COVID-19 pandemic on March 11, 2020 [2]. The combined efforts of researchers around the world, which made it possible to quickly identify the etiological agent and obtain information on the virus structure and life cycle, as well as to develop agents for the treatment of the atypical pneumonia caused by SARS-CoV, led to the emergence of vaccines, some of which have successfully passed

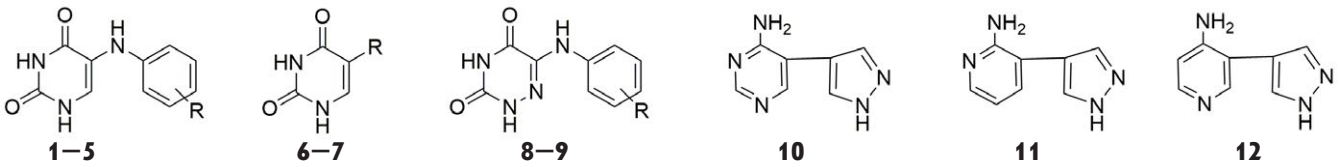

R = 3-Me (**1**), 4-Me (**2**), 4-Bu (**3**), 4-OBu (**4**), 4-OPh (**5**)

R = NHPh (**6**), NHBn (**7**)

R = H (**8**), 4-Bu (**9**)

5-Arylamino derivatives of uracil and 6-azauracil

Fleximer nucleoside analogs of 8-aza-7-deazaadenine, 8-aza-1,7-dideazaadenine, and 8-aza-3,7-dideazaadenine

Fig. 1. Heterocyclic base analogs

preclinical and clinical trials and are now used for mass vaccination [2].

Despite that, a COVID-19 diagnosis had been confirmed in more than 274 million patients in the world by October 27, 2021; of these, 4.96 million people had died [2]. To date, there are no generally accepted effective strategies to treat COVID-19. For this reason, the creation of specific drugs against this disease remains topical. Therapeutic agents based on antibodies, inhibitors of viral enzymes (RNA-dependent RNA polymerase, proteases, etc.), inhibitors of viral entry into the cell, etc. are currently being developed. Intensive research of drugs for treating other viral (influenza, HIV infection, hepatitis C, Ebola, etc.), bacterial, and parasitic infections, as well as autoimmune, oncological and other diseases, is currently underway as part of repurposing of approved drugs [3].

We screened the library of heterocyclic bases and nucleoside analogs with antiviral [4–8], antibacterial [7, 9–11], antiparasitic [12, 13], and antitumor [14, 15] activities.

EXPERIMENTAL

Stock 5 μM solutions of test compounds in 100% dimethyl sulfoxide (DMSO) were prepared. The SARS-CoV-2 virus strain PIK35 (GISAID ID EPI_ISL_428851) [16] was used to assess the antiviral activity of the compounds. The virus was passaged five times in Vero cells and stored as an infected cell suspension at –70°C. African green monkey kidney Vero cells were received from Biologicals (WHO, Switzerland; RCB 10-87). The cells were maintained in a DMEM medium (Chumakov Federal Scientific Center for Research and Development of Immune-and-Biological Products of the Russian Academy of Sciences, Russia) with 5% fetal bovine serum (Gibco, USA), 0.1 mg/ml streptomycin, and 100 U/ml penicillin (PanEco, Russia).

The phenotypic screening method [16] was used. Eight two-fold dilutions of compound stock solutions in a DMEM medium were prepared. The compound dilutions were then mixed with equal volumes of the viral suspension containing 50–200 $TCID_{50}$ per well and incubated at 37°C for 1 h. The virus–compound mixture was added to confluent Vero cell monolayers in duplicates. After 5-day incubation at 37°C, the cytopathic effect (CPE) was assessed using a microscope. EC_{50} values were calculated using the Karber method as previously described [16]. The experiment was repeated at least two times for each compound. N(4)-hydroxycytidine (NHC) and DMSO were used as a positive and negative control, respectively.

RESULTS AND DISCUSSION

The library of heterocyclic base (*Fig. 1*) and nucleoside (*Fig. 2*) analogs, previously synthesized by us, was screened phenotypically for activity against SARS-CoV-2. The first group of heterocyclic base analogs is 5-arylamino derivatives of uracil and 6-azauracil (*Fig. 1*), which were shown to act as non-nucleoside inhibitors of HIV and inhibitors of *Mycobacterium tuberculosis* growth [7, 11]. The second group includes new fleximer analogs of aza/deazapurine bases (*Fig. 1*) [17]. Aza/deazapurines, as well as the appropriate nucleosides, are known to exhibit a wide range of antiparasitic, antitumor, and antiviral properties [18]. At the same time, fleximer bases happen to exhibit high structural mobility (flexibility), which is due to a splitting of the purine ring into separate heterocyclic fragments. Free rotation around the C–C bond allows these compounds to better accommodate to the spatial structure of the target enzyme active site, which in some cases enables them to bypass point mutations in the enzyme, thus providing a mechanism that helps to avoid drug resistance [17].

Another group of compounds includes 5'-norcarbocyclic analogs of purine and pyrimidine nucleosides (*Fig. 2*). The structural feature of these analogs is that they lack the 5'-methylene group. Because of that lack, these compounds cannot be converted by

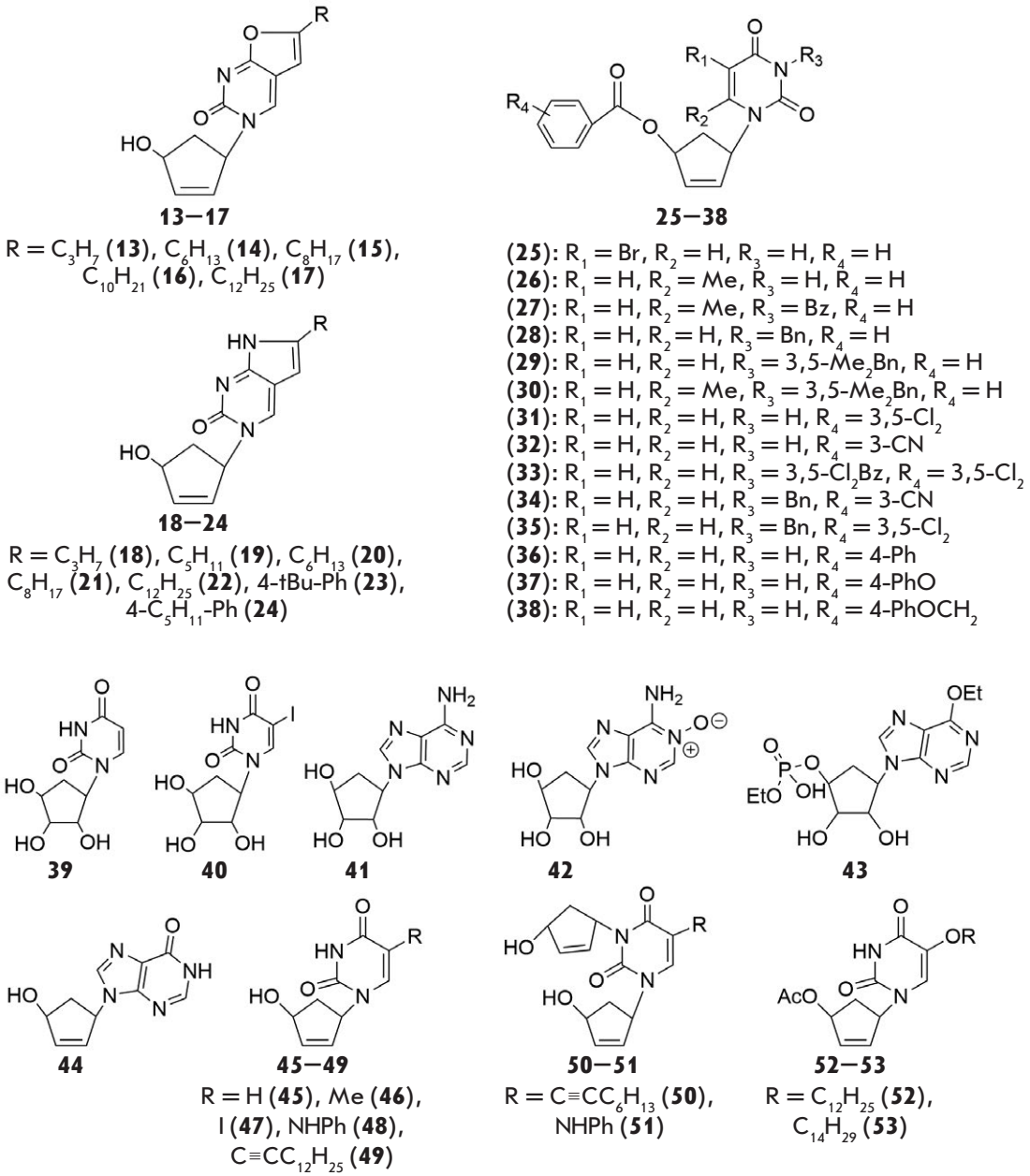

Fig. 2. 5′-Norcarbocyclic nucleoside analogs

cellular enzymes to phosphorylated derivatives and, thus, cannot exhibit biological activity in reactions typical of conventional modified nucleosides. However, representatives of this class of compounds can act as HIV non-nucleoside reverse transcriptase inhibitors (NNRTIs) and also exhibit antibacterial and antitumor activities [4–7, 9–11, 15].

The antiviral activity was recognized through the ability of the test compounds to inhibit Vero cell death induced by infection with the SARS-CoV-2 strain PIK35. A well-known inhibitor of SARS-CoV-2 replication, N(4)-hydroxycytidine (NHC), whose activity in this series of experiments was consistent with the previously obtained data, was used as a positive control [16]. A total of 53 compounds were tested, most of which showed no activity at concentrations < 100 μM. Only two compounds, namely 1-(4'-hydroxy-2'-cyclopenten-1-yl)-6-(4-tert-butylphenyl)-3*H*-pyrrolo[2,3-*d*]pyrimidin-2-one **23** and 1-(4'-hydroxy-2'-cyclopenten-1-yl)-6-(4-pentylphenyl)-3*H*-pyrrolo[2,3-*d*] pyrimidin-2-one **24**, showed any ability to inhibit SARS-CoV-2 replication in dose-dependent fashion

Antiviral activity and cytotoxicity constants of active compounds

Compound	EC_{50}, μM (M ± SEM)	CC_{50}, μM (M ± SEM)	Selectivity index (SI)
23	53 ± 18	75 ± 25	1.42
24	21 ± 6	53 ± 18	2.52
NHC	5.3 ± 0.9	> 100	> 19

with EC_{50} values of 53 and 21 μM, respectively (*Table*). They also exhibited a strong cytotoxic effect, which is consistent with the previously obtained data [14].

CONCLUSION

In this work, we performed phenotypic screening and identified two nucleoside analogs that can inhibit SARS-CoV-2 replication *in vitro*: 5'-norcarbocyclic derivatives of bicyclic furano[2,3-*d*]pyrimidines **23** and **24**. The structures of these compounds can be further optimized to develop an antiviral drug.●

This study was supported by the Russian Foundation for Basic Research (grant No. 20-75-00110). Synthesis of fleximer analogs of heterocyclic bases was supported by the Russian Science Foundation (grant No. 19-74-10048).

REFERENCES

1. Shi Z., Brugere-Picoux J. // Bull. Acad. Natl. Med. 2021. V. 205. P. 732–736
2. https://covid19.who.int/.
3. https://covid-nma.com/living_data/index.php.
4. Matyugina E.S., Valuev-Elliston V.T., Babkov D.A., Novikov M.S., Ivanov A.V., Kochetkov S.N., Balzarini J., Seley-Radtke K.L., Khandazhinskaya A.L. // Medchemcomm. 2013. V. 4. P. 741–748.
5. Matyugina E.S., Valuev-Elliston V.T., Geisman A.N., Novikov M.S., Chizhov A.O., Kochetkov S.N., Seley-Radtke K.L., Khandazhinskaya A.L. // Medchemcomm. 2013. V. 4. P. 1443–1451.
6. Matyugina E., Valyev-Elliston V.T., Novikov M.S., Alexandrova L.A., Chernoysova L.N., Kochetkov S.N., Khandazhinskaya A.L. // FEBS J. 2013. V. 280. P. 358–359.
7. Matyugina E.S., Novikov M.S., Babkov D.A., Valuev-Elliston V.T., Vanpouille C., Zicari S., Corona A., Tramontano E., Margolis L.B., Khandazhinskaya A.L., Kochetkov S.N. // Acta Naturae. 2015. V. 7. P. 113–115.
8. Matyugina E.S., Seley-Radtke K.L., Andronova V.L., Galegov G.A., Kochetkov S.N., Khandazhinskaya A.L. // Russ. J. Bioorg Chem. 2010. V. 36. P. 730–733.
9. Matyugina E., Khandazhinskaya A., Chernousova L., Andreevskaya S., Smirnova T., Chizhov A., Karpenko I., Kochetkov S., Alexandrova L. // Bioorgan. Med. Chem. 2012. V. 20. P. 6680–6686.
10. Matyugina E.S., Andreevskaya S.N., Smirnova T.G., Khandazhinskaya A.L. // Acta Naturae. 2012. V. 4. P. 73–77.
11. Matyugina E., Novikov M., Babkov D., Ozerov A., Chernousova L., Andreevskaya S., Smirnova T., Karpenko I., Chizhov A., Murthu P., Lutz S., Kochetkov S., Seley-Radtke K.L., Khandazhinskaya A.L./ / Chem. Biol. Drug Des. 2015. V. 86. P. 1387–1396.
12. Alzahrani K.J., Matyugina E.S., Khandazhinskaya A.L., Kochetkov S.N., Seley-Radtke K.L., de Koning H.P. // Bioorg. Med. Chem. Lett. 2017. V. 27. P. 3081–3086.
13. Khandazhinskaya A.L., Matyugina E.S., Solyev P.N., Wilkinson M., Buckheit K.W., Buckheit R.W., Chernousova L.N., Smirnova T.G., Andreevskaya S.N., Alzahrani K.J., Natto M.J., Kochetkov S.N., de Koning H.P., Seley-Radtke K.L. // Molecules. 2019. V. 24. P. 19E3433.
14. Klimenko A.A., Matyugina E.S., Logashenko E.B., Solyev P.N., Zenkova M.A., Kochetkov S.N., Khandazhinskaya A.L. // Molecules. 2018. V. 23. P. 2654.
15. Matyugina E.S., Logashenko E.B., Zenkova M.A., Kochetkov S.N., Khandazhinskaya A.L. // Heterocycl. Commun. 2015. V. 21. P. 259–262.
16. Kozlovskaya L.I., Volok V.P., Shtro A.A., Nikolaeva Y.V., Chistov A.A., Matyugina E.S., Belyaev E.S., Jegorov A.V., Snoeck R., Korshun V.A., Andrei G., Osolodkin D.I., Ishmukhametov A.A., Aralov A.V. // Eur. J. Med. Chem. 2021. V. 220. P. 113467.
17. Khandazhinskaya A., Eletskaya B., Fateev I., Kharitonova M., Konstantinova I., Barai V., Azhayev A., Hyvonen M., Keinanen T., Kochetkov S., Seley-Radtke K., Khomutov A., Matyugina E. // Organic. Biomol. Chem. 2021. V. 19. P. 7379–7389.
18. Matyugina E.S., Kochetkov S.N., Khandazhinskaya A.L.// Russ. Chem. Rev. 2021. V. 90. P. 1454–1491.

Extracellular Vesicles from Mycoplasmas Can Penetrate Eukaryotic Cells *In Vitro* and Modulate the Cellular Proteome

A. A. Mouzykantov[1*], E. V. Rozhina[2], R. F. Fakhrullin[2], M. O. Gomzikova[2], M. A. Zolotykh[2], O. A. Chernova[1], V. M. Chernov[1]

[1]Kazan Institute of Biochemistry and Biophysics, FRC Kazan Scientific Center of RAS, Kazan, 420111 Russia

[2]Kazan Federal University, Kazan, 420008 Russia

[*]E-mail: muzaleksei@mail.ru

Received July 07, 2021; in final form, November 09, 2021

DOI: 10.32607/actanaturae.11506

ABSTRACT **The extracellular vesicles (EVs) produced by bacteria transport a wide range of compounds, including proteins, DNA and RNA, mediate intercellular interactions, and may be important participants in the mechanisms underlying the persistence of infectious agents. This study focuses on testing the hypothesis that the EVs of mycoplasmas, the smallest prokaryotes capable of independent reproduction, combined in the class referred to as Mollicutes, can penetrate into eukaryotic cells and modulate their immunoreactivity. To verify this hypothesis, for the first time, studies of *in vitro* interaction between human skin fibroblasts and vesicles isolated from *Acholeplasma laidlawii* (the ubiquitous mycoplasma that infects higher eukaryotes and is the main contaminant of cell cultures and vaccines) were conducted using confocal laser scanning microscopy and proteome profiling, employing a combination of 2D-DIGE and MALDI-TOF/TOF, the Mascot mass-spectrum analysis software and the DAVID functional annotation tool. These studies have revealed for the first time that the extracellular vesicles of *A. laidlawii* can penetrate into eukaryotic cells *in vitro* and modulate the expression of cellular proteins. The molecular mechanisms behind the interaction of mycoplasma vesicles with eukaryotic cells and the contribution of the respective nanostructures to the molecular machinery of cellular permissiveness still remain to be elucidated. The study of these aspects is relevant both for fundamental research into the "logic of life" of the simplest prokaryotes, and the practical development of efficient control over hypermutable bacteria infecting humans, animals and plants, as well as contaminating cell cultures and vaccines.**

KEYWORDS **mycoplasma, vesicles, internalization, human fibroblasts, proteome.**

ABBREVIATIONS **EVs – extracellular vesicles; HSF – human skin fibroblast; 2D-DIGE – two-dimensional difference gel electrophoresis; MALDI-TOF/TOF – matrix-assisted laser desorption/ionization time-of-flight/time-of-flight; PBS – phosphate buffered saline.**

INTRODUCTION

It is unclear what are the molecular mechanisms underlying the interaction between mycoplasmas (the smallest prokaryotes capable of independent reproduction combined into the class Mollicutes) and the eukaryotic cells ensuring the persistence of infectious agents [1]. Thus far, it has been established that the interaction of micro- and macro-organism cells is mediated by EVs, which carry a broad range of compounds: among those, proteins, DNA, and RNA (including short RNAs) [2]. Bacterial EVs can penetrate into eukaryotic cells and modulate immunoreactivity; this ability has been well established in some of the pathogens of persistent infections. The EVs of mycoplasmas have been described [3, 4], but no evidence is available yet regarding their ability to penetrate into eukaryotic cells.

The present study addresses the ability of EVs from *A. laidlawii*, ubiquitous mycoplasma infecting higher eukaryotes and the main contaminant of cell cultures and vaccine preparations, to penetrate into eukaryotic cells cultured *in vitro* and modulate the cellular proteome.

EXPERIMENTAL SECTION

Cell cultures

A *A. laidlawii* PG8B culture in the middle of its growth log phase and a primary culture of human

skin fibroblasts (HSF – **H**uman **S**kin **F**ibroblast) were used. The fibroblasts were obtained from skin biopsies and cultured in an αMEM medium supplemented with 100 U/mL penicillin, 100 μg/mL streptomycin, 10% bovine serum and 2 mM *L*-glutamine at 37°C and 5% CO_2. Human skin samples were collected in accordance with the protocol of the experiment approved by the Expert Commission on Biomedical Ethics of the Kazan Federal University and the Republican Clinical Hospital (No. 218, November 15, 2012). Written informed consents were obtained from donors.

Isolation of extracellular vesicles

EVs from *A. laidlawii* were isolated as described in ref. [3]. The isolated vesicles were analyzed using transmission electron microscopy and scanning electron microscopy as described in ref. [3]. Microvesicles produced by HSFs in the presence and absence of *A. laidlawii* vesicles were isolated according to ref. [5]. The culture medium of the control and experimental HSF cultures was collected. Cells and debris were removed by centrifugation (1,500 *g*, 10 min). The supernatant was centrifuged at 100,000 *g* for 70 min (MLA-80 rotor, Beckman Coulter). The precipitates were resuspended in PBS and centrifuged at 100,000 *g* for 70 min. The washed precipitates were re-suspended in PBS, layered on an Optiprep density gradient (10-20-30-40-45%), and ultracentrifuged at 100,000 *g* for 17 h. Fractions were selected, washed three times to remove Optiprep, suspended in PBS, and stored at 4°C before analysis. The EVs from *A. laidlawii* were added to HSF in an amount of 100 μg (on the basis of total protein) and incubated for 4 h. The fibroblast cultures with and without EVs corresponded to the experiment and control, respectively. Vesicular DNA of *A. laidlawii* was detected by PCR, as described in ref. [6].

Confocal microscopy analysis

The preparations of EVs from *A. laidlawii* were stained with DiI, acridine orange and Hoechst 33342 to visualize the membrane, RNA and DNA, respectively. Preparations of HSF microvesicles were stained with anti-p53 antibodies conjugated to Alexa Fluor 647 and DiO for membrane imaging. The unbound dye molecules were removed using a concentrator with a cut-off limit of 3 kDa. The preparations were examined using a Carl Zeiss LSM 780 confocal laser scanning microscope.

To visualize the internalization of the EVs from *A. laidlawii*, the fibroblasts were cultured on cover glasses. EVs from *A. laidlawii* were stained with fluorescent dyes as described above and added to HSF. Fibroblasts were washed with buffer and fixed with 2.5% glutaraldehyde. Cell nuclei were stained with DAPI, and F-actin was stained with antibodies conjugated to Alexa Fluor 488. Slides were examined under a microscope; the data were analyzed using the ZEN 9.0 software.

Dark-field microscopy images of the stained HSF and EVs from *A. laidlawii* were obtained using an Olympus BX51 microscope [7]. The data were analyzed using the Exponent 7 software.

Enzyme immunoassay

For quantitative determination of cytokines, HSF cells were removed by centrifugation; the concentrations of interleukins (IL-6 and IL-8) in the supernatant were determined by ELISA (Vector-Best, Russia) according to the manufacturer's protocol.

Proteomic analysis

Proteomic analysis of HSF was performed according to ref. [8]. The cells were detached from the plastic using trypsin and washed three times using PBS to remove the nutrient medium. The cell precipitates were dissolved in a buffer (8 M urea, 2 M thiourea, 16.7% solution (30% CHAPS + 10% NP-40)) and treated with a mixture of nucleases (Micrococcal Nuclease Mix). The protein concentration in the samples was measured by the Bradford method. The proteins were stained with CyDye DIGE Cy3 (control) and CyDye DIGE Cy5 (experiment) dyes; the reaction was stopped with a 10 mM lysine solution. The staining effectiveness was tested using 1D electrophoresis in PAAG and gel scanning on a Typhoon Trio scanner. The samples were combined (equal amounts of each sample were collected), and dithiotreitol (DTT) up to 80 mM and ampholites 3-10 up to 0.2% were added and separated using 2D electrophoresis. The gels were scanned on a Typhoon Trio scanner. The gels were stained with silver nitrate to visualize protein spots.

The protein spots on the gels were analyzed using the PDQuest v.8.01 software (Bio-Rad). The spots in which the ratio between the protein contents in the control and experiment was higher than 1.5 were cut out. The gel pieces were washed in a 1 : 1 mixture of acetonitrile : 200 mM NH_4HCO_3 and then incubated with DTT and iodoacetamide. The gels were dehydrated using acetonitrile. A Trypsin working solution was added to the gel and incubated for 60 min at 4°C. Tryptic digestion was performed at 37°C overnight. Peptides were extracted using a 0.5 TFA solution. Protein identification using the Ultraflextreme MALDI-TOF/TOF mass spectrometer was carried out according to the protocol [8]. The peptide samples were mixed with a matrix solution (1% 2,5-dihydroxybenzoic acid, 20% acetonitrile, 0.5% TFA), applied

to the target, and air dried. Mass spectrometry was performed in the positive ion mode in the range of 500–4000 Da. The accuracy of monoisotopic mass measurements after recalibration on the basis of the peaks of trypsin autolysis was 0.007%, with allowance for the possible oxidation of methionine residues and modification of cysteine residues with acrylamide. The proteins were identified using the Mascot software in the Peptide Mass Fingerprint mode (Matrix Science) and the UniProt database. Protein identification was considered reliable ($p < 0.05$) at scores $\geqslant 44$.

The DAVID database (The Database for Annotation, Visualization, and Integrated Discovery) was used for the functional annotation of the identified proteins. The metabolic pathways and cellular processes in which these proteins participate were determined (according to KEGG); gene ontology was determined using GO (molecular function, biological process, cellular component).

Western blotting

Targeted quantitative determination of the proteins was carried out using western blotting. The proteins from HSF lysates were separated into PAAG and transferred to the Hybond C nitrocellulose membrane. Anti-p53, anti-HSP7C, and anti-β-actin antibodies (Sigma, USA), as well as secondary antibodies conjugated with horseradish peroxidase, were used. The membranes were incubated sequentially with primary and secondary antibodies and then stained with 3,3'-diaminobenzidine (Sigma). The gels were analyzed with the ImageJ software using β-actin as a control to normalize the signal intensity of the studied samples.

Statistical analysis

All the experiments were carried out in three replicas. The samples were analyzed 4 h after the incubation of HSF with mycoplasma EVs in all cases, and additionally 48 h after in the case of cytokine expression analysis. Statistical analysis was performed using the RStudio package. The values of $p < 0.05$ were considered statistically significant.

RESULTS AND DISCUSSION

Previously, we showed using PCR and RNA-Seq that EVs isolated from *A. laidlawii* PG8B contain DNA and RNA [9]. In this work, it was found that the EVs of *A. laidlawii* containing RNA are able to penetrate human skin fibroblasts cultured *in vitro*: mycoplasma EVs are found both in the cytoplasm and in the nucleus of eukaryotic cells during their co-incubation. *Figure 1G–I* shows the EVs of *A. laidlawii* visualized inside eukaryotic cells; *Fig. 1J*, *K* shows photos of isolated *A. laidlawii* obtained by transmission electron and scanning microscopy, respectively; *Fig. 2* shows the detection of DNA from *A. laidlawii* in fibroblasts using PCR.

Different fluorescent dyes make it possible to visualize DNA (Hoechst) and RNA (acridine orange), as well as the membrane lipids (DiI) of EVs from *A. laidlawii* (*Fig. 1A–C*). If the object simultaneously has a lipid membrane, DNA, and RNA, then when the corresponding photos are combined, a characteristic change in the color signal is recorded due to the superimposition of fluorescence, which is observed for mycoplasma EVs (*Fig. 1D*).

Since the size of the vesicles in *A. laidlawii* (the diameter of most of them is < 120 nm) does not allow a visualization of individual vesicles using confocal fluorescence microscopy, we also used higher resolution microscopy options to analyze vesicular preparations. Thus, the images of the EVs from *A. laidlawii* were obtained using transmission electron (*Fig. 1J*) and scanning (*Fig. 1K*) microscopy. Individual vesicles have their characteristic morphology. They are spherical nanostructures surrounded by a membrane, their size ranging from 30 to 120 nm.

When using dark-field fluorescence microscopy, mycoplasma vesicles are recorded as aggregates (*Fig. 1E–F*). Similar images were obtained for EVs from *Pseudomonas aeruginosa* [10]: stained with fluorescent dyes (DiO and EdU), isolated and internalized by A549 epithelial lung cells, the EVs of this bacterium were visualized in the form of clusters using confocal laser scanning microscopy. This may be due to the superimposition of the emissions of the dyes used from the adjacent individual objects. It still remains to be investigated whether this is also related to the peculiarities of the pathways for the internalization of bacterial EVs.

Short bacterial RNAs in vesicles might function as eukaryotic microRNAs and suppress translation by binding to mRNA targets [11]. This assumption was verified in model experiments with the short RNAs homologous to $tRNA^{Met}$ contained in *P. aeruginosa* vesicles. The interaction of the corresponding bacterial vesicular RNAs led to the suppression of IL-8 expression and inhibition of the innate immune response, contributing to the persistence of microorganisms. Earlier, we showed that EVs from *A. laidlawii* also contain short RNAs, including homologous $tRNA^{Met}$ [9]. However, no significant changes in the expression of IL-8, as well as another critical proinflammatory cytokine, IL-6, were detected in our study upon infection of HSF with the vesicles of mycoplasma (22.71 ± 0.89 and 19.69 ± 2.86 pg/mL in the control and experiment for IL-8, $p < 0.05$; 11.14 ± 0.22 and 11.42 ± 0.78 pg/ml in the control and experiment for IL-6, $p < 0.05$).

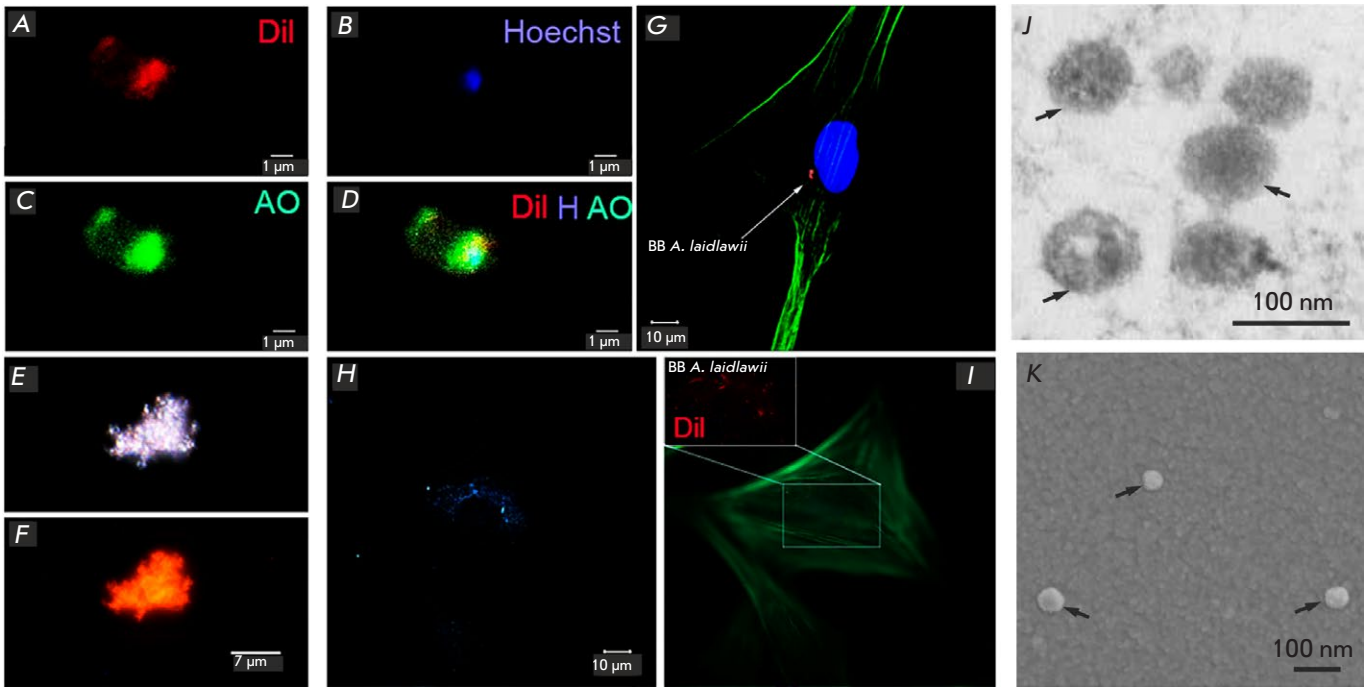

Fig. 1. Interaction of human skin fibroblasts with EVs of *A. laidlawii*. Visualization of the purified EVs of *A. laidlawii* (*A*–*F*, *J*, *K*) and the ones incubated with HSF (*G*–*I*). Confocal laser microscopy (*A*–*D*, *G*): (*A*) DiI tracer (vesicular lipid staining, red); (*B*) Hoechst (vesicular DNA staining, blue); (*C*) acridine orange (AO) (vesicular RNA staining, green); (*D*) merged images (DiI, Hoechst, AO). Dark-field (*E*, *H*) and fluorescence (*F*, *I*) microscopy: (*E*) dark-field image of the aggregate of vesicles and (*F*) with fluorescence of the DiI tracer; (*G*) fluorescence EVs of *A. laidlawii* stained with DiI (red) in the HSF cavity. The cell nucleus was stained with DAPI, actin filaments, with antibodies conjugated with Alexa Fluor 488 dye (green); (*H*) dark-field image of EVs of *A. laidlawii* in the HSF cavity; and (*I*) during the fluorescence of the DiI tracer, HSF actin filaments were stained with antibodies conjugated with Alexa Fluor 488 dye (green). Transmission electron (*J*) and scanning (*K*) microscopy of EVs of *A. laidlawii* (arrows indicate individual vesicles)

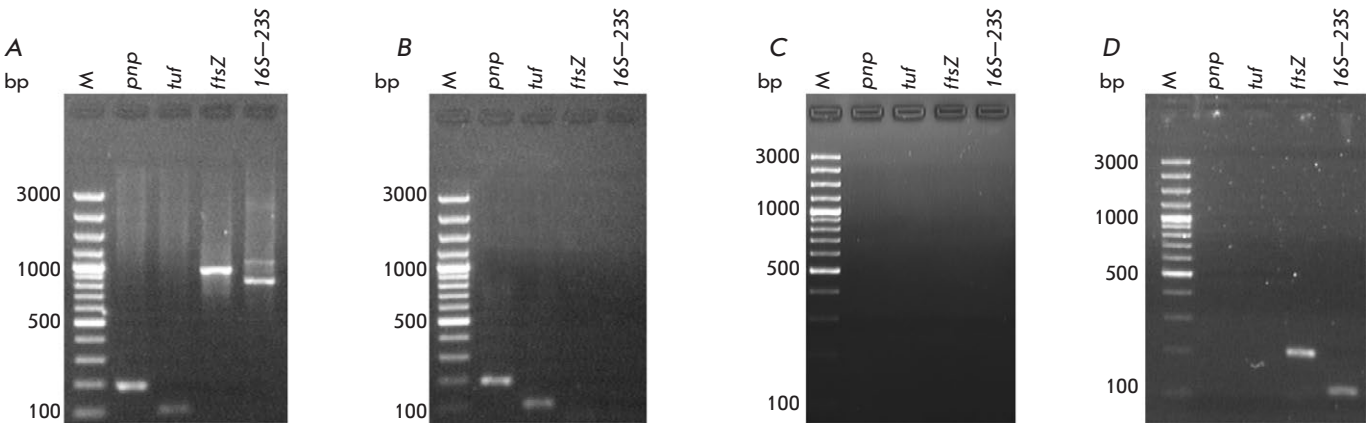

Fig. 2. Detection of *A. laidlawii* DNA in mycoplasma EVs and HSF by PCR. DNA was extracted from *A. laidlawii* cells (*A*), EVs of *A. laidlawii* (*B*), fibroblasts (HSF) incubated without and with the EVs of *A. laidlawii* (*C*, *D*, respectively). M – DNA Ladder Marker. In PCR, the primers specific to the nucleotide sequences of the *pnp*, *tuf*, and *ftsZ* genes (encoding polyribonucleotide nucleotidyl transferase, elongation factor Tu, and cell division protein FtsZ, respectively), as well as the 16S-23S rRNA intergenic spacer region of *A. laidlawii*, were used

The time and level of the changes in cytokine expression can vary significantly depending on the medium, cell line, bacterial strain producing vesicles, and the quantitative ratio between eukaryotic cells and bacterial vesicles. The time-dependent response of human fibroblasts to the internalization of *A. laidlawii* cells and expression of cytokines has still not been studied. There is only one known study [12] devoted to the analysis of time-dependent changes in the transcriptomic profile of human cells (HeLa) during internalization and persistence of mycoplasma cells (*Mycoplasma hominis*). In this study, significant changes in the expression of cytokine genes were revealed 4 and 48 h after the initiation of the co-incubation of bacterial and eukaryotic cells: in both cases, the IL-6 gene turned out to be in the stress-reactive pool, but not IL-8. In this regard, we analyzed the samples not only 4 h but also 48 h after the initiation of the co-incubation of mycoplasma EVs and HSF. A statistically significant change in the expression of IL-6 was detected (6.42 ± 0.6 and 5.13 ± 0.28 pg/mL in the control and experiment, respectively; $p < 0.05$), but not in the expression of IL-8 (8.59 ± 3.23 and 17.64 ± 5.88 pg/mL in the control and experiment, respectively; $p < 0.05$). The data obtained by us attest to the differences in the molecular mechanisms for the induction of immunocompromise in mycoplasmas and classical bacteria.

Tolerance of the innate immunity associated with the lack of any operational modulation of the expression of proinflammatory cytokines (IL-6 and IL-8) does not cancel cellular reactivity to the infectious agent: the molecular signature of the infection can be detected using modern high-resolution methods, including variants of immune electron microscopy, as well as omics profiling [13]. Having used a combination of 2D-DIGE and MALDI-TOF/TOF (the proteomic analysis technology based on the application of the two-dimensional gel electrophoresis of polypeptides stained with different (in the control and experiment, respectively) fluorescent dyes), followed by the identification of differentially presented proteins using MALDI-TOF/TOF and the Mascot software in the mode of Peptide Mass Fingerprint, as well as the DAVID functional annotation tool, we found that a HSF infection with the extracellular vesicles of *A. laidlawii* leads to a modulation of the fibroblast proteome: changes in the protein representation are recorded 4 h after the initiation of the incubation of mycoplasma EVs with eukaryotic cells; i.e., before any changes in the secretion of IL-6 and IL-8 cytokines are detected. Differentially expressed fibroblast proteins (deposited by us in the ProteomeXchange database, No. PXD027040) are involved in the folding, cytoskeleton formation, biogenesis of EVs (exosomes and microvesicles), immunoreactivity, and cell proliferation. Most of the identified proteins are stress-reactive: they can participate in the cellular response to bacterial and/or viral infections [14]. Among those, there are proteins that are associated with both a positive and negative regulation of apoptosis (TERA, LEG1 and ENPL, CH60, ANXA5, GRP78, HSPB1, CRYAB, respectively).

The known limitations of the 2D-DIGE and MALDI-TOF/TOF proteomic analysis variants (low-copy-number proteins cannot be visualized when gels are stained; high-copy-number proteins overlap and hide nearby spots; strongly alkaline proteins are poorly isoelectrofocused; high-molecular-weight proteins do not pass through the pores of the gels used; low-molecular-weight proteins cannot be effectively separated; hydrophobic proteins do not dissolve in the buffer used), including with respect to the detection of a pool of differentially expressed proteins in the eukaryotic cell (the ratio of the visualized, analyzed, reported, and theoretical proteomes differs significantly from the ratio in bacterial cells with a small genome, which is optimal for the relevant studies) [15, 16] determine its limits: not all proteins differentially expressed in a eukaryotic cell can be detected using global proteomic profiling. In this regard, in order to assess the expression of the relevant specific proteins that are not included in the identified stress-reactive pool, one needs to conduct additional targeted analyses (e.g., using Western blotting, which is also recommended for validating global proteomic profiling data [17]). Since p53, the key player in the outcome of pro- and anti-apoptotic processes, was not found within the pool of the identified proteins [18], we conducted a targeted analysis of the representation of this protein in the fibroblasts, as well as in the extracellular vesicles secreted by the fibroblasts (*Fig. 3*). According to our findings, infection of human skin fibroblasts with *A. laidlawii* vesicles increases the amount of p53 in cells and does not suppress the secretion of the protein: p53 is found in the extracellular vesicles derived from the fibroblasts of both the control and experimental samples.

The extracellular vesicles of eukaryotes include different groups of vesicles secreted into the extracellular space, which differ in function, size, composition, and biogenesis: exosomes, microvesicles, and apoptotic bodies. Microvesicles form upon protrusion of the plasma membrane; the diameter of these structures is 100–1,000 nm, and their density is 1.25–1.30 g/mL. Apoptotic bodies are released from the plasma membrane of cells at the late stage of apoptosis; the diam-

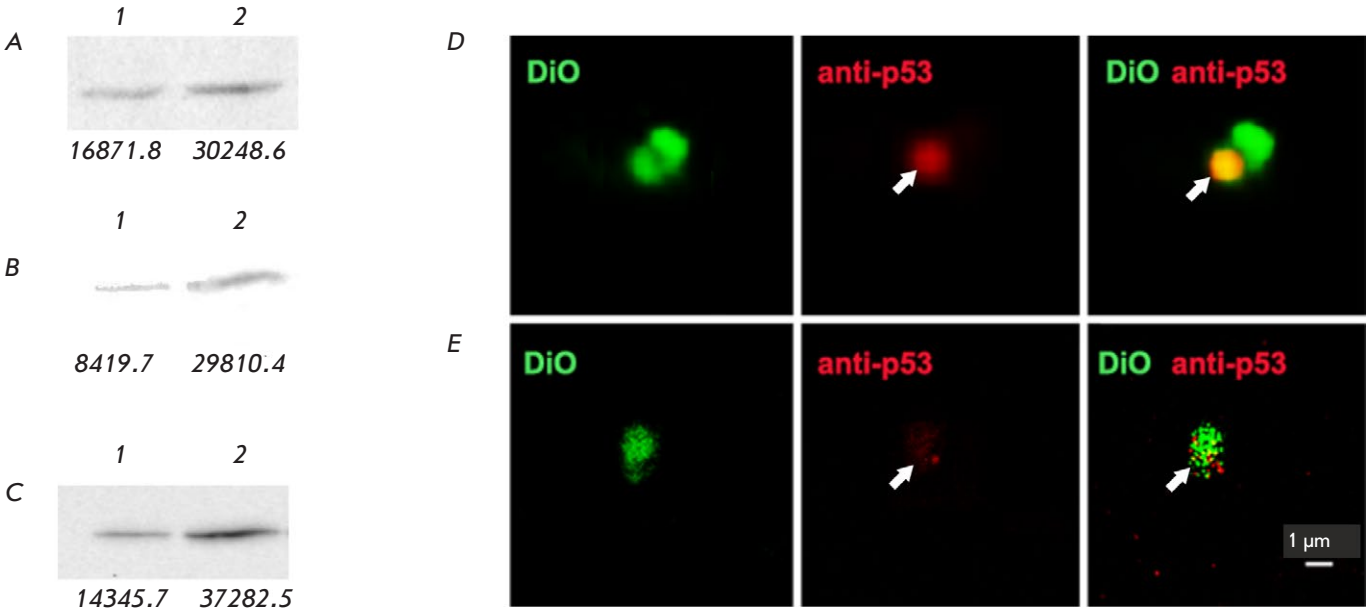

Fig. 3. Detection of proteins in human skin fibroblasts using Western blotting (*A*–*C*) and p53 in HSF-derived microvesicles by confocal laser scanning microscopy (*D*, *E*). Western blotting of cellular proteins with anti-β-actin (*A*), anti-p53 (*B*), and anti-HSP7C (*C*) antibodies. Lanes 1 and 2: proteins of fibroblasts incubated without and with the EVs of *A. laidlawii*, respectively. The intensity of the protein bands is determined by the ImageJ software and is indicated below the lanes. Protein p53 in the microvesicles produced by human skin fibroblasts incubated with (*D*) and without (*E*) EVs of *A. laidlawii*. Arrows indicate the p53 signal

eter of these structures is 1–5 μm, and their density is 1.18–1.28 g/mL. Exosomes form inside cells from late endosomes known as multivesicular bodies (when a late endosome merges with the plasmalemma, the exosomes find themselves outside the cell); the diameter of these structures is 30–150 nm, and their density is 1.13–1.21 g/mL [19, 20]. The difference in the size and density of vesicles belonging to the various groups is responsible for the likelihood of their differentiation: apoptotic bodies can be distinguished from smaller sized EVs (exosomes and microvesicles) by microscopy, while exosomes and microvesicles can be separated at the stages of ultracentrifugation and Optiprep density gradient ultracentrifugation because of the difference in their size and density. In the centrifugation mode used in our study, exosomes are not precipitated to the test tube bottom and lie higher in the density gradient than microvesicles. High-resolution microscopy visualization of the samples allows one to determine the size of these structures. No structures whose size would correspond to that of apoptotic bodies were found among our preparations: the diameter of individual vesicles isolated from the eukaryotic cells in the studied samples lay in the range of 200–800 nm, which indicates that they could belong to the group of microvesicles.

CONCLUSIONS

We have shown that EVs from *A. laidlawii*, a ubiquitous mycoplasma that is the main contaminant of cell cultures, are able to penetrate into eukaryotic cells *in vitro* and modulate the cellular proteome. The molecular mechanisms behind the interaction of mycoplasma vesicles with eukaryotic cells and the contribution of the corresponding nanostructures to the molecular machinery of cellular permissivity have yet to be clarified. Elucidation of these mechanisms is important both for fundamental research into the simplest prokaryotes and for the practical development of mechanisms to control hypermutable bacteria that infect humans, animals and plants, as well as contaminate cell cultures and vaccine preparations. ●

This work was carried out with the financial support of the State Assignment of the Federal Research Center "Kazan Scientific Center" of the Russian Academy of Sciences. The authors express their gratitude to the Head of the Laboratory of Cell Defense Mechanisms of the Institute of Cytology of the Russian Academy of Sciences, Doctor of Biological Sciences I.V. Guzhova for assistance in conducting targeted protein analysis.

REFERENCES

1. Browning G., Citti C. Mollicutes: molecular biology and pathogenesis. Caister: Acad. Press, 2014. 333.
2. Munhoz da Rocha I.F., Amatuzzi R.F., Lucena A.C.R., Faoro H., Alves L.R. // Front. Cell Infect. Microbiol. 2020. V. 10. P. 593160.
3. Chernov V.M. Mouzykantov A.A. Baranova N.B., Medvedeva E.S., Grygorieva T.Yu., Trushin M.V., Vishnyakov I.E., Sabantsev A.V., Borchsenius S.N., Chernova O.A. // J. Proteomics. 2014. V. 110. P. 117–2.
4. Gaurivaud P., Ganter S., Villard A., Manso-Silvan L., Chevret D., Boulé C., Monnet V., Tardy F. // PLoS One. 2018. V. 13:e0208160.
5. Iwai K., Minamisawa T., Suga K., Yajima Y., Shiba K. // J. Extracell. Vesicles. 2016. V. 5. P. 30829.
6. Mouzykantov A.A., Medvedeva E.S., Baranova N.B., Chernova O.A., Chernov V.M. // Data Brief. 2020. V. 32. P. 106049.
7. Akhatova F., Danilushkina, A., Kuku, G., Saricam, M., Culha, M., Fakhrullin, R. // Bull. Chem. Soc. Jpn. 2018. V. 91. № 11. P. 1640–1645.
8. Chernov V.M., Chernova O.A., Medvedeva E.S., Mouzykantov A.A., Ponomareva A.A., Shaymardanova G.F., Gorshkov O.V., Trushin M.V. // J. Proteomics. 2011. V. 74. № 12. P. 2920–2936.
9. Chernov V.M., Chernova O.A., Mouzykantov A.A., Medvedeva E.S., Baranova N.B., Malygina T.Y., Aminov R.I., Trushin M.V. // FEMS Microbiol. Lett. 2018. V. 1. P. 365.
10. Bitto N.J., Chapman R., Pidot S., Costin A., Lo C., Choi J., D'Cruze T., Reynolds E.C., Dashper S.G., Turnbull L., Whitchurch C.B., Stinear T.P., Stacey K.J., Ferrero R.L. // Sci. Rep. 2017. V. 7. P. 7072.
11. Koeppen K., Hampton T.H., Jarek M., Scharfe M., Gerber S.A., Mielcarz D.W., Demers E.G., Dolben E.L., Hammond J.H., Hogan D.A. et al. // PLoS Pathog. 2016. V. 12. e1005672.
12. Hopfe M., Deenen R., Degrandi D., Köhrer K., Henrich B. // PLoS One. 2013. V. 8. e54219.
13. Chernov V.M., Chernova O.A., Mouzykantov A.A., Lopukhov L.L., Aminov R.I. // Expert Opin. Drug Discov. 2019. V. 14. № 5. P. 455–468.
14. Wan Q., Song D., Li H., He M.L. // Signal Transduct. Target Ther. 2020. V. 5. № 1. P. 125.
15. Westermeier R., Naven T. Proteomics in Practice. Weinheim: WILEY-VCH, 2002.
16. Wasinger V.C., Pollack J.D., Humphery-Smith I. // Eur. J. Biochem. 2000. V. 267. P. 1571–1582.
17. Poli G., Ceni E., Armignacco R., Ercolino T., Canu L., Baroni G., Nesi G., Galli A., Mannelli M., Luconi M. // Oncotarget. 2015. V. 6. P. 5695–5706.
18. Aubrey B.J., Kelly G.L., Janic A., Herold M.J., Strasser A. // Cell Death Differ. 2018. V. 25. № 1. P. 104–113.
19. Cesselli D., Parisse P., Aleksova A., Veneziano C., Cervellin C., Zanello A., Beltrami A.P. // Front. Physiol. 2018. V. 9. P. 1394.
20. Zhang Y., Liu Y., Liu H., Tang W.H. // Cell Biosci. 2019. V. 9. P. 19.

A Comparative Analysis of CSF and the Blood Levels of Monoamines As Neurohormones in Rats during Ontogenesis

A. R. Murtazina, N. S. Bondarenko, T. S. Pronina, K. I. Chandran, V. V. Bogdanov, L. K. Dilmukhametova, M. V. Ugrumov*
Institute of Developmental Biology RAS, Moscow, 119334 Russia
*E-mail: michael.ugrumov@mail.ru
Received July 12, 2021; in final form, October 15, 2021
DOI: 10.32607/actanaturae.11516

ABSTRACT **According to the literature, the cerebrospinal fluid (CSF) in the cerebral ventricles contains numerous neuron-derived physiologically active substances that can function as neurohormones and contribute to volume neurotransmission in the periventricular region of the brain. This study was aimed at carrying out a comparative analysis of CSF and the blood levels of monoamines in rats during ontogenesis as an indicator of age-related characteristics of monoamine transport to body fluids and their function as neurohormones in volume neurotransmission in the periventricular region of the brain. We have shown that CSF in the perinatal period and adulthood contains the most functionally significant monoamines: dopamine, noradrenaline, and serotonin. A comparison of the monoamine levels in the CSF and blood of animals of different age groups revealed that CSF contains monoamines of predominantly neuronal (cerebral) origin and almost no monoamines derived from the general circulation. We also established that monoamines are found in the CSF at physiologically active levels that allow them to act as neurohormones in both reversible volume neurotransmission in the adult brain and irreversible regulation of brain development in the perinatal period.**
KEYWORDS **rat, brain, cerebrospinal fluid, plasma, monoamines, ontogenesis.**
ABBREVIATIONS **3-MT – 3-methoxytyramine; 5-HT – 5-hydroxytryptamine (serotonin); A – adrenaline; ALDH – aldehyde dehydrogenase; HVA – homovanillic acid; HIAA – 5-hydroxyindoleacetic acid; DβH – dopamine β-hydroxylase; DA – dopamine; DHBA – 3,4-dihydroxybenzylamine; DOPAC – 3,4-dihydroxyphenylacetic acid; COMT – catechol-O-methyltransferase; MAO – monoamine oxidase; NA – noradrenaline; P – postnatal day; PNMT – phenylethanolamine-N-methyltransferase; E – embryonic day.**

INTRODUCTION

Monoamine dopamine (DA), noradrenaline (NA), and serotonin (5-hydroxytryptamine, 5-HT), which are synthesized in brain neurons, play an important role in the regulation of brain function via volume neurotransmission (action on the entire neuronal surface) and synaptic neurotransmission (action in the synaptic area) [1]. In adult animals, brain monoamines are responsible for the reversible autoregulation of neurons synthesizing them and the regulation of other "-ergic" neurons. In the perinatal period of ontogenesis, monoamines act on the same receptors on target neurons and have an irreversible morphogenetic effect on the development of these neurons and the brain as a whole [2–5].

There is evidence that neuron-derived monoamines in the cerebrospinal fluid (CSF) in the cerebral ventricles enter the brain and participate as neurohormones in volume neurotransmission due to the absence of a CSF–brain barrier for them [1, 6]. Although monoamines are also synthesized in peripheral organs and reach the blood vessels, their neurohormonal effect on the brain can take place only before closure of the blood–brain barrier, which occurs in the early postnatal period [7]. However, an insignificant exchange of monoamines between the CSF and blood is possible in ontogenesis: (a) in the area of the choroid plexuses in the lateral ventricles, where substances enter the CSF from the blood; (b) at the border between ventricles in the caudal region of the brain

and the vascular system; (c) in the circumventricular organs of the brain lacking the blood–brain barrier [7, 8].

Despite the abundance of evidence to the presence of physiologically active substances, including monoamines, in the CSF and blood, the pattern of changes in the monoamine level in these body fluids during ontogenesis has not been elucidated yet. In addition, the monoamine level gradient at the CSF–blood border during various stages of ontogenesis has never been assessed before. Considering our recent data on the absence of a CSF barrier for monoamines during ontogenesis in rats [9], the levels of monoamines should be the same in the intercellular space in the periventricular region of the brain and in the CSF. Finding an answer to these questions will make it possible to determine at what stages of ontogenesis the CSF level of monoamines is high enough for them to act as neurohormones in the regulation of brain development and function.

Based on the above, the purpose of our study was to perform a comparative analysis of the CSF and blood levels of monoamines in rats during ontogenesis as an indicator of age-related characteristics of monoamine transport to body fluids and their participation as neurohormones in volume neurotransmission in the brain. To achieve this goal, the following tasks were set: (a) determine the level of monoamines DA, NA, adrenaline (A), and 5-HT as an indicator of the secretory activity of the corresponding neurons in rat CSF on embryonic day 18 (E18) and postnatal days 5 (P5) and 30 (P30); (b) determine the plasma levels of monoamines in these animals; (c) evaluate the ratio of CSF to the plasma levels of the monoamines as an integrated index of the existence of barriers for monoamines between the cerebral ventricles and the general circulation.

EXPERIMENTAL PROCEDURES

Animals

The study was performed in female and male Wistar rats on E18 and male Wistar rats on P5 and P30 (*Fig. 1*). To obtain dated offspring, pregnant female rats weighing 250–350 g were used. The day when sperm was detected in the vaginal smear was considered E1; the day of pup birth was considered P1. The animals were maintained under standard vivarium conditions with a 12-h light/dark cycle and free access to food and water. The experiments were carried out in accordance with the guidelines of the National Institutes of Health (NIH Guide for the Care and Use of Laboratory Animals) and the Bioethics Committee of the Koltsov Institute of Developmental Biology (Minutes No. 3 dated September 10, 2020, and Minutes No. 44 dated December 24, 2020).

All animal procedures were performed under anesthesia with either chloral hydrate (Sigma, USA) at a dose of either 100 mg/kg on P5 and 400 mg/kg on P30 and E18 or 1% isoflurane on P30 (Laboratorios Karizoo, Spain).

Collection of rat CSF and blood on E18, P5, and P30

CFS was collected from rats on E18 (n = 112), P5 (n = 30), and P30 (n = 20) (*Fig. 1*). On gestation day 18, the rats were subjected to laparotomy, fetuses were removed from the uterus leaving the umbilical cord intact. After that, a glass micropipette connected by a Teflon tube to a Hamilton syringe filled with a saline solution was inserted into each of the fetal lateral ventricles according to [10]. The micropipette's tip was filled with a small air bubble to avoid saline mixing with the CSF. An average of 1.5 ± 0.5 μL of CSF was obtained from both fetal ventricles.

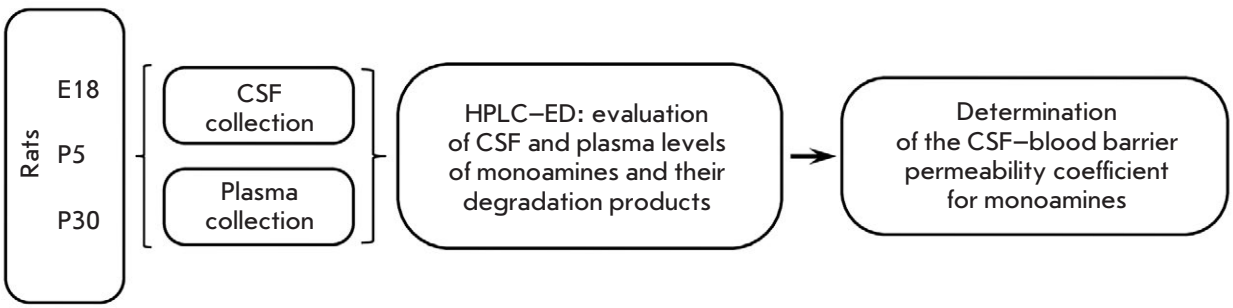

Fig. 1. Scheme of experiments in rats on embryonic day 18 (E18) and postnatal days 5 (P5) and 30 (P30): CSF and plasma collection, evaluation of the CSF and plasma levels of monoamines and their degradation products, determination of the CSF–blood barrier permeability coefficient for monoamines. HPLC–ED – high-performance liquid chromatography with electrochemical detection

CSF was collected from the cisterna magna of rats on P5 and P30 according to the previously described technique [11]. For this, an animal's head was secured in a stereotaxic apparatus (Narishige Scientific Instrument Lab., Japan) to access the cisterna magna. Then, a glass micropipette connected to a Hamilton syringe was inserted stereotaxically into the cisterna magna using the system described above. A total of 25 ± 10 and 55 ± 15 μl of CSF were collected from each rat on P5 and P30, respectively. After that, $HClO_4$ and 3,4-dihydroxybenzylamine (DHBA) (Sigma, USA), which is an internal standard for the determination of monoamines and their degradation products, were added to the CSF samples to final concentrations of 0.1 M and 25 pM, respectively. CSF obtained from 14 fetuses was used as the E18 sample, and CSF of three animals was used as P5 and P30 samples. CSF samples were frozen in liquid nitrogen and stored at –70°C prior to determination of monoamines DA, NA, and 5-HT and their main degradation products 3,4-dihydroxyphenylacetic acid (DOPAC), 3-methoxytyramine (3-MT), homovanillic acid (HVA), and 5-hydroxyindoleacetic acid (HIAA) (*Fig. 2*).

On P30, CSF was sampled from both the cisterna magna and lateral ventricles. For this, a guide cannula for a microdialysis probe (CMA-11 Guide Cannula, CMA, Sweden) was inserted stereotaxically into the lateral ventricle of the brain in rats (n = 4) anesthetized with isoflurane based on coordinates calculated according to the rat brain atlas (–0.4 mm caudal and 1.4 mm lateral to the bregma; 2.2 mm deep) [12]. The cannula was fixed to the skull bone using micro bone screws and dental cement (Protakril-M, Ukraine). After 48 h, a microdialysis probe (CMA 11 55 kDa Microdialysis Probe, CMA, Sweden) filled with artificial CSF (147 mM NaCl, 2.7 mM KCl, 1 mM $MgCl_2$, and 1.2 mM $CaCl_2$) was inserted into the guide cannula. The probe was connected to a CMA 4004 Microdialysis Pump (CMA, Sweden) through Teflon tubes. Microdialysis was initiated 3 h after probe insertion: lateral ventricles were perfused for 20 min at a flow rate of 2 μl/min. The resulting dialysis sample was mixed with 4 μl of 1 N $HClO_4$, frozen in liquid nitrogen and stored at –70°C until determination of monoamines and their degradation products (*Fig. 2*).

After CSF was sampled, blood was collected from the left ventricle of the heart of the same animals using an insulin syringe under chloral hydrate anesthesia. The volume of blood samples collected from the animals on days E18, P5, and P30 was 30 ± 5, 100 ± 10, and 2,000 ± 20 μL, respectively. Blood samples were supplemented with 5% ethylenediaminetetraacetic acid (EDTA) (Sigma, USA) and 10% sodium metabisulfite (Sigma). Samples were centrifuged at 1,350 g and 4°C for 10 min, the supernatant (plasma) was collected and mixed with 10% 1 N $HClO_4$ and 25 pmol of DHBA. Plasma was centrifuged at 16,500 g and 4°C for 20 min, the supernatant was frozen in liquid nitrogen and stored at –70°C until determination of monoamines and their degradation products (*Fig. 2*).

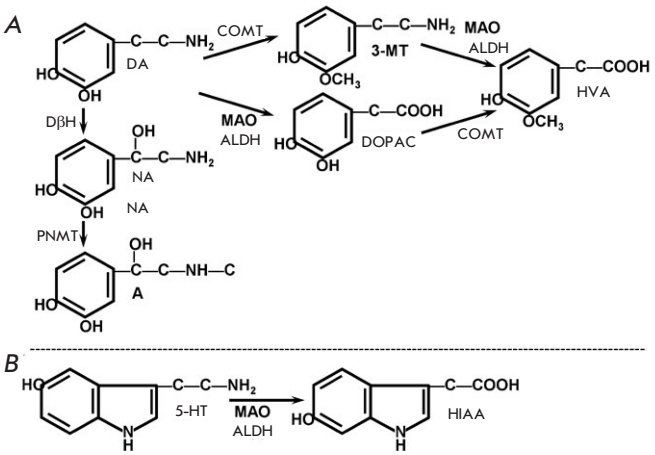

Fig. 2. Monoamines and some products of their degradation. DA – dopamine; NA – noradrenaline; A – adrenaline; DOPAC – 3,4-dihydroxyphenylacetic acid; 3-MT – 3-methoxytyramine; HVA – homovanillic acid; 5-HT – serotonin; HIAA – 5-hydroxyindoleacetic acid

High-performance liquid chromatography with electrochemical detection

The concentration of monoamines and their degradation products in CSF, plasma, and microdialysis samples was determined using high-performance liquid chromatography with electrochemical detection. CSF and plasma samples were divided into two parts. One part was extracted by precipitating catecholamines and their degradation products onto aluminum oxide, another part was not precipitated but was used directly to measure the 5-HT and HIAA levels. Microdialysis samples were not precipitated.

The test substances were separated using a 4 × 100-mm reversed-phase ReproSil-Pur ODS-3 column with a pore diameter of 3 μm (Dr. Majsch GMBH, Germany) at 28°C and a mobile phase flow rate of 1 ml/min using a LC-20ADsp Liquid Chromatograph Pump (Shimadzu, Japan) at a potential of 850 mV. Citrate-phosphate buffer (0.1 M; pH 2.58) containing 0.3 mM sodium octanesulfonate, 0.1 mM EDTA, and 8% acetonitrile (all Sigma reagents) was used as the mobile phase. Monoamines were deter-

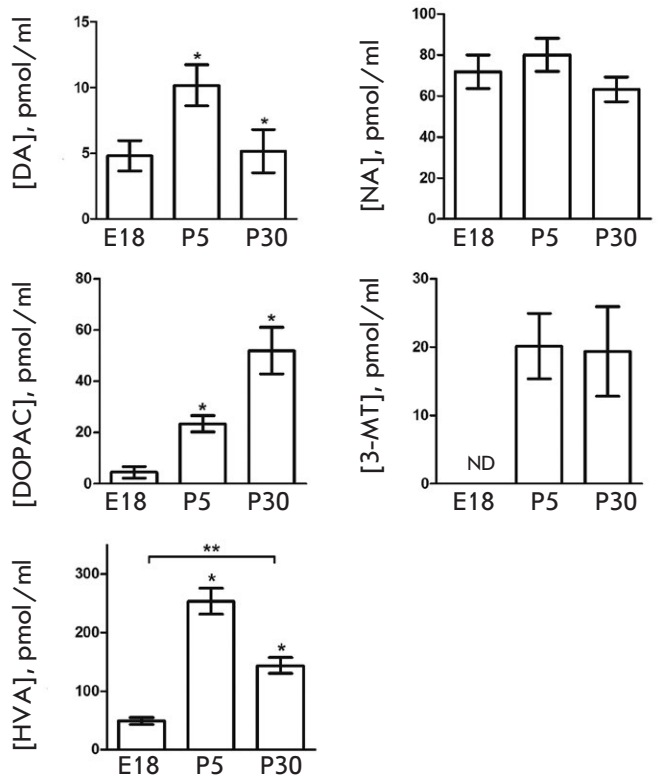

Fig. 3. CSF levels of catecholamines and some products of their degradation in rats on embryonic day 18 (E18) and postnatal days 5 (P5) and 30 (P30). DA – dopamine; NA – noradrenaline; DOPAC – 3,4-dihydroxyphenylacetic acid; 3-MT – 3-methoxytyramine; HVA – homovanillic acid. $^{*}p < 0.05$ – comparison with the previous age; $^{**}p < 0.05$ – comparison of the selected parameters; ND – not detected

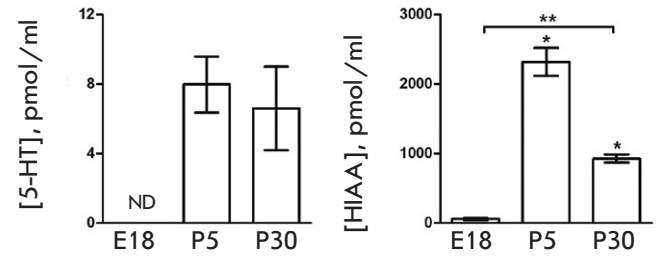

Fig. 4. CSF levels of serotonin (5-HT) and its degradation product 5-hydroxyindoleacetic acid (HIAA) in rats on embryonic day 18 (E18) and postnatal days 5 (P5) and 30 (P30). $^{*}p < 0.05$ – comparison with the previous age; $^{**}p < 0.05$ – comparison of the selected parameters; ND – not detected

mined using a DECADE II electrochemical detector (AntecLeyden, Netherlands) with a glassy carbon working electrode (0.85 V) and a silver chloride reference electrode. The peaks of monoamines and their metabolites were determined based on their retention time in a standard solution.

Statistical data analysis

A statistical analysis was performed using the GraphPad Prism 6.0 software (USA). Data are presented as the mean ± standard error of the mean (mean ± SEM). Differences were considered statistically significant at $p < 0.05$; $0.05 < p < 0.1$ was regarded as a tendency to differences; the differences were considered insignificant at $p > 0.1$. The statistical significance of the results was determined using the parametric Student's *t*-test (*t*-test) and the nonparametric Mann–Whitney U-test (U-test); the Bonferroni correction was used for multiple testing.

RESULTS

CSF levels of catecholamines, 5-HT, and their degradation products in the cisterna magna in rats during ontogenesis

The DA level is approximately 5 pmol/ml on E18; it increases twofold on P5 and reaches that of fetuses on P30 (*Fig. 3*).

The NA level does not change during the entire period of ontogenesis and remains at a high level (~70 pmol/ml) in all age groups. In contrast to DA and NA, A was detected in the CSF during neither the prenatal nor postnatal period.

In addition to catecholamines, their degradation products 3-MT (except for day E18), DOPAC, and HVA are found in the CSF of rats of all age groups (*Fig. 3*). Although 3-MT is not detected in the fetuses, it is observed at a fairly high level (~20 pmol/ml) in the CSF on P5 and P30. In contrast to 3-MT, DOPAC is detected as early as E18 at a concentration of almost 4.5 pmol/ml. This parameter increases about fivefold on P5 and decreases by 55% on P30. The end product of DA degradation, HVA, is detected at a high level (almost 50 pmol/ml) in the CSF as early as E18. This parameter increases about fivefold on P5 and decreases by 45% on P30.

No 5-HT is detected in rat CSF on E18; however, a high CSF level of 5-HT (8 pmol/ml) is noted on P5 and P30 (*Fig. 4*). The level of the end product of 5-HT degradation, HIAA, is quite high on E18; it exceeds that of 5-HT by almost 300 times. On P30, the CSF level of HIAA is reduced by more than twofold compared to P5 (*Fig. 4*).

Monoamines and their degradation products in the lateral ventricles of rats on P30

Of all monoamines and their degradation products, only DOPAC and HIAA were detected by microdialysis in the lateral ventricles of the rat brain on P30. At least three measurements were made to establish the baseline level of the test substances. The following DOPAC and HIAA levels were detected in dialysis samples: 5.2 ± 1.1 and 105.7 ± 14.8 pmol/ml, respectively.

Levels of catecholamines, 5-HT, and their degradation products in rat plasma during ontogenesis

The plasma level of DA in rats on E18 does not exceed 0.4 pmol/ml, it increases sixfold on P5, and decreases about twofold on P30 (*Fig. 5*). The pattern of A level changes during ontogenesis is about the same as that of DA: it increases 3.5-fold from E18 to P5 and then decreases threefold on P30. The NA level is an order of magnitude higher than that of DA in all age groups. Unlike for the CSF, A is determined in the plasma: its level increases by more than 50-fold from E18 to P5 and decreases 2.5-fold by P30. Both catecholamines and their degradation products are found in the plasma. While 3-MT is detected in the plasma only on P30, DOPAC (at a low concentration) is observed as early as E18. The DOPAC level increases significantly by P5 and remains the same by P30. The level of HVA, the end product of DA degradation, increases more than fourfold from E18 to P5 and becomes lower than that of the fetuses by P30 (*Fig. 5*).

The plasma level of 5-HT is approximately 5.5 pmol/ml on E18 (*Fig. 6*). It increases 85-fold by P5 and then decreases almost to that of the embryos on P30. The HIAA level changes in a similar way: it increases 10-fold from E18 to P5 and becomes two times lower than that during the embryonic period on P30.

Ratio of CSF to the plasma levels of monoamines and their degradation products in rats during ontogenesis

The CSF levels of DA, NA, and their degradation products are many times higher than their plasma levels in all age groups (*Fig. 7A*). However, maximum differences are noted during different periods of ontogenesis. For instance, the peaks in DA and NA levels are observed on E18, while DOPAC, 3-MT, and HVA levels reach their maximum on P30.

The CSF levels of 5-HT and HIAA exceed those in plasma on P30 (for 5-HT), P5 and P30 (HIAA) (*Fig. 7B*). It should be noted that the CSF level of 5-HT on P5 is 60 times lower than that in plasma.

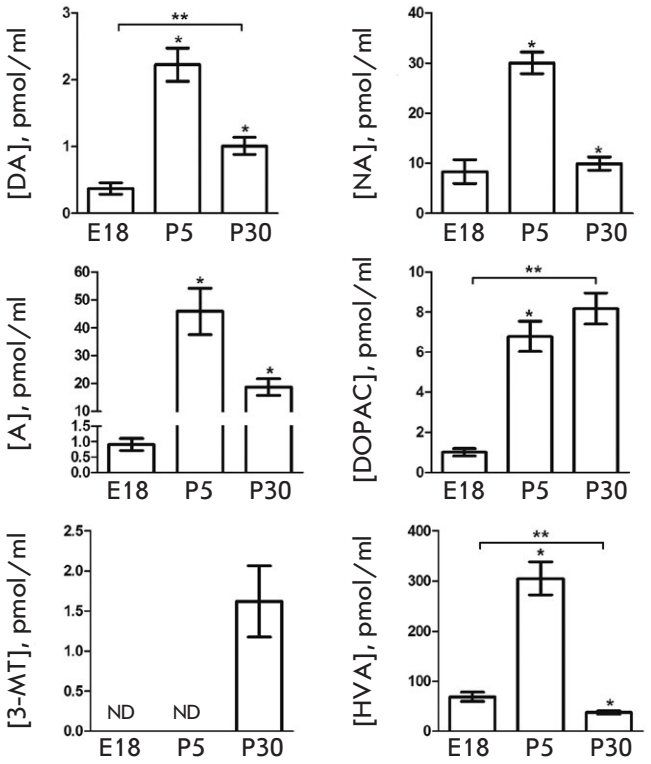

Fig. 5. Plasma levels of catecholamines and some products of their degradation in rats on embryonic day 18 (E18) and postnatal days 5 (P5) and 30 (P30). DA – dopamine; NA – noradrenaline; A – adrenaline; DOPAC – 3,4-dihydroxyphenylacetic acid; 3-MT – 3-methoxytyramine; HVA – homovanillic acid. $^{*}p < 0.05$ – comparison with the previous age; $^{**}p < 0.05$ – comparison of the selected parameters; ND – not detected

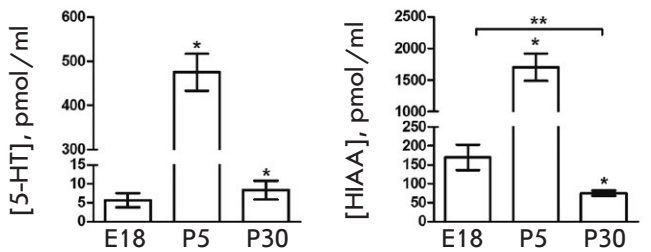

Fig. 6. Plasma levels of serotonin (5-HT) and its degradation product 5-hydroxyindoleacetic acid (HIAA) in rats on embryonic day 18 (E18) and postnatal days 5 (P5) and 30 (P30). $^{*}p < 0.05$ – comparison with the previous age; $^{**}p < 0.05$ – comparison of the selected parameters

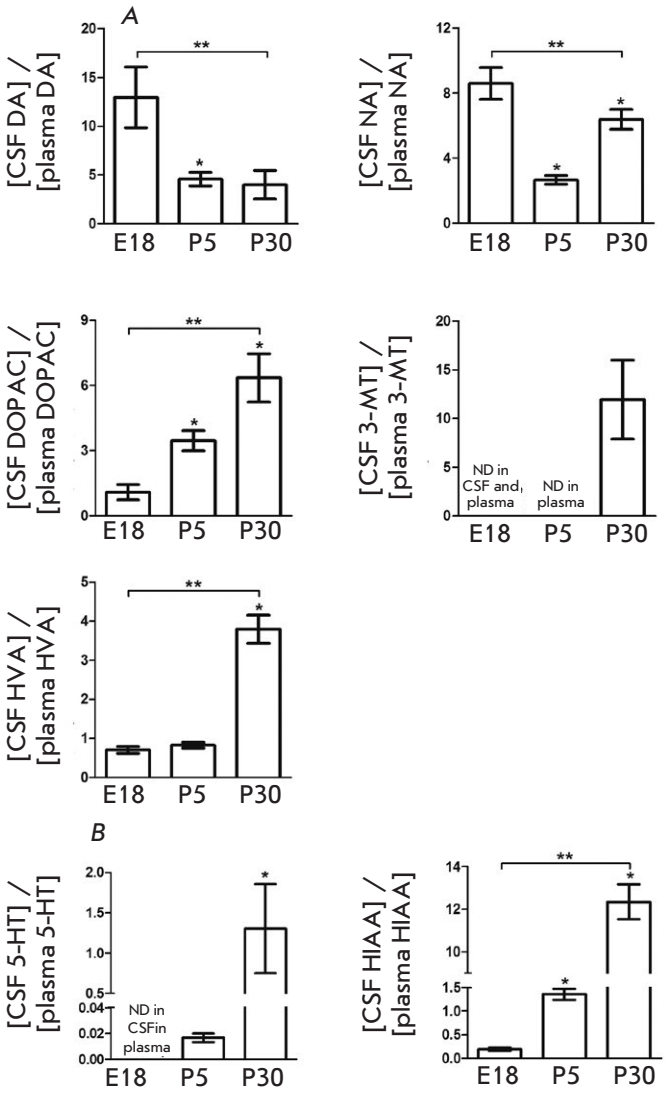

Fig. 7. Ratio of CSF to the plasma levels of catecholamines (*A*), 5-HT (*B*), and some products of their degradation (*A*, *B*) in rats on embryonic day 18 (E18) and postnatal days 5 (P5) and 30 (P30). DOPA – 3,4-dihydroxyphenylacetic acid; 3-MT – 3-methoxytyramine; HVA – homovanillic acid; 5-HIAA – 5-hydroxyindoleacetic acid. $^{*}p < 0.05$ – comparison with the previous age; $^{**}p < 0.05$ – comparison of the selected parameters; ND – not detected

DISCUSSION

The main goal of this work was to perform a comparative analysis of the CSF and blood levels of monoamines in rats during ontogenesis as an indicator of age-related characteristics of monoamine release into the body fluids and their role as neurohormones in brain development and function. Special attention is paid to the CSF as a body fluid that, on the one hand, receives monoamines from the brain and, on the other hand, releases monoamines to the periventricular region of the brain in the absence of a CSF–brain barrier, which then acts as neurohormones in volume neurotransmission. The discovery of the CSF-contacting neurons was the historical basis for hypothesizing the release of physiologically active substances from the brain to the CSF [8, 13].

CSF monoamines acting as neurohormones are potential participants in volume neurotransmission and the morphogenetic control of brain development

Despite the fact that dozens of neurotransmitters and neuromodulators are synthesized in brain neurons, monoamines DA, NA, and A are the most common classical neurotransmitters in the brain. These monoamines are involved in the regulation of the functional activity of target neurons in adult animals and the regulation of neuron and brain development in the perinatal period [2–5].

Based on the concept of qualitative differences in monoamine action at different stages of ontogenesis, the CSF level of monoamines was determined in rats at three age periods. The first age group included E18 rats, since the following events take place by this time: (a) formation of neurons from progenitor cells is completed; (b) the differentiating neurons migrate to the sites of their final localization in the brain; (c) neurons express a specific phenotype; and (d) axons of the differentiating neurons reach brain ventricles and blood vessels in the circumventricular organs, forming pathways for neurohormones to enter the CSF (axo-ventricular contacts) and blood vessels (axo-vascular contacts). The second age group included P5 rats. The following events take place by this time: (a) migration of differentiating neurons to the sites of their final localization is completed; (b) axo-ventricular and axo-vascular contacts are established; and (c) afferent synaptic innervation of neurons continues to form. The third age group included P30 rats. The following events take place by this time: (a) formation of synaptic contacts ends; (b) formation of the blood–brain barrier, which prevents penetration of most non-lipid neurotransmitters from the brain into the blood and vice versa, is completed [14–17].

From the standpoint of the neurohormonal effect of CSF monoamines on the brain neurons, the CSF level of monoamines is considered the most important functional parameter. Indeed, the previous, mainly *in vitro*, studies demonstrated that monoamines have a neurotransmitter effect on neurons at a wide range of concentrations: from 10^{-11} to 10^{-8} M [18]. Moreover, monoamines can affect neurons at even lower concentrations *in vivo* [19–21].

At the first stage of our study, it was necessary to determine whether the qualitative composition and level of monoamines change with the CSF flow from the lateral ventricles, where CSF is formed as a result of plasma filtration from the vessels of the choroid plexus to the cisterna magna: the caudal part of the ventricular system. For this, we compared the composition of monoamines and their degradation products in rat CSF obtained from the lateral ventricles by microdialysis and rat CSF of the cisterna magna collected on P30 using a micropipette. We found all monoamines and their degradation products detected by us in the cisterna magna, while only some products of monoamine degradation were observed in the lateral ventricles: DOPAC and HIAA. These data indicate that monoamines enter the CSF not from the plasma of the choroid plexus vessels and the nerve tissue surrounding the lateral ventricles but mainly from the nervous tissue caudal to the lateral ventricles of the brain.

Further, the composition of CSF obtained from the cisterna magna only was determined. Catecholamines DA and NA were found in the CSF of rats of all age groups; however, changes in their levels were significant with age. For instance, NA is present in the CSF at a significant level (7.2×10^{-8} M) on E18; it remains the same on P5 (6.3×10^{-8} M) and P30 (6.3×10^{-8} M). The obtained data indicate that noradrenergic neurons secrete monoamines into the CSF during the prenatal and postnatal periods. This assumption is supported by the fact that, according to the *in vitro* data, NA at approximately the same level as that of CSF can exert a neurotransmitter effect on neurons in adult rats [22–24]. Considering also the fact that receptors for NA and other monoamines are expressed even during the prenatal period [25–27], our data suggest that CSF NA is not only able to participate as a neurohormone in volume neurotransmission in adult animals but also exert a morphogenetic effect on the brain neurons in the perinatal period.

Age-related changes in the CSF levels of DA and NA have fundamental differences. The first difference is that the CSF level of DA (0.3×10^{-9} M) is at least an order of magnitude lower than that of NA (0.48×10^{-8} M) on E18. However, this does not reduce the possible morphogenetic effect of DA on target neurons. The CSF level of DA increases twofold (1×10^{-8} M) by P5, although it remains significantly lower than that of NA. It should be noted that the level of DA could have increased in the perinatal period (E18–P5) much more, if the activity of DA breakdown enzymes, MAO and COMT, had not increased simultaneously. This is evidenced by a significant increase in the levels of the products of MAO and COMT enzymatic activity: DOPA, 3-MT, and HVA in the perinatal period. Nevertheless, an increase in the CSF level of DA on P5 significantly increases the probability of its morphogenetic effect on differentiating target neurons and brain development in general [28]. The second difference in age-related changes between the CSF levels of DA and NA is a twofold decrease in the DA level on P30 compared to P5. This is an important, albeit indirect, indicator that the CSF DA can have a morphogenetic effect on target neurons, mainly in the early postnatal period.

The age-related pattern of the CSF level of 5-HT differs significantly from that of catecholamines. For instance, almost no 5-HT is detected in the CSF on E18, while its level almost reaches that of DA on P5. The CSF level of 5-HT could have increased to an even greater extent on P5, if not for a significant increase in the activity of the 5-HT degradation enzyme MAO by that period, as indicated by the high level of the product of its enzymatic breakdown: HIAA. The 5-HT level remains the same by P30. The above data indicates that the CSF 5-HT can both participate in volume neurotransmission in the postnatal period and regulate the development of target neurons and the brain in general in the early postnatal period in rats.

The brain is the only source of CSF monoamines during ontogenesis

As shown in our study, the CSF of rats on P5 and P30 contains monoamines at physiologically active levels. Furthermore, in contrast to 5-HT, catecholamines are also present in the CSF on E18. However, these data cannot serve as direct evidence that the brain is the only source of CSF monoamines. Indeed, we cannot exclude that monoamines enter the CSF not only from the brain neurons but from the bloodstream as well in the absence of a blood–brain barrier for monoamines in the perinatal period [14, 29, 30], with also taking into account the possibility of a metabolism between the CSF and blood in the choroid plexus in the lateral ventricles, in circumventricular organs, and the area of the caudal venous sinus even in adult animals [7]. In addition, one should not forget the fact that there are such important sources of monoamines as the adrenal glands, gastrointestinal tract, and the peripheral sympathetic nervous system [31–33].

An answer to the question of whether the brain is the only source of monoamines in the CSF can be found in a first approximation by calculating the integrated index of permeability of all possible barriers on the way of monoamines from the blood to the CSF in the form of the ratio of CSF to blood levels of monoamines. Three options can be considered: (1) the permeability coefficient equals to unity, indicating the

absence of a barrier between the CSF and the blood; (2) the permeability coefficient is greater than unity, which indicates the presence of a barrier for monoamine entry from the CSF to the blood; (3) the permeability coefficient is less than unity, which indicates the existence of a barrier preventing monoamine entry from the blood to the CSF.

To calculate the coefficient of permeability of barriers between the CSF and blood for monoamines, both the CSF and blood levels of monoamines were measured in rats during ontogenesis. Age-related changes in the plasma levels of the monoamines DA, NA, and 5-HT were found to be similar. These monoamines were detected in the blood at insignificant levels on E18, their levels increased significantly by P5 and then decreased almost to the E18 level by P30. However, the levels of individual monoamines in each age group varied significantly. For instance, on P5, the plasma level of NA was 15 times higher than that of DA and more than 150 times lower than that of 5-HT.

Determination of the ratio of CSF to the blood levels of monoamines showed that the permeability coefficient for barriers between the CSF and blood on E18 is 8.5 and 13 for NA and DA, respectively. This means that CSF catecholamines originate from the brain. These calculations could not be carried out for 5-HT, since 5-HT is not detected in the CSF of the fetus at such a time point. Although the permeability coefficient for catecholamines is reduced significantly, it remains above unity in the postnatal period. This indicates that, during this period, catecholamines enter the CSF only from the brain neurons.

In contrast to catecholamines, the permeability coefficient for 5-HT on P5 is only slightly less than unity and, then, sharply increases by P30. This indicates that the barrier preventing the exchange of monoamines between the CSF and blood also exists for 5-HT. The most important evidence that monoamines can penetrate the barriers on their way from the blood to the CSF is the high blood level of E in rats on P5 and P30 and its absence in the CSF in rats of the same age. The obtained data confirm the existence of barriers preventing the entry of substances from the CSF into the blood and vice versa in the pre- and postnatal period [34–36].

CONCLUSION

The following conclusions were made: (1) the cerebrospinal fluid of rats in the perinatal period and adulthood contains the most functionally significant monoamines: dopamine, noradrenaline, and serotonin; (2) the cerebrospinal fluid contains monoamines of predominantly neuronal (cerebral) origin and almost no monoamines derived from the general circulation; (3) monoamines are found in the cerebrospinal fluid at physiologically active levels that allow them to act as neurohormones in volume neurotransmission: as morphogenetic factors in irreversible regulation of neuronal development in the perinatal period and reversible regulation of the functional activity of target neurons in adult animals. ●

This study was supported by the Russian Science Foundation grant No. 20-14-00325.

REFERENCES

1. Fuxe K., Borroto-Escuela D.O. // Neural. Regen. Res. 2016. V. 11. № 8. P. 1220–1223.
2. Ugrumov M.V. // Int. J. Dev. Biol. 1997. V. 41. № 6. P. 809–816.
3. Gaspar P., Cases O., Maroteaux L. // Nat. Rev. Neurosci. 2003. V. 4. № 12. P. 1002–1012.
4. Pronina T., Ugrumov M., Adamskaya E., Kuznetsova T., Shishkina I., Babichev V., Calas A., Tramu G., Mailly P., Makarenko I. // J. Neuroendocrinol. 2003. V. 15. № 6. P. 549–558.
5. Izvolskaia M., Duittoz A.H., Tillet Y., Ugrumov M.V. // Brain Struct. Funct. 2009. V. 213. № 3. P. 289–300.
6. Shaywitz B.A., Anderson G.M., Cohen D.J. // Brain Res. 1985. V. 349. № 1–2. P. 225–232.
7. Abbott N.J., Pizzo M.E., Preston J.E., Janigro D., Thorne R.G. // Acta Neuropathol. 2018. V. 135. № 3. P. 387–407.
8. Kaur C., Ling E.A. // Histol. Histopathol. 2017. V. 32. № 9. P. 879–892.
9. Murtazina A.R., Pronina T.S., Chandran K.I., Dilmukhametova L.K., Bondarenko N.S., Bogdanov V.V., Blohin V.V., Ugrumov M.V. // Russ. J. Dev. Biol. 2021. V. 52. № 6. P. 467–475.
10. Zappaterra M.W., LaMantia A.S., Walsh C.A., Lehtinen M.K. // J. Vis. Exp. 2013. № 73. P. e50333.
11. Liu L., Duff K. // J. Vis. Exp. 2008. № 21. P. e960.
12. Ashwell K.W.S., Paxinos G. Atlas of the developing rat nervous system. 3d ed. London: Acad. Press, 2008.
13. Vígh B., Manzano e Silva M.J., Frank C.L., Vincze C., Czirok S.J., Szabó A., Lukáts A., Szél A. // Histol. Histopathol. 2004. V. 19. № 2. P. 607–628.
14. Ugrumov M.V. // Neurochem. Res. 2010. V. 35. № 6. P. 837–850.
15. Ugrumov M.V. Mechanisms of neuroendocrine regulations. Moscow: Nauka, 1999. 299p.
16. Nguyen L., Rigo J.M., Rocher V., Belachew S., Malgrange B., Rogister B., Leprince P., Moonen G. // Cell Tissue Res. 2001. V. 305. № 2. P. 187–202.
17. Niederkofler V., Asher T.E., Dymecki S.M. // ACS Chem. Neurosci. 2015. V. 6. № 7. P. 1055–1070.
18. Thomas G.B., Cummins J.T., Smythe G., Gleeson R.M., Dow R.C., Fink G., Clarke I.J. // J. Endocrinol. 1989. V. 121. P. 141–147.
19. Liu J., Morrow A.L., Devaud L., Grayson D.R., Lauder J.M. // J. Neurosci. 1997. V. 17. № 7. P. 2420–2428.
20. Dai S.Q., Yu L.P., Shi X., Wu H., Shao P., Yin G.Y., Wei Y.Z.

// Braz. J. Med. Biol. Res. 2014. V. 47. № 9. P. 759–765.
21. Martínez-Méndez R., Padilla-Cortés P., Gómez-Chavarín M., Gutiérrez-Ospina G. // PeerJ. PrePrints. 2016. V. 4. P. e1782v1. https://doi.org/10.7287/peerj.preprints.1782v1
22. Baba H., Shimoji K., Yoshimura M. // Anesthesiology. 2000. V. 92. № 2. P. 473–484.
23. Ghosh A., Purchase N.C., Chen X., Yuan Q. // Front. Cell. Neurosci. 2015. V. 9. P. 450.
24. Bacon T.J., Pickering A.E., Mellor J.R. // Cerebral Cortex. 2020. V. 30. № 12. P. 6135–6151.
25. Bruinink A., Lichtensteiger W. // J. Neurochem. 1984. V. 43. № 2. P. 578–581.
26. Schlumpf M., Bruinink A., Lichtensteiger W., Cortés R., Palacios J.M., Pazos A. // Dev. Pharmacol. Ther. 1987. V. 10. № 6. P. 422–435.
27. Happe H.K., Coulter C.L., Gerety M.E., Sanders J.D., O'Rourke M., Bylund D.B., Murrin L.C. // Neuroscience. 2004. V. 123. № 1. P. 167–178.
28. Zhang L., Lidow M.S. // Int. J. Dev. Neurosci. 2002. V. 20. № 8. P. 593–606.
29. Miyaguchi H., Kato I., Sano T., Sobajima H., Fujimoto S., Togari H. // Pediatr. Int. 1999. V. 41. № 4. P. 363–368.
30. Murtazina A.R., Nikishina Y.O., Bondarenko N.S., Dil'mukhametova L.K., Sapronova A.Y., Ugrumov M.V. // Brain Struct. Funct. 2019. V. 224. № 9. P. 3059–3073.
31. Catecholamine research: From molecular insights to clinical medicine: Advances in Behavioral Biology. V. 53 / Eds. Nagatsu T., Nabeshima T., McCarty R., Goldstein D.S. Springer, 2002. 558 p.
32. Goldstein D.S., Eisenhofer G., KopinI.J.l. // J. Pharmacol. Exp. Ther. 2003. V. 305. № 3. P. 800–811.
33. Bornstein S.R., Ehrhart-Bornstein M., Androutsellis-Theotokis A., Eisenhofer G., Vukicevic V., Licinio J., Wong M.L., Calissano P., Nisticò G., Preziosi P., et al. // Mol. Psychiatry. 2012. V. 17. № 4. P. 354–358.
34. Redzic Z. // Fluids Barriers CNS. 2011. V. 8. № 1. P. 3.
35. Saunders N.R., Daneman R., Dziegielewska K.M., Liddelow S.A. // Mol. Aspects. Med. 2013. V. 34. № 2–3. P. 742–752.
36. Bueno D., Parvas M., Nabiuni M., Miyan J. // Semin. Cell Dev. Biol. 2020. V. 102. P. 3–12.

Mechanism of Action of Monoclonal Antibodies That Block the Activity of the Lethal Toxin of *Bacillus Anthracis*

Ya. O. Romanenko, A. K. Riabko*, M. A. Marin, A. S. Kartseva, M. V. Silkina, I. G. Shemyakin, V. V. Firstova

Federal Budget Institution of Science State Research Center for Applied Microbiology and Biotechnology of Rospotrebnadzor, Obolensk, Moscow Region, 142279 Russia

*E-mail: ryabko_alena@mail.ru

Received March 19, 2021; in final form March 22, 2021

DOI: 10.32607/actanaturae.11387

ABSTRACT **Neutralization of the lethal toxin of *Bacillus anthracis* is an important topic of both fundamental medicine and practical health care, regarding the fight against highly dangerous infections. We have generated a neutralizing monoclonal antibody 1E10 against the lethal toxin of *Bacillus anthracis* and described the stages of receptor interaction between the protective antigen (PA) and the surface of eukaryotic cells, the formation of PA oligomers, assembly of the lethal toxin (LT), and its translocation by endocytosis into the eukaryotic cell, followed by the formation of a true pore and the release of LT into the cell cytosol. The antibody was shown to act selectively at the stage of interaction between *Bacillus anthracis* and the eukaryotic cell, and the mechanism of toxin-neutralizing activity of the 1E10 antibody was revealed. The interaction between the 1E10 monoclonal antibody and PA was found to lead to inhibition of the enzymatic activity of the lethal factor (LF), most likely due to a disruption of true pore formation by PA, which blocks the release of LF into the cytosol.**

KEYWORDS **anthrax, monoclonal antibodies, toxin-neutralizing activity, cytometric analysis, protective antigen, lethal factor.**

ABBREVIATIONS ***B. anthracis* – *Bacillus anthracis*; LT – lethal toxin; LF – lethal factor; rLF – recombinant lethal factor of *B. anthracis*; EF – edema factor; PA – protective antigen; rPA – recombinant protective antigen of *B. anthracis*; rPA-FITC – recombinant protective antigen of *B. anthracis* conjugated to fluorescein-5-isothiocyanate; rLF-Cy5 – recombinant lethal factor of *B. anthracis* conjugated to a fluorescent dye Cy5; MAPKK – mitogen-activated protein kinase kinase; MEK – mitogen activated kinase; mAb – monoclonal antibody; TNA – toxin-neutralizing activity; PBS – phosphate-buffer saline; MES – 2-(N-morpholino) ethanesulfonic acid; PAGE – polyacrylamide gel; PBS-T – phosphate-buffered saline with 0.05% Tween-20.**

INTRODUCTION

Anthrax is an anthropozoonotic infection caused by the gram-positive, aerobic, spore-forming, rod-shaped bacterium *Bacillus anthracis*. Depending on the route of bacterial administration, three primary forms of the disease are distinguished: gastrointestinal (alimentary route), cutaneous (contact route), and pulmonary (inhalation route). All forms of the disease can be fatal, but the airborne route of pathogen transmission is the most dangerous to human life [1, 2]. *B. anthracis* spores are from 1 to 5 μm in size, which enables them to easily enter the pulmonary alveoli upon inhalation. After penetration into the lungs, *B. anthracis* spores do not germinate but are quickly and efficiently phagocytized by alveolar macrophages and dendritic cells, which are then transported through the lymphatic ducts to the thoracic lymph nodes where the spores become vegetative cells that spread throughout the body and destroy cells [3].

The pathogenesis of anthrax is associated with two binary toxins and a capsule, which are encoded by the pX01 and pX02 plasmids. The pX01 plasmid encodes three components of the anthrax toxin: 83 kDa lethal factor (LF), 89 kDa edema factor (EF), and 85 kDa protective antigen (PA). The second plasmid, pX02, encodes the genes involved in the synthesis of the poly-D-glutamyl capsule. Removal of any plasmid decreases the virulence of bacteria [4].

The (effector) subunit A of anthrax binary toxins is represented by LF and EF, and the subunit B is represented by PA. Combining the A and B subunits results in the lethal toxin (LT), composed of PA and LF, and the edema toxin (ET), composed of PA and EF. The binary toxins were named according to their biological effects in animal models. Intradermal injection of ET (PA + EF) causes edema, and injection of a high concentration of LT (PA + LF) causes severe hypotension and death [5, 6].

The key subunit of toxins in the pathogenesis of anthrax is the PA that binds to receptors on the surface of immunocompetent cells and ensures the penetration of LF and EF into the cell. The receptor interaction of 83 kDa PA with the cell membrane is accompanied by the cleavage of a 20 kDa fragment by host furin-like proteases, resulting in the formation of 63 kDa PA. Monomeric PA63 oligomerizes and forms heptameric or octameric structures called prepores. Three LF or EF molecules bind to one heptamer, and 4 molecules bind to an octamer [7, 8]. After assembly of PA and LF/EF, the formed complex is internalized by the cell through clathrin-dependent endocytosis. The resulting endosome is gradually acidified. With changes in the environment's pH level, PA changes its conformation, penetrates into the endosome, and forms a true pore for LF/EF translocation into the cytosol [9]. LF is a zinc metalloprotease that cleaves mitogen-activated protein kinase kinases (MAPKs) in the cytosol, which ultimately leads to cell apoptosis [10, 11]. *Figure 1* presents all assembly stages and the toxic activity of LT and ET from *B. anthracis* as well as the key stages of the antitoxic activity of the monoclonal antibodies that specifically interact with the *Bacillus anthracis* protective antigen domain IV.

One of the interesting ways in which to protect the body from *B. anthracis* is to develop protective therapeutic antibodies. In recent years, therapeutic antibodies have become a potent tool in the fight against a whole range of pathologies [12, 13]. They are used as targeted agents for the elimination of pathological cells [14, 15]. Antibodies are very actively used as protective agents in toxic infections [11, 16, 17].

Figure 1 shows several possible pathways for disrupting the interaction between the toxin and the eukaryotic cell. In particular, it is possible to block the binding of PA to a cellular receptor or disrupt the formation of an adequate heptameric complex. It is also possible to block the binding of the toxin effector subunits to the prepore or inhibit the conversion of the prepore to the pore, which results in the inhibition of the kinase cascade.

To date, several LT-neutralizing monoclonal antibodies (mAbs) have been developed; most of these

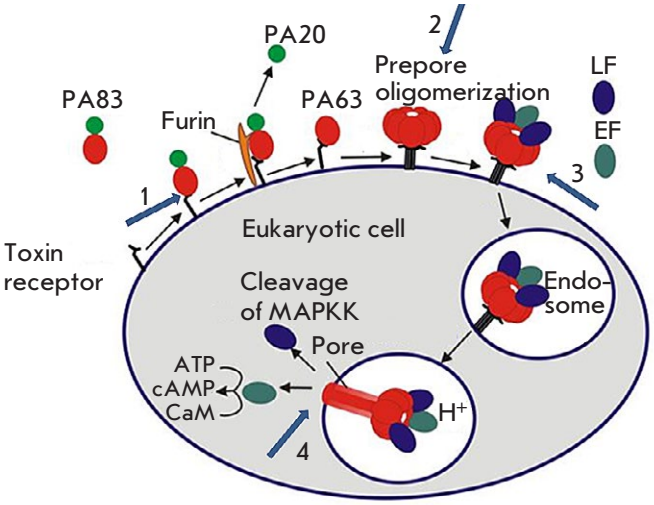

Fig. 1. Schematic model of the assembly and activity of *B. anthracis* toxins.
Numbered arrows indicate the key stages of the antitoxic activity of the 1E10 monoclonal antibody specifically interacting with domain IV of the *B. anthracis* protective antigen: 1. Binding of the mAb to the PA receptor; 2. Prevention of the assembly of an oligomeric PA63 prepore; 3. Inhibition of LF and EF binding to PA and prevention of endocytosis of toxin effector subunits; 4. Inhibition of conversion of the oligomeric PA63 prepore to the pore

are murine mAbs, but there are also human toxin-neutralizing antibodies (Raxibacumab, GlaxoSmith-Kline). Nevertheless, the search for new, more effective LT-neutralizing antibodies continues [18].

Previously, we generated 1E10 mAb which exhibits specific activity against the PA domain IV [19]. The results of studies on the J774A.1 cell line and a mouse model showed a pronounced ability of 1E10 mAb to neutralize anthrax LT (some data are not published). The purpose of this study was to identify the inhibition mechanism of the LT cytotoxic effect by the monoclonal antibody 1E10.

EXPERIMENTAL

In this study, we used recombinant proteins: protective antigen (rPA) according to [19] and lethal factor (rLF) according to [20]. The recombinant proteins have amino acid sequences of native *B. anthracis* PA and LF without signal peptides, as indicated in UniProtKB: P13423 (PAG_BACAN) and P15917 (LEF_BACAN), respectively, fused with the N-terminal 6×His-tag and c-myc epitope. rPA and rLF expressed in *E. coli* BL21 (DE3) were purified from the cell lysate by chromatography using a cOmplete His-Tag

Purification Resin metal-chelate sorbent (Roche, Germany). Biotinylated recombinant proteins were prepared by conjugation to biotin sulfosuccinimidyl (sulfo-NHS) ester (Sigma, USA). Fluorophore-labeled recombinant proteins (rPA-FITC and rLF-Cy5) were obtained by conjugation to FITC (Thermo Fisher, USA) and the Cy5 mono-reactive dye (Amersham, UK).

Evaluation of PA adhesion on the surface of J774A.1 macrophages in the presence of 1E10 mAb by flow cytofluorometry

To assess the binding of PA to receptors on the surface of J774A.1 macrophages (ATCC®TIB-67™), 1×10^6 cells per sample were incubated with fluorochrome-labeled rPA-FITC or rPA-FITC pre-incubated with 1E10 mAb at an equimolar ratio at 37°C for 1 h. J774A.1 cells were incubated with rPA-FITC or rPA-FITC + mAb at 37°C in a CO_2 incubator with gentle stirring on an orbital shaker for 1 h. After incubation, all samples were washed three times with phosphate-buffer saline heated to 37°C (PBS; 137 mM NaCl, 2.7 mM KCl, 10 mM Na_2HPO_4, 1.76 mM KH_2PO_4, pH 7.4) and fixed with 1% formalin. The samples were analyzed on a FACSAria III flow cytometer (Becton Dickinson, USA) using the BD FACSDiva software (version 8.0). The cells were first analyzed using forward (FSC) and side (SSC) scatter gating to determine size and granularity, respectively. The ability of 1E10 mAb to inhibit adhesion of rPA-FITC on the cell surface was assessed by gating in SSC-A/FITC-A channels.

Effect of 1E10 mAb on PA oligomerization

Full-length 83 kDa rPA (PA83) was cleaved to produce PA63 and PA20. For that purpose, rPA was incubated with trypsin (Roche, Germany) at a concentration of 1 μg/mL at room temperature for 45 min. At the end of the incubation, the activity of the enzyme was inhibited by addition of a trypsin inhibitor from soybean (Roche, Germany) to a final concentration of 10 μg/mL. The sample was left under the same conditions. To stimulate oligomerization in the solution, all samples were added with rLF at a molar ratio of rPA : rLF = 2 : 1. At the next stage, 1E10 mAb was added to cleaved rPA at molar ratios of 1:1, 1:2, or 1:3. Control samples contained uncleaved rPA83, as well as PA63 + PA20, without addition of the antibody. All samples were incubated at 37°C for 60 min. Then, all samples were added with a 2-(N-morpholino) ethanesulfonic acid (MES) solution, pH 5.5, to a final concentration of 50 mM and incubated at 37°C for 30 min. For further separation in gradient (4–20%) PAGE under non-denaturing and non-reducing conditions, a sample loading buffer (according to Laemmli) without mercaptoetonol was added to the samples. After electrophoretic separation, the samples were transferred onto a Hybond-C Extra nitrocellulose membrane (GE Healthcare, UK) using an automatic Trans-Blot® Turbo™ Transfer System (Bio-Rad, USA). After transfer, the membrane was blocked by immersing it in skim milk with a fat mass fraction of no more than 0.5% and incubated on a thermostatted orbital shaker at 300 rpm and 37°C for 1 h. The membrane was washed with phosphate-buffer saline containing 0.05% Tween-20 (PBS-T; 137 mM NaCl, 2.7 mM KCl, 10 mM Na_2HPO_4, 1.76 mM KH_2PO_4, 0.05% Tween-20, pH 7.4). Then, the membrane was incubated with biotinylated anti-PA monoclonal mouse antibodies (clone 4F5 with specific activity against the PA domain III produced at the State Research Center for Applied Microbiology & Biotechnology) at a dilution of 5 μg/mL at 37°C for 1 h. After incubation, the membrane was washed three times with PBS-T, incubated with streptavidin conjugated to horseradish peroxidase (Streptavidin-Peroxidase Polymer, Ultrasensitive, Sigma, United States) at a dilution of 1 : 5,000, and washed six times with PBS-T. The reaction was visualized with a substrate mixture solution (0.05% diaminobenzidine (Sigma, USA), 0.015% H_2O_2 in PBS, pH 7.4). The reaction was stopped by washing with distilled water; then, the membrane was dried in air.

Investigation of the effect of 1E10 mAb on LT endocytosis by flow cytometry

To confirm the rPA–rLF interaction and subsequent LT endocytosis, we used flow cytometry. For this purpose, macrophages of the J774A.1 cell line (1×10^6 cells per sample) were incubated with rPA-FITC and rLF-Cy5 in the presence or absence of 1E10 mAb. Solutions containing rPA-FITC and/or rLF-Cy5 in the presence or absence of mAb were pre-incubated at 37°C for 1 h and added to the cells. J774A.1 macrophages (1×10^6 cells) separately incubated with rPA-FITC + rLF and rLF-Cy5 + rPA, as well as intact unstained J774A.1 cells, were used as controls. All samples with cells were incubated at 37°C in a CO_2 incubator at gentle stirring on an orbital shaker for 30 min. After incubation, all the samples were washed three times with PBS heated to 37°C. Proteins were removed from the cell surface by adding a 0.01% trypsin solution, incubated at 37°C for 5 min, and washed three times with warm PBS. The cells were fixed with 1% formalin. Samples were analyzed on a FACSAria III flow cytometer. Gating was performed using forward (FSC) and side (SSC) scatter, and the effect of 1E10 mAb on the LF–PA interaction and LT

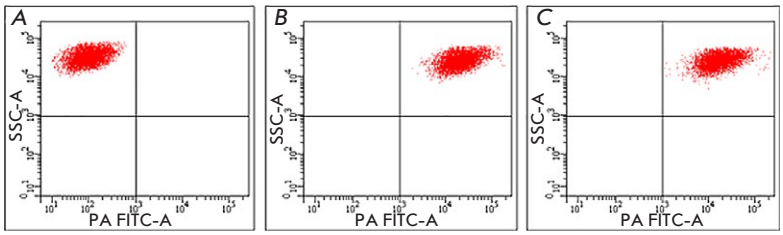

Fig. 2. Effect of 1E10 antibodies on rPA adhesion on the surface of J774A.1 cells. (*A*) – cell samples incubated in medium in the absence of rPA-FITC and 1E10 mAb. (*B*) – cell samples incubated with rPA-FITC. (*C*) – cell samples incubated with rPA-FITC pretreated with 1E10 mAb

endocytosis was assessed by gating in FITC-A and Cy5-A fluorescence channels.

Effect of 1E10 mAb on specific LT activity

Specific enzymatic activity of internalized LT was determined based on the presence of native or cleaved MEK. For that purpose, the following samples were prepared: J774A.1 mouse macrophages (1×10^7 cells) were incubated in the presence of LT at a molar ratio of rPA : rLF = 5 : 1 with and without 1E10 mAb. LT was pre-incubated with or without mAbs at 37°C for 1 h; then, the solutions were added to the cells and incubated at 37°C in a CO_2 incubator at gentle stirring on an orbital shaker for 30, 60, 120, and 240 min. J774A.1 macrophages (1×10^7 cells) without addition of LT or mAbs were used as an intact control. After incubation, the cells were precipitated by centrifugation; the cell pellet was lysed in 0.5% Triton X-100; then, a sample loading buffer (according to Laemmli) with mercaptoetonol was added to the samples. The resulting samples were applied to gradient (4–20%) PAGE. After electrophoretic separation, the Western blot analysis was performed using the standard technique described above. The membrane was incubated with rabbit monoclonal antibodies to MEK1 + MEK2 (Abcam, UK, ab200179) at a dilution of 1 : 10,000. After incubation with specific monoclonal antibodies to MEK, the membrane was washed with PBS-T and incubated with a goat anti-rabbit IgG antibody, (H + L) HRP conjugate, (Merck, Germany) at a dilution of 1 : 1,000 in PBS. The interaction was visualized by a color reaction using diaminobenzidine as described above.

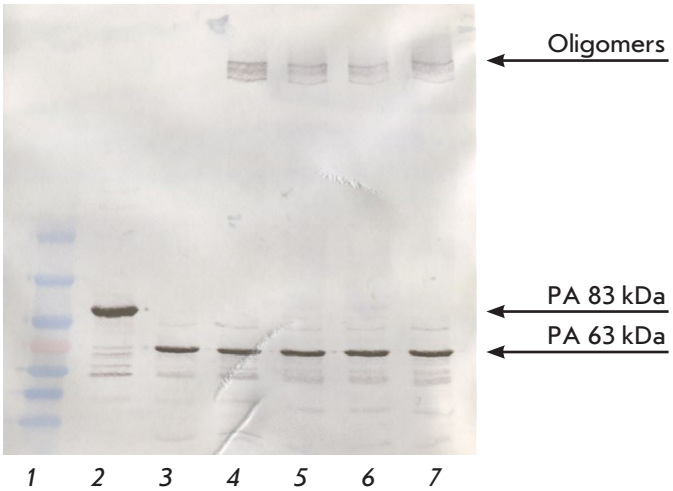

Fig. 3. Assessment of the 1E10 mAb ability to block the formation of PA63 oligomers. *1* – Molecular weight markers SM0671 (Fermentas, USA); *2* – Control rPA (83 kDa); *3* – PA63; *4* – PA63 + rLF; *5* – PA63 + 1E10 mAb (1:1) + rLF; *6* – PA63 + 1E10 mAb (1:2) + rLF; *7* – PA63 + 1E10 mAb (1:3) + rLF

RESULTS

Evaluation of the ability of 1E10 mAb to inhibit rPA adhesion on the surface of J774A.1 macrophage-like cells

Figure 2 shows the distribution of J774A.1 cells incubated with medium (*A*), FITC-labeled PA (*B*), and FITC-labeled PA pretreated with 1E10 mAb (*C*). A comparative analysis of the presented cytograms indicates identity of the J774A.1 cell distributions in *Figs. 2B* and *2C*. In both cases, after incubation with rPA-FITC, pretreated with 1E10 mAb or not, an equally high level of cell fluorescence was observed, which was an indication of adhesion of rPA-FITC to their surface. These findings indicate that 1E10 mAb does not block the binding of rPA to the surface of eukaryotic cells.

Evaluation of the ability of 1E10 mAb to block PA oligomerization

The effect of 1E10 monoclonal antibodies on PA oligomerization was studied using Western blotting. The addition of 1E10 mAb to cleaved 63 kDa PA at antigen:mAb molar ratios of 1:1, 1:2, and 1:3 did not affect oligomer formation (*Fig. 3*). Therefore, 1E10 mAb does not prevent PA oligomerization and prepore formation.

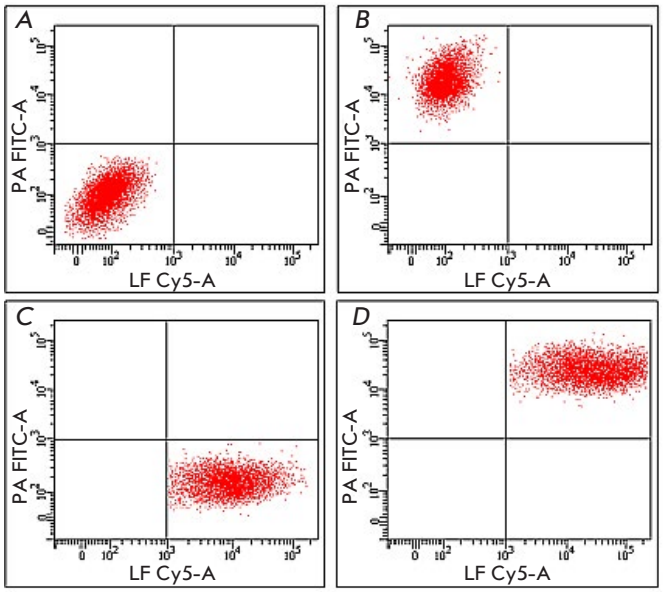

Fig. 4. Assessment of the 1E10 mAb effect on the rLF–rPA interaction and LT endocytosis. (*A*) – cell samples incubated in medium without LT or mAb. (*B*) – cell samples incubated with rPA-FITC and unlabeled rLF. (*C*) – cell samples incubated with unlabeled PA and rLF-Cy5. (*D*) – cell samples incubated with 1E10 mAb-pretreated rPA-FITC and rLF-Cy5

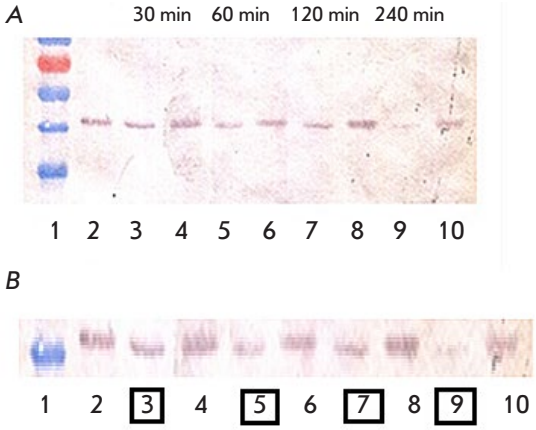

Fig. 5. Effect of 1E10 mAb on the rLF enzymatic activity towards MEK1 and MEK2. (*A*) – Western blot results correlated with molecular weight markers. (*B*) – Enlarged image of Western blot results. *1* – Molecular weight markers SM0671 (Fermentas, USA); *2* – Control: intact J774A.1 cells; *3* – J774A.1 cells + LT, incubation for 30 min; *4* – J774A.1 cells + (LT + 1E10 mAb), incubation for 30 min; *5* – J774A.1 cells + LT, incubation for 60 min; *6* – J774A.1 cells + (LT + 1E10), incubation for 60 min; *7* – J774A.1 cells + LT, incubation for 120 min; *8* – J774A.1 cells + (LT + 1E10), incubation for 120 min; *9* – J774A.1 cells + LT, incubation for 240 min; *10* – J774A.1 cells + (LT + 1E10), incubation for 240 min

Effect of 1E10 mAb on the rLF–rPA interaction and LT endocytosis

Figure 4 shows cytograms of J774A.1 cells. The results of a cytometric analysis showed that all J774A.1 cells in the presence of fluorochrome-labeled rPA and rLF pretreated with 1E10 mAb were characterized by a high level of intracellular fluorescence of FITC and Cy5 dyes (*Fig. 4D*), which is an indication that 1E10 mAb is unable to block the rLF–rPA interaction and LT endocytosis.

Effect of 1E10 mAb on specific LT activity

LF is a zinc-dependent endopeptidase that cleaves mitogen-activated protein kinases (MAPKKs), in particular MEK1 and MEK2, with removal of a 1.2 kDa peptide. *Figures 5A* and *5B* (lanes 3, 5, 7, 9) show that LT causes cleavage of MEK1 and MEK2 d, while LT pretreated with the 1E10 monoclonal antibody leaves MEK1 and MEK 2 intact. During long-term incubation (240 min), samples prepared from cell culture incubated with LT without addition of the mAb contained lower amounts of MEK1 and MEK 2 (*Figs. 5A* and *5B*, lane 9), which probably indicates the passage of rLF through the pore into the cell cytosol and the enzymatic activity of rLF towards MEK1 and MEK2, leading to cell apoptosis. Therefore, we have found that the 1E10 mAb–rPA interaction inhibits the enzymatic activity of LT towards MEK1 and MEK2.

DISCUSSION

In the Russian Federation, treatment of anthrax involves antibiotics and equine anti-anthrax immunoglobulin (33rd Central Research Institute of the Ministry of Defense of the Russian Federation, Russia) that contains polyclonal antibodies to antigens of the *B. anthracis* STI-1 vaccine strain and anthrax toxins. In generalized anthrax, antibiotics are not effective and the equine anti-anthrax immunoglobulin can cause side effects, including anaphylactic shock and serum sickness [20, 21]. The use of monoclonal antibodies provides a predictable efficacy in neutralizing the anthrax toxin, and the use of chimeric antibodies reduces allergization of the body. The use of mAbs against PA is the most promising strategy for the treatment of anthrax, which provides inhibition of

the toxic effect of anthrax toxins. This is due to the fact that PA is an essential LT subunit responsible for the toxic activity, which enables penetration of LF and EF into the cell cytosol. Our previously developed 1E10 mAb to PA domain IV had exhibited its lethal toxin-neutralizing activity and is considered a basis for the development of chimeric therapeutic mAbs. In this work, we analyzed the stages that might be affected by the lethal toxin-neutralizing activity of 1E10 mAb.

An analysis of the interaction of rPA with the surface membrane of J774A.1 macrophage-like cells, rPA oligomerization with prepore formation, rLF–rPA interaction, and LT endocytosis in the presence of 1E10 mAb revealed a lack of inhibitory activity 1E10 mAb towards these processes.

We supposed that 1E10 mAb, binding to PA, might disrupt the conformational rearrangements of PA during the formation of the pore for LF penetration into the cytosol, where it becomes enzymatically active. LF is known to hydrolyze MEK1 and MEK2 in the N-terminal region, with the cleavage of a 1.2 kDa peptide. MEK1 and MEK2 are mitogen-activated protein kinases (MAPKKs) that are involved in a variety of cellular processes. Using the MEK1 + MEK2 specific antibody, we showed that opsonization of PA by the 1E10 monoclonal antibody leads to the inhibition of the LT enzymatic activity towards MEK1 and MEK2.

CONCLUSION

Therefore, the mechanism of LT inhibition by the 1E10 monoclonal antibody involves the inhibition of the enzymatic activity of LF towards MEK1 and MEK2, which is likely associated with a disruption of the pore formation process and the impossibility of LF release into the cytosol.

In our opinion, this study has clearly demonstrated the potential of using therapeutic antibodies in the fight against infections. It should be noted that the COVID 19 pandemic clearly reinforced this conclusion. Along with great success in the development of vaccines, the use of virus-neutralizing antibodies in certain categories of patients is considered appropriate [22]. The generation of individual patient B-cell clones producing neutralizing antibodies is based on recently developed microfluidic technologies [23, 24]. These technologies have enabled a real breakthrough in the development of SARS-CoV-2-neutralizing therapeutic antibodies [25, 26]. The specificity of antibodies against the lethal toxin of *Bacillus anthracis*, which were produced in this study, may be further modified using combinatorial biology methods. ●

This study was conducted within the sectoral program of the Federal Service for Surveillance on Consumer Rights Protection and Human Wellbeing.

Conflict of interests. The authors declare that they have no conflicts of interest.

Compliance with ethical standards. This article does not contain any studies involving humans or animals as experimental objects.

REFERENCES

1. Bradley K.A., Mogridge J., Mourez M., Collier R.J., Young J.A. // Nature. 2001. V. 414. № 6860. P. 225–229.
2. Mock M., Fouet A. // Annu. Rev. Microbiol. 2001. V. 55. № 1. P. 647–671.
3. Marinin L.I. Human anthrax: epidemiology, prevention, diagnosis, and treatment [in Russian]. Obolensk. 2008. 408 p.
4. Hu K., Olsen B.R., Besschetnova T.Y. // Matrix Biology. 2017. V. 62. P. 105–114.
5. Noskov A.N. // Journal of Microbiology, Epidemiology, and Immunobiology. 2014. № 4. P. 92–101.
6. Jiang J., Pentelute B.L., Collier R.J., Zhou Z.H. // Nature. 2015. V. 521. № 7553. P. 545549.
7. Petosa C., Collier R.J., Klimpel K.R., Leppla S.H., Liddington R.C. // Nature. 1997. V. 385. № 6619. P. 833–838.
8. Wickner W., Schekman R. // Science. 2005. V. 310. № 5753. P. 1452–1456.
9. Hardenbrook N.J., Liu S., Zhou K., Ghosal K., Zhou Z.H., Krantz B.A. // Nat. Commun. 2020. V. 11. № 1. P. 1–10.
10. Krantz B.A., Finkelstein A., Collier R.J. // J. Mol. Boil. 2006. V. 355. № 5. P. 968–979.
11. Firstova V.V., Shemyakin I.G., Dyatlov I.A. // Infection and Immunity. 2019. V. 9. № 5–6. P. 639–647.
12. Belogurov A., Kozyr A., Ponomarenko N., Gabibov A. // Bioessays. 2009. V. 31. № 11. P. 1161–1171.
13. Durova O.M., Vorobiev I.I., Smirnov I.V., Reshetnyak A.V., Telegin G.B. // Mol. Immunol. 2009. V. 47. № 1. P. 87–95.
14. Stepanov A.V., Belogurov A.A., Ponomarenko N.A., Stremovskiy O.A., Kozlov L.V. // PLoS One. 2011. V. 6. e20991.
15. Glinka E.M., Edelweiss E.F., Sapozhnikov A.M., Deyev S.M. // Gene. 2006. V. 366. № 1. P. 97–103.
16. Belova E.V., Dubiley S.A., Kravchenko T.B., Kolesnikov A.V., Zakharova M.Yu., et al. // Molecular Genetics, Microbiology, and Virology. 2004. № 3. P. 21–26.
17. Kolesnikov A.V., Ryabko A.K., Shemyakin I.G., Kozyr A.V. // Bulletin of the Russian Academy of Medical Sciences. 2015. V. 70. № 4. P. 428–434.
18. Dixon T.C., Fadl A.A., Koehler T.M., Swanson J.A., Hanna P.C. // Cell. Microbial. 2000. V. 2. № 6. P. 453–463.
19. Belova E.V., Kolesnikov A.V., Zakharova M.Yu., Dubiley

S.A., Dyatlov I.A., Shemyakin I.G. // Bioorganic Chemistry. 2008. V. 34. № 5. P. 639–644.
20. Zakharova M.Yu., Kuznetsov N.A., Dubiley S.A., Kozyr A.V., Fedorova O.S., Chudakov D.M., Knorre D.G., Shemyakin I.G., Gabibov A.G., Kolesnikov A.V. // J. Biol. Chem. 2009. V. 284. № 27. P. 17902–17913.
21. Popescu N.I., Keshari R.S., Cochran J., Coggeshall K.M., Lupu F. // Microorganisms. 2020. V. 8. № 7. P. 1039.
22. Weinreich D.M., Sivapalasingam S., Norton T., Ali S., Gao H., Bhore R., Musser B. J., Soo Y., Rofail D., Im J. et al. // N. Engl. J. Med. 2021. P. 238–251.
23. Terekhov S.S., Smirnov I.V., Malakhova M.V., Samoilov A.E., Manolov A.I., Nazarov A.S., Danilov D.V., Dubiley S.A., Osterman I.A., Rubtsova M.P. et al. // Proc. Natl. Acad. Sci. USA. 2018. V. 115. № 38. P. 9551–9556.
24. Wine Y., Horton A.P., Ippolito G.C., Georgiou G. // Curr. Opin. Immunol. 2015. V. 35. P. 89–97.
25. Rappazzo C.G., Longping V.T., Kaku C.I., Wrapp D., Sakharkar M., Huang D., Deveau L.M., Yockachonis T.J., Herbert A.S., Battles M.B. et al. // Science. 2021. V. 371. № 6531. P. 823–829.
26. Guo Y., Huang L., Zhang G., Yao Y., Zhou H., Shen S., Shen B., Li B., Li X., Zhang Q., et al. // Nat. Commun. 2021. V. 12. № 1. P. 263. doi: 10.1038/s41467-021-22926-2.

GENERAL RULES

Acta Naturae publishes experimental articles and reviews, as well as articles on topical issues, short reviews, and reports on the subjects of basic and applied life sciences and biotechnology.

The journal *Acta Naturae* is on the list of the leading periodicals of the Higher Attestation Commission of the Russian Ministry of Education and Science. The journal Acta Naturae is indexed in PubMed, Web of Science, Scopus and RCSI databases.

The editors of *Acta Naturae* ask of the authors that they follow certain guidelines listed below. Articles which fail to conform to these guidelines will be rejected without review. The editors will not consider articles whose results have already been published or are being considered by other publications.

The maximum length of a review, together with tables and references, cannot exceed 50,000 characters with spaces (approximately 30 pages, A4 format, 1.5 spacing, Times New Roman font, size 12) and cannot contain more than 16 figures.

Experimental articles should not exceed 30,000 symbols (approximately 15 pages in A4 format, including tables and references). They should contain no more than ten figures.

A short report must include the study's rationale, experimental material, and conclusions. A short report should not exceed 12,000 symbols (5–6 pages in A4 format including no more than 12 references). It should contain no more than three figures.

The manuscript and all necessary files should be uploaded to www.actanaturae.ru:

1) text in Word 2003 for Windows format;
2) the figures in TIFF format;
3) the text of the article and figures in one pdf file;
4) the article's title, the names and initials of the authors, the full name of the organizations, the abstract, keywords, abbreviations, figure captions, and Russian references should be translated to English;
5) the cover letter stating that the submitted manuscript has not been published elsewhere and is not under consideration for publication;
6) the license agreement (the agreement form can be downloaded from the website www.actanaturae.ru).

MANUSCRIPT FORMATTING

The manuscript should be formatted in the following manner:

- Article title. Bold font. The title should not be too long or too short and must be informative. The title should not exceed 100 characters. It should reflect the major result, the essence, and uniqueness of the work, names and initials of the authors.
- The corresponding author, who will also be working with the proofs, should be marked with a footnote *.
- Full name of the scientific organization and its departmental affiliation. If there are two or more scientific organizations involved, they should be linked by digital superscripts with the authors' names. Abstract. The structure of the abstract should be very clear and must reflect the following: it should introduce the reader to the main issue and describe the experimental approach, the possibility of practical use, and the possibility of further research in the field. The average length of an abstract is 20 lines (1,500 characters).
- Keywords (3 – 6). These should include the field of research, methods, experimental subject, and the specifics of the work. List of abbreviations.
- INTRODUCTION
- EXPERIMENTAL PROCEDURES
- RESULTS AND DISCUSSION
- CONCLUSION

  The organizations that funded the work should be listed at the end of this section with grant numbers in parenthesis.
- REFERENCES

  The in-text references should be in brackets, such as [1].

RECOMMENDATIONS ON THE TYPING AND FORMATTING OF THE TEXT

- We recommend the use of Microsoft Word 2003 for Windows text editing software.
- The Times New Roman font should be used. Standard font size is 12.
- The space between the lines is 1.5.
- Using more than one whole space between words is not recommended.
- We do not accept articles with automatic referencing; automatic word hyphenation; or automatic prohibition of hyphenation, listing, automatic indentation, etc.
- We recommend that tables be created using Word software options (Table → Insert Table) or MS Excel. Tables that were created manually (using lots of spaces without boxes) cannot be accepted.
- Initials and last names should always be separated by a whole space; for example, A. A. Ivanov.
- Throughout the text, all dates should appear in the "day.month.year" format, for example 02.05.1991, 26.12.1874, etc.
- There should be no periods after the title of the article, the authors' names, headings and subheadings, figure captions, units (s – second, g – gram, min – minute, h – hour, d – day, deg – degree).
- Periods should be used after footnotes (including those in tables), table comments, abstracts, and abbreviations (mon. – months, y. – years, m. temp. – melting temperature); however, they should not be used in subscripted indexes (T_m – melting temperature; $T_{p.t}$ – temperature of phase transition). One exception is mln – million, which should be used without a period.
- Decimal numbers should always contain a period and not a comma (0.25 and not 0,25).
- The hyphen ("-") is surrounded by two whole spaces, while the "minus," "interval," or "chemical bond" symbols do not require a space.
- The only symbol used for multiplication is "×"; the "×" symbol can only be used if it has a number to its

right. The "·" symbol is used for denoting complex compounds in chemical formulas and also noncovalent complexes (such as DNA·RNA, etc.).
- Formulas must use the letter of the Latin and Greek alphabets.
- Latin genera and species' names should be in italics, while the taxa of higher orders should be in regular font.
- Gene names (except for yeast genes) should be italicized, while names of proteins should be in regular font.
- Names of nucleotides (A, T, G, C, U), amino acids (Arg, Ile, Val, etc.), and phosphonucleotides (ATP, AMP, etc.) should be written with Latin letters in regular font.
- Numeration of bases in nucleic acids and amino acid residues should not be hyphenated (T34, Ala89).
- When choosing units of measurement, SI units are to be used.
- Molecular mass should be in Daltons (Da, KDa, MDa).
- The number of nucleotide pairs should be abbreviated (bp, kbp).
- The number of amino acids should be abbreviated to aa.
- Biochemical terms, such as the names of enzymes, should conform to IUPAC standards.
- The number of term and name abbreviations in the text should be kept to a minimum.
- Repeating the same data in the text, tables, and graphs is not allowed.

GUIDENESS FOR ILLUSTRATIONS

- Figures should be supplied in separate files. Only TIFF is accepted.
- Figures should have a resolution of no less than 300 dpi for color and half-tone images and no less than 600 dpi.
- Files should not have any additional layers.

REVIEW AND PREPARATION OF THE MANUSCRIPT FOR PRINT AND PUBLICATION

Articles are published on a first-come, first-served basis. The members of the editorial board have the right to recommend the expedited publishing of articles which are deemed to be a priority and have received good reviews.

Articles which have been received by the editorial board are assessed by the board members and then sent for external review, if needed. The choice of reviewers is up to the editorial board. The manuscript is sent on to reviewers who are experts in this field of research, and the editorial board makes its decisions based on the reviews of these experts. The article may be accepted as is, sent back for improvements, or rejected.

The editorial board can decide to reject an article if it does not conform to the guidelines set above.

The return of an article to the authors for improvement does not mean that the article has been accepted for publication. After the revised text has been received, a decision is made by the editorial board. The author must return the improved text, together with the responses to all comments. The date of acceptance is the day on which the final version of the article was received by the publisher.

A revised manuscript must be sent back to the publisher a week after the authors have received the comments; if not, the article is considered a resubmission.

E-mail is used at all the stages of communication between the author, editors, publishers, and reviewers, so it is of vital importance that the authors monitor the address that they list in the article and inform the publisher of any changes in due time.

After the layout for the relevant issue of the journal is ready, the publisher sends out PDF files to the authors for a final review.

Changes other than simple corrections in the text, figures, or tables are not allowed at the final review stage. If this is necessary, the issue is resolved by the editorial board.

FORMAT OF REFERENCES

The journal uses a numeric reference system, which means that references are denoted as numbers in the text (in brackets) which refer to the number in the reference list.

For books: the last name and initials of the author, full title of the book, location of publisher, publisher, year in which the work was published, and the volume or issue and the number of pages in the book.

For periodicals: the last name and initials of the author, title of the journal, year in which the work was published, volume, issue, first and last page of the article. Must specify the name of the first 10 authors. Ross M.T., Grafham D.V., Coffey A.J., Scherer S., McLay K., Muzny D., Platzer M., Howell G.R., Burrows C., Bird C.P., et al. // Nature. 2005. V. 434. № 7031. P. 325–337.

References to books which have Russian translations should be accompanied with references to the original material listing the required data.

References to doctoral thesis abstracts must include the last name and initials of the author, the title of the thesis, the location in which the work was performed, and the year of completion.

References to patents must include the last names and initials of the authors, the type of the patent document (the author's rights or patent), the patent number, the name of the country that issued the document, the international invention classification index, and the year of patent issue.

The list of references should be on a separate page. The tables should be on a separate page, and figure captions should also be on a separate page.

The following e-mail addresses can be used to contact the editorial staff: actanaturae@gmail.com, tel.: (495) 727-38-60.